UNIVERSITAT DE BARCELONA

Holocene Climate variability in the Western Mediterranean Sea: an integrated oceanic and atmospheric perspective

Albert Català i Caparrós

UNIVERSITAT DE BARCELONA

Memòria de la Tesis presentada per

Albert Català i Caparrós

Holocene Climate variability in the Western Mediterranean Sea: an integrated oceanic and atmospheric perspective

Variabilitat climàtica de l'Holocè al Mar Mediterrani Occidental:
una perspectiva integrada de l'oceà i l'atmosfera

Sota la direcció de

la Doctora Isabel Cacho Lascorz i el Doctor Leopoldo D. Pena González

Programa de Doctorat de Ciències del Mar
Departament de Dinàmica de la Terra i de l'Oceà, Facultat de Ciències de la Terra
Universitat de Barcelona

Barcelona, 13 gener de 2023

Holocene Climate variability in the Western Mediterranean Sea: an integrated oceanic and atmospheric perspective

Variabilitat climàtica de l'Holocè al Mar Mediterrani Occidental:
una perspectiva integrada de l'oceà i l'atmosfera

Memòria de la Tesis Doctoral presentada per

Albert Català i Caparrós

sota la direcció de
la Dra. **Isabel Cacho Lascorz** i del Dr. **Leopoldo D. Pena González**

al Grup de Recerca Consolidat de Geociències Marines
del Departament de Dinàmica de la Terra i de l'Oceà de la Universitat de Barcelona
dins el programa de doctorat de Ciències del Mar

Barcelona, 13 de gener de 2023

El Doctorand | La directora | El director

Albert Català i Caparrós | Isabel Cacho Lascorz | Leopoldo D. Pena González

Aquesta Tesis ha estat realitzada al Departament de Dinàmica de la Terra i de l'Oceà a l Facultat de Ciències de la Terra de la Universitat de Barcelona, dins el Grup de Recerca Consolidat en Geociències Marines amb reconeixement de la Generalitat de Catalunya com a Grup de Recerca Consolidat (ref. 2017 SGR 315). La recerca que es presenta en aquesta Tesis ha estat finançada pel projecte TIMED associat a la ERC Consolidation Gran (ref. 683237) i per els projectes CHIMERA (ref. CTM2016-75411-R) i TRANSMOW (ref. : PID2019-105523RB-I00). També s'agraeix el suport per fiançar la instal·lació el laboratori blanc LIRA per el projecte d'infraestructures UNBA15-EE-2978

A la meva iaia
A la meva mare i al meu pare

Agraïments

Agradecimientos

A tothom

Agrair: quina bonica paraula amb tant de significat. Agrair és segurament un dels conceptes que en aquesta societat tant ens costa, que tant se'ns ha oblidat. Es pot agrair oralment, també en fets i segurament d'altres maneres. No obstant, sigui com sigui i sigui el que sigui, quan agraïm el què realment estem dient és que no ho hauríem pogut fer sense tu. Així doncs, a tothom que esteu aquí, gràcies, moltes i moltes gràcies, perquè sense vosaltres mai hauria arribat fins aquí.

Isa, qui ho hauria de dir. Encara recordo el dia que em vas trucar i em vas dir: sí vols tinc una feina al laboratori que podries fer, però només serà per tres mesos. Doncs tal dia farà 10 anys. Una dècada en la qual m'has donat la oportunitat de créixer com a científic. Durant tot aquest temps hem pogut compartir moltes coses tant a nivell professional com també personal. Per la part científica has sigut la persona que he tingut de referència, que t'escolto i penso, quan he d'aprendre. Sempre has tingut una possible interpretació de totes les dades, sempre t'he vist amb les ganes de voler saber més, de no donar-te per vençuda quan hi ha alguna cosa que no s'entén. De fet, quantes vegades he necessitat venir-te a veure quan estava capficat en qualsevol cosa que no entenia, que no li sabia donar cap explicació i ni resposta, que quasi desistia de continuar amb aquelles dades, i tu, de cop, girar-me tota aquesta perspectiva d'incomprensió i sortir d'allà pensant que el que tenia era meravellós. Molt poques persones tenen la capacitat de fer aquest exercici, però tu, ets capaç de donar-me les eines perquè m'empoderi. Perquè confiï molt més en mi, que em senti orgullós del què estic fent, i això ho has aconseguit tu. Moltes gràcies per haver confiat amb mi, moltes gràcies per fer-me créixer, moltes gràcies per haver-me donat la oportunitat. Moltes gràcies per ser-hi.

A ti Leo. Has sido otro de los pilares que me ha ayudado, y muchísimo a poder tirar para adelante esta tesis. Me has acompañando muy de cerca en todo este proceso, tanto en el mental, científico y técnico. Seguramente conmigo te has puesto las manos a la cabeza más de una vez. Pero poco a poco has conseguido que cada vez te las tengas que poner menos. Me has abierto la mente en no ser sobre-interpretativo con los datos, en realmente mirar lo que me cuentan y sobre todo a no ir más allá de los dichosos errores. Has estado allí para que aprenda y mejore como científico. Una cosa que mirando en perspectiva valoro muchísimo de ti y te estoy inmensamente agradecido es la confianza que me has dado en poder gestionar todo el tema del ICP-MS. Hiciste que me interesara por este tipo de análisis desde la parte más analítica, me

descubriste todo un mundo nuevo que ahora me apasiona. Y eso es gracias a ti, al interés que has puesto en explicarme cómo funciona todo, a escucharme cuando no entendía nada pero quinta vez. Gracias Leo por confiar en mí. Gracias por dejarme aprender, por hacerme poco a poco más científico, a que confíe mucho más en mí mismo. Muchas gracias por estar a mi lado.

Vull agrair al Grup de Recerca Consolidat de Geociències Marines per brindar-me la oportunitat de treballar dins d'aquest grup. Al seu, ara ja, ex-director en Miquel Canals que durant tants anys ha estat al peu del canó en tot moment. I a tots el membres del grup que heu fet que em senti com a casa. Hem compartit molts espais molt macos en l'àmbit de la recerca. Però també espais d'oci com excursions a castells, calçotades, soparets i festetes, que tots ells ajuden a construir un molt bon rotllo entre tots. Recentment recordo com una experiència molt i molt bonica la Dense Party. Aquest bon rotllo ajuda i moltíssim a tenir ganes de continuar treballant i que aquesta tesis hagi pogut sortir endavant. A tots vosaltres moltes gracies per tots els moments viscuts: Jaime, David, Toni, Galde, Anna Sànchez, Leo, Jose Luis, Isa, Liam, Guillem, Dimitris, Mercè, Jose Noel, Judit, Marc Cerdà, Jacobo, Ester, Marta, Sara Espinosa, Andreu, Maria de la Fuente, Sara Campderròs, Andrea, Mar, Marta Arjona Emma, Maria Jaume, Sergi Trias, Eduardo, Anna Aymà, Queralt, Uri, Rut, Olaia, Luis Valero, Itxaso, Patri, Aitor. També vull agrair aquelles persones que potser has estat menys temps pel departament, però que també m'han ensenyat i han deixat petja en mi: Giulia, Monica, Natale, Ana Santarosa, Javi.

Vull agrair als Centres Científics i Tècnics de la Universitat de Barcelona (CCiTUB) per poder analitzar totes les meves mostres a les seves instal·lacions. Però com ja se sap, els llocs no són res sense les persones que hi ha al darrera. Així que vull agrair a tots i totes les tècniques de la Unitat d'Anàlisi de metalls. Gràcies Bàrbara, Susana, Paco, Maite i Toni Padró. Tots vosaltres meu ajudat moltíssim a analitzar les meves mostres així com també a donar-me la llibertat de quedar-me sol a l'ICP-MS. En aquest aspecte m'heu donat la oportunitat i n'estic molt agraït de poder aprendre moltíssim com funcionen els ICP-MS. I així implicar-me al cent per cent en tot el procés d'anàlisi. Vull fer una menció especial a la Susana i per descomptat a la Maite. Moltes gràcies per aguantar-me durant tant de temps, amb els meus desordres en demanar-vos dies per poder analitzar. Que si ara et robo un dia Susana, que si ara ocupo mig mati o, què tal a les 6 de la tarda?. O ja no parlem si hem de canviar el sistema d'introducció. Deu ni do quina paciència heu tingut amb mi. Però la veritat, és que m'encanta venir-vos a veure. Segurament ho deveu haver notat. Sobre tot quan em dieu que us enviés un correu electrònic i al cap de 5 minuts ja entrava per la porta. Així m'estalviava enviar un correu, però el què guanyava era venir-vos a veure. I això diu molt de vosaltres. Així doncs, només puc agrair-vos moltíssim tot el què heu fet perquè pugui acabar aquesta tesis i totes les oportunitats que m'heu donat. Gràcies. També vull agrair a en Joaquin que ha fet que tots les resultats isotòpics mesurats en el forams pugin estar aquí.

Montse Guart, què faria jo sense tu. Sense cap dubte ets la persona que em desperta un somriure cada cop que et veig. Fas que anar a treballar sigui molt fàcil. Amb el anys m'he adonat que se m'enganxen certes coses de les persones; comentaris, expressions, maneres de fer etc. Però això no em passa amb tothom, sinó només amb les persones que realment em sento molt i molt còmode, lliure. I tu Montse, ets una d'aquestes persones. La il·lusió amb que ho fas tot i les ganes de compartir aquest alegria que tens amb tothom. Això simplement et fa increïble. I què més puc dir de tu. M'has ajudat amb tot el què ha calgut al laboratori. Al principi ens feies les comandes, recordes? Després vas dir que prou i els nens ens vam fer gran, però igualment si demanava alguna cosa, tu allà, la primera. I els agraïments també diuen que serveixen per disculpar-se. Així que, em sap greu que hagis hagut d'aguantar el meu desordre, tenir-ho tot pel mig, dir-te que demà ho recullo i aquest demà es trenta dies més tard (entre tu i jo. Ja sabem que són sis mesos, però si ho sap tothom quedo malament). Ai Montse, ja saps que sempre he pensat que no se què fas a la universitat. Perquè fins i tot la NASA es quedaria petita per tu. Gràcies per tot Montse.

Jaime, Oli, Patri, Judit. A vosaltres sou ser els primers que vaig conèixer quan vaig entrar aquí. Quan vaig començar amb tot aquest projecte que és la tesis. De vosaltres he après i m'enduc moltíssimes cosetes. D'en Jaime a entendre tot el món sedimentari i les granulometries i la importància que tenen També a ser extremadament meticulós amb certs protocols de laboratori (tot i que tots sabem que em queda molt per aprendre) de la Oli, l'estil, el disseny, fer que les coses siguin boniques. De la Patri, m'ho has ensenyat tot, de fet, la meva instructora. Ara no sabria què es un foram sí no m'ho haguessis explicat mai. Poden haver-hi moltes coses de cadascun, però de tots quatre és que heu entrat a formar part del meu món.

Ester, aquesta energia que has tingut en tot moment ha fet que aquesta tesis pogués tirar endavant. En moltes ocasions t'has assegut al meu costat a explicar-me com funcionaven moltíssimes coses, com el càlcul d'errors, les químiques, altres moments més personals. Sempre has tingut un momentet (o momentàs) per escoltar-me i ensenyar-me. Has tingut molta paciència amb mi, en tot el meu desordre i planificació de dies de laboratori. Moltes gràcies Ester per haver-me facilitat tant tota la feina, haver-me aguantat fotent-te la xapa i haver-me ensenyat tantíssimes coses. En aquesta tesis hi ha una gran part de tu. Moltíssimes gràcies.

Maria de la Fuente, que fuerza me has dado! Me acuerdo un día que me dijiste que no existían preguntas tontas y por lo tanto, todas las preguntas se podían hacer. Esa frase me ha acompañado desde que me la dijiste. Me ha ayudado muchísimo a ser mucho más lanzado, a creer muchísimo más en mí mismo, a perder la vergüenza. También me has enseñado muchísimo a ser una persona fuerte a creer en lo que pienso. Pero también, que bien me lo paso siempre cuando estoy a tu lado, en el barco, en una calçotada, en un día así por casualidad que nos contamos la vida... Y la mezcla de todas estas cosas hace que me sienta muy muy agradecido de que me hayas acompañado durante este proceso! Marieta, muchas gracia por ser así! Gracias!

Jose Noel que te vas a quedar ciego! Que decir de ti Jose, una de las personas más maravillosas que he conocido. Contigo he aprendido muchas cosas como la perseverancia, la constancia, la organización y la lista la podría alargar y alargar. Me acuerdo perfectamente cuando fuimos a Bremen a muestrear como locos en el MARUM y ya que estábamos allí pues nos comimos esos cachopos alemanes. Que ricos eh?! Hacía muy poco que habías llegado a Barcelona y en ese viaje ya me caíste genial. Me has ayudado muchísimo en toda la experiencia que conlleva hacer una tesis y como decía de ti he aprendido muchísimas cosas. Contigo, esa frase de mayor quiero ser como tú, es bien real. ¿Y te acuerdas ese viaje-mudanza a Francia? Que bien nos lo pasamos, aunque triste porque te marchabas de Barcelona. Pero pese a la distancia de Francia, la pandemia y ahora por fin en Granada estamos allí y siempre encontramos un huequito para vernos y disfrutar de la vida. Así que Jose, gracias por entrar a formar parte de mi vida.

Maria Jaume, comencem. Abans vull fer un petit incís a tots els lectors. Si en algun moment no enteneu que estic dient o escrivint, si us plau, contacteu amb la Maria Jaume que us farà una traducció simultània entre el meu idioma i el català/castellà/anglès. Ai Marieta, com... (aquella paraula que no sabem si sentim o no), tot i que ara si que potser la podem dir. Maria, fa molts anys que ens coneixem i jo crec que cada any que passa ens fa estar més a prop un de l'altre. En aquesta tesis has sigut una persona importantíssima, i també puc dir que si he arribat fins aquí, és en gran part gracies a tu. En molts moments m'has arrancat un somriure, per no dir una bona estona de rialles. Has aconseguit que canvies la visó de moltes coses, fent que li tragués ferro a allò que m'ofuscava. Tens l'enorme capacitat de transformar-me i aprendre a deixar fluir les coses. Realment, María, ets d'aquelles persones que necessito tenir al meu costat, que em fa feliç quan hi ets i que et trobo molt a faltar quan no hi ets. Maria, moltíssimes gràcies per haver-me acompanyat durant tant temps i haver estat incondicionalment al meu costat.

Benvolguda Judit. Tots dos sabem que *nacímos para ser perras*, però resulta que hem acabat tenint un doctorat. Que jo hagi arribat fins aquí, en una part molt i molt, però que molt gran, és gràcies a tu. Segurament sempre em sentiré que mai t'agraeixo prou el què has fet per mi. I ho dic de tot cor. Ets aquella persona completament altruista que m'has escoltat sempre, que m'has recolzat, que m'has fet tirar endavant en els moments que he estat una miqueta al pou. Has treballat amb mi, encara que potser allò no era la teva feina, però ho has fet simplement per ajudar-me, per què allò que féssim fos més amè. Sempre hi ets, sempre hi has sigut quan t'he necessitat. Se perfectament que sense tu, res hauria sigut el mateix. Formes part dels meus pilars com a persona, els que m'ajuden a no caure en cap sentit. Però si ho faig, se que ho faré sobre una bona base, que ets tu. Compartint la vida amb tu m'has ensenyat a ser molt més crític, a donar valor als petits gestos, a portar una vida molt més eco-rebel (rebel com tu, perquè tu ets la tres voltes rebel). Podria omplir i omplir pagines agraint-te tot el què he sentit al teu costat, el realment imprescindible que has sigut per mi en tot aquest trajecte, però llavors potser algú em diria *aviam què passa* amb la teva tesis. Judit, moltíssimes, moltíssimes gràcies.

Vier recordo el moment que et vaig trucar per dir-te que la Isa m'havia ofert començar el doctorat. En aquell moment vaig necessitar explicar-te tot el què em passava pel cap, les meves pors, si deia que si, o pel contrari deia que no. Feia molt temps que anava darrera d'això però quan se'm va proposar em vaig espantar. Gràcies per ajudar-me a trencar totes les pors, escoltar-me i acompanyar-me en aquest procés. I gràcies també per aguantar tota aquella tarda a la Rosa, jo parlant-te del zirconi i tu intentant entendre alguna cosa. I ara ja ho veus, finalment ho he escrit. Així que moltes gràcies per acompanyar-me en el procés.

Floretes aquest treball del cole està sent molt dur. Martina, Íngrid, Roger, Guillem, Raquel i Aniolet. Ha sigut molt difícil tot aquest temps de tancament de la tesis sense veure-us. Es segurament en aquests moments quan te n'adones que us necessito a la meva vida i que molt temps sense veure-us, us trobo a faltar molt. Gràcies per acompanyar-me en tot aquest procés, per entendre que hagi estat tant desaparegut i per ser els primes en respondre quan us necessito. Sempre hi sou i per mi sou família.

Jofre, que ja està! Durant els últims anys de la tesis has estat al peu del canó, aguantant segurament un rotllos considerables. Però aquesta recta final l'has viscut de molt i molt a prop. Des de fer-me de despertador, a portar-me menjar, a diverses trucades al dia... però tot això es podria resumir a que m'has estat acompanyat i molt, durant tot aquest procés. I t'he de dir, i és molt sincer, aquesta tesis no la podria haver acabat sense tu. Has sabut gestionar totes les meves emocions, m'has animat cada dia perquè continues endavant, a que no defallís en cap moment, en fer-me recuperar el somriure. Has aconseguit que en cap moment em sentis sol, que sempre em sentís acompanyat. I ja no parlaré de la part finalíssima a contra rellotge. En tot aquest procés de la tesis, m'he adonat que has estat incondicionalment al meu costat. I sentir això, és increïble. Soc molt feliç sabent que ets aquí. I Jofre, anirà plorant els núvols grisos, però ploraran d'alegria i de felicitat perquè se, que estàs al meu costat.

A la incondicional i incombustible família, moltes gràcies. Moltes gràcies a tots pels ànims i el suport que m'heu donat en tot aquest camí i en tots els altres de la meva vida.

Contents

Chapter III: Results

Chapter IV: Discussion

List of figures

Chapter I: Introduction

Chapter II: Methodology

Chapter III: Results

Chapter IV: Results

(CAT)

Resum de la Tesis

La regió mediterrània és molt sensible a la variabilitat climàtica moderna. Està situada en una zona climàtica subtropical temperada i envoltada quasi íntegrament per grans masses continentals fent que tant el clima com l'oceanografia estiguin controlats en gran mesura per la variabilitat climàtica dels sistemes atmosfèrics subtropicals i subpolars. El mar Mediterrani occidental intercanvia les aigües amb l'oceà Atlàntic a través de l'estret de Gibraltar, on les aigües superficials Atlàntiques entren al Mediterrani, mentre que les aigües Mediterrànies surten cap a l'Atlàntic en profunditat, fent així un intercanvi net de calor i sals que és molt sensible als canvis climàtic presents i passats. Aquesta tesi presenta un nou enfocament per a l'estudi i la comprensió de la variabilitat climàtica natural passada de la regió Mediterrània mitjançant l'anàlisi dels canvis ocorreguts a l'oceà i a l'atmosfera durant l'Holocè. Aquesta tesi pretén millorar la nostra comprensió sobre els mecanismes i les respostes climatològiques i oceanogràfiques que han modulat el clima del sud de la Península Ibèrica durant els últims 11.700 anys. A més, es presenten nous avenços metodològics relevants en eines geoquímiques «d'última generació» per estudiar els canvis hidrològics passats i, per primera vegada, es validen aquests mètodes utilitzant uns registres de sèries temporals modernes al Mar d'Alboran. Aquesta tesi s'ha basat en quatre punts clau:

En el primer punt clau es presenta un nou registre d'alta resolució que reconstrueix les temperatures superficials del mar (SST de l'anglès Sea Surface Temperatures) durant l'última desglaciació i l'Holocè. Es basa en les relacions de Mg/Ca mesurades en el foraminífer planctònic *Globigerina bulloides*. Aquest nou registre es compara amb altres registres de Mg/Ca, així com també amb altes registre prèviament publicats de SST a través d'alquenones de la mateixa regió i també durant el mateix període temporal. En tots el casos s'observa un al nivell de coherència entre els diferents registres de Mg/Ca, però alhora hi ha grans discrepàncies quan es compara amb els registres d'alquenones. S'argumenta que aquestes discrepàncies venen determinades per un canvi en la resposta dels dos indicadors (*G. bulloides* i alquenones) durant la desglaciació. Es fa la hipòtesi que *G bulloides* presenta una estratègia de resiliència, canviant la seva temporada principal de creixement i en conseqüència, durant la desglaciació el Mg/Ca registre un escalfament més petit que el que registren les alquenones. D'altre banda, durant l'Holocè, la variabilitat que s'observa en la reconstruccions de les SST a través del Mg/Ca és molt més elevada que no pas en els registres de les alquenones. Es proposa que les SST reconstruïdes a partir del Mg/Ca registren la variabilitat de temperatures durant la primavera, mentre que les alquenones, que mostren menys oscil·lacions, en realitat estan representant una mitja anual de les temperatures superficials del mar. El registre de Mg/Ca derivat a SST diferencia l'Holocè en tres períodes: (1) el període més càlid que succeeix durant l'Holocè Inferior (11.7 – 9 ka BP); (2) un refredament continu durant l'Holocè Mig que culmina al 4.2 ka BP registrant el període més fred de l'Holocè; (3) l'Holocè Superior (4.2 ka fins l'actualitat) on no es registre cap escalfament

o refredament però les oscil·lacions d'escala mil·lenària de SST s'incrementen. Aquest registre de SST es posa en context amb l'Atlàntic, discutint com es modifiquen les aigües Atlàntiques quan entren al Mediterrani, així com també la implicació que te la circulació de l'Atlàntic Nord. Així doncs, es proposa un estret lligam entre els patrons de circulació de l'Atlàntic Nord amb l'entrada d'aigües al mar Mediterrani que controlen la variabilitat climàtica de l'Holocè en aquesta regió.

El segon punt clau d'aquesta tesi es basa en el desenvolupament d'un nou mètode ràpid, eficient i fiable per preparar mostres de sediments lítics per a l'anàlisi d'isòtops radiogènics ($^{87}Sr/^{86}Sr$, $^{143}Nd/^{144}Nd$, $^{208}Pb/^{204}Pb$, $^{207}Pb/^{204}Pb$ i $^{206}Pb/^{204}Pb$). Es desenvolupen dos nous mètodes: el primer amb l'objectiu d'aconseguir una digestió total de la fracció lítica, mentre que el segon té l'objectiu de separar i purificar els diferents sistemes isotòpics (Sr, Nd, Pb) de la fracció lítica mitjançant l'ús d'una única columna cromatogràfica amb la resina DGA. El nou mètode de separació de Sr, Nd i Pb per columnes cromatogràfica es desenvolupa en un sol pas utilitzant un sistema de buit de pressió controlada aplicat a cada columna.

El tercer punt clau d'aquesta tesi es basa en un nou enfocament per estudiar la procedència de la fracció de sediments lítics capturada per una trampa de sediments entre els anys 1997 i 1998 davant de la costa de Màlaga. Aquesta trampa de sediments va capturar les partícules litògenes que s'enfonsaven al mar d'Alboran amb una resolució aproximadament quinzenal cobrint doncs un any complet. Així doncs, d'aquesta manera es va obtenir un registre anual dels canvis en la quantitat i la naturalesa de les partícules litogèniques. Per caracteritzar l'àrea font d'aquestes partícules que arriben al mar d'Alboran, es s'ha desenvolupat un estudi sistemàtic de procedència utilitzant tècniques de geoquímica d'isòtops. En particular, els isòtops radiogènics de $^{87}Sr/^{86}Sr$, $^{143}Nd/^{144}Nd$, $^{208}Pb/^{204}Pb$, $^{207}Pb/^{204}Pb$ i $^{206}Pb/^{204}Pb$ s'han mesurat en la fracció de sediments lítics, i la senyal d'aquestes relacions isotòpiques mesurades s'ha comparat amb la senyal de les àrees fonts potencials i els seus corresponents valors isotòpics de referència. En aquest sentit, a causa de la ubicació singular del mar d'Alboran les partícules litogèniques s'introdueixen típicament tant a partir de descàrregues fluvials i/o a partir de plomes de pols atmosfèrica provinent del desert del Sàhara. Aquests nous isòtops d'Sr i Nd indiquen clarament que la font primària de sediments que arriben a les trampes de sediments provenen majoritàriament de les descàrregues fluvials. Tot i que hi ha evidències de presència de pols sahariana en totes les mostres, aquesta senyal és generalment molt diluïda degut a la quantitat de sediments transportats pels rius. Però, només durant els períodes de l'any amb un mínim d'escorrentia fluvial és possible distingir clarament la senyal isotòpica del Sàhara en les mostres de sediments litogènics. Comparant els registres d'isòtops radiogènics generats amb els registres instrumentals de precipitació a Màlaga i les descàrregues del riu Guadalhorce (situats davant de la trampa de sediments) s'observa que les variacions observades en la composició isotòpica dels materials terrígens (particularment les relacions d'isòtops Sr) estan estretament relacionades amb les precipitacions i les descàrregues fluvials. Amb aquest estudi és clarament possible diferenciar a través de la relació $^{87}Sr/^{86}Sr$ aquells esdeveniments que ocorren durant les primeres

pluges que es produeixen després de l'estació seca (tardor i hivern primerenc), especialment aquells associats als esdeveniments torrencials i també aquells períodes al final de l'estació de pluges seguides per condicions d'estiu sec (finals d'hivern a tardor).

El quart punt aprofita els canvis descrits en les mesures d'isòtops radiogènics en les trampes de sediments actuals com a resposta als canvis en els patrons de precipitacions a la Mediterrània occidental. Utilitzant aquests nous resultats com a anàlegs actuals, ara és possible extrapolar aquest model de barreja isotòpica per reconstruir els canvis passats en els patrons de pluja durant l'Holocè. Amb aquest objectiu en ment, en aquesta tesi s'han mesurat les relacions isotòpiques de $^{87}Sr/^{86}Sr$, $^{143}Nd/^{144}Nd$, $^{208}Pb/^{204}Pb$, $^{207}Pb/^{204}Pb$ and $^{206}Pb/^{204}Pb$ en la fracció litogènica dels sediments marins, en el mateix testimoni del Mar d'Alboran on es van mesurar les Mg/Ca-SST. Aplicant els models de barreja d'isòtops radiogènics desenvolupats per a les trampes de sediments, es mostra que durant l'Holocè la font de descàrrega fluvial es relativament constant en aquesta ubicació. A més es mesura la composició elemental del sediment total en XRF- core scanner i els valors obtinguts es tracten estadísticament utilitzant un anàlisis de components principals. Aquest tractament estadístic revela que Zr i K són potencialment afectats per canvis hidrològics. Basant en les mesures d'isòtops radiogènics en la fracció lítica dels sediments marins, així com amb l'anàlisi de XRF, permet subdividir l'Holocè en tres períodes climàtics principals segons els canvis en els patrons de precipitació: (1) l'Holocè inferior (11.7 - 7.6 cal kyr BP), descrit amb un règim de precipitacions relativament constant, amb una reducció de l'erosió i del transport de sediments fluvials cap al mar; (2) l'Holocè mitjà (7.6 - 4.2 cal kyr BP) que es descriu com un període transitori marcat per un augment progressiu de l'erosió i el transport de sediments dels rius, potencialment com a resposta a un augment regional de l'aridesa i/o un augment en el caràcter torrencial de les pluges, arribant a una màxima expressió en el registre sedimentari al voltant de 4.2 cal kyr BP. (3) el període de l'Holocè tardà (4,2 – 0 cal kyr BP) és marcat per una variabilitat mil·lenària més forta en comparació amb els intervals anteriors. S'argumenta que aquest últim període correspon a l'establiment de patrons de pluja anàlegs a les condicions actuals.

(ENG)

Abstract

The Mediterranean region is very sensitive to modern climate variability. Located in a temperate subtropical climatic zone and surrounded almost entirely by large continental masses, the Mediterranean region climate and oceanography are largely controlled by the climatic variability of the subtropical and subpolar atmospheric systems. The western Mediterranean Sea exchanges seawater through the Strait of Gibraltar with the Atlantic Ocean, where inflowing surface waters from the Atlantic Ocean enter this region. In contrast, Mediterranean waters outflow into the Atlantic at depth, a net exchange of heat and salts that is very sensitive to present and past climatic changes. This thesis presents a new approach to studying and understanding past natural climatic variability of the Mediterranean region by analysing the changes in the ocean and the atmosphere during the Holocene. This thesis aims to improve our understanding of the mechanisms and climatic/oceanographic responses that have modulated the southern Iberian Peninsula climate during the last 11.700 years. In addition, relevant methodological advances in «state-of-the-art» geochemical tools are implemented here to study past hydrological changes and, for the first time, these methods are validated using a modern time series record in the Alboran Sea. This thesis has been built on four main key points:

First, a new high-resolution deglacial and Holocene Sea Surface Temperature (SST) reconstruction is presented for the Alboran Sea (western Mediterranean), based on Mg/Ca ratios measured in the planktonic foraminifera *Globigerina bulloides.* This new SST record is evaluated by comparison with other Mg/Ca–SST records and previously published alkenone–SST reconstructions from the same region. The comparison shows a high degree of coherence between the different Mg/Ca–SST records but strong discrepancies compared to the alkenone–SST records. We argue that these discrepancies arise from differences in the sensitivity of the proxy–response to environmental changes. A working hypothesis in this thesis is that the discrepancy in SSTs reflects a resilience strategy of planktonic foraminifera *G. bulloides,* shifting its main growing season into the colder SST upwelling season (spring) thus explaining the shorter deglacial warming in Mg/Ca records compared to alkenones. Interestingly, Holocene short–term SST variability is larger in the Mg/Ca–SST record than in the alkenone–SST records. It is proposed that the larger Mg/Ca–SST variability reflects spring temperature variability, while the smoothed alkenone–SST variability represents averaged annual temperatures. The Mg/Ca–SST record differentiates the Holocene into three periods: (1) the Early Holocene (11.7 – 9 kyr BP) with the warmest SST values recorded; (2) the Middle Holocene (9 – 4.2 kyr BP) characterised by a continuous cooling trend that culminated in the coldest Holocene SST at around 4.2 kyr BP; (3) the Late Holocene (4.2 kyr BP to present) characterised by the lack of clear cooling/warming trends but enhanced millennial-scale variability. This SST evolution is discussed in the context of the changing physic-chemical properties of inflowing Atlantic surface water associated with changes in the North Atlantic circulation conditions as well as with regional hydrographical and atmospheric changes. It is proposed that a close mechanistic link between North Atlantic

circulation patterns and the inflow of surface waters into the Mediterranean played a crucial role in controlling the Holocene climatic variability of this region.

The second key point of this thesis is based on developing a new fast, efficient and reliable method to prepare lithogenic sediment samples for the radiogenic isotope analysis ($^{87}Sr/^{86}Sr$, $^{143}Nd/^{144}Nd$, $^{208}Pb/^{204}Pb$, $^{207}Pb/^{204}Pb$ and $^{206}Pb/^{204}Pb$). Two new methods are developed: the first is targeted to achieve a total digestion of the lithogenic fraction, whereas the second is aimed at separating and purifying the different isotopic systems (Sr, Nd, Pb) in the lithogenic fraction by using a one single pass chromatographic column with the DGA resin. The new chromatographic separation method for the Sr, Nd and Pb is developed in a single step using a controlled-pressure vacuum system applied to each column.

The third key point of this thesis is based on a novel approach to studying the provenance of the lithic sediment fraction captured by a sediment trap between 1997 and 1998 in front of the Malaga coast. This sediment trap captured the sinking lithogenic particles in the Alboran Sea with an approximately bi-weekly resolution for a complete year; thus, an annual record of changes in the amount and nature of particles was obtained. A systematic provenance study is developed using isotope geochemistry techniques to characterise the source area of the lithogenic particles arriving in the Alboran Sea. In particular, the radiogenic isotopes of $^{87}Sr/^{86}Sr$, $^{143}Nd/^{144}Nd$, $^{208}Pb/^{204}Pb$, $^{207}Pb/^{204}Pb$ and $^{206}Pb/^{204}Pb$ were measured in the lithogenic sediment fraction, and the measured isotopic ratios signal were compared with the potential source areas and their corresponding isotopic endmember values. In this sense, due to the singular location of the Alboran Sea, lithogenic particles are typically introduced by both from fluvial discharges and/or atmospheric dust plumes from the Sahara desert. These new Sr and Nd isotope results clearly indicate that river discharge is the primary source of sediments arriving into the sediment traps. Even though there is evidence for a degree of presence of Saharan dust signal in all the samples, this endmember is generally significantly diluted by the sheer mass of sediments transported by rivers. Only during periods of the year with minimum river runoff, it is possible to clearly distinguish the Sahara isotopic signature in the lithogenic sediment samples. A comparison of the newly generated radiogenic isotope records with instrumental rainfall gauge records in Malaga and the Guadalhorce river discharges (located in front of the sediment trap) indicates that the observed variations in the isotopic composition of terrigenous materials (particularly Sr isotope ratios) are closely linked to the rainfall and river discharges. Therefore it is now possible to clearly differentiate through the $^{87}Sr/^{86}Sr$ ratio those events when the first rains occurred after the dry season (autumn and early winter), especially those associated to the torrential events and also those periods at the end of the rainy season followed by dry summer conditions (late winter to autumn).

The fourth point takes advantage of the mechanistic changes described in the radiogenic isotope measurements in present-day sediment traps as a response to changes in rainfall patterns in the western Mediterranean Sea. Using these new results as a present-day analogue, it is possible now to extrapolate this isotopic mixing model to reconstruct past changes in rainfall

patterns during the Holocene. With this goal in mind, in this thesis has been measured $^{87}Sr/^{86}Sr$, $^{143}Nd/^{144}Nd$, $^{208}Pb/^{204}Pb$, $^{207}Pb/^{204}Pb$ and $^{206}Pb/^{204}Pb$ isotope ratios in the lithogenic fraction of marine sediments, at the same core site located in the Alboran Sea where the Mg/Ca-SST were measured. By applying the radiogenic isotope mixing models developed for the sediment traps, it is shown that a relatively constant fluvial discharge source of sediments during the Holocene at this location. Moreover, the elemental composition of the bulk sediment measured on the XRF-core scanner is statistically treated using the principal component analyses. This treatment reveals that Zr and K are potentially affected by hydrological changes. Based on the new measurements of radiogenic isotopes in lithogenic sediments as well as bulk XRF analysis, we can clearly subdivide the Holocene into three main climatic periods as defined by changes in the rainfall patterns: (1) the Early Holocene (11.7 – 7.6 cal kyr BP), described as relatively constant rainfall regime, reduced erosion and transport of fluvial sediments towards the sea; (2) the Middle Holocene (7.6 – 4.2 cal kyr BP) which is described as a transitional period marked by a progressive increase in erosion and sediment transport by rivers, potentially as a response to a regional aridification increase and/or enhanced torrential character of the rains, reaching a maximum expression in the sedimentary record at around 4.2 cal kyr BP. (3) the Late Holocene period (4.2 – 0 cal kyr BP) is punctuated by stronger millennial-scale variability compared to the previous intervals. It is argued that this last period corresponds to the establishment of rainfall patterns analogue to present-day conditions.

Chapter 1

Introduction

“And at once I knew, I was not magnificent”
Holocene, Bon Iver

1.1 Earth Climate System

Climate is defined as the long-term (about 30 years) average of weather parameters such as air temperatures and precipitation for a particular region. Based on these parameters, the climates on Earth have been classified into five main groups (Köppen-Geiger, 1936). Earth ecosystems, including humans, have adapted to these climates, and actually, they play an essential role in our lives. Climate conditions dictate the kind of clothes we wear, the kind of houses we build, the plants we crop and thus our food, but they also define several of the characteristics of our cultures and our behaviour, among many other aspects of our lives. Therefore, the climate defines the planet's living way, and thus any change in climate could have a profound impact on our planet's life. In the current context of global climate change, life on Earth faces several threats, and it becomes a scientific priority to improve our understanding of the Earth's climate system.

Looking at the climate system from a long time perspective allows us to understand better the main drivers or forces that transform this system. Major changes in the climate system have been driven by external forcings or changes imposed by processes or elements externs to the Earth's Climate System. However, they have the potential to modulate the climate by introducing radiative changes to it. These external forcings include changes in plate tectonics, the Earth's orbit, and the Sun's strength (Fig. 1.1; Ruddiman, 2001). Any variation in these external forcings would directly impact the atmosphere, vegetation, ice, land surface and the ocean. Each of these earth components are interconnected and form the climate system (Fig. 1.1). The response produced by the external forcings on the climate system will define the character of any climate change. These external forcings trigger a disequilibrium in the climate system affecting one (or more) of its components resulting in a series of changes that can put into action different climate feedbacks (Fig. 1.1). When the changes within the climate system amplify the response to the initial change; they define as a positive feedback. Conversely, when the response to the initial change is reduced, it is a negative feedback. An example of positive climate feedback is triggered by an initial cooling in the system that increases the snow and ice cover and thus increases the albedo or the Earth's reflectivity. Consequently, the initial cooling would further increase, letting more snow and ice form (Ruddiman, 2001). This has been a powerful positive feedback operating during past climate variability, but it is currently operating in the opposite direction.

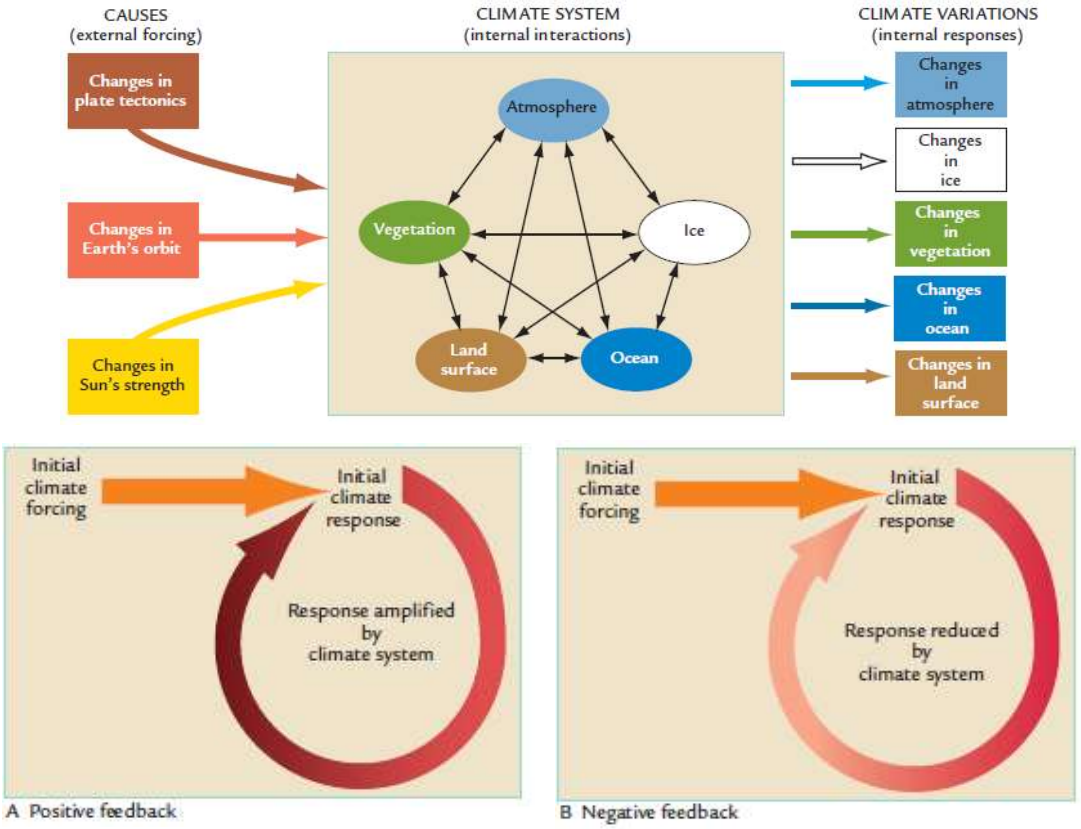

Figure 1.1 – *In the upper panel, the Earth's climate system and interactions of its components. In the lower panel, an example scheme for positive and negative feedback. (Source: Ruddiman, 2001)*

1.1.1 The atmospheric system

The Earth's climate is powered by the incoming radiation of the Sun, which is transformed into heat. The incoming radiation from the Sun spreads unequally over the Earth's surface, with higher intensity at lower latitudes (between the tropics) and lower in higher latitudes (near the poles). The atmosphere tends to compensate for this general heat imbalance redistributing it by an atmospheric transport structured into three convection cells for each hemisphere. These cells form the general circulation of the atmosphere (Fig. 1.2a). The position of these three-cell systems determines the major atmospheric variations controlling the current climate regions. The enhanced insolation at the equator warms the air that rises and condenses in altitude, forming a band of heavy rainfall called the Intertropical Convergence Zone (ITCZ) (Fig. 1.2a). This convergence zone is the engine of the Hadley Cells that extend from the equator to 30° latitude N and S, where the air descends and forms a high pressures systems of very dry winds and without precipitation. Consequently, major desert systems develop around these latitudes (Sahara, Gobi, Atacama, Australia, Kalahari and Great Basin). After the Hadley cells, toward higher latitudes, develop the Ferrel Cells that transport warm air toward higher latitudes that finally collide at around 60° with the cold air originating in the poles and transported by the Polar Cells. The boundary of these two cells, called the polar front, induces a lower pressure system, producing high precipitations linked to the frontal systems (Fig. 1.2a). Therefore, these

atmospheric cells are responsible for the energy and humidity transfer across latitudes and regions. Their boundaries control the position of the main wind bands known as Jet Stream (Fig. 1.2b). These atmospheric systems' position has latitudinal variations shifting towards lower latitudes, driven mainly by seasonal changes in insolation. This led to changes in the position of cold or warm air masses or the development of droughts or heavy rainfalls.

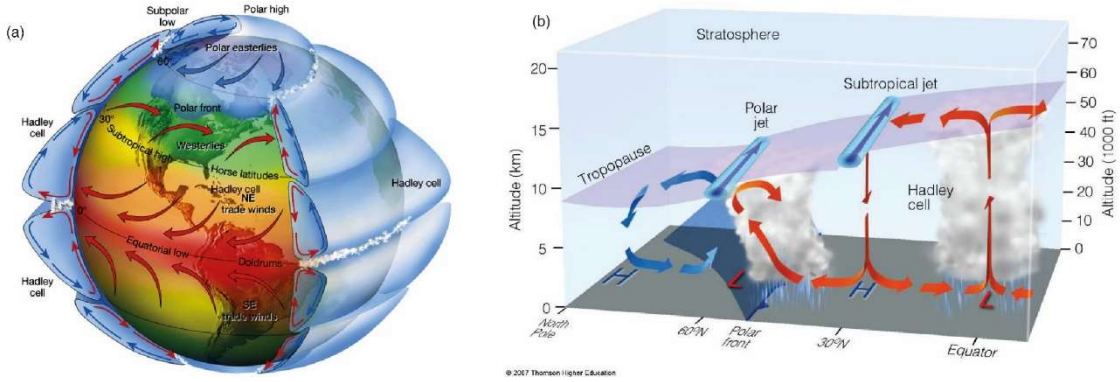

Figure 1.2 – General Circulation of the Atmosphere. *(a) General patterns of the atmospheric circulation (b) Circulation associated with each cell and the boundary interactions forming the jet streams.*

1.1.2 The oceanic system

The ocean is another crucial element within the Earth's Climate System which is also directly heated by the incoming radiation, and as the atmosphere, with its movement, redistributes that energy across different latitudes. The ocean surface is moved by the prevailing winds fuelled by the general atmospheric circulation. However, due to the Coriolis Effect, the surface currents do not follow the same direction as the winds; they are turned, creating oceanic gyres. In the Atlantic Ocean, as a result of the westerly component of the mid-latitude winds and the easterly component of the tropical winds, a prominent subtropical gyre is formed. This oceanic clockwise gyre tends to concentrate the water transport towards the western boundary of the gyre due to the Coriolis Effect, where its transport reaches the highest depths (600 to 1000 meters below the sea level) (Fig 1.3). This western boundary current moves northwards, originating the well-known Gulf Stream along the east coast of North America. This current continues north-eastwards towards Europe as the North Atlantic Current (NAC), bifurcating in the eastern North Atlantic (Fig. 1.3). A significant fraction moves southwards and then westwards to close the subtropical gyre, while the branch that escapes northwards reaches the subpolar gyre (SPG). All this meridional movement of the surface currents forms part of the so-called Atlantic Meridional Overturning Circulation (AMOC), a crucial component in the Earth's climate system. the surface component of the AMOC transports buoyant waters northward (Gulf Stream and NAC) towards higher latitudes in the North Atlantic. During their northward displacement, waters change their proprieties through intense heat loss and evaporation, leading to increased density. As a result, the North Atlantic Deep Water is formed and travels southward, becoming a key component of the global ocean circulation (Weijer *et al.,* 2022; Buckley and Marshall, 2016). (Fig. 1.3).

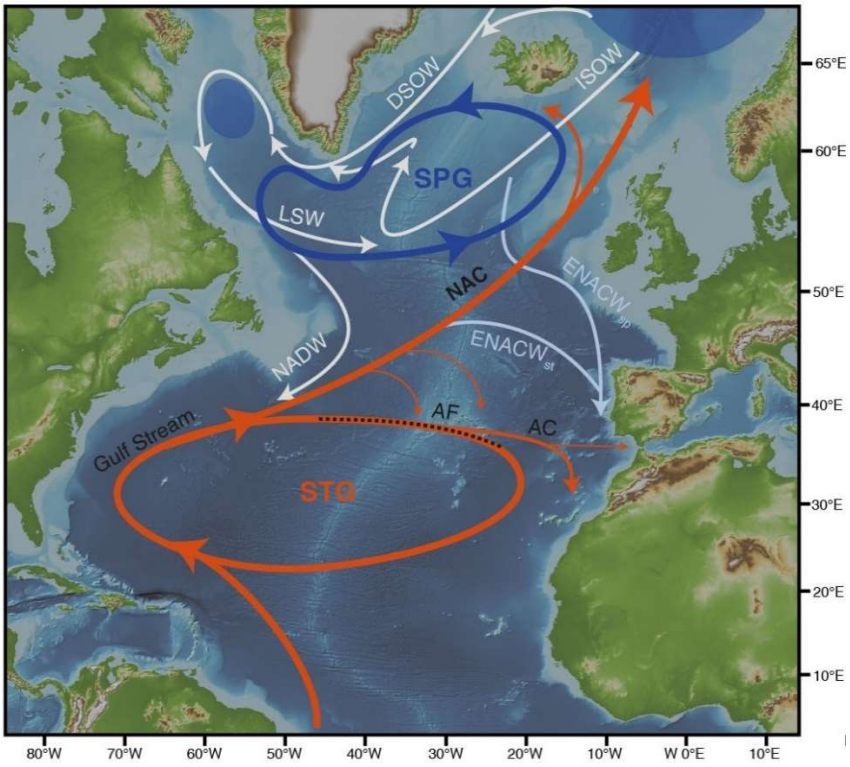

Figure 1.3 - Schematic North Atlantic Ocean Circulation. *In red are the main surface currents: NAC – North Atlantic Current; AC – Azores Current. In light grey, the main intermediate and deep waters: LSW – Labrador Sea Water; DSOW – Denmark Strain Overflow Water; ISOW – Icelandic-Scotland Outflow Water; NADW – North Atlantic Deep Water. In light blue, the central waters: ENACWsp – st – Eastern North Atlantic Central Water Subpolar or Subtropical. STG – Subtropical gyre; SPG – Subpolar gyre. In a black dashed line: AF – Azores Front. Blue-filled circles: Locations of the deep water formation. Basic map obtained from Marine Geoscience Data System © 2008-2018 – all rights reserved.*

1.1.3 Interconnections atmosphere – ocean

Both ocean and atmosphere are the two climatic components that can transport heat from lower to higher latitudes. Specifically, the Atlantic Ocean is unique in transporting net heat from the Southern Hemisphere across the equator to boreal latitudes (Volkov *et al.,* 2019). Much of the heat transported with the northward branch of the NAC is transferred to the atmosphere and, due to the westerlies, contributes to the temperate climate in northwest Europe (Sutton and Hodson, 2005). Therefore, the ocean and the atmosphere are well interconnected. The intensity and position of the atmospheric cells over the Atlantic show an interannual scale variability represented by the North Atlantic Oscillation (NAO; Fig 1.4a), defined as the pressure differences between the semi-permanent Icelandic Low-Pressure System and the Azores High-Pressure system. NAO presents variations from sub-seasonal to multi-decadal time scale and is associated with the positioning and strengthening of the polar front that is ultimately associated with the jet stream (Gerber and Vallis, 2009). A week jet stream becomes latitudinally undulated, allowing an advection of warm air masses to the central North Atlantic, blocking the west-northward displacement of the storm tracks, forcing them to move towards lower latitudes. This blocking would produce an Atlantic moisture advection towards the western Mediterranean (Fig

1.4a). This atmospheric configuration is attributed to a negative NAO phase, where the pressure system between the Icelandic Low and the Azores High is minima. Also, during the NAO(-), the polar vortex is weakened, allowing cold air artic masses to invade southern European latitudes, like the Mediterranean region (Fig 1.4a). On the contrary, a reinforced jet stream would be less undulated, restricting the polar front to northern latitudes, and thus the Atlantic storm tracks would move westwards in higher latitudes. Higher pressure differences create this atmospheric configuration and thus NAO(+). Also, during this positive phase, the polar vortex would be enhanced, restringing the cold air artic masses at boreal latitudes favouring the northward movement of the warm subtropical masses reaching European positions (Fig 1.4a).

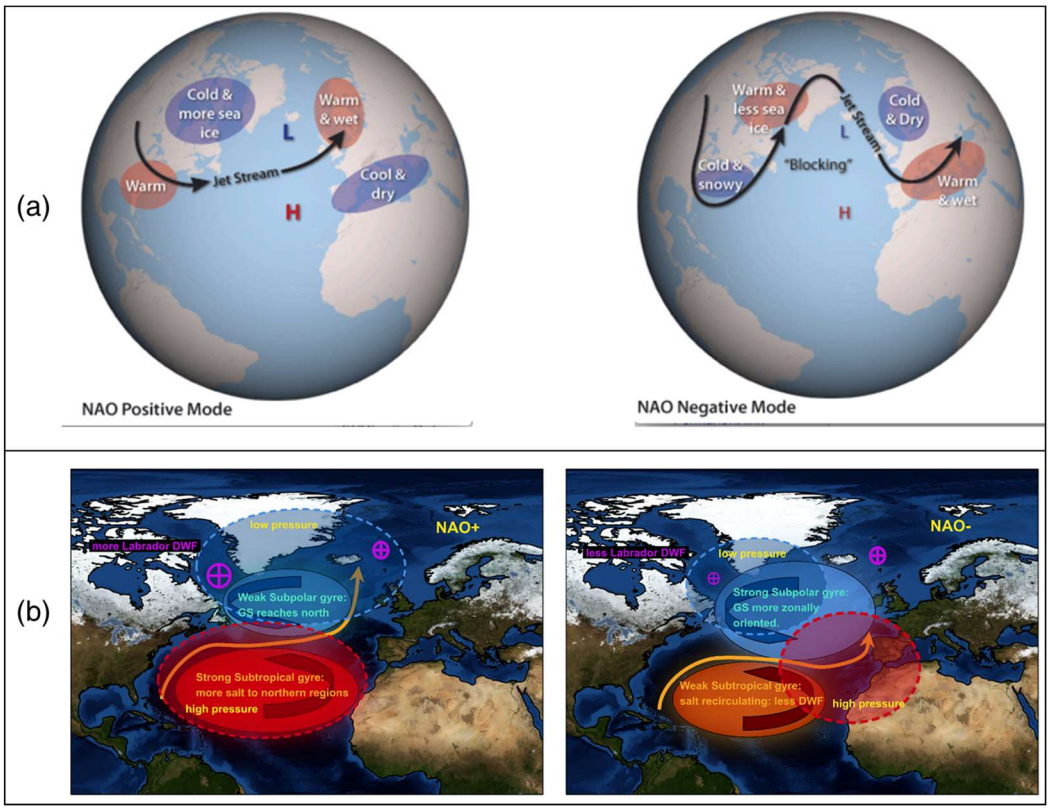

Figure 1.4 - North Atlantic Oscillation modes and their responses to the North Atlantic Ocean. *(a) On the left, the Positive mode of the NAO; on the right, the Negative mode of the NAO (Images modified from the NOAA (July 22, 2016) (b) On the left, the surface ocean circulation during positive NAO phases; on the right the surface ocean circulation during negative NAO phases (Images modified from de Toma et al., 2022)*

The North Atlantic Ocean also triggers the North Hemisphere climate variability. The strengthening or weakening of the AMOC could be driven or prevented by changes in the STG and/or SPG or vice versa. Potential links between the AMOC and the NAO have been widely studied. However, due to the multiple atmospheric and oceanic feedbacks involved, it is complex to establish a simple relationship. However, modelling these potential interconnections at present days has been observed that persistent positive NAO phases produce an STG circulation enhancement (Fig 1.4b), favouring the northward propagation of saltier and warm waters (northward displacement of the NAC; Langehaugh *et al.,* 2012) but inducing a weakening of the SPG, producing a heat loss of the water masses (Koul *et al.,* 2020) that ultimately increase the

deep water formation (van Aken et al. 2011; Lohmann *et al.,* 2009; Yashayaev 2007; Curry et al. 1998) and thus, AMOC strength (de Toma *et al.,* 2022; Delworth and Zeng, 2016). During positive NAO phases, the NAC reaches northern positions but is less eastward displaced (Fig 1.4b), allowing the southeastward displacement of the subpolar waters. The ocean response to the NAO-like atmospheric forcings has been observed in approximately 5 -10 years (Delworth and Zeng, 2016; Zhai *et al.,* 2014; Huang *et al.,* 2012; Lohmann *et al.,* 2009). Also, the AMOC amplitude variation does not vary much as the forcing time scale increases from 20 to 100 years. However, the amplitude of the large-scale climatic responses increases substantially (Delworth and Zeng, 2016). This is crucial in assessing the impact of NAO-induced AMOC variations on past climates.

1.2 Paleoclimatology

Paleoclimatology is the science that studies the Earth's climate history previous to anthropogenic interferences in order to learn about the processes that control Earth's climate. The Earth's climate has passed through different warmer or colder epochs, even though periods are free of permanent ice (hothouse) or with permanent ice sheets (icehouse). This climate evolution was controlled by a natural process often responding to external forcings that somehow introduced some imbalance in the radiative budget of the Climatic System. Thus, understanding how natural climate variability sheds light on framing the current climate change induced by humans on the natural climate evolution and gives insight into those positive and negative feedbacks that have the potential to ultimately modulate the Earth's climate independently of the initial trigger of the change.

Paleoclimatology is a relatively modern science developed during the 20th century. However, Louis Agassiz pioneered suggesting past climate changes during the early nineteenth century. He published in 1836 the "Great Ice Age", where he explained the evidence for the past presence of large glacier enhancement as the succession of cold and warm climatic periods. Later in the nineteenth century, Oswald Heer published "The Primeval World of Switzerland (1865)", which found fossil leaves and fruits attributed to the early Cenozoic. He assumed that these fossils could be an analogue for the modern ones and calculated the first paleo-temperatures obtaining that the Cenozoic was warmed around 3.5°C than today (Fairbridge *et al.,* 2009). From the 20th century until the present, the knowledge of the past climate has been constantly improved to such an extent that small changes can be identified and reproduced in specific regions. In this sense, the most recent geologic period has been widely studied and has provided new insights into past climate history.

The Quaternary, the most recent geology period (started 2.58 million years ago), started with the building of a permanent ice sheet over Greenland. The Quaternary is characterised by a sequence of glacial and interglacial cycles (Emiliani, 1955; Lisiecky and Raymo, 2005). Initially, these cycles were pathed by a 41.000 years cycle (41 kyr), but after 1.08 Ma, these glacial/interglacial cycles shifted toward larger cycles of about 100 kyr. The path of these cycles has been recognised to follow the astronomical forcings that lead to changes in the insolation distribution over the Earth (Shackelton, 1967; Imbrie and Imbrie, 1978). Thus, according to the Milankovitch theory (Milankovitch, 1941), summer insolation at northern latitudes is considered the main driver of the changes in ice sheets extension that would trigger the glacial or interglacial period.

In order to achieve a complete understanding of the past climate, the paleoclimatology uses different climatic archives of a very varied nature, such as marine, lake sediment or ice cores, cave speleothems, corals, and tree rings, among others. These archives stored a short of capsules that contain several biological, geochemical or physical information about the environment in which they were formed that can ultimately be translated into past climate

conditions. The analysis of these capsules provides indirect information that we can use to reconstruct climate variables such as past sea temperatures, the CO_2 concentration of the atmosphere, and the sourcing of different lithogenic particles, among others. Scientifically, these capsules are called proxies, allowing us to reconstruct the past climatic signal through their measurements. Paleoclimatology uses a large range of proxies, as examples: radiogenic isotopes on terrigenous particles ($^{87}Sr/^{86}Sr$, $^{143}Nd/^{144}Nd$) as indicators of climate conditions on land, trace elements on biological carbonates (Mg/Ca) as an indicator of marine surface temperatures, stable isotopes on biological carbonates ($\delta^{18}O$) as indicators of local salinity changes, or the elemental composition of the bulk sediment (Zr/Al, Mn/Al, Si/Al) as a further indicator of climate conditions on land. These are examples of those proxies applied in the present study. They can be complemented with several other sources of information, such as pollen distribution, grain size analyses, and faunal assemblages, among others. In this regard, our proxy evolution along time often does not respond to a simple climatic parameter (oceanic, atmospheric, vegetation). Thus, paleoclimatology needs to combine several proxies to better contrast the potential variability in one of these parameters (multi-proxies approaches), and ideally, they need to be validated by other comparable reconstructions in nearby locations (multi-records approach).

1.3. Marine sediment archives to reconstruct the past climate and oceanography

Marine sediment cores provide exceptional archives to reconstruct the climate and the oceanic conditions over the past times. These sediments are composed of a mix of lithogenic material supplied by the surrounding continents and biogenic particles from marine organisms that once they die, let some of their remains deposited on the sea floor. These sedimentary particles are gradually settle above the others, forming layers that capture the information progressively on time. The lithogenic components can provide information on the processes responsible for sediment transport, like winds, riverine inputs and also on the source area of these particles. On the other hand, biogenic particles are composed mainly of carbonate as foraminifera shells, although other carbonate components such as corals, coccolithophores or silicic remains as diatoms can also be present. The analysis of the assemblage distribution of the biogenic remains and also of their chemical signal provide very valuable information about past marine environmental conditions ultimately linked to climate.

A major effort in paleoceanography is devoted to improving the understanding of the applied proxies. In this sense, a strategy to learn more about the variables controlling the deposition of these different sedimentary components is to analyse sediment trap particles collected throughout a temporal period for which environmental conditions can be recorded. Sediment traps are deployed at different depths of the seawater column and they capture the falling particles within defined periods of time, obtaining a time series of the different components that form marine sediments. In this way, the preferential growth month/season can be identified for different planktonic species, but it is also possible to establish the relationship between the terrestrial components and meteorological conditions. This strategy will be one of the goals of this thesis.

1.4 The Western Mediterranean Region

1.4.1 Current Climatology

The Mediterranean region is located in the northern border line between the influence of two atmospheric systems: the southern side is dominated by the African subtropical high pressures associated with the Hadley cell, and the northern part where dominates the southern boundary of the North Atlantic depression system carrying the storm track on the limit between the Ferrel and Polar cell (Fig 1.6). Consequently, the Mediterranean region becomes very sensitive to minor and large changes in the atmospheric circulation. The precipitation is mainly controlled by the southward displacement of the cold fronts associated with a negative NAO phase, mainly during winter and early spring (Trigo *et al.,* 2002). Conversely, during summer and early fall, the Azores high-pressure system is strengthened, forcing the Atlantic fronts towards northern latitudes, producing a precipitation deficit over the Mediterranean. However, the Mediterranean region is an essential reservoir of heat and moisture (Lionello *et al.,* 2006), which contribute to the increase of precipitation through the Mediterranean south-easterly convective storm concomitant with the Atlantic storms blocked (Moreno *et al.,* 2014; Insua-Costa *et al.,* 2022)

The precipitation over the western Mediterranean is also defined by its torrential character (extreme rainfall events), which has increased during the last decades in the context of global climate warming (Allan *et al.,* 2008; Casanueva *et al.,* 2014; Donat *et al.,* 2016; IPCC-2022). In the context of this climate change situation with potential catastrophic social and economic consequences of this enhanced torrential character, the interest of the scientific community in understanding also past natural variability in the regions has increased during the last years (e.g. Ramos *et al.,* 2014; Krichak *et al.,* 2015; Khodayar *et al.,* 2016; Cardoso-Pereira *et al.,* 2019; Khodayar *et al.,* 2021; Gil-Guirado *et al.,* 2022; Insua-Costa *et al.,* 2022). The torrential rain events in the southwestern Mediterranean region occur towards late fall and winter and to less degree during spring (Grimalt-Gelabert *et al.,* 2021; Gil-Guirado *et al.,* 2022). Winter rainfalls associated with the negative NAO phase can occur as torrential precipitation. However, spatiotemporal synoptic databases indicate that the Atlantic storms rarely cause heavy torrential rainfalls in the western Mediterranean (Gil-Guirado *et al.,* 2022). The occurrence of torrential rainfalls is mainly derived from the cut-off lows (DANA in Spanish) usually centred in North Africa that displace northwards to the Alboran Sea (Jansà *et al.,* 2001; Nieto-Ferreira, 2021; Gil-Guirado *et al.,* 2022). If this situation occurs during the fall season when the Mediterranean Sea still holds the warm temperatures from the summer, evaporation is intensified. This enhanced moisture advection when rich higher cold levels, heavy rainfall events are triggered (Gil-Guirado *et al.,* 2022). Some studies also support that the process associated with this Mediterranean advection is more efficient than those related to the north Atlantic moisture (Taszarek *et al.,* 2021; Insua-Costa *et al.,* 2022). However, recent studies support that this Mediterranean source advection would not be sufficient to produce catastrophic torrential rainfalls; thus, a remote moisture sources contribution is necessary (Insua-Costa *et al.,* 2022). In this sense, it has been proposed that this

additional moisture source had a tropical origin, concretely from the tropical African region (Knippertz *et al.,* 2010; Wu *et al.,* 2013; Winschall *et al.,* 2014; Krichak *et al.,* 2015; Turato *et al.,* 2004; Duffourg *et al.,* 2011, 2013; Lorente-Plazas *et al.,* 2020). Some studies have even documented tropical Pacific moisture sources associated with heavy rainfalls in the western Mediterranean provably linked with positive El Niño-Southern Oscillation (ENSO) events (Mariotti *et al.,* 2002; Shaman *et al.,* 2011; Krichak *et al.,* 2014).

1.4.2 Current Oceanography

The Mediterranean Sea is a semi-closed sea acting as a concentration basin because the evaporation exceeds precipitation and river inputs (Fig 1.6). The western Mediterranean circulation is mainly structured in three main layers: surface, intermediate and deep water masses (Lionello, 2012; Rohling *et al.,* 2009). The surface water enters to the Mediterranean through the Gibraltar Strain, compensating the excess of evaporation. This less saline Atlantic water mass is rapidly modified when crossing the Alboran Sea (Modified Atlantic Water, MAW), which describes two semi-permanent anticyclonic gyres (Western and Eastern Alboran Gyres, WAG and EAG). This surface water moves eastwards over the North African coast and distributes along the whole Mediterranean Sea (Millot, 1987, 1999). The deep water is formed in the Gulf of Lions as a dense water mass (Western Mediterranean Deep Water; WMDW) which flows to the Alboran Sea, and it outflows to the Atlantic Ocean combined with the intermediate water (Levantine Intermediate Water; LIW) both as a high-dense water mass (Mediterranean Outflow Water; MOW).

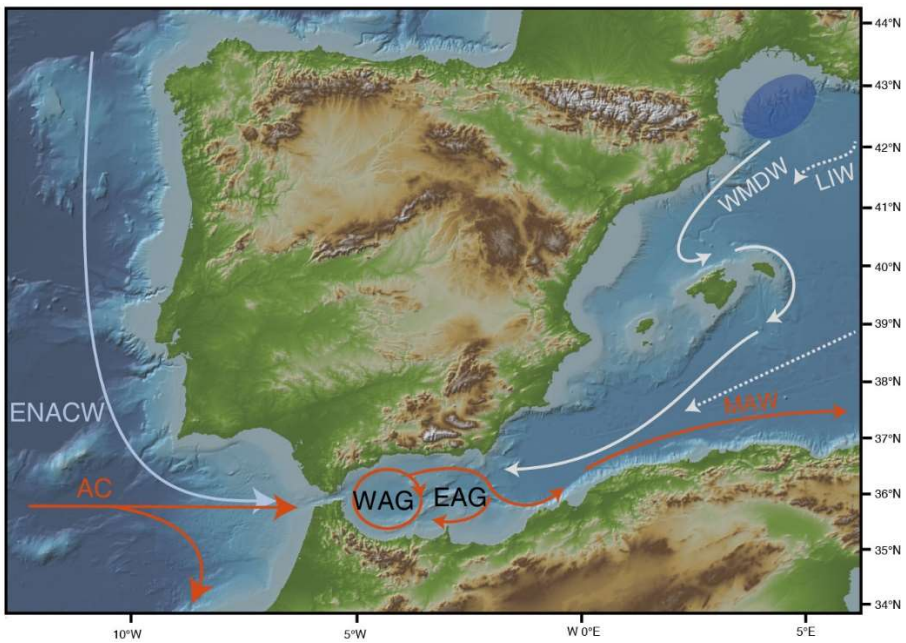

Figure 1.5 - Schematic Western Mediterranean Circulation. *In red are the main surface currents: AC – Azores Current; MAW – Modified Atlantic Water. In light grey, the main intermediate and deep waters: LIW – Levantine Intermediate Water; WMDW – Western Mediterranean Deep Water. In light blue, the central waters: ENACW – Eastern North Atlantic Central Water. WAG – Western Alboran Gyre; EAG – Eastern Alboran Gyre. Blue-filled circle - Location of the deep water formation. Basic map obtained from Marine Geoscience Data System © 2008-2018 – all rights reserved.*

1.4.3 Geological framework

The Betic Arc is located in the westernmost Mediterranean Sea, bounded by the Betic and Rif orogenic belts surrounding the Alboran Sea basin (Fig.1.7). This region became a complex during the Cenozoic when a subduction, slab fragmentation and rollback occurred within a slow convergence context between the African and Europen tectonic plates (Varas-Reus *et al.,* 2017). The Betic Cordillera form the northern branch of the Gibraltar arc, while the Rif Cordillera is located in the southern Gibraltar arc. Both cordilleras formed during the same orogeny and share the same compositional structures. They are divided into three main tectonic domains: (1) The External Units composed of sedimentary rocks; (2) the Flysch (Maghrebien) Trough Units, which derived from sediments deposited on the ocean (Durand-Delga *et al.,* 2000; Guerrera *et al.,* 2005) and (3) the Internal Units formed by the Maláguide (Ghomaride), Alpujárride (Sebtides) and Nevado-Filábride Complexes, which are mainly composed by metamorphic, meta-sedimentary and sedimentary rocks (Moroccan names).

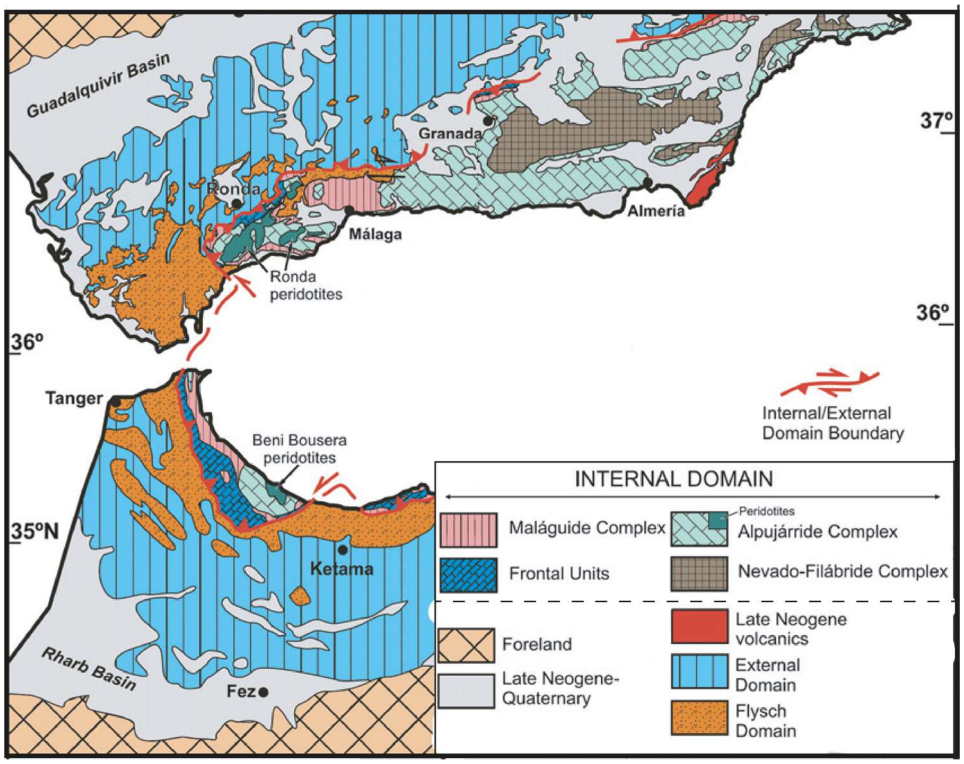

Figure 1.6 – Geological map of the Betic Cordillera and Rif. *Map modified from Sánchez-Navas et al., 2014*

1.5 The present interglacial: The Holocene

The Holocene is the current geological epoch, and its onset is located at 11.65 cal kyr BP when the last deglaciation ended and relatively warm temperatures dominated in both hemispheres (Walker *et al.,* 2009). The Holocene is the last epoch of the Quaternary period and corresponds to the last interglacial of many glacial-interglacial cycles that preceded it along the Pleistocene (the first epoch of the Quaternary). The Holocene has been divided into three different stages called Early Holocene (11.65 – 8.2 cal. kyr BP), Middle Holocene (8.2 – 4.2 cal. kyr BP) and the Late Holocene (from 4.2 cal. kyr BP until the present) formally called Greenlandian, Northgrippian and Meghalayan stages/ages (Walker *et al.,* 2018). The overall climatic and oceanographic variations during the Holocene have been widely investigated because the interglacial conditions strongly impacted human development worldwide. In this sense, this climatic change determined the end of nomadic human behaviour, letting to their settlement with the development of agriculture and animal domestication that led to a significant human expansion and development of more complex human civilizations, building villages and towns. Therefore, human beings have been ancestrally linked to the clime, and thus, we are highly dependent on it.

The Early Holocene is coincident with the minimum precession cycle which led to a maximum in summer insolation forcing up to higher latitudes of the northern hemisphere (e.g. Marchal *et al.,* 2002; Lorenz and Lohmann, 2004; Tzedakis, 2007; Wanner *et al.,* 2008; Tinner *et al.,* 2009; Bartlein *et al.,* 2011). At the beginning of the Holocene, the residual Laurentide ice sheets were progressive melting at high latitudes (Carlson *et al.,* 2008), a situation that led to several oceanic and atmospheric reorganizations in the context of the North Atlantic region. During the deglaciation and also early Holocene, the injection of fresh and cold pulses of meltwaters into the north Atlantic, concretely into the Labrador Sea, stratified the upper water column that led to reducing the deep-water formation and, thus, slowed down the AMOC (Dickson *et al.,* 1996; Thornalley *et al.,* 2009). It is important to note that AMOC variations during the Holocene occurred within the interglacial AMOC mode, so there was always an active AMOC, and the oscillations were smoother than those that occurred during the glacial and also deglaciation periods. The early Holocene melting waters from the Laurentide ice sheets reached southern positions over the Azores latitudes (Repschläger *et al.,* 2017, 2015), limiting the northward transport of warm and saltier subtropical water masses. This contributed to enhancing the freshening of high latitudes North Atlantic. The combined effect of these residual ice sheets with the maximum summer insolation in the northern Hemisphere controlled the atmospheric and oceanic triggering a strengthening of the westerlies and shifting them towards lower latitudes (Despart *et al.,* 2013; Renssen *et al.,* 2009). Further south, at tropical latitudes, the northern African continent was influenced by the northward shift in the ITCZ position that produced an enhancement in moisture availability over this region, including the Sahara. These conditions started previously in the Holocene (during the last deglaciation 14.8 cal. kyr BP), triggered by the increasing summer insolation. Over the western Mediterranean, this general oceanic and

atmospheric configuration (summer insolation maxima, ice sheets relict and AMOC reduced) was expressed with an increase of the winter moisture advection potentially derived from the southward expansion of the North Atlantic winter westerlies wind belt (Colombu *et al.,* 2022; Gomes *et al.,* 2020; García-Alix *et al.,* 2021; Toney *et al.,* 2020; Wagner *et al.,* 2019; Zielhofer *et al.,* 2017; Chaboud *et al.,* 2014; Fletcher *et al.,* 2012). The orbital configuration during the early Holocene (minimum in the precession cycle) also had regional implications over the western Mediterranean, probably derived from the described general oceanic-atmospheric patterns, which produced a strong seasonality with the enhancement of winter precipitation but severed droughts during summers, although leading to a higher total annual precipitation (Bosmans *et al.,* 2015; Brayshaw *et al.,* 2011). Thus, this situation involved a significant forest expansion during the onset of the early Holocene (Ramos-Román *et al.,* 2018; Combourrieu-Nebout *et al.,* 2009; Fletcher and Sánchez-Goñiz 2008). The wettest conditions over the western Mediterranean were reached from 9.5 to 7.6 cal. kyr BP that has been named the Western Mediterranean Humid Period (WMHP) (García-Alix *et al.,* 2021; Ramos-Román *et al.,* 2018; Fletcher and Sánchez-Goñiz 2008). The WMHP coincided with a progressive reduction in meltwater pulses over the North Atlantic, reaching the minimum influence after 8.5 cal. kyr BP, a situation that contributed to a gradual enhancement of the deep water formation concomitant with a strengthening of the SPG circulation (Collin *et al.,* 2019; Thornalley *et al.,* 2009). This oceanic reconfiguration would invoke a progressively northward migration of the winter North Atlantic westerlies storm tracks, increasing the storminess over northern latitudes (Goslin *et al.,* 2018). In this regard, the Azores current (AC) linked to the north boundary of the STG was progressively moved towards northern positions (Repschläger *et al.,* 2017), and winter storm over the western Mediterranean region associated with the North Atlantic westerlies wind belt weakened. In spite of these potential latitudinal fluctuations of the winter storm tracks, they were emplaced preferentially on the southern positions. The consequent progressive loss of Atlantic moisture over the western Mediterranean could have been partially replaced by enhanced Mediterranean moisture advection (García-Alix *et al.,* 2021), a situation that would explain the WMHP.

During the mid-Holocene, from around 8 to 6 cal. kyr BP occurred an oceanic-atmospheric reconfiguration due to the onset of a progressive northward transport of the warm and saltier subtropical subsurface water masses. Although, it was not until around 7 cal. kyr BP that the STG water masses interact with the SPG letting to the onset of the modern transport of warm subsurface subtropical waters towards the subpolar region (Repschläger *et al.,* 2017). At the same time, the Labrador Sea Water (LSW) formation started (Kissel *et al.,* 2013; Perner *et al.,* 2013; Hoogakker *et al.,* 2011), probably related to the subsurface subtropical water masses reaching the Labrador Sea through the NAC and the SPG. However, the operation modes between the STG and SPG act in antiphase. When STG storage heat and salt, the SPG become fresher (Repschläger *et al.,* 2017; Cléroux *et al.,* 2012, Thornelley *et al.,* 2009), reducing the LSW formation. However, the reduction of the LSW formation enhanced the warm and saltier water towards the SPG, which enhanced the LSW formation. Thus, the STG and SPG circulation acted as a negative feedback (Born and Stocker, 2014; Thornelley *et al.,* 2009). This mechanism

observed during the Holocene has also been described in the modern North Atlantic circulation (de Toma *et al.,* 2022). Regarding the Mediterranean region, an aridification trend started at around 7.2 cal. kyr BP (e.g. Mesa-Fernández *et al.,* 2018; García-Alix *et al.,* 2017; Jiménez-Espejo *et al.,* 2014; Anderson *et al.,* 2011; Combourieu-Nebout *et al.,* 2009) provably triggered by the progressive loss of Atlantic source moisture, potentially driven by the north Atlantic reconfiguration. The correlation between the north Atlantic and the western Mediterranean region has been widely explored, linking the Mediterranean aridification events to cooling events in the North Atlantic during the early mid-Holocene (Fletcher *et al.,* 2012; Zielhofer *et al.,* 2017). These sub-millennial aridification events were probably related to the northward migration of the winter storm track (Zielhofer *et al.,* 2017; Fletcher *et al.,* 2012).

From 6.0 to 4.0 cal. kyr BP occurred a major atmospheric and oceanic reconfiguration in the north Atlantic. The ITZC was already shifted northwards (around 4° N), enhancing the precipitation over tropical Africa (Menivel *et al.,* 2021), and the post-glacial AMOC recovery had reinforced this northward ITCZ shift. But the ongoing insolation decline during the middle Holocene determined the ending of the AHP. When the summer insolation crossed the threshold of 0 on the precession cycle (~500 $W \cdot m^{-2}$), negative feedbacks triggered this AHP demise (Menivel *et al.,* 2021). Associated with this AHP decline, a rapid cooling event occurred in the North Atlantic associated with a relative AMOC slowdown that let an increasing the arctic sea ice (England *et al.,* 2008; Werner *et al.,* 2016; Oppo *et al.,* 2003; Kim *et al.,* 2007; Ayache *et al.,* 2018). This cooling expanded towards the Alps (Magny *et al.,* 2004), reaching the Gulf of Cadiz (Kim *et al.,* 2004) and the Alboran Sea (Martrat *et al.,* 2014; Cacho *et al.,* 1999). This situation triggered oceanic and atmospheric feedbacks that let the ITZC to migrate southward to its modern position and letting to the Sahara aridification (Collins *et al.,* 2017). Consequently, the African Easterly Jet located between the Hadley and Ferrel cell increased its strength, reducing the advection of Atlantic humidity towards the western Mediterranean and letting its aridification after 6.0 cal. kyr BP (Carrión *et al.,* 2002; Fletcher *et al.,* 2012; Fletcher and Sánchez-Goñi *et al.,* 2008; Combourieu-Nebot *et al.,* 2009; Anderson *et al.,* 2011; Magny *et al.,* 2012; Jiménez-Espejo *et al.,* 2014; Zielhofer *et al.,* 2017; Ramos-Román *et al.,* 2018; Toney *et al.,* 2020; Zielhofer *et al.,* 2017; García-Alix *et al.,* 2021).

During the Late Holocene (4.0 cal. kyr BP until present), climate conditions over the western Mediterranean region have been mostly controlled by the modern pattern of variability of the NAO (Olsen *et al.,* 2012; Zielhofer *et al.,* 2017; García-Alix *et al.,* 2021). When positive NAO phases prevailed, it occurred a northward shift of the winter storm tracks triggering an Atlantic atmospheric blocking. This situation would enhance the contribution of Mediterranean source moisture, a situation that would switch when centennial-decadal-scale oscillations to negative NAO phases occurred. When a transition in the moisture advection source occurred from the Atlantic to the Mediterranean region, the precipitation season would change from winter (Atlantic) to spring (Mediterranean)(Zielhofer *et al.,* 2017; Toney *et al.,* 2020; García-Alix *et al.,* 2021).

1.6 Objectives of the Thesis

The main scientific objective of this PhD Thesis is to gain further s insight into the western Mediterranean regional climate variability during the Holocene. Singular emphasis has been placed on deciphering the interplay of the oceanic and atmospheric processes operated in the region during the present interglacial. With this goal in mind, a novel toolset of "state-of-the-art" analytical techniques has been developed and applied in combination with other classical analytical approaches to understand better the potential interregional teleconnections between the North Atlantic and the Mediterranean region. In order to accomplish this general objective, six specific objectives have been performed:

1. To validate *G. bulloides* Mg/Ca-derived Sea Surface Temperature (SST) as a reliable proxy to reconstruct the regional oceanographic conditions by comparing this newly generated record with other existing SST records from the same foraminifera species in the western Mediterranean Sea.
2. To establish a comparison and identify similarities and discrepancies observed between the Mg/Ca-derived SST record with other existing SST reconstructions based on biomarkers (alkenones). Differences between proxy sensitivity to changing environmental conditions can provide invaluable information about past climate variability in the region.
3. To evaluate the potential climatic and oceanographic links between the western Mediterranean SST evolution, both through changes in the inflow of Atlantic waters as well as in the broader context of North Atlantic climatic variability during the Holocene.
4. To establish and optimise new analytical methods using radiogenic isotopes (Sr, Nd and Pb) in the lithogenic sediment fraction as a provenance proxy of sediments arriving into the study area. This goal includes the development and testing of a newly redesigned procedure to digest marine sediment samples and the optimisation of the sample purification protocols to separate simultaneously Sr, Nd and Pb in one single analytical step prior to the analysis of the radiogenic isotope ratios
5. To identify and quantify the contribution of potential lithogenic sediment sourcing areas using the isotopic signature captured in terrigenous particles by studying a year-long sediment trap time series. This will also establish the potential transport mechanism of the terrigenous particles captured in the sediment traps.
6. To use the radiogenic isotope signature measured in lithogenic material in sediment traps as a modern analogue to reconstruct potential changes in sediment source areas or processes in the Alboran Sea during the Holocene. This objective will allow to compare oceanic and atmospheric processes in the Western Mediterranean Sea and identify their potential connections with global climate changes during the Holocene.

Chapter 2

Methodology

“Come, come alone,
come with friends, come with faults,
come however you are.
Just come,
let yourself be wrong,
but come however you are”

Trusty and true, Damien Rice”

2.1 Material and Methods

2.1.1 Studied Marine Sediment Cores

The main focus of this thesis is the sediment core HER-GC-ALB-2 collected in 2009 during the HERMESIONE research oceanographic cruise on board *BIO Hespérides*. This gravity core (hereafter ALB-2 for simplicity) covers a continuous sedimentary sequence of 337 cm in the Alboran Sea, southward of the Malaga Margin at 36°0'44.8020" N and 4°16'24.3804" W from a water depth of 1313 m b.s.l (Fig. 2.1 and Table 2.1). ALB-2 is strategically located at the centre of the Western Alboran Gyre (WAG), which produces a hydrographic funnelling effect, capturing the suspended particles from the edges of the gyre and concentrating them towards the centre (Fabrés *et al*., 2002). Therefore, the ALB-2 locations have the potential for recording higher sedimentation rates than the overall ones for the zone.

This thesis also includes new results from two additional sediment cores MD95-2043 and MD99-2343. Both were collected in the International Marine Past Global Changes Study program (IMAGES) on board *R/V Marion-Dufresne* and retrieved using a calypso piston system. The marine sediment core MD95-2043 covers a sedimentary sequence of 32.24 m in the Alboran Sea, from the Eastern Alboran Gyre (EAG) at 36°8.6' N and 02°36.3' W and from a water depth of 1841 m b.s.l (Fig. 2.1 and Table 2.1). The MD99-2343 covers a sedimentary sequence of 32.44 m in the Balearic Sea, at the northeast of Minorca Island at 40°29.84' N and 04°01.69' E, from a water depth of 2391 m b.s.l. (Fig. 2.1 and Table 2.1), on the periphery of a contourite drift deposit. This contourite is formed by deep contour currents formed by the southward branch of the WMDW (Velasco *et al*., 1996) that sinks in the Gulf of Lions. This water masse flows southwards following a cyclonic circulation, which is forced to turn into an S-SE direction when it finds the Balearic promontory leading to the formation of a contourite drift deposit (Velasco *et al.,* 1996, Canals *et al.,* 2012).

These two sediment cores, MD95-2043 and MD99-2343, have previously been the focus of several researches that have applied micropaleontological, geochemical, and sedimentological techniques. In these cases, this thesis adds further information to the data already published.

2.1.2 Sediment Trap samples

In order to gain a better understanding of the processes controlling the studied sediment core records, this thesis also works with samples from a sediment trap that covers a whole annual cycle. This is the ALB-1 mooring line (Fabrés *et al*., 2002) which was deployed on the continental slope of the Malaga Margin, in the Alboran Sea, at 36°14.39' N and 04°15.41' W, as a part of the MTP II-MATER project (Mediterranean Targeted Project II – Mass Transfer and Ecosystem Response). Two sediment traps were placed along this mooring line at different depths, although for this study, only the shallow trap ALB-1-S (471m depth) has been used (Fig. 2.1 and Table

2.1). The mooring line was also equipped with a Technicap PPS3 sediment trap and Aanderaa current meter. The design of the PPS3 (0.125 m^2 of collecting area, cylindroconical shape, 12 receiving cups), instrumentation set up and the configuration of the mooring lines are described in Heussner *et al*., 1990. The collecting period for the ALB-1-S was from July 1997 to May 1998.

Sample	Material Recovery	Location				Depth (mwd)	References
		Latitude		Longitude			
Sediment Core	HER-GC-ALB-2	36°0'44.80"	N	04°16'24.38"	W	1313	Català et al., 2019
	MD95-2043	36°8'598"	N	02°37'269"	W	1841	Cacho *et al*., 1999
	MD99-2343	40°29.84'	N	04°01.69'	E	2391	Frigola *et al*., 2007
Sediment Trap	ALB-1-S	36°14.39'	N	04°15.41'	W	471	Fabrés *et al.,* 2002
Atmospheric Dust	SMI	39°38'17"	N	02°59'52"	E		Català *et al.,* (unnpublished)
	BCN	41°23'03"	N	02°07'09"	E		Català *et al.,* (unnpublished)
	ENA	42°26'49"	N	00°41'35"	W		Català *et al.,* (unnpublished)

Table 2.1 – Material recovery locations: *Locations of the materials used in this thesis. Depths in meters of water depth are only referred to as the marine sediment cores and the sediment trap.*

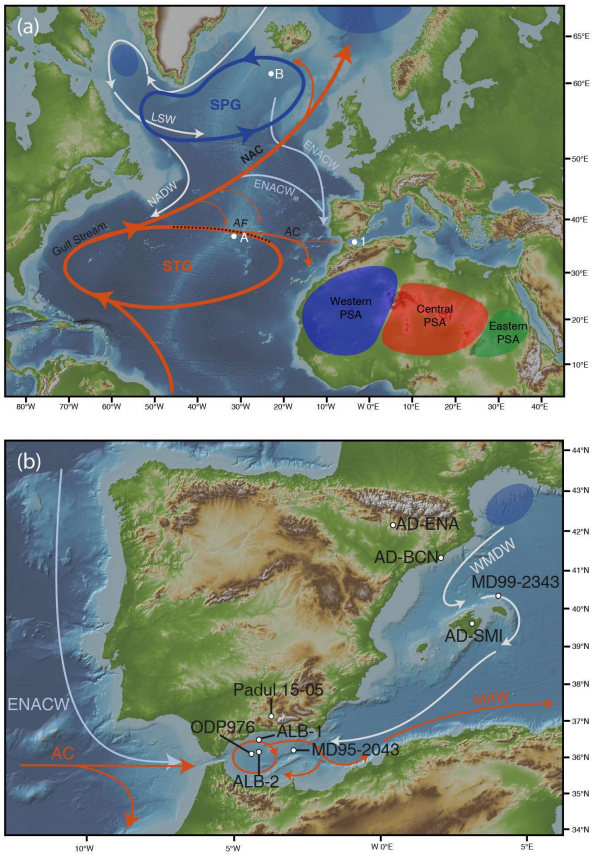

Figure 2.1 – Location of the studied sites and schematic Oceanic Circulation. (a) *Locations: 1. Western Mediterranean. (A). GEOFAR-K16, (B) RAPiD-12-1k. Oceanography: In red, the main surface currents: NAC – North Atlantic Current; AC – Azores Current. In light grey, the main intermediate and deep waters: LSW – Labrador Sea Water; DSOW – Denmark Strain Overflow Water; ISOW – Icelandic-Scotland Outflow Water; NADW – North Atlantic Deep Water. In light blue, the central waters: ENACWsp – st – Eastern North Atlantic Central Water Subpolar or Subtropical. STG – Subtropical gyre; SPG – Subpolar gyre. In a black dashed line: AF – Azores Front. Blue circles: Locations of the deep water formation* ***(b)*** *Sediment cores: ALB-2, ODP976, MD95-2043 and MD99-2343. Sediment Trap: ALB-1. Atmospheric dust: AD-SMI, AD-BCN, AD-ENA. Lake records: Padul 15-05 and LdRS (Laguna del Rio Seco). In red the main surface currents: AC – Azores Current; MAW – Modified Atlantic Water. In light grey, the main intermediate and deep waters: LIW – Levantine Intermediate Water; WMDW – Western Mediterranean Deep Water. In light blue, the central waters: ENACW – Eastern North Atlantic Central Water. WAG – Western Alboran Gyre; EAG – Eastern Alboran Gyre. Blue-filled circle - Location of the deep water formation. Basic map obtained from Marine Geoscience Data System © 2008-2018 – all rights reserved.*

2.1.3 Atmospheric Dust samples

Within the framework of this thesis, three atmospheric dust samples were collected using handmade collection devices during significant rainfall events that occurred in Sineu (Majorca Island), Barcelona, and Ena (South-Centre Pyrenees). The exact locations of the samples were for Sineu (SMI) at 39°38'17" N and 02°59'52" E; Barcelona (BCN) at 41°23'03" N and 02°07'09" E; Ena (ENA) at 42°26'49" N and 00°41'35" W (Fig. 2.1 and Table 2.1). The sample from Barcelona was collected on the 14th of September 2021, and the Sineu sample on the 15th of September 2021, both corresponding to the same rain episode. On the other hand, the sample from Ena was collected on the 6th of February 2021 during a snow event.

2.2 Material description and sampling

2.2.1 Marine Sediment Cores

ALB-2 core was divided into four sections: section 1 of 93 cm, section 2 and 3 of 100 cm, and section 4 of 31 cm. The last 13 cm of section 4 corresponds to the core catcher. Visual inspection of the ALB-2 core shows a gradual colour change from the core-top towards the base (Fig 2.2). The first 10 cm were formed with dark-greyish brown (10YR 4/2 Munsell colour code) muds with high water content, while the next 50 cm comprised greyish brown (2.5Y 5/2) muds with abundant content in foraminifera. From 60 cm to the bottom, sediment is predominantly dark-greenish grey (10Y 4/1) mud, also with high foraminifera content. Thin black and dispersed layers were also observed at different core depths (Fig 2.2). There are no evidences for bioturbation, erosional gaps or hiatuses.

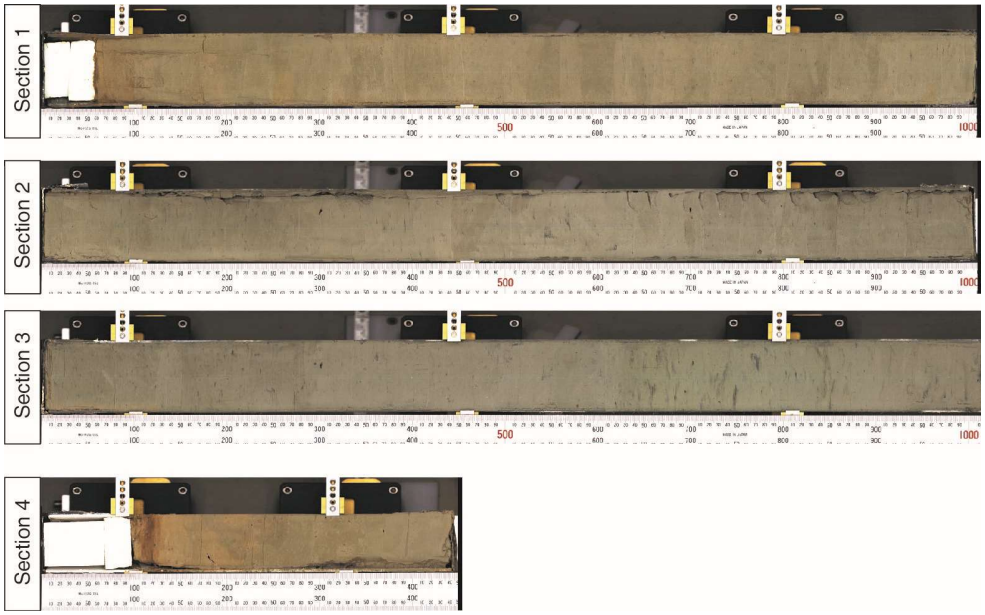

Figure 2.2 – Pictures of the ALB-2 Sediment Core. *The four sections obtained for the ALB-2 core. The scale of each section is in mm.*

Description from the core MD95-2043 from the Eastern Alboran Sea is not available.

In the case of core MD99-2343, this thesis has studied only the uppermost 600 cm. This core has been widely studied, particularly the upper part corresponding to the last 50 kyr BP (Frigola *et al.,* 2007 and 2008; Sierro *et al.,* 2005). The core description for the uppermost 600 cm) showed grey silty clays with some dispersed sandy layers, which were moderately bioturbated with high content in foraminifera and nannofossils. During the recovery operation, the uppermost 20cm of core were lost on-board.

Every core section was longitudinally split into two halves: working and archive sections, respectively. The working sections of each core were fully sampled in 1 cm thick slices, although

the later used resolution changed depending on the sedimentation rates of individual sites and the specific targets of the proxies (Table 2.2). In the case of the ALB-2 core, the sampling resolution was every 1 cm for the Mg/Ca and isotopes analysis. Radiocarbon analysis to construct the age model was done in 14 selected intervals, and 40 samples were chosen for radiogenic isotope analysis (Nd, Sr, Pb) in the detrital sediment fraction (Table 2.2). In addition, the archive sections of core ALB-2 were used for non-destructive elemental composition analysis using the XRF-core scanner (see section 2.6 Bulk elemental composition of sediments). For MD95-2043 and MD99-2334 cores, the geochemical analysis were performed at variable sampling resolution (Table 2.2).

Sample	Location	Name	Results	Performed with	Sample num.	Resolution (cm)	Published
Sediment Core	Alboran Sea	ALB-2	SST	*G. bulloides*	324	1	Català *et al.*, 2019
			$\delta^{18}O$	*G. bulloides*	324	1	Català *et al.*, 2019
			Elemental Composition	XRF-core scanner	324	1	New in this thesis
			Sr-Nd-Pb	Lithogenic Fraction	40	~8	New in this thesis
			^{14}C	Multi-specific	14	-	New in this thesis
	Alboran Sea	MD95-2043	SST	*G. bulloides*	228	~7	New in this thesis
			SST	Alkenones	336	~5	Cacho *et al.*, 1999
			$\delta^{18}O$	*G. bulloides*	156	~5	Cacho *et al.*, 1999
	Balearic Sea	MD99-2343	SST	*G. bulloides*	250	~7	Català *et al.*, 2019
			$\delta^{18}O$	*G. bulloides*	216	~3	Frigola *et al.*, 2007
			^{14}C	Multi-specific	19	-	Frigola *et al.*, 2007; Català *et al.*, 2019
Atmospheric Dust	Barcelona	*BCN*	Sr-Nd-Pb	Lithogenic Fraction	1	-	New in this thesis
	Sineu	SMI	Sr-Nd-Pb	Lithogenic Fraction	1	-	New in this thesis
	Ena	*ENA*	Sr-Nd-Pb	Lithogenic Fraction	1	-	New in this thesis
Sediment Trap	Alboran Sea	ALB1-S	Sr-Nd-Pb	Lithogenic Fraction	22	-	New in this thesis

Table 2.2 – Summary of the material used in this thesis: *Summary of the analyses performed in the studied materials indicating its resolution*

Sediment samples from all three cores were treated using the same procedure before the analytical measurements. Sediment samples were frozen and subsequently freeze-dried to eliminate water and disaggregate sediments. Afterwards, 2/3 of each sediment sample (7-10 gr of dry sediment) was introduced into a 100 ml vial filled with distilled water and gently shaken for 2 hours for the posterior trace elements and stable isotope analyses (see section 2.3 Stable Isotopes and 2.4 Trace Elements). The other 1/3 of the original sample was kept for other potential analyses as radiogenic isotope analysis. After agitation, sediment samples were washed through a 63 μm sieve with pressurised distilled water to separate the silt-clay from the sand fraction. Special care was taken at this step to thoroughly remove the silt-clay fraction, particularly at the interior of the foraminifera shells. Silt-clay residues in the foraminifera shells can be a potential source of contamination in geochemical analysis. After washing, the fraction above 63 μm was dried in an oven at 60°C.

2.2.2 Sediment Traps

Sediment trap samples cover the time period from July 1997 to May 1998, and they were recovered in three different phases: (I) 01/07/1997 – 31/10/1997, (II) 15/11/1997 – 10/03/1998, (III) 01/04/1998 – 22/05/1998. The sampling interval for individual samples was 10-11 days for the whole series, with the exception of the samples between the 20th of April to the 16th of May, which represent three days. The collecting cups of the traps were filled before deployment with

5% (v/v) formaldehyde solution in 0.45 µm-filtered seawater. The solution was buffered by saturation with analytical-grade sodium tetraborate. The poisoning solution limits settling particles' degradation and prevents swimmers' physical disruption (Fabrés *et al.*, 2002). For the studied period, 36 samples were recovered for the ALB-1-S and stored in dark conditions at 4°C until further processing in the laboratory. Once in the laboratory, samples were visually checked, and the supernatants were removed (Heussner *et al.*, 1990, Fabrés *et al.*, 2002). The 36 trap samples were sub-sampled for different analyses published by Fabrés *et al.*, 2002, and the rest were stored in the 5% (v/v) formaldehyde solution as an archive. Out of the initial 36 samples, 14 of them were completely exhausted in a previous analysis; therefore, the work performed in this thesis has been focussed on only 22 samples (Table 2.2). Before the samples were processed in the laboratory, the formaldehyde solution was rinsed out. These rinses involve transferring the samples into 50 mL centrifuge tubes, centrifuging at 5000 rpm for 30 min and decanting the supernatant. Afterwards, samples were filled with 40 mL of UP-Water and placed on a vortex until its complete disaggregation and centrifuge. This process was repeated five times to ensure that the 5% (v/v) formaldehyde solution was removed entirely. Samples were dried up and stored until the treatment for radiogenic isotopes (see section 2.5 Radiogenic Isotopes)

2.2.3 Atmospheric Dust

Since the studied dust samples were collected during wet deposition events, each sample was first transferred from the handmade collection devices into a beaker and dried at 60°C. All three samples had an oxide-red colouration and clay grain size. Samples were transferred from the beakers into small plastic bottles and stored until the treatment for radiogenic isotopes (Table 2.2) described in the next section (see section 2.5 Radiogenic Isotopes).

2.3 Stable Isotopes

2.3.1 Basics of stable isotopes

Stable isotopes are non-radioactive atoms of the same chemical element, which differ only in their number of neutrons (Wolfe, 1992). Although this neutron differences, the number of protons and electrons are the same and thus have the same electronic configuration. Therefore, different isotopes from the same element change in weight but not in their chemical properties, which are determined by the number of electrons. However, slight chemical effects due to the differences in mass occur. For example, oxygen has three different isotopes (^{18}O, ^{17}O and ^{16}O), and depending on these different neutrons, the stable isotopes are classified as lighter or heavier. Thus, during a chemical reaction, those molecules that bear the light isotope react more easily than those with the heavy isotope. This process happens, for instance, during evaporation, when the light isotope ($H_2{}^{16}O$) becomes more easily evaporated than the heavy one ($H_2{}^{18}O$). Therefore, during a chemical or physical process, like evaporation would occur an enrichment of one isotope relative to another and this process is defined as an isotopic fractionation (α). This factor is the ratio of the concentrations of the two isotopes in one compound divided by the ratio in the other compound and can be defined with the following expression:

$$\alpha = \frac{R_1}{R_2}$$

Where R_1 is the isotopic ratio of one compound while R_2 is the isotopic ratio in the other compound.

The absolute abundance of an isotope is challenging to measure, while the relative isotopic differences can be measured with high precision (Hoefs, 1987). Thus the isotopic composition of a substance, expressed in the δ terminology, compares the isotopic ratio of the measured substance with a reference standard whose ratio value is well known. The resulting isotopic ratio is defined by the following expression:

$$\delta_{sample}(‰) = \left(\frac{R_{sample} - R_{standard}}{R_{standard}}\right) 10^3$$

Where R_{sample} is the isotopic ratio of the sample and $R_{standard}$ is the isotopic ratio of the reference standard. Therefore, the δ values show the differences between the isotopic ratios of the sample and that from the reference standard. Positive values would indicate that the samples are enriched in the heavier isotope in relation to the standard, and conversely, negative values would indicate that the measured sample is depleted in the heavier isotope in relation to the standard. For water samples, the used standard is the VSMOW (Vienna Standard Mean Oceanic Water), while for carbonates (the most used in paleoceanographic studies), the used standard is the VPDB (Vienna Pee Dee Belemnite).

2.3.2 Stable oxygen isotopes ($\delta^{18}O$) in paleoceanography

The $\delta^{18}O$ measured in foraminifera shells is a widely used technic in paleoceanography, often, these records set the basis to construct chronological frameworks, but they are also very useful for reconstructing past oceanographical conditions. The very first record of $\delta^{18}O$ measured in the carbonated foraminifera shells was produced by Emiliani (1955), who interpreted the signal as water temperature changes, and he was also a pioneer in defining the Marine Isotopic Stages (MIS) still used nowadays. Previously, Epstein *et al.* (1953) had defined the first empirical equation to relate $\delta^{18}O$ to temperature for inorganic calcite precipitation, whose use in foraminifera was later validated by Shackleton (1974)based on the benthonic foraminifera. Subsequent studies in different species of foraminifera have shown that the temperature effect over the $\delta^{18}O$ of the foraminifera calcite is relatively constant and in agreement with previous estimations, around 0.23‰/°C (Bemis *et al.,* 1998). The very first studies considered that the $\delta^{18}O$ of the seawater (hereafter $\delta^{18}O_{sw}$ for simplicity) was relatively constant through time. However, Shackleton, (1967), by producing the very first record of $\delta^{18}O$ in benthic species, evidenced that glacial-interglacial changes in the ice sheet volumes substantially changed the $\delta^{18}O_{sw}$ and that signal became recorded in the foraminifera $\delta^{18}O$. When ocean water evaporates, the light isotope (^{16}O) preferentially passes to the atmosphere. Then, when precipitation occurs, it preferentially collects the available heavy isotopes (^{18}O), leaving the remaining water vapour isotopically depleted (low $\delta^{18}O$). When precipitation occurs at high latitudes, the available water vapour has been progressively enriched in the light oxygen isotope (^{16}O). This process is known as the Rayleigh distillation process. During a glaciation period, the ice sheets are built up and preferentially store ^{16}O, letting the ocean water relatively enriched in the ^{18}O and thus increasing the $\delta^{18}O_{sw}$ values. Thus, the $\delta^{18}O_{sw}$ signal associated with the growth and melting of the ice sheets affects the whole ocean and becomes stored in the foraminifera carbonate shells. This feature set the basses for using the foraminifera $\delta^{18}O$ records as a chronostratigraphic tool. But the foraminifera $\delta^{18}O$ signal also incorporates other more local oceanographical information, which can be particularly relevant for planktonic foraminifera since surface ocean properties can change drastically among past climate changes. Therefore, in addition to the ice sheets related $\delta^{18}O_{sw}$ signal, the foraminifera $\delta^{18}O$ can also record regional changes in temperature and the hydrological cycle, like the evaporation and precipitation balance that in turn would be associated with regional salinity. In the context of the Mediterranean Sea, the target of the thesis, where an excess of evaporation occurs, past changes in this valance would be reflected in the $\delta^{18}O_{sw}$ and transferred to the $\delta^{18}O$ from the foraminifera.

There exist other secondary factors that could produce an imprint on the foraminifera $\delta^{18}O$ and, to some extent, mask the oceanographical signals described above. Habitat migrations in the water column along the live foraminifera cycle have been described and can impact the foraminifera $\delta^{18}O$ (Gupta, 2002). On the other hand, foraminifera $\delta^{18}O$ can also be affected by

dissolution processes during the particle settling and sediment burial, modifying the original isotopic signal (Le and Shackleton, 1992). This study has taken care of these potential disturbance artefacts by ensuring the collection of well-preserved shells for the geochemical measurements and also, to avoid the mix of foraminifera shells from different stages of the vital cycle, the analysed shells were always picked between a very restricted size range.

2.3.3 Laboratory procedure

A total of 325 samples from the ALB-2 core were selected to analyse oxygen isotopes ($\delta^{18}O$). The oxygen isotope record for the MD95-2043 and MD99-2343 cores were already published by Cacho *et al*. (1999) and Frigola *et al*. (2007), and the laboratory and analytical procedure described in there but was comparable to that used for ALB-2 core. Around 10 specimens of *G. bulloides* were hand-picked between 250-355 μm size fraction to obtain a homogenous population. Then, the selected specimens were crushed between two glass slides under a binocular microscope to ensure the opening of the chambers and allow for cleaning of the shell interior. Samples were cleaned with 500 μL of methanol in an ultrasonic bath for 30 s to mobilise the clay particles. The residual methanol was removed, and samples were dried before analysis. The detailed protocol is provided in Annex 1 – Foraminifera isotopes cleaning protocol.

2.3.4 Analytical technique of Isotope-Ratio – Mass Spectrometry

The analyses were performed with an isotope-ratio mass spectrometer (IRMS), Finnigan-MAT 252. Mass Spectrometer (Fig. 2.7) at CCiT-UB, which allows the accurate measurement of small differences in the abundances of these isotopes. Foraminifera samples are weighted and placed into glass vials adapted to the carbonate micro-sampler CarbonKiel-III, which converts the solid carbonate into a gas (CO_2). The sample gas is purified and concentrated previously to be transferred to the IRMS, which ionises the gas sample molecules. This ionised gas is accelerated with high voltage, and the ion beams are focused on the magnet. The magnet deflects the ions according to their mass charge (m/z). Therefore, the accelerating voltage and the magnetic field's strength determine the ions' trajectory. The lighter ions like ^{16}O become more affected than those heavier like ^{18}O, thus separating the isotopes between different masses. Ions incoming from the magnet hit the Faraday cups detector, which generates an electrical signal. Each cup is connected to its own amplifier, which converts the electrical signal to digital and records the intensity of the signals generated in the particular cup. The IRMS allows the detection of two ionic beams at the same time.

The analytical precision of laboratory standards for $\delta^{18}O$ was better than 0.08 ‰, based on calibrated-internal standards run every six samples. Calibration to Vienna Pee Dee Belemnite (VPDB) was carried out following NBS-19 standards (Coplen, 1996).

2.4 Trace elements

2.4.1 Mg/Ca ratios in foraminifera as SST proxy

The foraminifera shells are mainly formed (99%) by calcite ($CaCO_3$), while the remaining 1% are trace elements such as Mg, Ba or Cd (Lea, 1999). These minor elements are incorporated into the structure of the shell directly from the seawater during the calcite precipitation. These elements can substitute the $Ca^{+2,}$ which typically forms the calcite since they have a similar ionic radius and the same oxidation state. This type of substitution is called isomorphism, which means the substitution of some element in certain crystallographic positions during the mineral formation. Therefore, the proportion of element substitution in the foraminifera calcite would reflect some extent, the seawater composition of that element, but other physical and chemical environmental conditions can also affect the degree of substitution of some elements, as it is the case f temperature, pH or salinity (Lea, 1999). In this sense,

Mg^{+2} is one of the elements that can easily substitute the Ca^{+2} during the calcification process, and the temperature control on its incorporation has been extensively studied through different experiments. Cultures of planktonic foraminifers under controlled environmental conditions have provided a solid evidence to relate environmental temperature to the Mg^{+2} incorporation, a feature further supported by Mg and Ca measurements on foraminifera from core top samples (Nürnberg, 1995; Nürnberg *et al.,* 1996a). Similarly, the temperature control on the Mg and Ca exchange has also been observed in benthonic foraminifera (Izuka, 1988; Rosenthal *et al.,* 1997; Rusell *et al.,* 1994). Several attempts to calibrate the Mg/Ca as a paleothermometer have demonstrated that Mg/Ca increases exponentially by a rate of 3% per °C (Lea *et al.,* 1999). The general calibration expression, which relates the sea temperature and the Mg/Ca ratios, is expressed as:

$$Mg/Ca\ (mmol \cdot mol^{-1}) = be^{mT}$$

where b is the pre-exponential constant, m is the exponential constant, and T is the temperature in °C (Lea *et al.,* 1997). Foraminifera culture experiments confirmed that each species has a different incorporation rate derived from the vital effects (Nürnberg, 1995; Nürnberg *et al.,* 1996a; Lea *et al.,* 1999; Toyofuku *et al.,* 2000). In this regard, Elderfield and Ganssen (2000) proposed the first specific calibration for *G. bulloides* based on core top measurements from the North Atlantic Ocean. Cisneros *et al.* (2016) expanded the *G. bulloides* calibration from the Elderfield and Ganssen (2000) to warmer temperatures based on core top foraminifera samples from the Mediterranean Sea. In order to oceanographically interpret the temperature signal derived from a specific foraminifera specie, it is necessary to know its habitat preferences in terms of both seasonality and water depth. *G. bulloides* is the studied specie in this thesis, which was selected because of its abundance in the sedimentary record and because it tends to live in the upper 100m of the water column and thus can be used as a proxy of SST. Sediment

trap studies in the Western Mediterranean have shown that *G. bulloides* blooms during the spring season but also in a few proportions during the fall bloom (Bárcena *et al.,* 2004; Rigual-Hernández *et al.,* 2012;). Thus the Mg/Ca derived SSTs reconstructed in this study are interpreted to mainly reflect spring temperatures, although it is considered that during the last deglaciation, this seasonality could have been different.

2.4.2 Laboratory Procedure

A total of 325, 228, and 249 samples were selected for the cores ALB-2 (1 cm resolution), MD95-2043 (7 cm resolution on average), and MD99-2343 (7 cm resolution on average), respectively (Table 2.1 – Samples Summary Table). In each sample, around 50-60 specimens of *G. bulloides* were picked between 250-355 µm size fraction to obtain a homogenous population. Each sample was gently crushed between two glass slides under a binocular microscope to open their chambers and remove possible remaining clays from the inside. This favours contaminant removal during chemical cleaning. The cleaning procedure used for foraminiferal trace elements analysis was based on Barker *et al*. (2003) and Pena *et al*. (2005) (further details on this procedure can be seen in Annex 2 – Foraminifera Mg/Ca cleaning protocol). This procedure consists of four steps:

(1) Clay removal step is designed to detach clay minerals remaining on the shells by using three different ultra-pure (UP) water rinses to bring clays into suspension. This is followed by two methanol rinses to further remove the clays; due to the lower methanol viscosity, clays can be more easily detached from carbonate fragments. Finally, an extra UP-Water rinse is carried out to remove any methanol residue.

(2) Reductive step is the most aggressive step for the foraminifera's shells, and it is designed to remove a variety of contaminants like Fe-Mn oxides. This step uses a mixture of hydrazine hydroxide, citric acid, and ammonia. For 30 minutes, samples are placed in a 90° hot bath and sonicated briefly every 2 minutes to promote the reaction. After this chemical attack, samples are rinsed six times with UP-Water to remove the reagents completely.

(3) Oxidative step is designed to remove any possible organic matter trace which could overestimate the final Mg values (Hastings *et al*., 1996; Rathburn and De Deckker, 1997). This step uses a mixture of sodium hydroxide and hydroxide peroxide that reacts with the sample in a boiling water bath for 10 minutes. Samples are rinsed three times with UP-water to eliminate any chemical reagent trace.

(4) Weak acid leaching to eliminate any possible contaminant phase that could still be attached to the shells. This step is performed with a very diluted nitric acid attack, and afterwards, samples are rinsed three times with UP-Water to eliminate possible traces of the acid.

Before the analysis, all the samples were dissolved in 3 mL of 2% nitric acid spiked with 20 ppb of Rh as an internal standard, centrifuged to avoid possible remaining solid particles, and transferred into clean vials (further details on this procedure can be seen in Annex 3 – Foraminifera Mg/Ca dissolution protocol)

2.4.3 Instrumental analysis of Mg/Ca ratios

Foraminifera major and trace elements in this thesis have been measured using a single-quadrupole Inductively Coupled Plasma Mass Spectometer (ICP-MS) Perkin-Elmer Elan 6000 at the Centres Científics i Tecnològics of the Universitat de Barcelona (CCiT-UB).

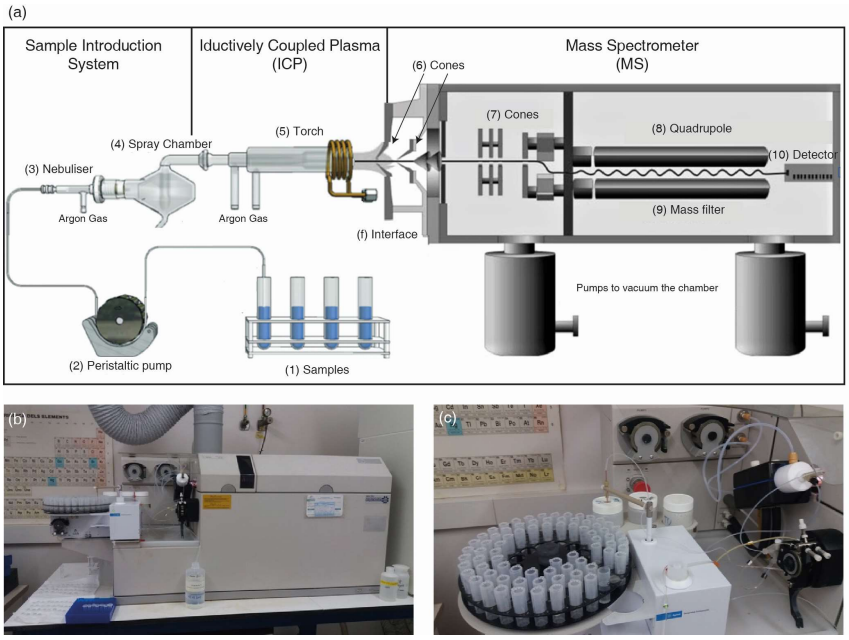

Figure 2.3 - Schematic diagram and pictures of an inductively coupled plasma mass spectrometer: *a) Schematic diagram of an ICP-MS from the samples (1) to the detector (10). Diagram has been modified from Brennan Dublude and Thomas, 2015; Wilschefsky and Batxer, 2019 and Balaram, 2019). b) General picture of the ICP-MS Agilent 7500ce at the Centres Científics i Tecnològics of the Universitat de Barcelona (CCiT-UB) including the sample introduction system, the ICP and the MS. c) Focused view on the sampler device, peristaltic pump and spray chamber. Pictures b and c courtesy of J. Torner.*

This instrument, like others ICP-MS, is composed of two parts: the plasma interphase (ICP), where the ion source is formed, and the MS, which houses the quadrupole mass filter and the secondary electron multiplier (SEM) detector (Fig. 2.3). The sample solution is pumped to a nebulizer using a peristaltic pump which allows a constant liquid volume entrance. The nebulizer converts the liquid into a fine spray using an argon gas flux. When the spray mist passes through the spray chamber, the larger droplets formed are removed, while the argon gas flow carries the very fine droplets to the ICP torch (Fig. 2.3). In this torch, the plasma is formed, which is substantially ionised Ar gas, which reaches around 10000°C. When the spray mist enters, the plasma gets atomized and finally ionised. Once the sample is ionised, it is carried into an interface formed by two cones disposed in a line. Both cones have a hole centered with the plasma torch,

which discriminates from the total plasma ions into a small beam that is accelerated through an electric field into the mass spectrometer. This interface separates the plasma ion source (ICP) at atmospheric pressure from the mass spectrometer (MS), which is emplaced into a vacuum chamber (Fig. 2.3). The ion beam goes through a stack of ion lenses that focus all masses from the ion beam to increase the amount of ions that reach the detector per unit of time (instrumental sensitivity). After the lens stack, the ions pass into the quadrupole, filtered by the mass-to-charge ratio (m/z). A quadrupole consists of two pairs of rods that create a specific voltage for each m/z. Once the specific voltage is applied, all other m/z will be displaced, and the chosen m/z will pass through the mass filter (quadrupole) without distortion until the detector. With each quadrupole scan, the ions present at each mass are passed to the detector and converted to an electronic signal. This specific voltage applied is changed for each m/z, allowing analysis of all the desired elements.

2.4.4 Process of the analytical results

The sample Rh spiking was used as an internal standard to calculate the net intensities, thus removing the analytical drift. During the analysis, a standard solution was also analysed for every four samples. This standard solution was gravimetrically prepared with known concentrations of Mg, Ca, Mn, Al, Sr, Cd, and Rh. It was produced with a ratio (element/Ca) comparable to that expected for the samples. For the ALB-2 core, this gravimetrical standard solution was used to obtain the analytical reproducibility, which was for the whole analytical process at 1.62% (1σ) for the Mg/Ca ratio. However, for the MD95-2043 and MD99-2343 cores, the data to estimate analytical reproducibility was not available. Consequently, the uncertainties associated with these cores for major and trace elements analyses are larger than those associated with the ALB-2 sediment core, which is the main focus of this thesis. The gravimetrical standard solution was also used to correct the Mg/Ca ratios for each ICP-MS round using the standard-sample bracketing (SSB) method, which is also used to correct the instrumental drift for a single round. Procedural blanks were routinely produced to detect potential contamination during the sample cleaning and dissolution process.

2.5 Radiogenic Isotopes

2.5.1 Basics of radiogenic isotopes

As the stable oxygen isotope, radiogenic isotopes are atoms that share the same atomic number but with different atomic masses due to their different number of neutrons. But radiogenic isotopes have the particularity to be daughter isotopes produced from the decay of a radioactive parent isotopes. Radioactive decay (Becquerel, 1986) is the spontaneous nuclear transformation of a radioactive parent isotope (^{R}P) to produce a radiogenic daughter (^{R}D) isotope (Choppin *et al.,* 2002; Banner *et al.,* 2004). Thus, the radioactive parent isotope is unstable and decays to a radiogenic stable daughter isotope. During this decay, alpha (α) or beta (β) particles are emitted (Fig. 2.4).

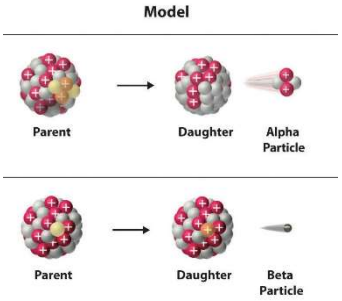

Figure 2.4– *Alpha and beta decay scheme. In the upper panel, the alpha decay. In the lower panel, the beta decay*

This radioactive decay from the radioactive parent to the radiogenic isotope could be in a single decay process,

$$^{87}Rb \rightarrow {}^{87}Sr + \beta^{-}$$

$$^{147}Sm \rightarrow {}^{143}Nd + \alpha$$

or involving several decay processes.

$$^{238}U \rightarrow {}^{230}U \rightarrow {}^{230}Th \rightarrow, \ldots, {}^{206}Pb$$

The decay mechanism is constant and thus can be expressed as a rate of radioactive decay of a given isotope which is proportional to the number of radioactive parents at a given time. Therefore, the ratio between the radioactive parent with the radiogenic daughter ($^{R}P/^{R}D$) is a function of time. Since isotope measurements are easily made as an isotope ratio widely uses the expression between the radiogenic daughter with the non-radiogenic stable isotope ($^{R}D/^{N\text{-}R}I$ being ^{R}D the radiogenic daughter and $^{N\text{-}R}I$ the non-radiogenic isotope; e.g. $^{87}Sr/^{86}Sr$, $^{143}Nd/^{144}Nd$). Thus, the evolution of $^{R}D/^{N\text{-}R}I$ ratio would constantly increase over time in a homogeneous Earth from the initial formation to the present day, allowing us to predict the relation in any context. However, the Earth's structure is not homogeneous, forming different layers from the inner core to the most recent crust. This differentiation also occurs due to the element behaviour incorporating different elements/isotopes in crystalline structures. Since the Earth's crust and mantel have distinct ranges of $^{R}D/^{N\text{-}R}I$ ratios owing to their distinct mineral composition, the $^{R}D/^{N\text{-}R}I$ evolution as a function of time will be directly depending on the sample or reservoir $^{R}P/^{R}D$ ratio (Banner *et al.,* 2004). Therefore, from the early Earth to the Earth's crust, $^{R}D/^{N\text{-}R}I$ ratio would increase due to the accumulation of $^{R}P/^{R}D$ by differentiation of the Earth's mantle via partial melting and crustal fractionation processes. The resulting Earth crust reflects a wide range of $^{R}D/^{N\text{-}R}I$ values due to the magmatic, sedimentary and metamorphic processes. However, even in

this wide range, the older crustal rocks tend to have higher $^{R}P/^{R}D$ values than the younger crustal rocks, and thus the radiogenic isotopes signal is closely linked to the geology of each zone (Grousset and Biscaye, 2005).

2.5.2 Radiogenic Isotopes as provenance proxies

In a marine context, most of the detrital sediments have their origin on the surrounding continents. The main mechanisms, but not the only, to incorporate these detrital sediments into the ocean are through river discharges or by eolian inputs. Therefore, these sediments will incorporate both the mineralogy and the geochemical fingerprints of their source. In order to decipher the potential source is necessary to characterize the radiogenic isotopic composition in both the marine sediments and the potential source provinces. Then, if the potential provinces have well-differentiated isotopic signals, it would be possible to decipher the provenance of the detrital sediments. Usually, different radiogenic isotopes such as Sr, Nd and Pb are combined to characterise better the potential origin of the detrital sediments as well as their potential transport mechanisms (e.g., Grousset *et al.,* 1988, 1992, 1998; Jullien *et al.,* 2007; Scheuvens *et al.,* 2013; Rodrigo-Gámiz *et al.,* 2015).

In the Mediterranean See, the main potential sources of the detrital sediments inputs are indeed from the European or North African rivers as well as to the dust transport from the Saharan desert. The different Sahara provinces have been widely characterized in terms of the radiogenic Sr and Nd isotopes signal since they are the main source for atmospheric particles in the world, and thus they play a crucial role in climate, ecosystems and air quality. The sources of Saharan dust have been classified in six provinces in base on their isotopic identity called Preferential Source Areas (PSA) (Fig. 2.5); Scheuvens *et al.,* 2013; Abouchami *et al.,* 2013). However, a recent study has grouped them into only three isotopic PSAs (Fig. 2.5; Jewell *et al.,* 2020) based on a high-resolution dust source activation frequency (Schepanski *et al.,* 2012). This PSA approximation provides a framework to establish changes in the contribution of different continental dust regions on geological timescales (Jewell *et al.,* 2020). Regarding the detrital sediments from river supply inputs, most drainage basins have not been widely characterized isotopically, with the exception of the Nile river in the eastern Mediterranean (e.g., Weldeab *et al.,* 2002a, 2002b, 2003; Revel *et al.,* 2010; Blanchet *et al.,* 2013. Although the isotopic characterization of the western Mediterranean river sediments is still lacking, some crustal rocks formations, such as the Betic Cordillera rock complexes, have been characterised for their Sr and Nd isotopic ratios (e.g., Bea *et al.,* 2010; Rossetti *et al.,* 2013; Bosch *et al.,* 2014; Varas-Reus *et al.,* 2017). Thus, this thesis combines, for the first time in the area, the different radiogenic signals from the Betic Cordillera rock complexes to obtain a potential riverine radiogenic end member from the zone.

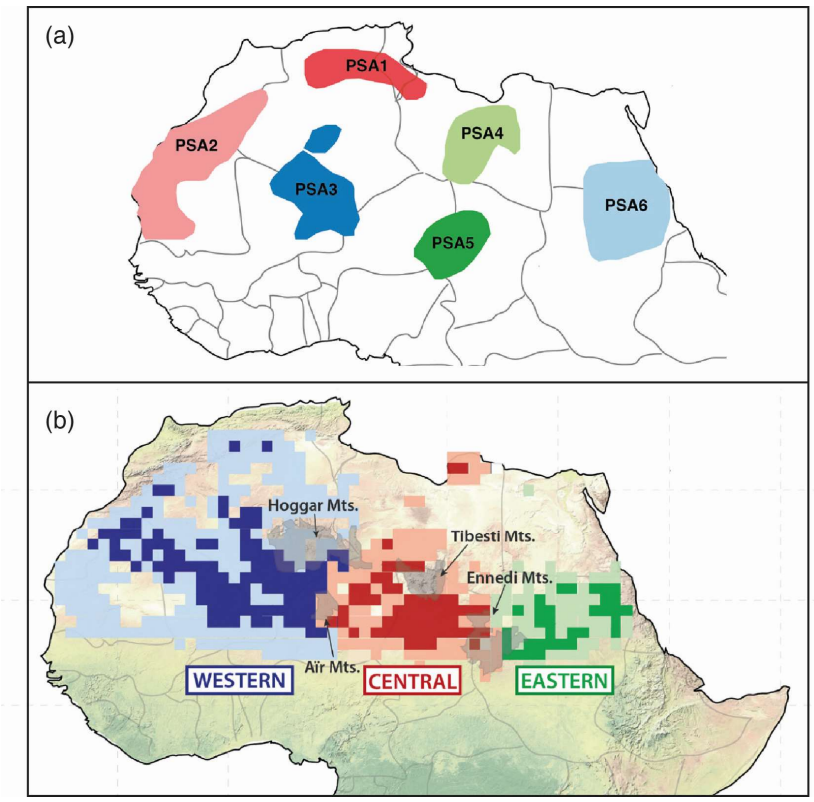

Figure 2.5 – Geographical definition of North African Preferential Dust Sources Areas (PSA) comparison. *Figures adapted from Jewell et al (2020). (a) PSA defined from 1 – 4 and 6 from Scheuvens et al (2013) and 5 Abouchami et al (2013). (b) PSAs proposed by Jewell et al (2020)*

2.5.3 Background on sample treatment, digestion and element separation for radiogenic isotopes

Bulk Sediment Sample Leaching

The first step to analyse the radiogenic signal from the detrital fraction of the marine sediments is to remove all the sedimentary components which are not lithic particles, that involved the carbonated organic fraction, organic matter, and the authogenic Fe-Mn oxyhydroxides. Typically, the biogenic silica should also be removed, but in the context of the Mediterranean Sea, this step is not required since it is not preserved in the sediments because Mediterranean waters are sub-saturated in silica. The effective removal of these components is relevant since they could potentially introduce a bias on the final radiogenic isotopic signal. Once the bulk sediment is leached, samples are ready for digestion.

Sample Digestion

The sample digestion process is fundamental and consists of the complete dissolution of the solid sediment, but it is critical to avoid any isotopic fractionation or element lost during the process. The digestion method needs to be adapted to the characteristics of the sample materials and the specific objectives of the study (Chao and Sanzolone, 1992). In this sense, there are

extensive literature on different digestion methods applicable to geological samples (Chao and Sanzolone, 1992; Potts and Robinson, 2003; Nóbrega *et al.,* 2006; Mariet *et al.,* 2008; Hu *et al.,* 2010; Zhang *et al.,* 2012; Jewda *et al.,* 2015; Yang *et al.,* 2022). Most of these methods use strong mineral acids like HF, HNO_3, HCl, $HClO_4$ or, more recently, NH_4F_2 or NH_4F. Each of these acids has different specifications and properties. For example:

- Hydrofluoric acid (HF) is the most effective mineral acid for breaking up strong Si-O bonds. Despite this silicate effectiveness in the digestion process, their product, SiF_4, is volatile and is lost in open-vessel digestion procedures. In addition, one of the products of the digestion is the formation of salts (fluoride salts), which are poorly soluble in almost all acids except with the $HClO_4$. Therefore, HF is usually combined with HNO_3 and with $HClO_4$. It is also essential to note that HF is one of the most hazardous mineral acids used in the laboratory. Any HF spills on the skin must be immediately washed with copious cold water, and the affected area must be treated with a gel containing calcium or even sub-cutaneous infiltrations of calcium.

- Nitric acid (HNO_3) is one of the most widely used digestion reagents since it is the primary oxidant liberating trace elements from many materials and its product forms, unlike HF, a highly soluble nitrate salt.

- Hydrochloric acid (HCl) is an excellent reagent to digest carbonates, phosphates, many metal oxides, and metals. The same basic silicates can be completely or partially digested with the HCl, but at high temperatures, it can better digest many silicates and refractory minerals, and their products form soluble chlorate salts.

- Perchloric acid ($HClO_4$) at high temperatures is the most powerful oxidizing mineral acid however reacts explosively with organic compounds. Thus, $HClO_4$ is usually used in combination with other acids like HNO_3, firstly to avoid or reduce the potential explosiveness and to increase the oxidizing reaction. The product of $HClO_4$ is perchlorate salts which are generally highly soluble. The high boiling point of this acid ensures a complete digestion of those refractory minerals, even better than HF. However, due to the high boiling point plus the potential explosiveness difficult a complete evaporation and could be harmful to the determination of some elements (Jarvis, 1992).

- Ammonium biflouride (NH_4F_2) has been successfully used recently (Mariet *et al.,* 2008; Hu *et al.,* 2010; Zhang *et al.,* 2012) to completely digest mafic and felsic samples. This digestion method ensures to digest of most of the sample in a shorter time (around 10 hours), unlike the other methods that use mineral acids. However, due to the high boiling point of the NH_4F_2 (239.5°C), samples are warmed up to reach 230°C, which reduce considerably the lifetime of the most used vials during digestion, the Teflon vials.

Beyond the reagents, another crucial factor to consider during the digestion process relies on the digestion method technique. Usually, samples are digested using opened or closed Teflon vessels or reactors but also is used the microwave method. Each of these methods has differences, mainly in the temperature and pressure of the reactions. Therefore, the detailed revision of the reagent properties and the digestion methods is essential to assess the appropriate procedure for the target of the study. Here are described the most relevant specifications of each digestion technique tested in this thesis.

- Closed reactors and sand bath: For this digestion protocol, powdered samples are introduced into reactors and filled with different acid species (usually HNO_3 HF and $HClO_4$) at different proportions. Closed reactors are placed into a stove and heated. When reactors are heated, the pressure inside increases, producing complete digestion. The sand bath is used to evaporate the acid species especially useful for evaporating the $HClO_4$ allowing it to reach higher temperatures (240°C).
- Closed Teflon vials: For this digestion procedure, powered samples are introduced into Teflon vials and filled with different acid species (usually HNO_3 HF and HCl) in different proportions. The major difference between the reactors and vials relies on the capacity of the reactors to hold up high pressures. When vials are heated, the pressure inside each one increases but to a lower degree than in the reactors. Therefore, in some cases, depending on the mineralogy of the sample, the complete sample digestion with Teflon vials could be challenging.
- Microwave-assisted digestion: This digestion procedure uses a microwave that produces electromagnetic radiation with a typical power of 1500W for heating. This device also provides a mechanism to increase the pressure inside each reactor. The radiating energy is absorbed by both the acids and the samples, which enhances the chemical reaction that completes the decomposition of the sample. Furthermore, both the high pressure and the high temperature cause the brust of the samples, thus allowing new surfaces to come into contact with the reagents and increasing the digestion rate (Nadkarni, 1984).

Therefore, in order to determine an effective digestion procedure, several elements need to be considered, such as nature, riskiness and of the viability of the reagents, possible residuals, elemental recuperations, isotopic relations, potential fractionation processes, time inverted, material fatigue among other minor details. The applied digestion procedure needs to keep a balance between the advantages and disadvantages derived from each of these parameters.

Column Chromatography: Elemental Separation

After the digestion and before the analysis, the targeted elements present in the sample need to be separated and purified. This separation is performed by column chromatography. Columns are loaded with a resin, also called stationary phase, which is a solid material attached to an inner support that has good adsorption and is suitable for separating the analytes (Fig. 2.7a). The digested sample is introduced into the column being loaded on the highest point of the

column. The sample would be retained in the stationary phase by adding different acids or the same acid with different concentrations. The targeted elements are then sequentially extracted by adding changeable volume and concentration of acids. Those elements with low affinity into the stationary phase would be less retained, and they will flow down earlier through the column. Conversely, those elements with higher retention capacity would remain into the stationary phase. Then, by changing the acids, the mobile phase will act as a solvent promoting the separation of the components in the sample to form bands, but also it will elute the components (Fig. 2.6a).

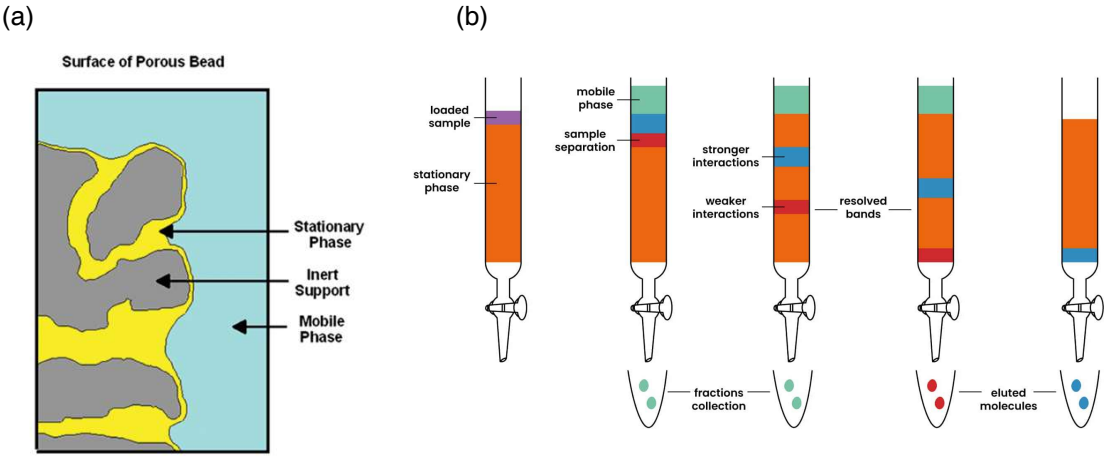

Figure 2.6 – Basics of extraction chromatography. *(a) simplified depiction of a portion of an extraction chromatographic resin bead showing the three major components of an EXC sy tem:the inert support, the stationary phase, and the mobile phase. (b) Schematic functionality of a chromatographic column. (Schemes from TrisKem International.*

Traditionally two types of resin have been used: the extraction and the ion exchange resin. The extraction resin (Fig. 2.6b) improves from the ion exchange resin the elemental selectivity, the separation yields and the capacity to separate multiple elements in one stage (Míková and Denková, 2007; de Muynck *et al.,* 2009). In this sense, the extraction resin has been widely used to separate elements such as Sr, Nd and Pb from a single digestion sample. However, in order to separate and purify these elements has been traditionally used a chromatographic method based on 4 stage columns, which consumes a long laboratory time and personal effort. This traditional 4 stage columns chromatographic method consist in:

(1) Separate the Pb in a specific Pb-resin column (Resin: AG1-8X). In this column stage, the Pb is purified and collected, and the REE are collected. In some cases, the Pb chemistry is repeated twice.

(2) Tru-spec column Chemistry. In this chemistry, the REE cut from the Pb column chemistry is used. In this column stage, both Rb and Sr cations together, and the REE are separated and collected.

(3) Sr-spec column Chemistry. In this stage column, the Rb and Sr elution collected in the previous chemistry is used to purify the elution of Sr.

(4) Ln-spec Nd column chemistry. In this stage column, the REE collected in the Tru-Spec column is used in order to isolate and collect the Nd.

This 4-column stages chemistry implies a large laboratory time consumption of about 2 weeks per batch of 12 samples. Besides this, it has also been reported that the Sr-spec column suffers a significant memory effect when the resin is reused several times (Pin and Bassin, 1992; Pin *et al.,* 1994; Deniel and Pin, 2001). The Ln-spec resin also suffers severe ageing during the REE separation of silicate rocks and produces changes in the elution profiles (Pin *et al.,* 1997; Míková and Denková, 2007).

However, Retzmann *et al.* (2017) propose a novel fast and reliable sample preparation procedure for the simultaneous separation of Sr, Nd and Pb using the DGA-Resin (TrisKem International). The DGA-Resin was first used and characterized by Horwitz *et al.* (2005). The Retzmann *et al.* (2017) study shows a fully automated set-up that allows unattended processing of the three isotopic systems from one sediment sample, taking 2h x sample and producing 12 samples per day. This substantially reduces laboratory time consumption compared to traditional separation methods. However, to perform this method proposed by Retzmann *et al.* (2017) is needed, the FAST-MC™ (Elemental Scientific, Omaha, USA), which is a fully automated low-pressure ion exchange chromatography system. Despite this Retzmann *et al.* (2017) procedure, this thesis proposed a novel procedure using the DGA-Resin to separate the three isotopic systems of Sr, Nd and Pb from one single digestion using an electro-valve controlled vacuum system (TrisKem Vaccum Box). This thesis improves the separation of the required elements, which was not solved in the Retzmann *et al.* (2017) procedure. This implemented system allows performing about 12-15 samples in 6h.

2.5.4 Laboratory Procedure for samples treatment, digestion and element separation for radiogenic isotopes

A total of 66 samples were selected to analyse the radiogenic isotope composition (Sr, Nd, and Pb) in the lithogenic fraction. From the total, 22 samples were from sediment trap ALB-1, 3 from the atmospheric dust, and 40 were from the ALB-2 core (Table 2..2). The following steps to prepare the samples to analyse the radiogenic isotopes were:(1) bulk sediment sample leaching; (2) sample digestion, and (3) elemental separation using the chromatographic columns.

(1) Bulk Sediment Sample Leaching Procedure

The chosen bulk sediment leaching procedure has been adapted from previous studies (Chester and Hughes, 1997; Bayon *et al.*, 2002; Gutjahr *et al.*, 2007; Povea *et al.*, 2015, Jewell *et al.*, 2022) (further details on this procedure can be seen in Annex 4). This procedure consists on:

Firstly, around 100 mg of bulk sediment per sample was hand-ground using an agatha mortar and pestle until a very fine dust was obtained. Ground samples were transferred into cleaned conic centrifuge tubes. The first leaching step consists of removing the organic matter using hydrogen peroxide (30% H_2O_2). This attack was repeated three times until samples did not react with the hydrogen peroxide by forming gas. The second attack consists of removing the biogenic carbonate using a buffered solution of acetic acid and sodium acetate at around pH 4. This solution dissolves the biogenic carbonate, mostly foraminifera, without dissolving the lithogenic carbonate fraction. This step was repeated three times. The third attack was performed using a combination of hydroxylamine hydrochloride, acetic acid, and Na-EDTA buffered at around pH 4. This step is designed to remove the Fe-Mn oxyhydroxide fraction, mostly present in the marine sediments. This attack was repeated twice. After completing the leaching procedure, samples were stored before the final sample digestion.

(2) Sample Digestion Protocol using nitric, hydrochloric and hydrofluoric

The digestion protocol applied in this thesis for the terrigenous sediment samples is adapted from Yang *et al*. (2022) (further details on this procedure can be seen in Annex 5). About 50 mg of powder leached sampled was placed into a Teflon vial, and added a mixture of concentrated HCl, HNO_3, and HF (2:2:1). Vials were closed and heated on a hotplate at 120°C for 48h. Then, samples were evaporated to almost dryness at 120°C, and the remaining residue formed a pearl-like dense texture. Then, 4mL of aqua-regia were added to each sample and evaporated straightaway at 100°C until almost dryness. Then, 4 mL of aqua-regia were added and heated on a hotplate at 120°C for 1h. After this, each sample was evaporated near dryness at 100°C, and next, 1mL of DD-HNO_3 was added in order to displace the chlorides and heated for 1h at 120°C. Then, each aliquot was dried down and re-dissolved in 2mL 1 mol·L^{-1} of HNO_3. After the complete digestion, samples were stored in preparation for chromatographic columns.

(3) Column Chromatography: Elemental Separation

The chromatographic separation of Sr, Nd, and Pb isotopic systems is performed with a single and simultaneous separation procedure using a 2mL-bed volume column of the so-called DGA Resin (N,N,N',N'-tetra-*n*-octyldiglycolamide, TrisKem International) in an electro-valve controlled vacuum system (TrisKem Vaccum Box). DGA resin functioning is based on the element retention time or elution at different acid species and their concentrations (Pourmand and Dauphas, 2010). The following procedure is modified from Retzmann *et al*. (2017) (further details on this procedure can be seen in Annex 6). This procedure consists on:

After the digestion, an aliquot of each sample is measured on the ICP-MS. These analyses are performed in batches of 12 samples. For each aliquot, the concentrations of Sr, Nd and Pb are measured. Every sample of each batch is diluted according to the Pb concentration in order to obtain above 40 ppb of Pb in a final sample volume of 1mL in 1 mol·L^{-1} HNO_3 concentration. Once the dilutions are performed and the cartridge cleaned and conditioned, 0.5mL at 1 mol·L^{-1}

HNO_3 of each sample is loaded in each column. The sample matrix is rinsed with 8mL at 1 mol·L^{-1} HNO_3. Next, Sr is eluded and picked up in 8mL at 0.2 mol·L^{-1} HNO_3. Then Pb is eluded and picked up in 8mL at 5 mol·L^{-1} HNO_3, Ca and a portion of Ce are rinsed by adding 35mL of 0.1 mol·L^{-1} HNO_3 followed by the Ce complete rinsing with 2mL of 2 mol·L^{-1} HCl. Then Nd is eluded and picked up in 12mL of 1.5 mol·L^{-1} HCl. Finally, Sm is rinsed with 20mL of 0.1 mol·L^{-1} HCl, followed by the cartridge cleaning. Both Nd and Pb are evaporated and dissolved in 2% - HNO_3 for the analysis in the multi-collector ICP-MS.

Sr was extra-purified using a 1mL-bed volume column of the Sr-Spec resin (4,4'(5')-di-t-butylcyclohexano-18-crown-6, TrisKem International) in the electro-valve controlled vacuum system (TrisKem Vaccum Box). The Sr samples picked up in the DGA-Resin are acidified by adding 2.7mL of concentrate HNO_3 doubled-distilled (hereafter HNO_3 D-D to simplify) in order to obtain a final sample acid concentration of 4 mol·L^{-1} HNO_3. Then the final sample volume will be 10.76mL at 4 mol·L^{-1} HNO_3. Before the sample loading, each cartridge was cleaned and conditioned by adding 20mL of UP-water followed by 10mL of 4 mol·L^{-1} HNO_3. Samples are loaded, adding the 10.76mL 4 mol·L^{-1} HNO_3. Rb is rinsed, adding 5mL of 4 mol·L^{-1} HNO_3. Sr is eluded and picked up in 10mL of UP-water. Finally, the cartridge is cleaned, adding MQ-water and 6 mol·L^{-1} HCl. Sr is evaporated and dissolved in 2% - HNO_3 for the analysis in the multi-collector ICP-MS.

2.5.5 Analytical technique of Multi-Collector Inductively Coupled Plasma–Mass Spectrometer

The Nd, Sr and Pb isotope ratios for the ALB-2 core, sediment traps samples and atmospheric dust samples were determined using a Plasma 3 Multi Collector Inductively Coupled Plasma Mass Spectrometer (Nu Instruments-AMETEK) at Centres Científics i Tecnològics of the Universitat de Barcelona (CCiT-UB; Fig. 2.7)

The Multi-Collector ICP-MS is a hybrid mass spectrometer which combines an inductively coupled plasma (ICP) plasma source, an energy filter, a magnetic sector analyser and multiple collector for the ions measurements. The introduction system is similar to the single quadrupole, even though samples in low concentrations can be desolvated in the nebuliser using an Aridus. The Aridus allows introducing the sample into the plasma torch in a dry state (without the solvent, in this case, acid 2% -HNO_3). This mechanism reduces solvent-base interferences such as oxides and hydrides. Once the sample is in the plasma torch and is ionised, ions are carried through the Ar gas to the mass spectrometer. These ions are accelerated through an electrical potential gradient. Moreover, ions are focused into a beam through different slits and electrostatically charged plates. The ion beams pass through an energy filter, which creates a constant energy spectrum into the ion beams. Then, ions are separated based on their mass-to-charge ratio when the ion beams pass through a magnetic field. These separated ions on their mass-to-charger are

directed into the collectors, where the ions are converted into voltage. The isotope ratios are calculated by the voltage comparison of the different collectors.

2.5.6 Analytical procedure

For the determination of the $^{143}Nd/^{144}Nd$ isotope ratios, the contribution of the ^{144}Sm interference on the ^{144}Nd signal, caused by potential samarium traces in the samples, was mathematically corrected by measuring the ^{147}Sm signal and assuming a natural $^{144}Sm/^{147}Sm$ ratio of 0.20480. An internal correction of the mass bias was carried out using the exponential law (Wombacher and Rechkämper, 2003), assuming a reference $^{146}Nd/^{144}Nd$ ratio of 0.7219. Additionally, the isotope ratios obtained after these corrections were normalised to the JNdi-1 standard using the sample-standard bracketing method and a reference $^{143}Nd/^{144}Nd$ value of 0.512115 (Tanaka *et al.*, 2000). Nd isotopic composition is expressed as:

$$\varepsilon_{Nd} = \left[\left(\frac{\left(\frac{143Nd}{144Nd}\right)_{sample}}{\left(\frac{143Nd}{144Nd}\right)_{CHUR}}\right) - 1\right] 10^4$$

where CHUR is the Chondritic Uniform Reservoir and represents a present-day Earth value of $(^{143}Nd/^{144}Nd)_{CHUR} = 0.512638$ (Jacobsen & Wasserburg, 1980).

For the determination of the $^{87}Sr/^{86}Sr$ isotope ratios, the contribution of ^{87}Rb to the ^{87}Sr signal was mathematically corrected from the measurement of the ^{85}Rb signal, assuming a natural $^{87}Sr/^{85}Sr$ ratio of 0.38562. The ^{86}Kr interference on ^{86}Sr, caused by impurities in the argon gas, was also corrected by measuring the ^{83}Kr signal and assuming a $^{83}Kr/^{86}Kr$ value of 0.66453. An internal mass bias correction using the exponential model was also applied to the $^{87}Sr/^{86}Sr$ ratio, using the traditionally accepted $^{86}Sr/^{88}Sr$ ratio value of 0.1194 (Nier, 1938). An additional normalisation using sample-standard bracketing was performed with NIST SRM 987 measurements before and after each sample and using a reference value for the $^{87}Sr/^{86}Sr$ ratio of 0.710249 (Azmy *et al.*, 1999).

Finally, for the determination of the $^{208}Pb/^{204}Pb$, $^{207}Pb/^{204}Pb$, $^{206}Pb/^{204}Pb$, $^{208}Pb/^{206}Pb$, and $^{207}Pb/^{206}Pb$ isotope ratios, several corrections were applied. The isobaric interference of ^{204}Hg on ^{204}Pb was mathematically corrected from the ^{202}Hg signal, assuming a natural $^{204}Hg/^{202}Hg$ ratio of 0.23007. Instrumental mass bias was corrected with the exponential model using Thallium (Tl) as an internal standard. For this, the samples/standards were spiked with a natural Tl solution while keeping a Sr/Tl ratio of approximately 10, and the $^{205}Tl/^{203}Tl$ natural ratio value was assumed to be 2.3875. The mass bias corrected ratios were then normalised to the NIST SRM 981 certified values using the sample-standard bracketing method. The reference values used were 36.721, 15.491, 16.937, 2.1681, and 0.91464 for the $^{208}Pb/^{204}Pb$, $^{207}Pb/^{204}Pb$, $^{206}Pb/^{204}Pb$, $^{208}Pb/^{206}Pb$, and $^{207}Pb/^{206}Pb$ ratios, respectively.

2.6 Bulk elemental composition of sediments

2.6.1 Laboratory Procedure

The bulk elemental composition of sediments was analysed for the ALB-2 core at 1 cm resolution using the X-ray Fluorescence (XRF) Core Scanner in the CORELAB at the University of Barcelona (Fig. 2.7c). This non-destructive analysis was performed by scanning the surface of the archive half from the ALB-2 sediment core. The surface of the archive half was previously smoothed with a glass plate to remove any irregularity and roughness. The sediment surface was covered by 4 μm- thick Ultralene film to eliminate the air between the sediment and the analyser prism, to prevent possible contamination in each measurement, and avoid possible sediment dryness during the analysis (Richter *et al.*, 2006; Tjallingii *et al.*, 2007). Previous to the analysis, the ALB-2 sediment core was photographed using the high-quality camera installed in the same XRF Core Scanner structure.

2.5.2 X-ray Fluorescence (XRF) Core Scanner

The determination of the bulk elemental composition of sediments for the ALB-2 core was performed using an Avaatech III Core Scanner system (Serial No. 21) at the CORELAB in the Facultat de Ciències de la Terra at the Universitat de Barcelona (Fig 2.7c). The XRF-core scanner provides the elemental composition from the sediment samples in a non-destructive, high-resolution, and fast analysis (Jansen *et al.*, 1998; Richter *et al.*, 2006; Rothwell and Rack, 2006). In compensation for the conventional X-ray fluorescence, the core scanner provides a semi-qualitative result, although recent studies (Cerdà-Domènech *et al.*, 2019) improve the conversion to quantitative results.

The XRF-core scanner measurements are directly performed on the sediment surface from the split core. For each measure, the X-ray source bombarded the sediment through a prism of 1.2 cm^2, directly resting on the sediment. The entire circuit is filled with helium to displace the air absorption. The principle of X-ray fluorescence is based on the excitation of atoms. When an atom from the sediment is excited by a primary X-radiation (generated by the X-ray source), an electron from the inner shell is ejected. Then, an electron from the outer shell fills the resultant vacancy emitting fluorescence radiation (secondary radiation) that is measured by the detector. Different fluorescence radiations mean different wavelengths, which are characteristic of each element. Finally, the results build a spectrum with different wavelengths (elements) and amplitudes (qualitative concentration of each element).

The largest the mass of the atom is, the more energy is needed to excite the inner shells and eject an electron. For this reason, the following excitation conditions were applied to the sediment cores:

- For the low energy measurements, a voltage of 10 kV was applied, a current of 0.5 mA and an excitation time of 10 s. These conditions were applicable to the following elements: Al, Si, Cl, K, Ca, Sc, Ti, V, Cr, Mn and Fe.

- The medium energy measurements were performed using a voltage of 30 kV, a Pd-thick filter to absorb the radiation from the lighter elements, a current of 2.0 mA, and an excitation time of 25 s. The elements excited with these conditions were: Ni, Cu, Zn, Br, Rb, Sr, Y, Zr, Mo, and Pb.

- For the high energy measurements, the voltage was 50 kV, with a Cu filter, to absorb the radiation from the lighter and medium elements, a current of 2.0 mA, and an excitation time of 35 s. In this case, the measured elements were: Ag, Cd, Sn, Te, I, and Ba.

These three different set-ups were applied along the records. The final intensities of the elements were obtained by processing the X-ray spectra with the Iterative Least square software (WIN AXIL) package from Canberra Eurisys.

Figure 2.7 – Images of the used instruments in this study: *a) Plasma 3 Multi Collector Inductively Coupled Plasma Mass Spectrometer (Nu Instruments-AMETEK) at Centres Científics i Tecnològics of the Universitat de Barcelona (CCiT-UB). Picture courtesy of Panthalassa. b) Finnigan-MAT 252 mass spectrometer at CCiT-UB. c) Avatech III Core Scanner system at Facultat de Ciències de la Terra. Pictures b and c courtesy of J. Torner.*

Chapter 3

Results

“Stair á mig lítill álfur
breytir mér í, en hreyfist ekki
úr stad sjálfur
starálfur”

Starálfur, Sigur Rós

3.1 Biogeochemistry from sediment cores

The following chapter describes the main results from ALB-2, MD95-243 and MD99-2343 core sites newly obtained during this thesis (Table 2.1). Chapter sections are arranged to introduce each proxy record separately.

3.1.1 Chronologies and age model

The chronology of core ALB-2 is based on fourteen ^{14}C AMS dates measured on planktonic foraminifera samples that were handpicked from the 215–355 µm fraction (8–33 mg). The top ten radiocarbon dates are based on monospecific samples of *Globorotalia inflata*, and the four older dates are based on multi-specific samples of planktonic foraminifera (Annex 9, S2). Radiocarbon ages were calibrated using MARINE13 calibration curves (Reimer *et al.,* 2013) that incorporate the global ocean reservoir effect (R ~400 yr). The age model was built using the Bayesian statistics software Bacon with the statistical package R (Blaaw and Christien, 2011) for marine sediments. From the core top to the first ^{14}C AMS date (10 cm), the age model was calculated using linear regression, assuming the age of the core top to be that of the sediment core recovery (2009 yr CE or -59 yr BP) (Fig. 3.1). The chronology at the base of the core was established using isotopic stratigraphy by correlating a well-expressed positive excursion in the δ18O-ALB2 to a well-dated comparable structure in the $\delta^{18}O$-MD95-2043 measured in both cases on *G. bulloides* (Fig. 3.1). According to the generated age model, the ALB-2 core covers the last 15 kyr BP with an average sedimentation rate of 22 cm/kyr, providing a time resolution of about 45 yr for the applied sampling interval (1 cm).

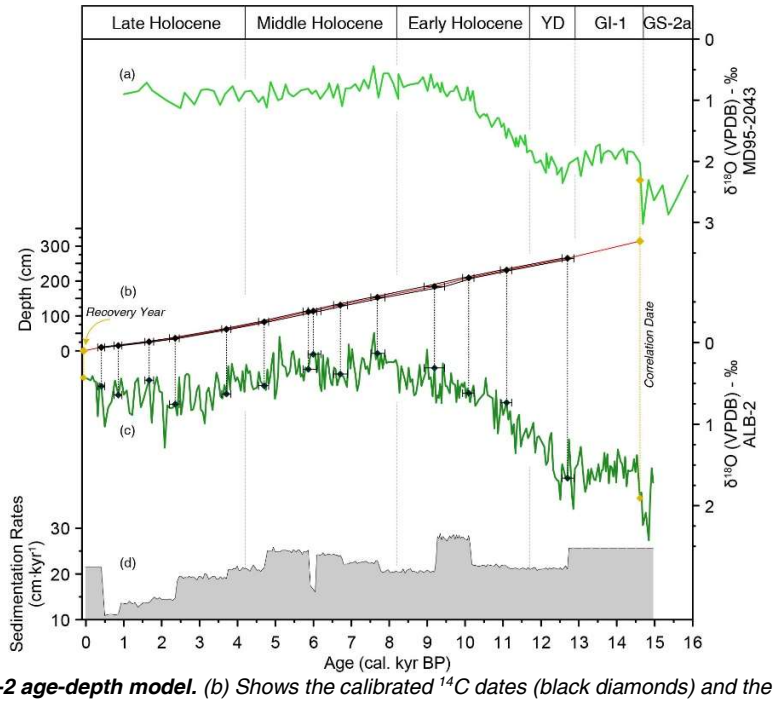

Figure 3.1 - ALB-2 age-depth model. *(b) Shows the calibrated ^{14}C dates (black diamonds) and the age-depth model within the 95% confidence intervals (black lines); the red curve shows the single best model based on the weighted mean age for each depth. Yellow diamonds correspond to the tie-points correlated with the well-expressed event in (a) MD99-2343 $\delta^{18}O$ record at the base, as well as the yellow diamond at the top, indicating the recovery year at the core-top. (c) Show each date on the ALB-2 $\delta^{18}O$ ‰ (VPDB) record. (d) The ALB-2 sedimentation rates.*

The age model for MD99-2343 was improved from that originally published by Frigola *et al.,* (2007), with nine new ^{14}C AMS dates incorporated into the previous age model (Annex 9, S2). The updated age model has nineteen ^{14}C AMS dates covering the last 17 kyr BP. Radiocarbon ages were calibrated using MARINE13 calibration curves (Reimer *et al.,* 2013) that incorporates the global ocean reservoir effect (R ~400 yr). The age model was built using the Bayesian statistics software Bacon with the statistical package R (Blaaw and Christien, 2011) (Fig. 3.2). The upper 20 cm of this core was lost during its retrieval, but for chronological purposes, the age of the missed core top was assumed to be the recovered year (1999 yr CE or -49 yr BP). The chronology during deglaciation was improved by adding two tie points by correlating a marked $\delta^{18}O$ structure in both the Minorca core MD99-2343 and the Alboran core MD95-2043 (Fig. 3.2).

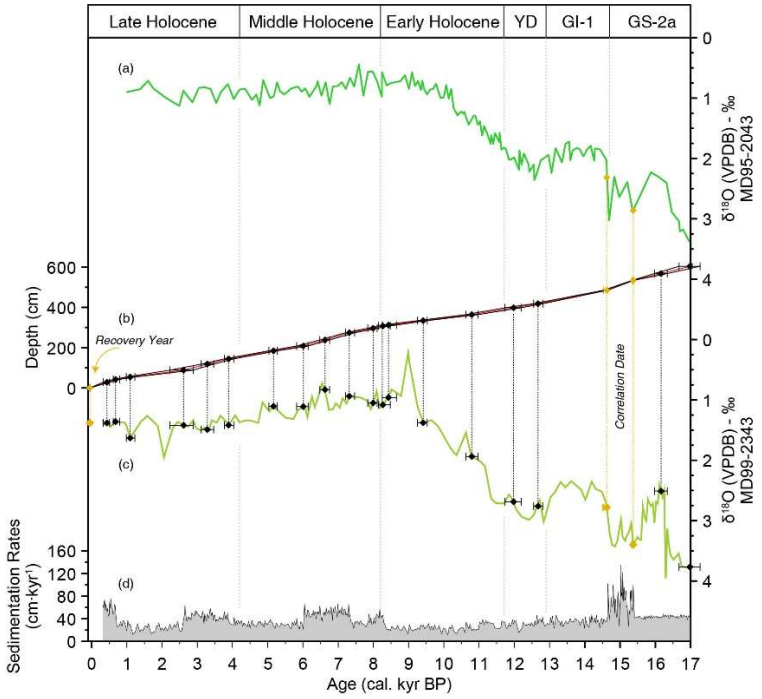

Figure 3.2 - MD99-2343 age-depth improvement from Frigola et al. (2007). *(b) Shows the calibrated ^{14}C dates (black diamonds) and the age-depth model within the 95% confidence intervals (black lines); the red curve shows the single best model based on the weighted mean age for each depth. Yellow diamonds correspond to those tie-points correlated with the well-expressed events in (a) MD99-2343 $\delta^{18}O$ record at the base and the recovery year at the top. (c) Show each date on the MD99-2343 $\delta^{18}O$ (VPDB) record. (d) The MD99-2343 sedimentation rates.*

3.1.2 Stable Isotopes

The ALB-2 *G. bulloides* $\delta^{18}O$ (VPDB) record clearly shows the isotopic depletion associated with the last termination until the late Holocene (Fig 3.3 The highest values of around 2.25‰ (note y-axis is reversed in the graph) are recorded at the end of the Greenland Stadial 2a (GS-2a). The oxygen isotope depletion associated with the last termination starts at ~ 12.7 kyr cal. BP until ~7.6 kyr cal. BP when it reaches the maximum $\delta^{18}O$ values around 0‰. Therefore, during this isotopic depletion, the $\delta^{18}O$ signal declined to around 1.80‰. After 7.6 kyr cal. BP, $\delta^{18}O$ values are maintained on average of 0.25 ‰, with several short-scale oscillations, until around 5 kyr cal. BP. At this point, $\delta^{18}O$ values describe a slight enrichment of 0.75‰ until ~2 kyr cal. BP when $\delta^{18}O$

values remain stable until the present, with average values of 0.60 ‰ and several larger-scale oscillations (Fig 3.3).

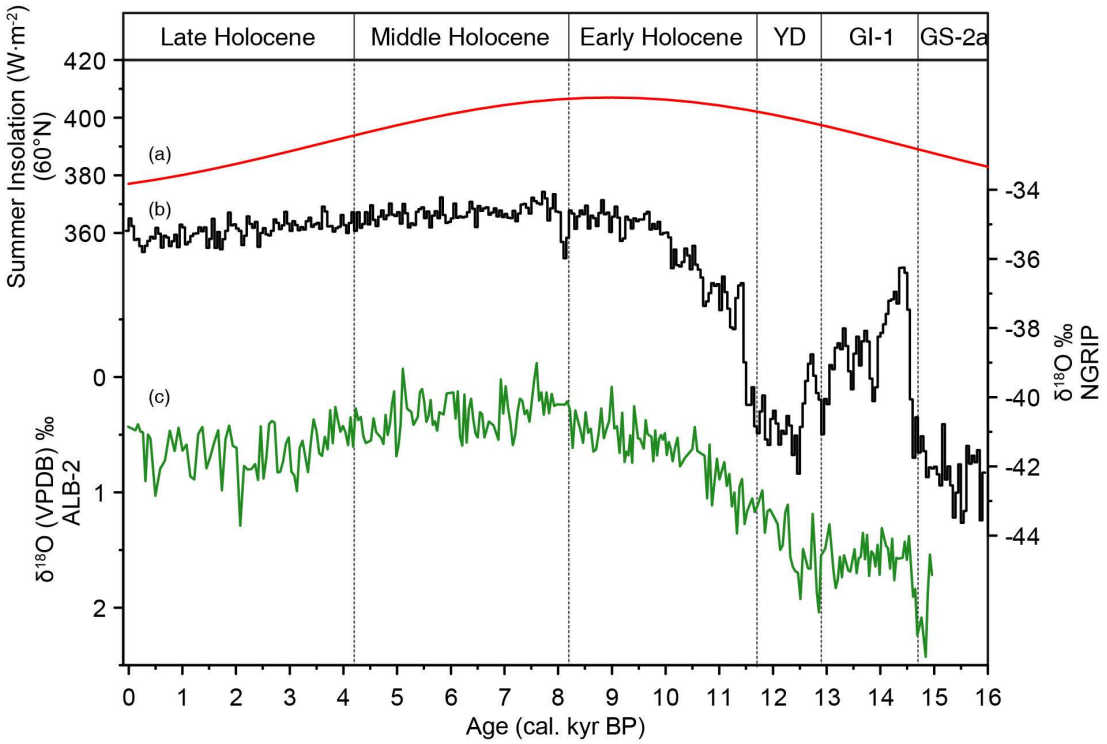

Figure 3.3 - ALB-2 G. bulloides $\delta^{18}O$ (VPDB) record compared with the North Atlantic global framework.
(a) Summer insolation at 60°N. (b) North Greenland Ice Core Project (NGRIP) $\delta^{18}O$ record. (c) ALB-2 $\delta^{18}O$ (VPDB)

3.1.3 Potential contamination for trace elements reconstructions

In order to check the reliability of the measured *G. bulloides* Mg/Ca ratios as a proxy for paleotemperatures, we have also measured elemental ratios such as Al/Ca and Mn/Ca to identify potential contamination caused by Fe-Mn oxides and/or aluminosilicates in the samples (Barker *et al.,* 2003; Pena *et al.,* 2005). These contaminant phases could be responsible for anomalously high *G. bulloides* Mg/Ca ratios and, therefore, overestimated sea surface temperatures (SST). Few samples were discarded according to values above 2σ of each Mn/Ca ratio (0.29 mmol·mol^{-1}) and Al/Ca ratio (1.74 mmol·mol^{-1}) (Fig. 3.4 a and b - Contamination). Furthermore, no co-variations of Mn/Ca and Al/Ca with Mg/Ca were found (Fig. 3.4 a and b).

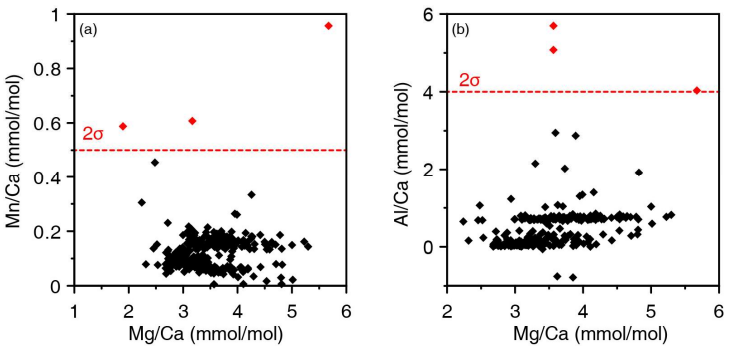

Figure 3.4 - Potential contamination for the trace elements reconstructions.
Comparison between the ALB-2 G. bulloides Mg/Ca ratios with (a) Al/Ca and (b) Mn/Ca ratios. In both plots, red dots correspond to those samples above 2σ resulting in potentially contaminated and, thus, removed to the following Mg/Ca derived to SST calculations in order to avoid overestimated SSTs

3.1.4 Mg/Ca derived to Sea Surface Temperatures

Here are presented the three new *G. bulloides* Mg/Ca Sea Surface Temperatures records from the ALB-2, MD95-2043, and MD99-2343 cores (Fig. 3.5).

The ALB-2 Mg/Ca derived SST record describes five well-differentiated periods (Fig. 3.5a-b). The first period, from the past to present, corresponds to the deglaciation when SST increases around 7.8±1.8°C in 1.75 kyr (2.8 mmol·mol^{-1} Mg/Ca). This means that the rate of warming for the deglaciation recorded in the ALB-2 was around ~4.5°C·kyr^{-1} (1.6 mmol·mol^{-1}·kyr^{-1} Mg/Ca). The SST increase associated with the deglaciation became truncated during the Younger Dryas period (Fig. 3.5a-b) with relatively warm SST on average around ALB-2- 19.5±0.6°C; 4.4±0.4 mmol·mol^{-1} Mg/Ca. During the early Holocene, maximum temperatures (21.9±1.9°C) were reached at around ~11 kyr (Fig. 3.5a-b). After this early Holocene maximum SST, a general cooling trend is recorded until the present, punctuated by several short-term oscillations (oscillations around 1.5°C). The Holocene section of the ALB-2-SST record can be further subdivided into three main intervals: (1) Early Holocene (11.7–9 kyr cal. BP) when SSTs were warmest and relatively stable (no significant trends), with an average value of 19.6±0.8°C (4.4±0.5mmol·mol^{-1} Mg/Ca) (Fig. 3.5a-b). (2) Middle Holocene displays a general cooling trend of ~4°C (~1.45mmol·mol^{-1} Mg/Ca) ending at around 4.2 kyr cal. BP when minimum Holocene SSTs were reached (15.5±1.5°C; 3.0mmol·mol^{-1} Mg/Ca) (Fig. 3.5a-b), (3) Late Holocene does not show any clear warming/cooling trend (average SST of 16.9±0.7°C; 3.5±0.3mmol·mol^{-1}) but shows larger SST variability (~2°C; ~1.3mmol·mol^{-1}) than during previous intervals (Fig. 3.5a-b – SST).

The MD95-2043-SST record from the Western Alboran Sea (Fig. 3.5c-d) and the MD99-2343-SST record from the Balearic Sea (Fig. 3.5e-f) have lower sampling resolution than the ALB-2 SST (Fig. 3.5a – SST) record. Despite different working resolutions, comparing all three SSTs records clearly shows a good agreement in the main SST patterns measured (Fig. 3.5). The magnitude of the deglacial SST warming is similar in all three records (6 – 7°C), and this warming is interrupted during the Younger Dryas (YD). It is worth noting that the YD interruption is not registered as an SST cooling but rather a period of relatively warm, stable and unchanging SSTs (16.5±1.6°C; the average for the MD95-2043 and MD99-2343). Maximum SSTs occurred around ~11 kyr cal. BP in all three records, followed by a general cooling trend that can be observed during the Early-Middle Holocene until the onset of the Late Holocene.

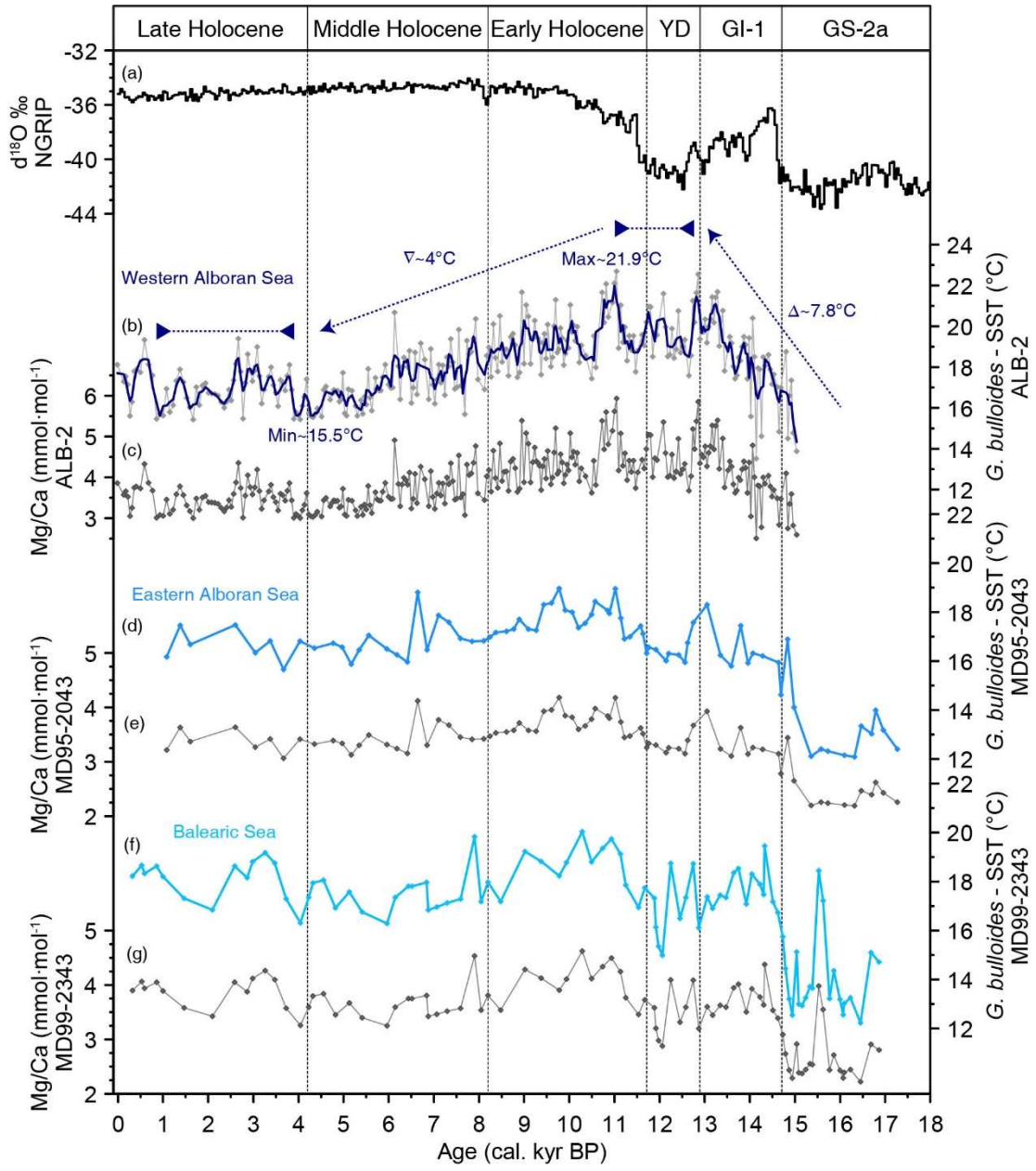

Figure 3.5 - Mg/Ca derived to SST for the ALB-2, MD95-2043 and MD99-2343 cores.
(a) The North Greenland Ice Core Project (NGRIP) $\delta^{18}O$ record in order to contextualise the following records in the temporal climatic framework. *(b) ALB-2 SST (°C). Light-grey dots correspond to each SST result, while the navy-blue line shows the three-point average. (c) ALB-2 Mg/Ca values. Dark-grey dots correspond to each Mg/Ca result. (d) MD95-2043 SST (°C) obtained through the (e) Mg/Ca ratios. (f) MD99-2343 SST (°C) obtained through the (d) Mg/Ca ratios*

3.2 Sedimentological proxies from the ALB-2 core

3.2.1 Elemental composition from XRF-core scanner

The relative elemental abundances of bulk sediments obtained from the XRF-core scanner for the ALB-2 were statistically treated using the Principal Components Analysis (PCA) approach. The PCA approach achieves to reduce the dimensionality of all relative elemental abundances measured and increases the interpretability of the dataset while preventing the maximum amount of information. For this analysis, we have used the relative abundances of the following elements: Al, Si, K, Ca, Ti, Mn, Fe, Br, Rb, Sr, Zr and Ba. As a result of the PCA (PCA-a), two principal components (PC) were identified: PC-1, which explains 36% of the total variance, and PC-2, which explains 31% (Fig. 3.6a). For this approach, Kaiser Meyer-Olkin (KMO) adequacy was 0.69. KMO test measures how suited the data is for the factor analysis, and values above 0.5 would be suitable to perform the PCA. When representing the data in two dimensions (PC-a vs PC-b), the different elements become distributed in four well-differentiated clusters (Fig. 3.6a). The first cluster comprises Si, Al and K, which could be attributed to the major elements typically present in aluminosilicates, mostly clay minerals (Fig. 3.6a). The second cluster is formed by Zr, Ti, Fe, and Rb. These elements can be associated whether as accessory elements in the aluminosilicates structures or as oxide minerals, such as ilmenite, rutile or zircon. Therefore, the first and second groups can be potentially associated with terrigenous particles. The third group clusters Ca, Ba, and Sr, mainly related to biogenic processes (Fig. 3.6a). Finally, the last group is formed by Mn and Br, elements usually associated with redox processes. At each cluster, elemental groups show a positive correlation in abundance.

In order to better understand the natural processes controlling the distribution of the different elemental groups, both group 1 (Si, Al and K) and group 2 (Zr, Ti, Fe, and Rb) were isolated and reanalysed in another PCA (PCA-b) (Fig. 3.6b). For this new principal component analysis, PC-1 and PC-2 explain 56% and 30% of the variance, respectively. For this PCA-b, the KMO adequacy is 0.66. In this PCA reanalysis, all elements clearly separate into two differentiated groups along the PC-2 axis (Fig. 3.6b). Interestingly, Ti and K invoke a higher loading factor on the PC-1 (0.93 and 0.88, respectively) than the other elements. This information indicates that the natural processes which produce changes along PC-1 are mainly represented by Ti and K. Regarding PC-2, elements become well-differentiated into two groups (Fig. 3.6b). Group 1, in positive correlation, incorporates Si, Al and K, while group 2, in negative correlation, incorporates Ti, Fe, Rb and Zr. The major loading factors for the PC-2, both in positive and negative correlation, are Si (0.76) and Rb (-0.59).

The elemental distribution on PC-1 and PC-2 provides a rapid classification of elements based on their correlations. Moreover, the PCA statistical technique provides a correlation of each data point between the original variables within the PC-1 and PC-2. This correlation is the loading factor. In this case, each data point measures the relative elemental abundances along the ALB-2 core and, thus, along the studied time period. Thus, the loading factor gives the correlation of each measurement within the PC-1 or PC-2 along the studied time period. In this case of study,

the loading factors given in PC-2 of the PCA-b (the PCA using only the groups 1 and 2; Fig. 3.6b – PCA) could potentially explain the correlation of each group of terrigenous along the covered period. (Fig 3.6c). Thus, by representing the evolution of PC-2 loading factors over the studied time period (Fig. 3.6c), we observe that during the period from 15 to 5 kyr cal. BP, the light elements (group 1, Si, Al and K) are more predominant, punctuated by several short-scale oscillations towards the heavy elements group (group 2, Zr, Ti, Fe, Rb) (Fig. 3.6c). After ~ 5 kyr cal. BP to the present, the heavy elements group become predominant, gaining weight towards the present (Fig. 3.6c).

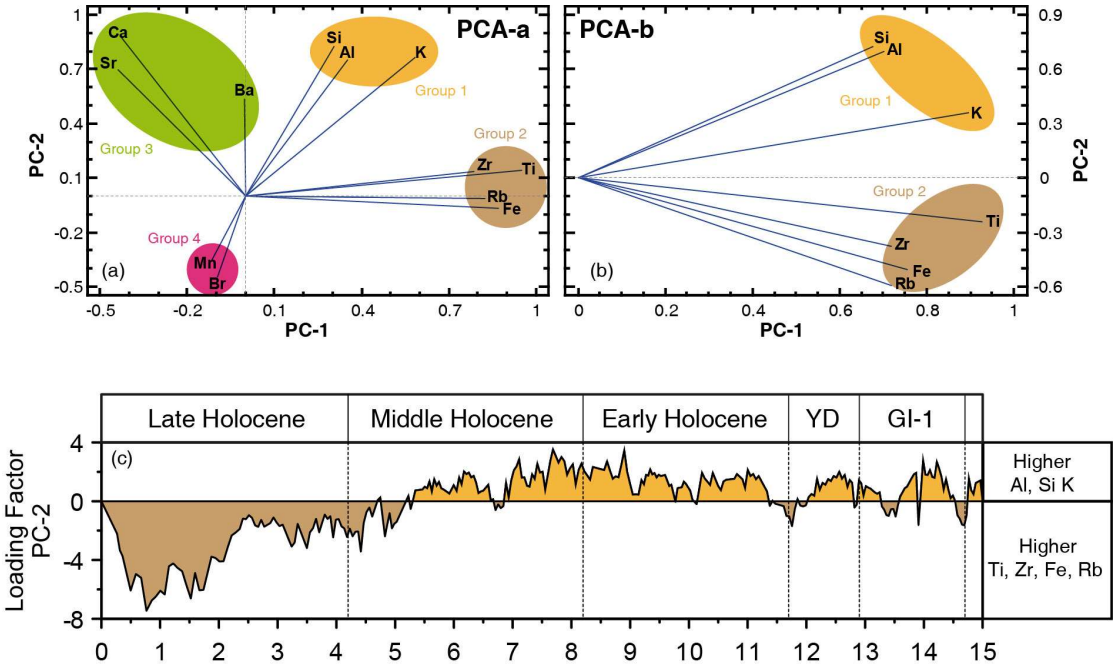

Figure 3.6 - Statistical distribution of the elemental composition of the ALB-2 core. *(a) Elemental composition measured in the XRF-core scanner statistically distributed in four groups based on the variables PC-1 and PC-2 (b) Statistical distribution of the group 1 and 2 based on a new PCA (c) Loading factor of the variable PC-2 in the PCA-b along the time. It indicates periods with a higher contribution of Al, Si and K (positive values in light orange) and, conversely, those with a higher contribution of Ti, Zr, Fe and Rb (negative values in light brown).*

3.3 Radiogenic Isotopes method development

This thesis develops a new full comprehensive method to work on three different isotopic systems (Sr, Nd and Pb) from the detrital fraction of the marine sediments. This new method is based on two interdependent protocols since the sample digestion to the elements' separation and purification using the chromatography technique. In this chapter are deployed the results of different protocols, both in digestion and chromatography, which have been developed in order to achieve a new fully competitive protocol improving those existing ones.

3.3.1 Digestion Protocol

In order to chemically digest the lithogenic fraction of the marine sediments from ALB-2, sediment trap ALB1-S and the atmospheric dust, five different digestions protocols were tested. These five digestion protocols were:

(I) Perchloric, nitric and hydrofluoric sand bath digestion protocol
(II) Nitric and hydrofluoric digestion protocol
(III) Nitric and hydrofluoric microwave-assisted digestion protocol
(IV) Ammonium difluoride digestion protocol
(V) Nitric, hydrochloric and hydrofluoric digestion protocol

For these tests, a large homogeneous sediment sample from ALB-2 was selected, allowing for many replicated analyses. Also, reference material BCR-2 (Wilson, S.A: 1997) was also processed in order to test the efficiency and accuracy of the different chemical digestion protocols used. Total elemental yields of the digestion protocols have been calculated by comparing the Sr, Nd and Pb total recoveries with the certificate reference material concentrations (Fig. 3.7 – Digestion Results and Table 3.1 – Recuperations). Total elemental recoveries for the ALB-2 digested sediment samples are difficult to estimate as there are no previous studies on the elemental concentrations of these sediments. However, using splits of the same large homogenised sediment sample makes it possible to compare final elemental recoveries in relative terms among them, which is invaluable for validating the different digestion protocols. Besides the recoveries also, the radiogenic isotopic ratios of Sr, Nd and Pb have been measured in the reference material BCR-2 and compared with the previously published ratios by Weis *et al.,* 2006 in order also to test the efficiency and accuracy of the different chemical digestion protocols used. The radiogenic isotopes in the ALB-2 homogenised sediment sample have also been systematically measured in each digestion.

BCR-2 samples were directly digested without applying the leaching procedure proposed by Jweda *et al.,* 2015. This previous leaching was proposed to remove the Pb contamination that BCR-2 suffered during its preparation. However, this contamination has been reported as homogeneous in all BCR-2 powders, and most studies report its isotopic values without the Pb leaching (Raczek *et al.,* 2003; Weis *et al.,* 2006). The ALB-2 samples were previously treated

before each digestion approach with the leaching protocol in order to eliminate potential contaminations of the lithogenic fraction and achieve a pure lithogenic radiogenic signal.

Order	Digestion Method	Recuperations BCR-2						Modified from
		Sr %	[ppm±2σ]	Nd %	[ppm±2σ]	Pb %	[ppm±2σ]	
(I)	Perchloric, nitric and hydrofluoric sand bath digestion protocol	67.5	[234±10.7]	79.0	[22±1.0]	73.2	[8±1.0.2]	
(II)	Nitric and hydrofluoric digestion protocol	90.7	[314±2.36]	49.6	[13.8±0.11]	102.4	[11.3±0.07]	*Jewda et al., 2015*
(III)	Nitric and hydrofluoric microwave-assisted digestion protocol	53.5	[185±2.6]	56.8	[16±0.5]	81.9	[9±0.3]	
		86.9	[301±4.2]	56.6	[16±0.3]	88.4	[10±0.2]	
		44.9	[155±2.6]	28.9	[8±0.1]	79.1	[9±0.1]	
		55.9	[194±0.6]	46.1	[13±0.2]	74.1	[8±0.1]	
(IV)	Ammonium difluoride Procedure	90.2	[321±8.9]	97.5	[27±0.5]	94.6	[10±0.2]	*Zhang et al., 2012*
(V)	Nitric, hydrochloric and hydrofluoric digestion protocol	101	[349±14]	109	[30±1.1]	91.5	[10±0.5]	*Yang et al., 2022*

	Sr ppm±2σ	Nd ppm±2σ	Pb ppm±2σ
Reference Conentration	346±14	28±2	11±2

Order	Digestion Method	Recuperations ALB-2 Sample						Modified from
		Sr %	[ppm±2σ]	Nd %	[ppm±2σ]	Pb %	[ppm±2σ]	
(I)	Perchloric, nitric and hydrofluoric sand bath digestion protocol	60.5	[57.1±14.8]	99.6	[14.0±4.9]	70.4	[5.7±1.7]	
(II)	Nitric and hydrofluoric digestion protocol	64.4	[60.9±0.3]	86.8	[13.5±0.06]	155.0	[12.6±0.13]	*Jewda et al., 2015*
(III)	Nitric and hydrofluoric microwave-assisted digestion protocol	60.3	[57.0±1.9]	9.8	[1.5±0.0]	114.4	[9.3±0.2]	
		67.1	[63.4±1.1]	11.9	[1.8±0.0]	144.7	[11.8±0.1]	
		80.5	[76.1±0.9]	45.1	[7.0±0.2]	94.9	[7.7±0.1]	
		11.0	[10.4±0.2]	8.0	[1.2±0.0]	15.1	[1.2±0.0]	
(IV)	Ammonium difluoride Procedure	48.5	[45.8±7.7]	70.8	[10.9±1.5]	77.9	[6.3±0.1]	*Zhang et al., 2012*
(V)	Nitric, hydrochloric and hydrofluoric digestion protocol		*Ref. Conc.*		*Ref. Conc.*		*Ref. Conc.*	*Yang et al., 2022*

	Sr ppm±2σ	Nd ppm±2σ	Pb ppm±2σ
Reference Conentration	94±7.8	16±2.3	8±0.2

Table 3.1 - Recuperation comparison between the different digestion protocols. *The upper table shows the values for the BCR-2 samples. The lower table shows the values for the ALB-2 samples. Both tables show each digestion approach and their recovery values for both BCR-2 and ALB-2 samples. Each digestion approach shows the recoveries in percentage for each element (Sr, Nd and Pb %) in the function of the reference material values (referred to at the bottom of the table). Also are shown the recovered concentrations in ppm with the 2σ error for each element.*

(I) Perchloric, nitric and hydrofluoric sand bath digestion protocol

Around 100 mg of powder was weighted into a Teflon reactor for each aliquot digested in this protocol. Each aliquot of powder was submerged in 2.5mL of double-distilled (DD) concentrated nitric acid (HNO_3), 10mL of ultrapure concentrated hydrofluoric acid (HF) and 2mL of concentrated perchloric acid ($HClO_4$) and placed closed in a stove at 90°C for 12h. After this, each reactor was opened and placed on a sand bath at 250°C to evaporate until incipient dryness, and additional 2mL of concentrated $HClO_4$ was added. The aliquot was dried down until it reached a dense-pearl texture, and each aliquot was then re-dissolved in 2mL of 1 mol·L^{-1} DD HNO_3.

Both BCR-2 and ALB-2 samples were fully digested upon visual inspection. BCR-2 recoveries were around 67.5% for Sr (234±10.7 ppm); ~79.0% for Nd (22±1.0 ppm), and ~73.2% for Pb (8± 0.2 ppm) (Fig. 3.7 a-c – Digestion Results and Table 3.1 – Recuperations). Regarding the ALB-2 recoveries were for Sr around 60.5% (57.1±14.8 ppm), ~99.6% for Nd (14.0±4.9 ppm) and ~70.4% for Pb (5.7±1.7 ppm).

The chromatographic separation for the digested powders of BCR-2 and ALB-2 were performed. However, during the separation protocol, any required elements were successfully recovered in their elution step. Consequently, the radiogenic isotope ratios for both Sr, Nd and Pb are unavailable for this digestion protocol. The potential mechanisms that involve the

unrecovered elements are further explained in the discussion in chapter 4.2. A complete procedure to analyse Sr, Nd and Pb isotopes in the detrital sediments fraction.

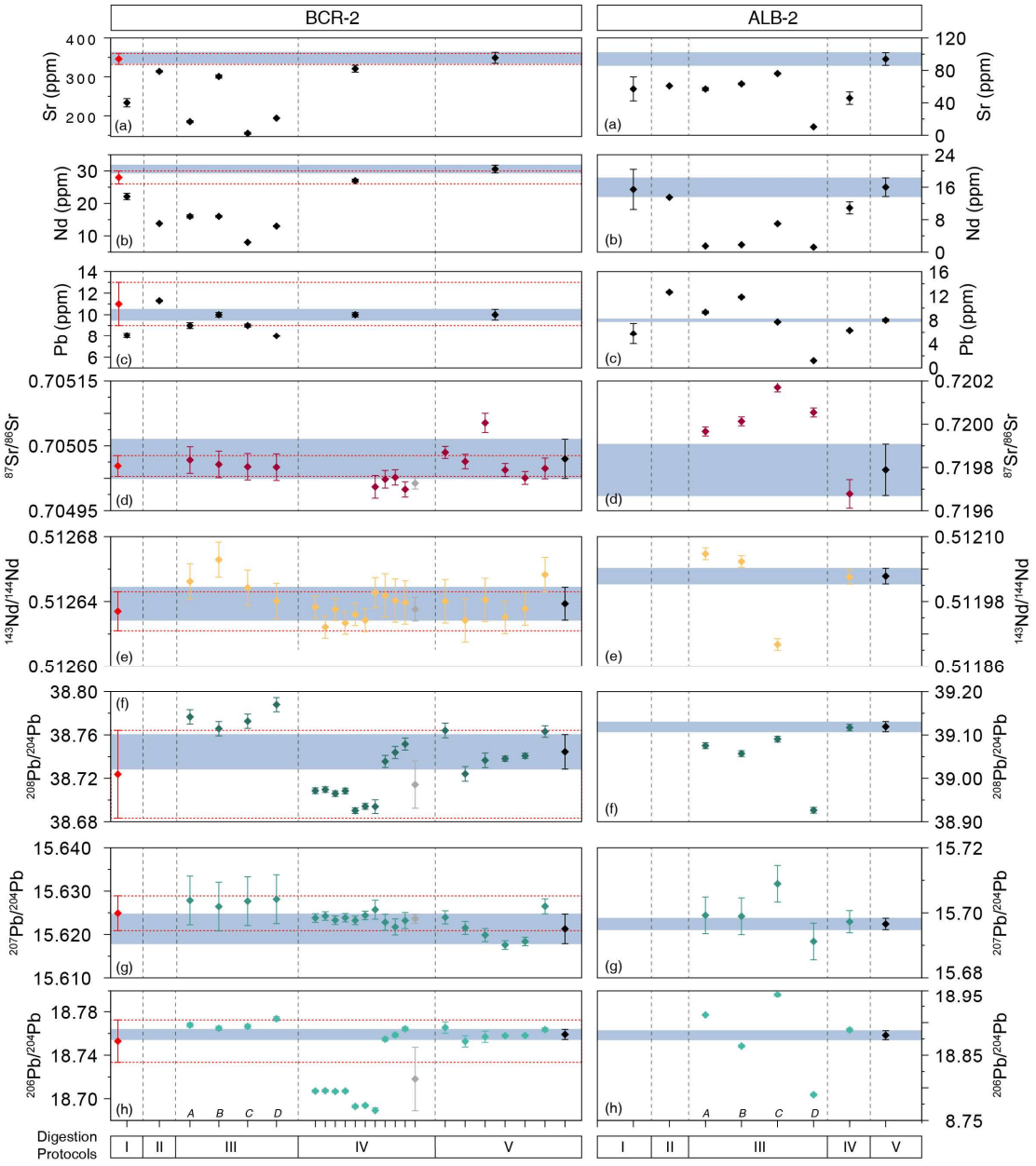

Figure 3.7 - Recoveries and isotopic values for each digestion protocol for both BCR-2 and ALB-2 samples. *From (a) to (c) are shown the recuperation values in ppm with the error bars for each digestion protocol for the BCR-2 and ALB-2 samples. From (d) to (h) are shown the isotopic ratios associated with each digestion protocol. The BCR-2 panel shows in red diamonds the certificated recuperation values (*Wilson, S.A., 1997*) and the published isotopic values (Weis et al., 2006), both with the associated error. The red dotted band show the limits of the errors. Grey and black diamonds show the average of the measured values for the digestions protocols IV and V, respectively. The blue-filled rectangle shows the limits of the errors associated (2σ standard deviation) to the average value of the digestion V. The ALB-2 panel also shows in digestion V the black diamonds corresponding to the average values. The blue-filled rectangle shows the limits of the errors associated (2σ standard deviation) to the average value of the digestion V for the BCR-2.*

(II) Nitric and hydrofluoric digestion protocol

This digestion protocol was originally proposed by Jweda *et al.,* 2015 to digest volcanic rock powder like BCR-2. For each aliquot digested following this protocol, around 50 mg of powder was weighed into a Teflon vial. For each aliquot of powder was added a mixture of 4mL of double distilled concentrated HNO_3 and 2mL of ultrapure concentrated HF and sonicated for 15 minutes. Aliquots were closed and placed on a hotplate for 12h at 120°C. Then each aliquot was evaporated at 120°C until it reached a dense-pearl texture. Afterwards, 2mL of concentrated DD-HNO_3 was added and placed on a hotplate for 12h at 120°C and dried down. Upon dryness, samples were re-dissolved in 1mL of 1 $mol \cdot L^{-1}$ DD-HNO_3.

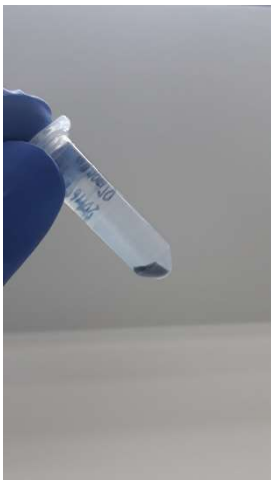

Figure 3.8 – *Black residue after the digestion protocol II.*

Even though BCR-2 samples were in appearance completely digested, ALB-2 terrigenous samples presented abundant black residue (Fig 3.8). Elemental recoveries for BCR-2 were successful for Sr and Pb with a values range comparable with those certificates (Weis *et al.,* 2006); around 90.7% for Sr (314±2.4ppm) and ~102.4% for Pb (11.3± 0.1 ppm) (Fig. 3.7 a-c – Digestion Results and Table 3.1 – Recuperations). However, Nd recoveries for BCR-2 were surprisingly lower, with values around 49.6% (13.8±0.1 ppm). Regarding the ALB-2 recoveries were for Sr around 64.4% (60.9.1±0.3 ppm), ~86.8% for Nd (13.5±0.1 ppm) and ~70.4% for Pb (5.7±1.7 ppm).

Due to the ALB-2 terrigenous samples presenting abundant black residue, this digestion protocol was inefficient to total digest this marine sample, so the chromatographic separation for both BCR-2 and ALB-2 digested powders were not performed.

(III) Nitric and hydrofluoric microwave-assisted digestion protocol

For each aliquot digested in this protocol, around 15 mg of powder was weighed into the microwave Teflon vials. Four different approaches (from A to D) were designed to be used with the microwave digestion system (Milestone UltraWAVE ECR). All four approaches used the same instrumental conditions applying a microwave power of 1500W, heated at 220°C and a pressure of 110 bar for 20 min. Different relative proportions of DD-HNO_3 – HF were selected for each method, in all cases with a final volume of 3mL. The four different approaches based on the acid proportions were:

(*A*) 2:1 - HNO_3: HF
(*B*) 2.5:0.5 - HNO_3: HF
(*C*) 1.5:1.5 - HNO_3: HF
(*D*) 1:2 - HNO_3: HF

Aliquots digested with the A and B approach apparently showed a complete digestion for both BCR-2 and the ALB-2 sediment aliquots. In the case of approaches C and D, fluorine residues were observed in the digested samples. BCR-2 recoveries were inversely correlated with the relative proportion of HF used for digestion (Fig. 3.7 a-c and Table 3.1). Thus, comparing the recoveries for the approaches B and D (less and higher relative HF proportion respectively) were for Sr 86.9% vs 55.9% (301±4.2 ppm vs 194±0.6 ppm), for Nd 56.6% vs 46.1% (16±0.3 ppm vs 13±0.2 ppm) and for Pb were 88.4% vs 74.1% (10±0.2 ppm vs 8±0.1 ppm) (Fig. 3.7 a-c and Table 3.1). This inverse correlation with the relative proportion of HF was not the case for the ALB-2 aliquots. Approach C, with a relatively equal proportion of HNO_3 and HF, showed the highest recoveries, while approach D, with a higher HF proportion, showed the lowest recoveries (Fig. 3.7 a-c and Table 3.1). Comparing the C and D recoveries values were for Sr 80.5% vs 11.0% (76.1±0.9 ppm vs 10.4±0.2 ppm), Nd 45.1% vs 8.0% (7.0±0.2 ppm vs 1.2±0.0 ppm) and Pb 94.9% vs 15.1% (7.7.1±0.1 ppm vs 1.2±0.0 ppm). ALB-2 Pb recoveries for approaches A and B were over-concentrated, obtaining values of 114.4% (9.3±0.2 ppm) and 144.7% (11.8±0.1 ppm), respectively (Fig. 3.7 a-c and Table 3.1) while Nd showed for these approaches low recoveries 9.8% (1.5±0.0 ppm) and 11.9% (1.8±0.0 ppm) respectively. Thus, these recoveries results observed for the ALB-2 aliquots show that each digestion approach acts uniquely in each element while there are consistent in the BCR-2 digestions (Fig. 3.7 a-c and Table 3.1)

Sr, Nd and Pb isotope ratios were obtained for the four microwave digestion approaches both in BCR-2 and ALB-2 samples (Fig. 3.7 d-h). The $^{87}Sr/^{86}Sr$ ratios for the BCR-2 show similar values between the four different digestion approaches and record the same values within the error as those previously published by Weis *et al.,* 2006 for BCR-2 (Fig. 3.7 d and Table 3.2). The $^{87}Sr/^{86}Sr$ ratios for the ALB-2 display substantial differences for each digestion approach, with different measured values beyond analytical uncertainty (Fig. 3.7 d and Table 3.2). Thus, these results show that neither of the BCR-2 $^{87}Sr/^{86}Sr$ ratios are affected by the different digestion approaches, conversely to the ALB-2 aliquots.

$^{143}Nd/^{144}Nd$ ratios measured for the BCR-2 show an evident pattern based on the relative proportion of HF used during the digestion. The $^{143}Nd/^{144}Nd$ ratio decreases at 25±11ppm from the least to the maximum amount of HF added (Fig. 3.7 and Table 3.2). Protocols A and B show the highest $^{143}Nd/^{144}Nd$ ratios, whereas C and D yield $^{143}Nd/^{144}Nd$ ratios closer to those reported by Weis *et al.,* 2006. Regarding the $^{143}Nd/^{144}Nd$ ratio on the ALB-2 samples, lower ratios are observed on the sample with a higher HF amount. However, no clear relation between the total amount of HF used and the final Nd isotope ratio measured can be established with the existing dataset (Fig. 3.7 e and Table 3.2).

All Pb ratios measured for the BCR-2 show higher values than those reported in the literature (Weis *et al.,* 2006). $^{208}Pb/^{204}Pb$ and $^{206}Pb/^{204}Pb$ ratios results inversely correlate with the relative proportion of HF used for the digestion (Fig. 3.7 f and h and Table 3.2). Conversely, $^{207}Pb/^{204}Pb$ ratios do not show this correlation (Fig. 3.7 g and Table 3.2). The Pb ratios for the

ALB-2 display substantial differences for each digestion approach, with different measured values beyond analytical uncertainty (Fig. 3.7 f to h and Table 3.2). The inverse correlation observed for the BCR-2 $^{208}Pb/^{204}Pb$, and $^{206}Pb/^{204}Pb$ ratios with the relative proportion of HF was not the case for the ALB-2 aliquots.

(IV) Ammonium difluoride digestion protocol

This protocol was originally proposed by Zhang *et al.,* 2012 and Hu *et al.,* 2013 as a fast digestion system for powdered rocks. The ammonium difluoride digestion procedure used for this thesis has been adapted from the previous authors. For each aliquot digested following this protocol, around 50 mg of powder was weighed into a Teflon vial. In each sediment aliquot was added four times the sample weight of distilled ammonium difluoride (4:1 proportion). Vials were placed on the hotplate for 3h at 230°C. After cooling, 2mL of concentrated DD-HNO_3 were added and placed again on the hotplate for 1h at 160°C. Then samples were evaporated until the residue formed a pearl-dense texture. When this residue was obtained, 1mL of concentrated DD-HNO_3 and 2mL of UP-Water were added and placed for 6h at 120°C. Finally, samples were evaporated and re-dissolved with 1mL 1 mol·L^{-1} DD-HNO_3.

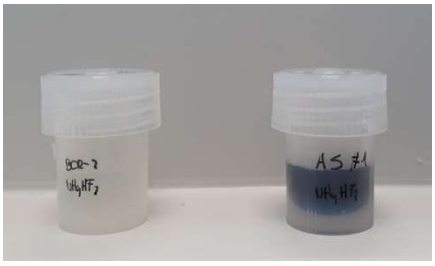

Figure 3.9 – Visual comparison of BCR-2 and ALB-2 in digestion IV *Comparison done at the end of the digestion protocol IV between the BCR-2 sample (left) and ALB-2 (right). The ALB-2 sample clearly shows a remaining black residue*

Differences in the final digestion solutions between the BCR-2 and ALB-2 samples were apparent. The BCR-2 standard was completely digested without any visible residue. On the other hand, most of the ALB-2 samples were not completely digested, and a black-fine residue was present in most cases (Fig. 3.9). Regarding recoveries (Fig. 3.7 a-c and Table 3.1), the ammonium difluoride successfully digested the BCR-2 samples with more than 90% recovery for each element. For the ALB-2 samples, Nd and Pb recoveries are higher than the other previous procedures, around 70-80%, but Sr recovery was poor (~49%) (Fig. 3.7 a-c and Table 3.1).

Ten different BCR-2 samples were analysed to obtain the Sr, Nd and Pb isotope ratios digested with the ammonium difluoride method (Fig. 3.7 d-h and Table 3.2 ts). $^{87}Sr/^{86}Sr$ ratios were only measured in four samples. The $^{87}Sr/^{86}Sr$ average value obtained for the BCR-2 was 0.704992±9ppm (Fig. 3.7 d and Table 3.2). This $^{87}Sr/^{86}Sr$ ratio is slightly under the BCR-2 reference value of 0.705019±16ppm (Weis *et al.,* 2006). $^{87}Sr/^{86}Sr$ ratio average value for the ALB-2 replicates is 0.7019678±66ppm (Fig. 3.7 Table 3.2).

The $^{143}Nd/^{144}Nd$ ratio for the BCR-2 (Fig. 3.7 e and Table 3.2), the average value obtained is 0.512635±7ppm in good agreement with the reference value of 0.512634±12ppm (Weis *et al.,*

2006). The complete sequence of $^{143}Nd/^{144}Nd$ ratios measured displays a shift in values. This sequence is temporally arranged in the function of the performed analyses. Thus, the first digestions performed display lower $^{143}Nd/^{144}Nd$ values than those performed later. The $^{143}Nd/^{144}Nd$ ratio for the ALB-2 is 0.512025±13ppm (Fig. 3.7 e and Table 3.2 I).

The Pb ratios for the BCR-2 average values obtained for $^{208}Pb/^{204}Pb$ is 38.7142±218ppm; $^{207}Pb/^{204}Pb$ is 15.6236±11ppm and for $^{206}Pb/^{204}Pb$ is 18.7181±292ppm (Fig. 3.7 f to h Results and Table 3.2). The $^{208}Pb/^{204}Pb$ and $^{206}Pb/^{204}Pb$ ratios for the BCR-2 shift along the results sequence. Thus, following the same pattern observed in the $^{143}Nd/^{144}Nd$ ratios, the first digestions performed display lower $^{208}Pb/^{204}Pb$ and $^{206}Pb/^{204}Pb$ values than those performed later (Fig. 3.7 f and h and Table 3.2). In both Pb ratios, the early digestion is distal from the reference values, while the last is in good agreement with the reference reported values (Weis *et al.,* 2006). Conversely, the $^{207}Pb/^{204}Pb$ ratio does not show this shift along the temporal sequence, and the average values agree with the reference reported values (Weis *et al.,* 2006) (Fig. 3.7 g and Table 3.2). The results for the three Pb isotopic systems in the ALB-2 aliquots are: $^{208}Pb/^{204}Pb$ 39.1169±77ppm; $^{207}Pb/^{204}Pb$ 15.6973±34ppm and $^{206}Pb/^{204}Pb$: 18.887±27ppm (Fig. 3.7 f to h –).

(V) Nitric, hydrochloric and hydrofluoric digestion protocol

This digestion method was modified by Yang *et al.,* 2022 to digest bulk sediment samples. For each aliquot digested following this protocol around 50 mg of powder was weighed into a Teflon vial. In each sediment aliquot was added a mixture of concentrated HCl, HNO_3, and HF (2:2:1). Each aliquot was closed and heated on a hotplate at 120°C for 48h. Then, samples were evaporated near dryness at 120°C until the residue formed a pearl-like dense texture. Following in each aliquot were added 4mL of aqua-regia and evaporated straightaway at 100°C until near dryness. Then, 4 mL of aqua-regia were added and heated on a hotplate at 120°C for 1h. After this, each sample was evaporated near dryness at 100°C, and then, 1mL of DD-HNO_3 was added in order the displace the chlorides and heated for 1h at 120°C. Then, each aliquot was dried down and re-dissolved in 2mL 1 mol·L^{-1} of HNO_3. Further details on this procedure can be seen in Annex 6).

Both BCR-2 and ALB-2 samples were completely digested, and no black residue was observed for the ALB-2 samples. BCR-2 recoveries were around 101% for Sr (349±14 ppm); ~109% for Nd (30±1.1 ppm), and ~91.5% for Pb (10± 0.5 ppm) (Fig. 3.7 a-c and Table 3.1). The recovered values with this digestion procedure completely agree within the errors with those certificate values for the BCR-2 reference material (Wilson S.A., 1997). ALB-2 recoveries were higher than in all other digestion protocols obtaining Sr concentrations of 94±7.8 ppm; for Nd 16±2.3 ppm and for Pb 8±0.2 ppm.

Six different BCR-2 samples were digested to obtain the Sr, Nd and Pb isotopic values for this nitric, hydrochloric, and hydrofluoric digestion procedure (Fig. 3.7 d-h and Table 3.2). The average values obtained for the $^{87}Sr/^{86}Sr$ ratio were 0.705030±30ppm (Fig. 3.7 d and Table 3.2),

in good agreement with the published values by Weis *et al.,* 2006 (0.705019±16ppm). The average $^{87}Sr/^{86}Sr$ ratio for the ALB-2 obtained with this digestion procedure was 0.719789±119ppm (Fig. 3.7 d).

The measured $^{143}Nd/^{144}Nd$ ratios for the BCR-2 (Fig. 3.7 e and Table 3.2) completely match those published, obtaining an average of 0.512639±10ppm (Published $^{143}Nd/^{144}Nd$ values: 0.512634±12 by Weis *et al.,* 2006). The $^{143}Nd/^{144}Nd$ average ratio obtained for the ALB-2 was 0.512027±14ppm (Fig. 3.7 e).

About the BCR-2 Pb ratios, both $^{208}Pb/^{204}Pb$, $^{207}Pb/^{204}Pb$ and $^{206}Pb/^{204}Pb$ show high reproducibility in the measurements (Fig. 3.7 f and h and Table 3.2). The values for the three isotopic systems perfectly agree with the published references. BCR-2 average values measured or the $^{208}Pb/^{204}Pb$, $^{207}Pb/^{204}Pb$ and $^{206}Pb/^{204}Pb$ ratio were 38.7444±159ppm (38.7237±405ppm); 15.6213±34ppm (15.6249±40ppm) and 18.7591±46ppm (18.7529±195ppm) respectively (referenced values from Weis *et al.,* 2006). Regarding the three Pb isotopic systems for the ALB-2 (Fig. 3.7 f – g), results obtained with this digestion were for $^{208}Pb/^{204}Pb$ 39.1191±117ppm; $^{207}Pb/^{204}Pb$ was 15.6966±17ppm and for $^{206}Pb/^{204}Pb$ was 18.8806±69ppm.

This digestion protocol achieves comparable Sr, Nd and Pb recoveries for the BCR-2, within the error, with those certificate values (Wilson S.A., 1997). Moreover, for the Sr, Nd and Pb ratios, this protocol achieves similar values to those reported (Weis *et al.,* 2006). Also, this digestion protocol accomplishes the higher elemental concentrations for the ALB-2 sediment aliquots.

3.3.2 Chromatographic Separation

Before isotope ratio measurements, each elemental isotopic system must be separated from the sample matrix and from other interfering elements (e.g. Rb & Sr; Sm & Nd; Hg & Pb). With this goal in mind, chromatographic separations are typically carried out to purify samples. For this purification is used the DGA Resin (TrisKem International) which allows to separate and purify Sr, Nd and Pb only using one single-stage chemistry. Moreover, to increase the time efficiency of these elemental separations is also used an electro-valve controlled vacuum system (TrisKem Vaccum Box). Thus, in order to obtain the final elution profile and full recoveries of Sr, Nd and Pb with this novel DGA-electro-valve combination, different experiments were performed, changing both the column bed-volume and the volume of acids used for elution as well as their concentrations.

Bed-volume column

Two different experiments were performed to evaluate the retention and the elements elution profiles on the DGA Resin. The first approach used a 1mL-bed volume column, similar to previous studies (Romaniello *et al.,* 2015; Retzmann *et al.,* 2017; Zimmermann *et al.,* 2019). For

the second approach, was used a 2mL-bed volume column. In order to compare both methods, the same elution scheme was performed based on Retzmann *et al.,* 2017 (Table 3.2). For both approaches were used a sample gravimetrically prepared with the combination of different elements at 2 mol·L^{-1} – DD-HNO3 concentration. Also, for both approaches, a 1mL sample was loaded.

The resulting elution profile obtained with the 1mL-bed volume column (Fig. 3.10) showed a significant co-elution of Sr during the Rb rinsing step immediately after the sample loading. Due to this co-elution, around 95% of Sr was prematurely lost. For Pb, there was also leakage both during the loading and elution of Sr steps; consequently, only about 30% of Pb was recovered during the Pb elution step. Following the elution profile, Ca and Ce were washed during 35mL. The first element that eluted was Ca, and at the end of this volume, Ce also started eluting. Upon performing the switch to hydrochloric based acids to elute Nd, it is also observed a co-elution of Ce with the Nd cut. Despite this co-elution, Nd total recoveries were excellent (99%).

Using the 2mL-bed volume columns did not significantly modify the elution schemes of the 3 elements when compared to 1mL-bed volume columns. Only minor displacements in the elution profiles were observed, but poor elemental recoveries and co-elution of interfering elements were still present (Fig. 3.10 b). Around 77% of Sr was lost during the Rb rinsing. Pb was leaked into the Sr elution step, even though Pb yield was generally improved (67%) Ca and Ce showed a similar scheme than in the 1mL-bed volume column. Nd recovery was around 99%.

Based on these results, all further improvements in the chromatographic protocols were based on the 2mL-bed volume columns (further details are discussed in Chapter IV – Discussion).

Modified from Retzmann *et al.,* 2017

Step	Purpose/analyte	Volume	Acid
1	Condition Column	6mL	2mol·L^{-1} HNO_3
2	Load Sample	1mL	2mol·L^{-1} HNO_3
3	Rinse Matrix (Rinse Rb)	5mL	2mol·L^{-1} HNO_3
4	Elute Sr	5mL	0.2mol·L^{-1} HNO_3
5	Elute Pb	5mL	5mol·L^{-1} HNO_3
6	Wash Ca and Ce	35mL	0.1mol·L^{-1} HNO_3
7	Elute Nd	9mL	2mol·L^{-1} HCl
8	Rinse Matrix (Rinse Sm and other REE)	8mL	0.1mol·L^{-1} HCl

Purposed elution profile (this thesis)

Step	Purpose/analyte	Volume	Acid
1	Condition Column	10mL	1mol·L^{-1} HNO_3
2	Load Sample	0.5mL	1mol·L^{-1} HNO_3
3	Rinse Matrix (Rinse Rb)	8mL	1mol·L^{-1} HNO_3
4	Elute Sr	8mL	0.2mol·L^{-1} HNO_3
5	Elute Pb	8mL	5mol·L^{-1} HNO_3
6	Wash Ca and Ce	35mL	0.1mol·L^{-1} HNO_3
7	Wash Ce	2mL	2mol·L^{-1} HCl
8	Elute Nd	12mL	1.5mol·L^{-1} HCl
9	Rinse Matrix (Rinse Sm and other REE)	20mL	0.1mol·L^{-1} HCl

Table 3.2 - Comparison of the elution parameters *of the Retzmann et al., 2017 separation method and the proposed separation protocol of Sr, Pb and Nd using a self-packed 2 mL DGA column.*

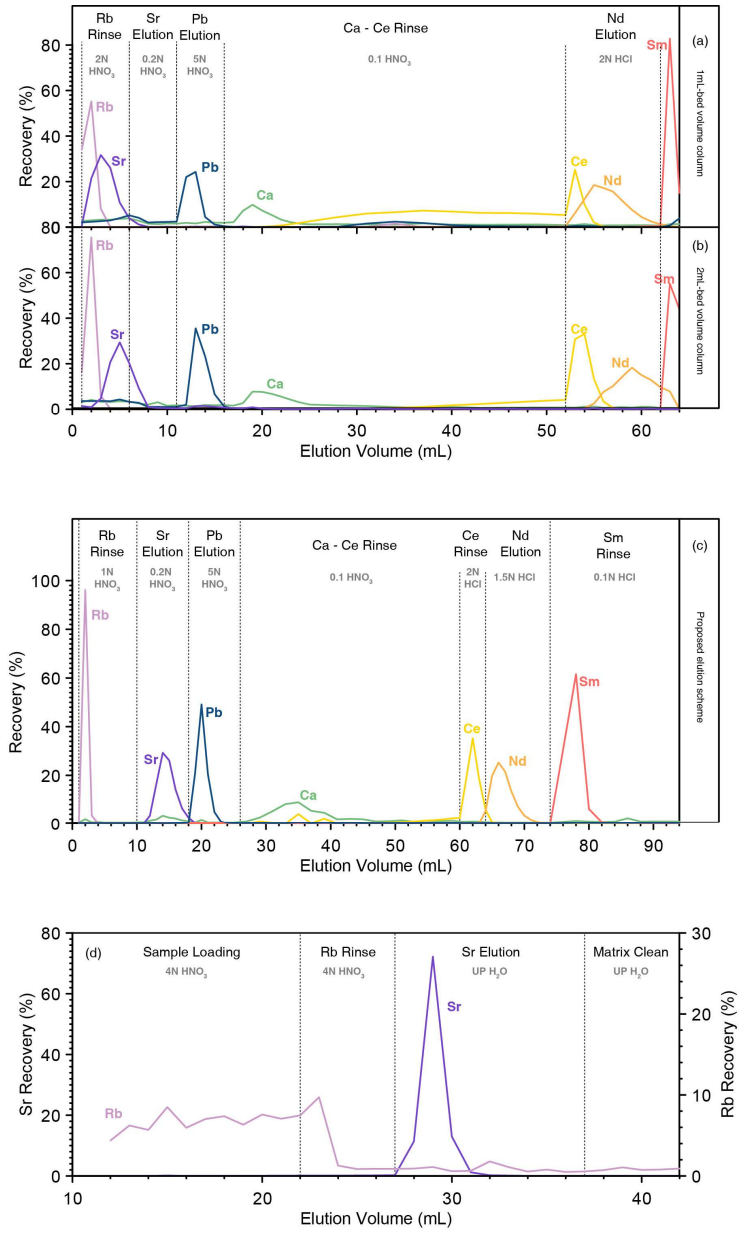

Figure 3.10 - Elution profiles for recovering Sr, Pb and Nd.
For the (a) and (b) is used the elution scheme proposed by Retzmann et al., 2017. From (a) to (c) is used the DGA-Resin. (a) Elution scheme using 1mL-bed volume column; (b) Elution scheme using 2mL-bed volume column; (c) Proposed elution scheme in this study;(d) Elution scheme to purify the Sr elution with the Sr-Spec Resin.

Acids concentrations and acid volumes

For the previous approaches using 1mL and 2mL-bed volumes were used a sample HNO_3 acid concertation of 2 $mol \cdot L^{-1}$. However, based on the specific retention coefficients for each element on DGA, HNO_3 acid concertation for the samples was changed from 2 $mol \cdot L^{-1}$ to 1 $mol \cdot L^{-1}$. Before introducing the samples, each one was diluted to obtain a final concertation of 40ppb of Pb. Subsequently, samples were loaded in a 0.5mL volume (further details are discussed in Chapter IV – Discussion).

The core key of Sr, Nd and Pb separation rests with isolating each element without the interference of others. With this aim, the main efforts focused on separating Rb from Sr, Sr from Pb, Pb from Ca, and Ce from Nd. The main changes are explained, but further details are discussed in Chapter IV – Discussion (a detailed elution scheme can be seen in Annex6). Rb and Sr were separated by changing the sample acid concentration from 2 mol·L^{-1} to 1 mol·L^{-1} HNO_3 (Fig. 3.10c; Table 3.10b). Also, the Rb rinsing was enlarged from 5mL to 8mL using 1 mol·L^{-1} HNO_3. During the Rb rinsing step, around 99% of Rb was washed. The separation from Sr and Pb was performed by enlarging the Sr elution from 5 to 8mL of 0.2 mol·L^{-1} HNO_3. During this step, Sr was recovered at around 96%. To increase the total Pb amount recovered, the Pb elution was enlarged from 5 to 8mL of 5 mol·L^{-1} HNO_3. This modification allowed the recovery of around 97% of Pb (Fig. 3.10c). After the Ca-Ce washing was added 2mL of 2 mol·L^{-1} HCl to separate Ce from Nd. Ce directly eluted at these HCl concentrations, while Nd started to elute. After this 2mL, the acid concentration was changed to 1.5 mol·L^{-1} hydrochloric acid Ce dramatically ceased its elution, and the Nd elution increased (Fig. 3.10c). Therefore, Ce elution was strained in 2 mL, and at 1.5 mol·L^{-1} hydrochloric acid Nd was collected in 12 mL volume. Nd recuperations was around 99% (Fig. 3.10c).

The presence of Rb during the Sr analyses could interfere with the final Sr isotopic results biasing toward lower values. Therefore, to avoid possible Rb interferences on the sediment samples, an extra purification of Sr was performed using the Sr-Spec Resin (a detailed elution scheme can be seen in Annex 7). The Sr samples eluted from the DGA-Resin were acidified to obtain a 4 mol·L^{-1} HNO_3 acid concentration. The final volume of the samples was 10.76mL, which was added to the Sr-Spec column. While the sample was introduced and flowing through the column, Rb started to elute. Even though most of the Rb was eluted during the sample loading, 5mL of 4 mol·L^{-1} HNO_3 acid was loaded to guarantee the complete Rb elimination (Fig. 3.10d). The Sr was eluted in 10mL of UP-Water, recovering around 97% (Fig. 3.10d).

3.4. Radiogenic isotopes in the lithogenic fraction

This section shows the results for the lithogenic fraction Sr, Nd, and Pb isotope ratios measured on the ALB-2 marine sediment core, the ALB-1-S sediment traps and the atmospheric dust samples. Sample treatment, purification and isotope ratio analysis followed the modified protocols detailed in annexes 5, 6 and 7.

3.4.1 ALB-2 Marine Sediment Core

34 lithogenic fraction samples from the ALB-2 marine sediment core were analysed to measure the radiogenic Sr, Nd and Pb isotope ratios for the last 15 kyr cal. BP (Fig. 3.11).

The $^{87}Sr/^{86}Sr$ record describes three distinct intervals during the studied period. Between the deglaciation and the onset of the middle Holocene, higher $^{87}Sr/^{86}Sr$ ratios are recorded with average values around 0.720643±17ppm (Fig. 3.11a). Following this period, an isotopic shift towards lower $^{87}Sr/^{86}Sr$ ratios is registered, reaching the lowest values of around 0.719539±36ppm at the onset of the late Holocene. Lower $^{87}Sr/^{86}Sr$ values are recorded during the late Holocene with average values around 0.719849±37ppm (Fig. 3.11a).

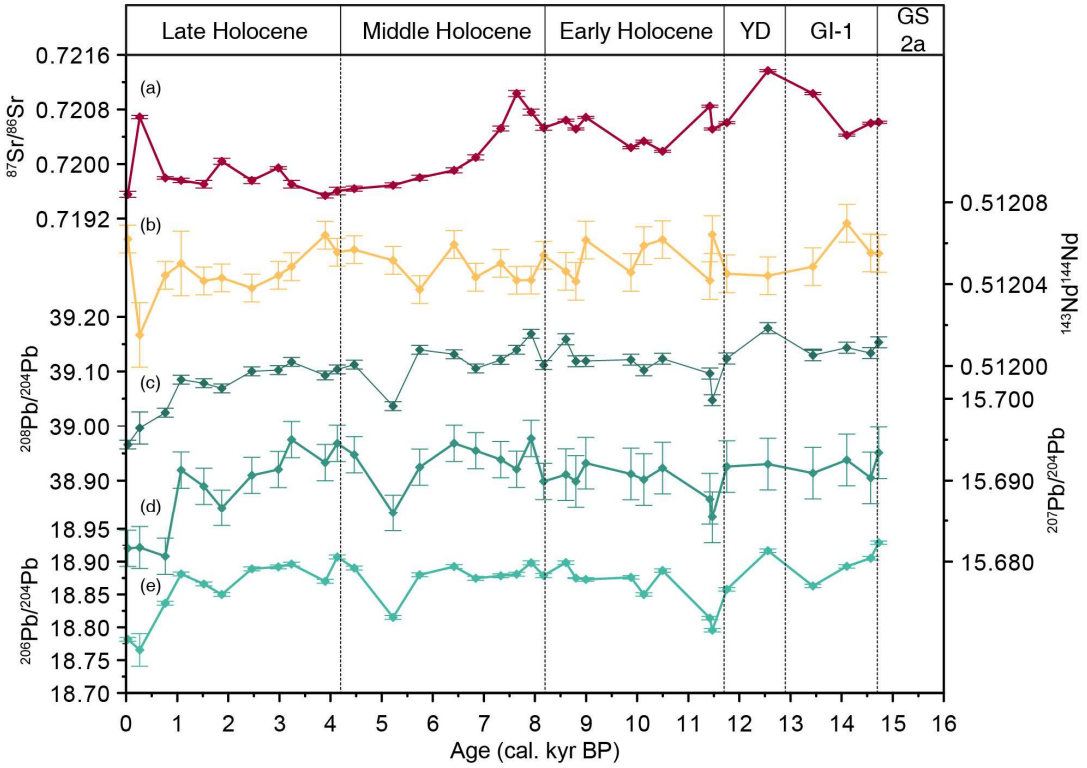

Figure 3.11 - Radiogenic isotope records from the ALB-2 core. *Age is shown in the X-axis expressed in kyr. (a) $^{87}Sr/^{86}Sr$, (b) $^{143}Nd/^{144}Nd$, (c) $^{208}Pb/^{204}Pb$, (d) $^{207}Pb/^{204}Pb$, and (e) $^{206}Pb/^{204}Pb$ records. Each value has associated with its error bar in 2σ*

The $^{143}Nd/^{144}Nd$ isotope ratios obtained on the ALB-2 sediment core show relatively minor oscillations along the studied interval. The larger oscillations are seen during the deglaciation until the onset of the late Holocene. During the late Holocene, variability in the $^{43}Nd/^{144}Nd$ values

becomes minimum, with a decreasing trend in the $^{143}Nd/^{144}Nd$ values towards the present. The total range of $^{143}Nd/^{144}Nd$ values extends from 0.512070±9ppm to 0.512037±7ppm (Fig. 3.11b).

The three Pb isotopic systems show relatively small variations along the recovered period. However, in the $^{208}Pb/^{204}Pb$, $^{207}Pb/^{204}Pb$ and $^{206}Pb/^{204}Pb$ ratios significantly lower ratios compared to the averages are recorded in the most recent samples. These low $^{208}Pb/^{204}Pb$, $^{207}Pb/^{204}Pb$ and $^{206}Pb/^{204}Pb$ ratios compared with the averages are: 38.9965±293ppm (avg.39.1046±95ppm); 15.6817±26ppm (avg. 15.6904±26ppm) and 18.7655±248ppm (avg. 18.8693±34ppm) respectively. Two additional “excursion” events are recorded at 11.4 and 5.2 kyr cal. BP in the Pb isotope ratios, with relatively lower values than the average record (Fig. 3.11c-e).

3.4.2 ALB-1-S Sediment Trap

The 23 lithogenic samples collected from the ALB-1-S provide three novel isotopic records along a well-studied sediment trap time-series in the western Mediterranean Sea (Fig. 3.12).

The $^{87}Sr/^{86}Sr$ record shows three well-differentiated phases during the recorded year (Fig. 3.12a). Relatively high and intermediate $^{87}Sr/^{86}Sr$ ratios occur from early summer until the early fall (June to October) and from late winter until late spring (February to May). During both periods, the average $^{87}Sr/^{86}Sr$ = 0.721241±12ppm. Two rapid events in both periods recorded significant isotopic changes in the detrital sediments. In the event that took place around 26/07/1997, $^{87}Sr/^{86}Sr$ = 0.722528±25ppm and during the event around 09/05/1998, $^{87}Sr/^{86}Sr$ = 0.722544±17ppm. Lower Sr isotope ratios occur from late fall until late winter with average $^{87}Sr/^{86}Sr$ values of 0.720041±11ppm.

The $^{143}Nd/^{144}Nd$ isotope ratios for the ALB-1-S show similar values throughout the recovered year with an average of 0.512031±7ppm (Fig. 3.12b). This is also the case for Pb isotope ratios, recording values that are mostly stable through the recovered year with averages for $^{208}Pb/^{204}Pb$, $^{207}Pb/^{204}Pb$ and $^{206}Pb/^{204}Pb$ of 38.9093±310ppm; 15.6775±34ppm and 18.7328±286ppm respectively (Fig. 3.12c-e).

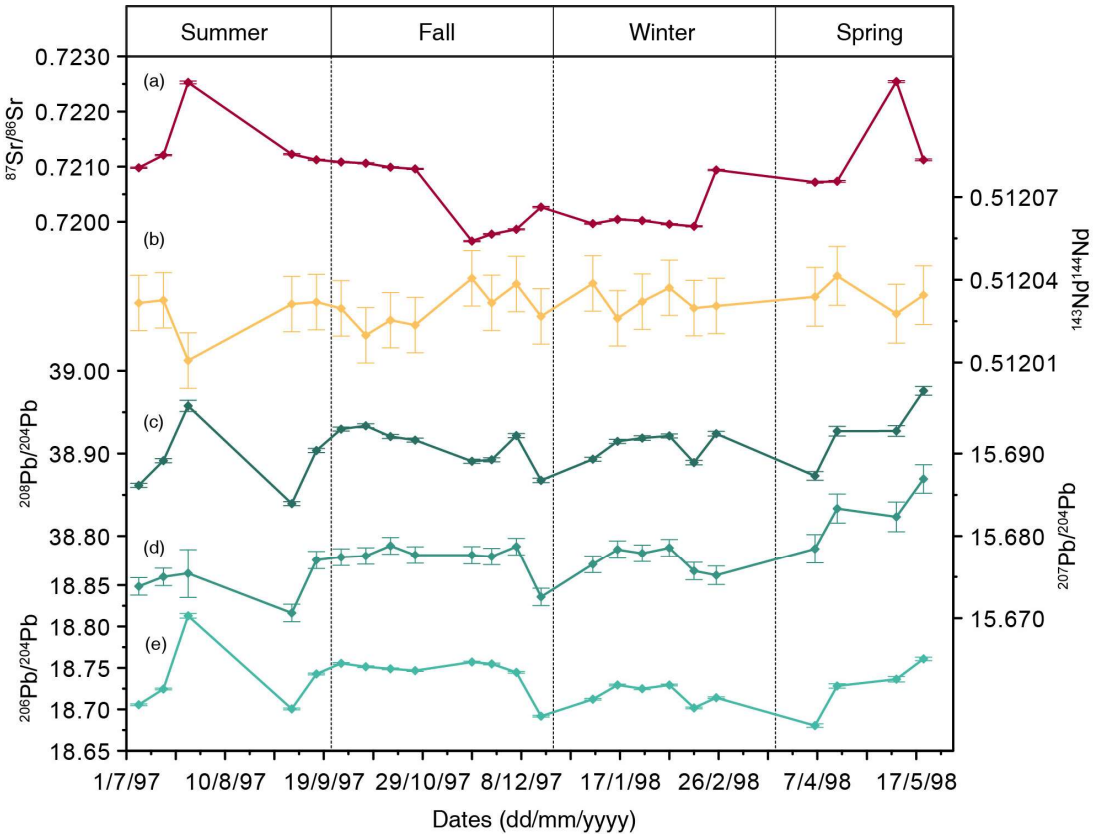

Figure 3. 12 - Radiogenic isotope records from the ALB-1-S sediment trap. *The X-axis is expressed in days/month/year. (a) $^{87}Sr/^{86}Sr$, (b) $^{143}Nd/^{144}Nd$, (c) $^{208}Pb/^{204}Pb$, (d) $^{207}Pb/^{204}Pb$, and (e) $^{206}Pb/^{204}Pb$ records. Each value has associated with its error bar in 2σ.*

3.4.3 Atmospheric Dust

The isotopic values for the three atmospheric dust samples collected in Sineu Mallorca Island (SMI-AD), Barcelona (BCN-AD) and Ena-A (ENAa-AD) and its replicate (ENAb-AD) were for $^{87}Sr/^{86}Sr$: 0.723167±11ppm SMI-AD; 0.723999±11ppm for BCN-AD; 0.723956±11ppm and 0.723906±12ppm for ENAa-AD and ENAb-AD respectively (Fig. 3.13a). Therefore similar values were obtained for the BCN-AD, ENAa-AD and ENAb-AD with a deviation of 46ppm between the three samples. Otherwise, the Sineu (SMI-AD) sample shows different relative values with a deviation from the other three samples of 557ppm (Fig. 3.13a).

The $^{143}Nd/^{144}Nd$ values measured for the three samples and the ENA-AD replicate were: 0.51194±10ppm for SNI-AD; 0.511951±10ppm for BCN-AD and, 0.511945±10ppm and 0.511941±10ppm for ENAa-AD and ENAb-AD respectively (Fig. 3.13b). All samples and the replicate display very similar values with a 5ppm deviation.

Results obtained for the $^{208}Pb/^{204}Pb$ were: 38.9759±27ppm for SNI-AD; 38.8173±25ppm for BCN-AD, and 38.9835±25 and 39.0013±25 for ENAa-AD and ENAb-AD respectively (Fig. 3.13-b-c). The Pb isotope ratio values for SNI-AD and ENA-AD and replica are similar, with a deviation between them of 130ppm. However, the dust sample from Barcelona (BCN-AD) shows

significantly lower values with a deviation from the other three results of 1200 ppm. Values measured for the $^{206}Pb/^{204}Pb$ isotopic system were: 18.8011±10ppm for SMI-AD; 18.6518±10ppm for BCN-AD, and 18.8288±10ppm and 18.8038±10ppm for ENAa-AD and ENAb-AD respectively (Fig. 3.13). For the $^{206}Pb/^{204}Pb$ isotopic system, a similar pattern is observed to $^{208}Pb/^{204}Pb$. While SMI-AD and ENAa-b show similar values (153ppm deviation), the Barcelona sample deviates towards lower values around 1227ppm. Regarding the $^{207}Pb/^{204}Pb$ values were: 15.6762±11ppm for SMI-AD; 15.6622±11ppm for BCN-AD and, 15.6774±11ppm and 15.6711±10ppm for ENAa-AD and ENAb-AD respectively (Fig. 3.13). For this isotopic system, all values, even the BCN-AD sample, display comparable values with a deviation of 34 ppm.

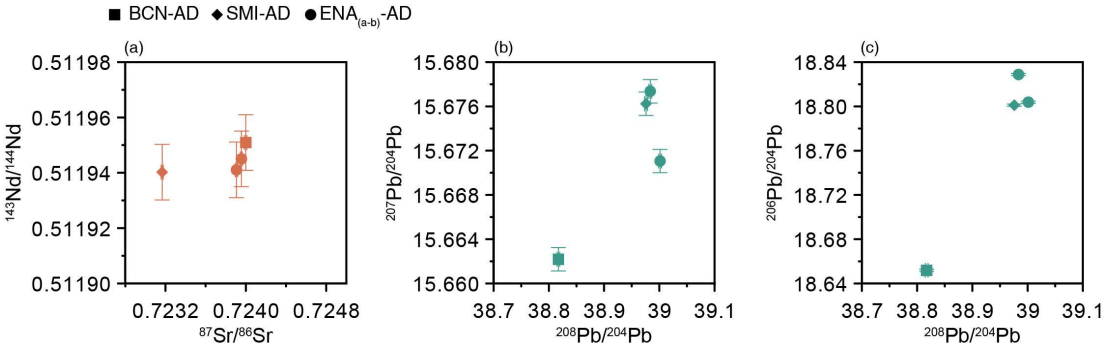

Figure 3.13 - Radiogenic isotope values from the collected atmospheric dust. *Each value has associated with each error bar expressed in 2σ. The Barcelona sample (BCN-AD) is shown in squares, the Sineu sample (SMI-AD)in diamonds and the Ena in circles (ENA-AD). The Ena sample has a duplicate. (a) $^{86}Sr/^{87}Sr$ vs $^{143}Nd/^{144}Nd$. (b) $^{208}Pb/^{204}Pb$ vs $^{207}Pb/^{204}Pb$ and (c) $^{206}Pb/^{204}Pb$.*

Chapter 4

Discussion

“So tomorrow doesn't worry me,
and though the path be untraveled
at least I'm free”

Sing for the wind, Roo Panes

4.1 Holocene marine evolution in the Alboran Sea

4.1.1 Multi-*G. bulloides* – $\delta^{18}O$ records comparison

We now compare the new $\delta^{18}O$ record from ALB-2 to other previously published high-resolution $\delta^{18}O$ records from the western Mediterranean (Cacho *et al.,* 1999; Frigola *et al.,* 2007; Jiménez Amat and Zahn, 2015) to evaluate the regional significance of the recorded signal (Fig. 4.1). The main patterns in the $\delta^{18}O$ records show an extraordinary resemblance to each other. Even several centennial-scale structures can be correlated through the cores, taking into account the individual core chronological uncertainties (Fig. 4.1c). The isotopic depletion associated with the last termination ends in all four records at around 9 cal. kyr BP. Throughout the Holocene, all the *G. bulloides* $\delta^{18}O$ records are relatively stable, with several short oscillations (0.2 ‰–0.3‰) and a slight enrichment trend toward the Late Holocene (Fig. 4.1b). This comparison supports the regional value of the captured paleoceanographic signal and the robustness of the individual age models.

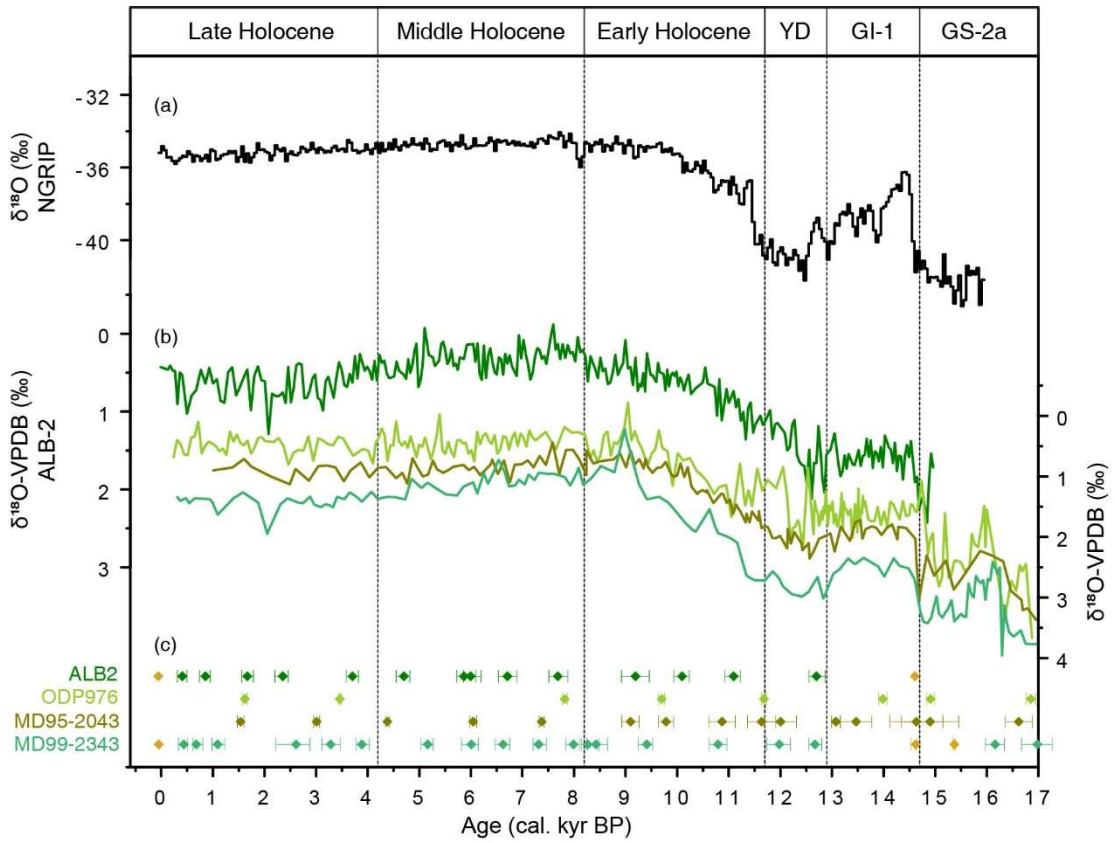

Figure 4.1 - Comparison of $\delta^{18}O$ (VPDB) records and their ^{14}C calibrated dates from the western Mediterranean Sea over the last 17 cal. kyr BP. *(a) $\delta^{18}O$ ‰ NGRIP record; (b) from the top to the base in green colour, ranges $\delta^{18}O$ ‰ (VPDB) records from the cores ALB2, ODP976 (Combourieu-Nebot et al., 2002), MD95-2043 (Cacho et al., 1999) and MD99-22343 (Minorca Drift). Note ALB2 $\delta^{18}O$ ‰ (VPDB) record is plotted with an independent y-axis from the others in order to help with figure compression; (c) ^{14}C calibrated dates with the available errors from each record shown above. Each date is coloured the same as the record, excluding the yellow dots representing tie-points.*

In terms of absolute values of the *G. bulloides* $\delta^{18}O$ records, clear differences can be detected between the cores. Both the ALB-2 and ODP976 cores, located in the westernmost part of the Alboran Sea, display the lightest values (note that the curves in Fig. 4.1b are plotted on independent y-axes). Core MD95-2043, located in the eastern part of the Alboran Sea, shows heavier $\delta^{18}O$ values than the other two Alboran records (Fig. 4.1b). Finally, core MD99-2343, located north of the island of Minorca, shows the heaviest $\delta^{18}O$ values. Such an isotopic pattern is consistent with the regional oceanography, showing the lightest $\delta^{18}O$ values at those sites with a stronger influence of North Atlantic surface inflow, while the $\delta^{18}O$ values become heavier along its path into the Mediterranean Sea. This situation reflects the excess of evaporation within the Mediterranean Sea that results in an enhancement of the salinity (Béthoux, 1980; Lacombe *et al.,* 1981) but also of the marine water $\delta^{18}O$ values. It is interesting to note that the presented isotopic records show a strong gradient between the western and eastern Alboran Sea (about 0.5 ‰), probably due to strong surface mixing with the underlying Mediterranean waters driven by the two anticyclonic gyres (Tintore *et al.,* 1988; Millot, 1999), supporting the argument that the Atlantic inflow became rapidly modified within the Alboran Sea. The isotopic change from the eastern Alboran Sea core (MD95-2043) and the Minorca core (MD99-2343) is even larger (~0.7 ‰), reflecting the long path of these inflowing Atlantic waters through the western Mediterranean before reaching Minorca.

4.1.2 Sea Surface Temperatures: Multi-record and multi-proxy comparison

According to the ALB-2 Mg/Ca SST record, the Holocene maximum temperatures (20.0±1.0°C; uncertainties of the average values represent 1σ; uncertainty values are those derived from the Mg/Ca SST calibration) were reached at the onset of the Holocene ~11.0 kyr (Fig. 4.2 b); a general cooling trend until the present characterizes this record, punctuated by several short-term oscillations (maximum of 2°C). However, the ALB-2 SST record can be divided into three main intervals. The first interval corresponds to most of the Early Holocene (11.7–9 cal. kyr BP) when SSTs were warmest and relatively stable (no significant trend), oscillating at around an average value of ~17.2±1.3°C (Fig. 4.2 b). The second interval displays a general cooling trend of ~4°C ending at around 4.2 cal. kyr BP when minimum Holocene SSTs were reached (~13.6±1.2°C) (Fig. 4.2 b). The last and most recent interval does not show any clear warming/cooling trend (average SST of ~14.9±1.2°C) and intense SST oscillations (~2.0°C) of longer durations than those recorded during previous intervals (Fig. 4.2b).

The ALB-2 *G. bulloides* Mg/Ca SST record has been compared to three other SST records from the western Mediterranean Sea that were calculated following the same Mg/Ca SST procedure (Fig. 4.2 b-e). The comparison between the four chronology records is very robust (Fig. 4.1c) and totally independent for the Holocene period (ALB-2 and MD99-2343: this study; ODP976: Combourieu Nebout *et al.,* 2002; MD95-2043: Cacho *et al.,* 1999). The sampling resolution of the ALB-2 record is higher than for the other sites, but the main patterns agree well between all the compared records. Maximum SSTs occurred around 11 cal. kyr BP in all records,

and also a general cooling trend can be observed during the Early–Middle Holocene, ending in all cases before the Late Holocene (Fig. 4.2b-e). Absolute values also show a good agreement; when the resolution is high enough, some millennial-scale structures can even be correlated between the four records. This multicore comparison strongly supports the value of G. bulloides Mg/Ca in this region as an SST proxy and gives confidence that the obtained SST records reflect true regional environmental conditions. Nevertheless, these Mg/Ca SST reconstructions show differences from the previously published SST reconstructions based on alkenone measurements that need further discussion (Fig. 4.2f; Cacho *et al.,* 2001; Martrat *et al.,* 2004, 2014; Jiménez-Amat and Zahn, 2015).

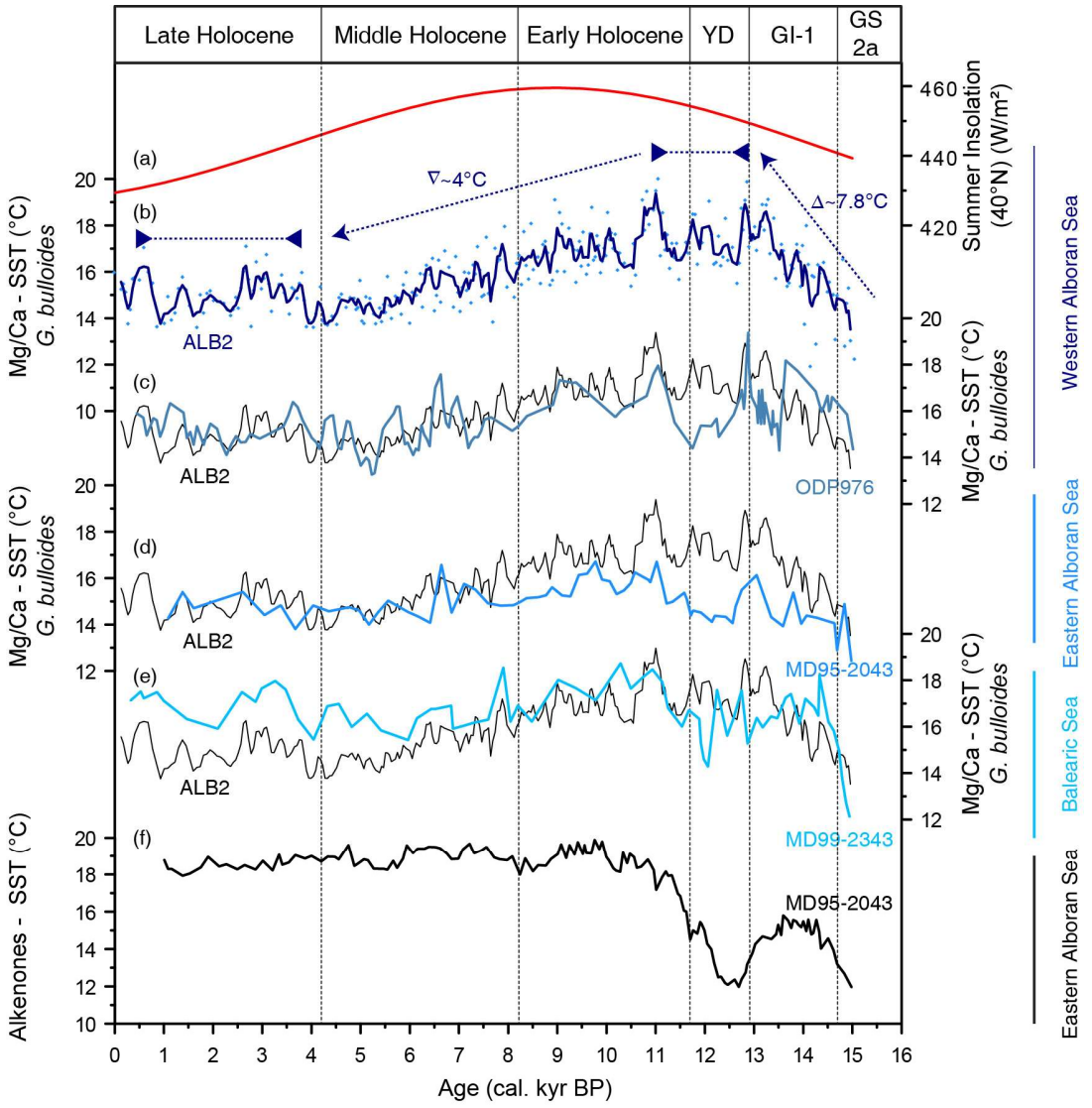

Figure 4.2 – Western Mediterranean SST multi-record comparison for the last 16 cal. kyr BP. *(a) in red, summer insolation at 40°N; (b) Mg/Ca–SST (°C) from the ALB2. Light-blue dots correspond to each SST result; the three-point average is in dark bold blue. Dark blue arrows above the record correspond to the three Holocene intervals described in the text (c, d, and e), Mg/Ca–SST (°C) from ODP976 (Jiménez-Amat and Zahn 2015), MD95-2043, and MD99-2343, respectively (bold blue colour) compared with the ALB-2 three-point average Mg/Ca–SST (°C) (black line underneath). Note that both records from each plot are plotted on the same y-axis; (f) Alkenones–SST (°C) from MD95-2043 (Cacho et al., 1999).*

Alkenone SST reconstructions are based on the relative abundance of di- and tri-unsaturated C_{37} alkenones – mostly produced in the Alboran Sea by the marine coccolithophore *Emiliania huxleyi* (Volkman *et al.,* 1980; Prahl *et al.,* 2000; Ausin *et al.,* 2015). The comparison between *G. bulloides* Mg/Ca SST and the alkenone SST (also studied by Jiménez-Amat and Zahn, 2015) shows remarkable differences in both their absolute values and main patterns, even when both proxies are measured for the same core, as observed in core MD95-2043 and also ODP 976 (Fig. 4.3c). For the Holocene, maximum SSTs in the alkenone record were reached later than for the Mg/Ca SST records (~10 cal. kyr BP). Thenceforth the alkenone SST record shows a rather flat pattern for the whole Holocene, with a slight cooling trend of about 1°C. In contrast, ALB-2 *G. bulloides* Mg/Ca SST (Fig. 4.3c–e) shows larger variability over both the short and long term. Holocene absolute SST values in the alkenone record are warmer (20–18°C) than those recorded by the Mg/Ca record (20–13°C).

Alkenone SST records have been interpreted and calibrated with annual average temperatures (Ternois *et al.,* 1997; Sicre *et al.,* 1999; Prahl., *et al.,* 2000; Cacho *et al.,* 2001; Versteegh *et al.,* 2007; Martrat *et al.,* 2004, 2014). This is consistent with the results from sediment trap series from the western Mediterranean Sea that detect coccolith productivity throughout the year, although enhanced during the spring and autumn seasons and more scarce during the very stratified and oligotrophic summer months (Bárcena *et al.,* 2004; Hernández-Almeida *et al.,* 2011). In contrast, sediment trap studies from the same region indicate that *G. bulloides* has a narrower seasonal window, growing during the spring months (April–May); however, a secondary smaller bloom occurs during autumn (November–December) (Bárcena *et al.,* 2004; Rigual-Hernández *et al.,* 2012). This information fits well with the results of the reviewed G. bulloides Mg/Ca calibration for the western Mediterranean (Cisneros *et al.,* 2016). The preferential depth habitat of *G. bulloides* is above the thermocline within the upper 60m of the water column (Schiebel and Hembleben, 2017) as well, because it needs nutrients supplied by vertical mixing (Rao *et al.,* 1988; Hemleben *et al.,* 1989; Kemle-von Mücke and Hemleben, 1999; Bárcena *et al.,* 2004). Present seasonal and depth temperature distribution at the ALB-2 location can be evaluated with the World Ocean Atlas 2013 (Boyer and Mishonov, 2013) data set that averages measurements from 1955 to 2012 (Fig. 4.3a). Annual average temperatures of 17.8°C occur for the upper 10m of the water column, in good agreement with core top alkenone SST reconstructions (Fig. 4.3a). On the other hand, the estimated core top G. bulloides Mg/Ca SST of the ALB-2 core is 15.5°C, showing a closer match to the measured temperatures at 25–45m depth during spring (April–May), in agreement with the main season and depth habitat of *G. bulloides* (Bárcena *et al.,* 2004; Rigual-Hernández *et al.,* 2012; Schiebel and Hembleben, 2017). The *G. bulloides* habitat preference has been further tested by estimating the theoretical carbonate $\delta^{18}O$ signal expected for present seawater conditions of the upper 100 mwd (Fig. 4.3b). This estimation is based on the available data from Pierre (1999). This exercise illustrates that the measured *G. bulloides* $\delta^{18}O$ values in the top samples from ALB-2 (0.42±0.1‰) are indeed comparable to those estimated for April–May from 5 to 40mwd (Fig. 4.3b). Therefore, isotopic composition confirms

the interpreted *G. bulloides* habitat of 25–45m depth during the April–May months based on the Mg/Ca data. Consequently, alkenone–Mg/Ca SST offset is consistent with the habitat preferences for both season and depth of the two proxy carriers involved, *E. huxleyi* and *G. bulloides* (Fig. 4.3a–b).

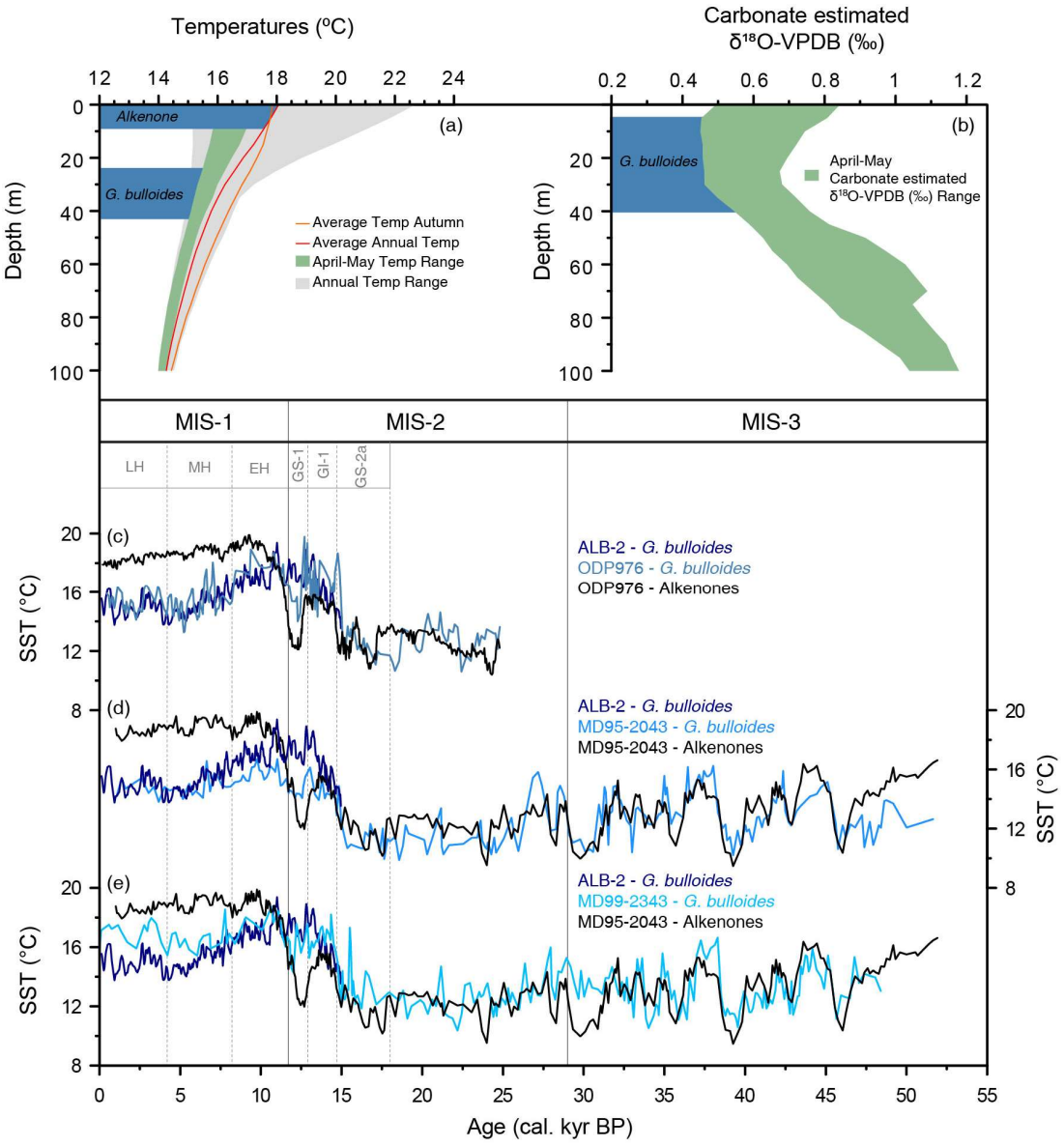

Figure 4.3 - Western Mediterranean SST from alkenone and G. bulloides Mg/Ca multi-comparison for the last interglacial and the following (present) interglacial period. *(a) temperatures (b) carbonate estimated $\delta^{18}O$ VPDB (‰) profile for the first 100 m from site 503737B, obtained from WOA13 0.25deg measured during the years 1955–2012 (T. Boyer, 2013). The horizontal blue band indicates the preferential depth concerning the profile temperatures (a) and carbonate estimated $\delta^{18}O$ VPDB (‰) (b) of G. bulloides (average April-May temperatures and carbonate estimated $\delta^{18}O$ VPDB (‰) in green) and alkenone (annual average temperatures in red); Note that each of the following comparisons has the same y-axis; (c) the blue lines (ALB-2; this study and ODP976; Jiménez-Amat and Zahn 2015) G. bulloides Mg/Ca–SST, compared with the alkenone SST (Martrat et al., 2014) from the same ODP976 record; (d) the blue lines (ALB-2 and MD95-2043; both in this study) G. bulloides Mg/Ca–SST compared with the alkenone–SSTs from the same MD95-2043 record (Cacho et al., 1999; (e) the blue lines (ALB-2 and MD99-2343; both in this study) G. bulloides Mg/Ca–SST compared with alkenone–SST from the MD95-2043 record (Cacho et al., 1999).*

Another differential feature between the two proxies is the rather smooth behaviour of the alkenone signal, in contrast to the Mg/Ca signal (Fig. 4.2 and 4.3). This has previously been reported and attributed to the intrinsic characteristics of the proxy measurements (Laepple and Huybers, 2013). The number of individuals that integrate the SST signal in a single measurement is several orders of magnitude larger in the alkenones, averaging the signal of all alkenones contained in the sample, while the Mg/Ca analyses average about 40–50 specimens (Laepple and Huybers, 2013). This situation favours the integration of several averaged years in the alkenone SST signal, while the Mg/Ca SST signal would be more sensitive to a unique season (spring) and with a higher weighting toward the most favourable growth years (Jiménez-Amat and Zahn, 2015). As a consequence, Mg/Ca records should result in a higher noise signal but may reflect better extreme changes within single seasons than the alkenone record, whereas seasonal changes may become diluted in the large averaged signal.

In addition, we need to point out that the larger difference between the studied Mg/Ca and alkenone SST reconstructions correspond to the deglacial period (at the end of GS-1 or the Younger Dryas – YD). Both alkenone and Mg/Ca SST records show a cooling of ~3–4°C at the onset of the GS-1 (YD), but the big difference occurs at the end of this interval. Both the alkenones and Mg/Ca records show an early intra-YD warming (Cacho *et al.,* 2001), and then the alkenone SSTs continue the deglacial warming while the Mg/Ca record shows a cooling trend. In order to better explore this discrepancy, we have also compared these two records for the glacial period in Fig. 4.3 c–e. *G. bulloides* Mg/Ca SSTs during the last glacial period record the same oscillations and absolute values as do alkenone SSTs, and they both agree on the first warming of the deglaciation, but clearly, the second warming phase of deglaciation does not appear in any of the three considered Mg/Ca records (Fig. 4.3 c–e). Thus, this is a proxy characteristic that may reflect the limited capacity of *G. bulloides* to adapt to the large temperature change that occurred during deglaciation. *G. bulloides* has different genotypes adapted to different ranges of water temperatures, from transitional to subpolar waters (Kucera and Darling 2002; Kucera *et al.,* 2005), but *G. bulloides* starts to be scarce in water with temperatures over 20°C. This agrees with the maximum temperatures recorded during both the glacial and interglacial periods in the Mg/Ca records (Fig. 4.3 c–e). Consequently, we can interpret that *G. bulloides* has a resilient capacity to change its growing season in order to survive the large deglacial SST changes in the region. We propose that, during the glacial period as well as the first part of deglaciation, *G. bulloides* could have had its maximum representation during the autumn bloom when upwelling conditions reappeared after the warm sea summer stratification. That could have allowed *G. bulloides* to grow in a relatively mild upwelling season during the glacial period. Nowadays, autumn SST values are comparable to the annual average SST values, and that could explain the comparable SST values of both alkenone and Mg/Ca proxies. However, the second deglacial warming might have been too extreme for *G. bulloides,* and they would have therefore moved to the spring upwelling bloom with colder SSTs than those during autumn. Consequently, we hypothesize that the absence of the second deglacial warming in the *G. bulloides* Mg/Ca record may reflect a

resilience strategy to change its habitat toward the spring bloom. At the beginning of the Holocene, when SST variability was lower and within its habitat tolerance, *G. bulloides* became a good sensor of interglacial SST variability (Figs. 4.2 and 4.3). Alternatively, it can be argued that *G. bulloides* changed its preferential depth growth habitat in order to survive that large deglacial SST warming. However, in any case, we consider that the shorter deglacial warming of the Mg/Ca SST, in contrast to the alkenone SST record, reflects a resilience strategy of *G. bulloides* rather than reflecting the actual intensity of the deglacial SST warming in the region. In contrast, during the Holocene, the SST changes were within the *G. bulloides*' tolerance range, and thus this part of the record should truly record SST changes. It is important to remark that any change in the habitat preference of G. bulloides would have also affected the $\delta^{18}O$ signal – this is particularly relevant when a temperature correction is applied to this record in order to obtain $\delta^{18}O_{sw}$. In that case, the application of the alkenone SST record would introduce a large heavy anomaly in the $\delta^{18}O_{sw}$ during deglaciation, and that would reflect the habitat change of one of the proxy carriers rather than actual changes in the regional oceanography. This observation reveals the relevance of using signals ($\delta^{18}O$ and SST) of the same species of foraminifera for such estimations.

4.1.3 Holocene evolution in Alboran surface hydrography

The overall Holocene SST evolution in the Alboran Sea is described in three different phases (Fig. 4.4 c): (a) a maximum SST during the Early Holocene (11–9 cal. kyr BP),(b) a cooling trend throughout the Middle Holocene (9– 4.2 cal. kyr BP), and (c) relatively colder temperatures with intense millennial-scale oscillations for the Late Holocene (4.2–0 cal. kyr BP). This general SST pattern also agrees well with that described for the North Atlantic and western Mediterranean Sea in relation to regional data compilations (Marchal *et al.,* 2002; Kim *et al.,* 2004; Rimbu *et al.,* 2004; Wanner *et al.,* 2008) and with the expected Holocene redistribution of solar energy by the changing orbital configuration according to the atmosphere-ocean general circulation model of Lorenz and Lohmann (2004) (Fig. 4.4 a and c). Nevertheless, the magnitude of the Holocene SST changes in the Alboran Sea (above 5°C) exceeds that expected by simply orbital changes in insolation (~1.6°C in the atmosphere) (Lorenz and Lohmann, 2004). Therefore, other factors need to be considered to explain the magnitude of the recorded SST changes.

The period of maximum SST in the Alboran Sea (11– 9 cal. kyr BP) occurred while the North Atlantic Ocean was still under the influence of meltwater pulses from the Laurentide ice sheet (Fig. 4.4 b) that injected freshwater over the surface of the North Atlantic Ocean. This situation induced a stratification in the North Atlantic and, consequently, a weakening of the SPG circulation (Thornalley *et al.,* 2009). At lower latitudes, it has been proposed that the heat transport from the STG toward the North Atlantic was reduced (Repschläger *et al.,* 2017). The consequent heat accumulation in the STG could have hence contributed to a warmer inflow into the Mediterranean Sea and thus may have led to the observed maximum SST in the Alboran Sea (Fig. 4.4 c). But it is also relevant to note that this Early Holocene warm period (11–9 cal. kyr BP) in the Alboran Sea corresponds to the last stage of an organic-rich layer (ORL) formation (Fig.

4.4 e). This ORL has been associated with a strong western Mediterranean stratification phase, resulting from the deglacial sea level rise, which reduced vertical mixing (Cacho *et al.,* 2002; Rogerson *et al.,* 2008). As a consequence of this situation, the modification of Atlantic inflow water along its path into the Mediterranean could have been reduced, thus favouring the persistence of warm conditions in the inflowing subtropical waters.

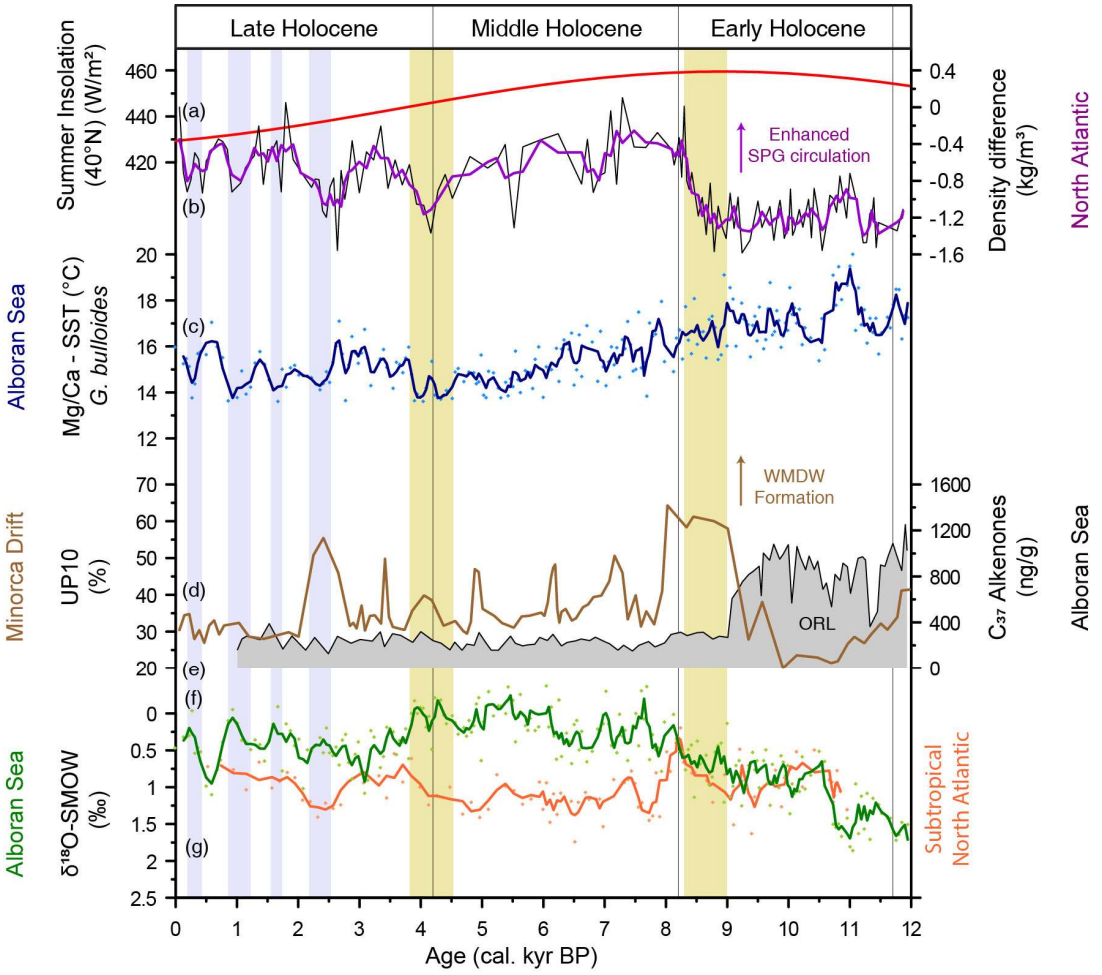

Figure 4.4 – Holocene evolution for the Alboran Sea surface hydrography related to oceanographic processes in the North Atlantic*; (a) in red, the summer insolation at 40°N; (b) in purple, the three-point average of density differences (kg/m³) between G. bulloides and G. inflate from the North Atlantic record RAPiD-12-1K (Thornalley et al., 2009); (c) the new Mg/Ca–SST (°C) presented in this work from the ALB2 (Alboran Sea) – light-blue dots correspond to each SST result and in dark bold blue, the three point average; (d) in brown, the UP10 fraction (%) from the Minorca drift core MD99-2343 (Frigola et al., 2007); (e) the grey filled line represents the concentration of C_{37} alkenones in the Alboran Sea record MD95-2043 (Cacho et al., 2002); (f) in green, the new $\delta^{18}O_{sw}$‰ (SMOW) presented in this work from the ALB2 (Alboran Sea); (g) in orange, the calculated $\delta^{18}O_{sw}$‰ (SMOW) from the south Azores record GEOFAR-KF16 (Repschläger et al., 2017). Vertical bar centred: 8.4–9 cal. kyr BP corresponds to the Alboran Sea and North Atlantic synchrony in oceanographic changes; 4.2 cal. kyr BP corresponds to the double peach structure observed for ALB-2 Mg/Ca–SST. The four vertical grey bars during the Late Holocene correspond to cold events of the ALB-2 Mg/Ca–SST.*

At around 9 cal. kyr BP, the Alboran SST record (Fig. 4.4 c) starts a progressive cooling trend that culminates in reaching minimum values of around 4.2 cal. kyr BP. The onset of this cooling trend coincides with the development of a well-mixed surface layer (Fig. 4.4 b) in the North Atlantic due to the reduction of deglacial melting (Thornalley *et al.,* 2009). This situation would have allowed enhanced transport of subtropical waters towards higher latitudes, releasing the previous heat accumulation in the STG and potentially leading to cooler water flowing into the Mediterranean Sea. In addition, 9 cal. kyr BP also marked the end of the western Mediterranean stratification phase that led to the formation of the last ORL in the Alboran Sea (Fig. 4.4 e). This end occurred at the time of a strong increase in the speed of deep water currents (Fig. 4.4 d) associated with the formation of the WMDW (Frigola *et al.,* 2007). The reduction in surface stratification in the Alboran Sea would have led to increased water mixing of the inflowing Atlantic waters, which could have contributed to the observed cooling trend. This situation was apparently also linked to an increase in the local upwelling conditions developed by the establishment of the western anticyclonic gyre of the Alboran Sea that, according to coccolith assemblages, occurred after 7.7 cal. kyr BP (Ausin *et al.,* 2015). In addition, the described SST cooling trend for this period could also have been promoted by some additional atmospheric forcing. Several authors have suggested a southward displacement of North Atlantic westerlies during this period, inducing a southern penetration of winter storm tracks (Desprat *et al.,* 2013; Fletcher *et al.,* 2012; Chabaud *et al.,* 2014; Zielhofer *et al.,* 2017). Therefore, a combination of factors, internal and external to the Alboran Sea, could have accounted for the observed SST cooling trend from 9 kyr until 4.2 cal. kyr BP, when a change occurred in both the short and long-term variability.

At about 4.2 cal. kyr BP, a double cold peak structure of a minimum SST occurred (Fig. 4.4 c), reaching ~13:6°C, representing the minimum values of the record. After this event, the long-term cooling trend ceased while an intense millennial-scale variability developed, involving SST oscillations over 2°C. This event is apparently synchronous with a peak in the record of deep water current intensity (Fig. 4.4 d), suggesting that deep convection was a strengthened event but not more than during previous and later Holocene events of this record (Frigola *et al.,* 2007). On the other hand, the North Atlantic record (Fig. 4.4 b) indicates that the 4.2 cal. kyr BP event corresponded to one of the Holocene's millennial-scale stratification events, interpreted as a weak mode of SPG circulation (Thornalley *et al.,* 2009). This situation contrasts with that observed during the Early Holocene period when weak SPG circulation coexisted with maximum SSTs in the Alboran Sea.

Interestingly, after the 4.2 cal. kyr BP event, both the Alboran and the North Atlantic records show an intense millennial-scale variability, with minima in Alboran SSTs occurring systematically during periods of weak SPG circulation (Fig. 4.4 b and c). However, further information would be required to establish a mechanism that could potentially link these apparent changes in the Late Holocene AMOC to properties in the Atlantic inflow in the Alboran Sea.

Further insight into the Holocene evolution of the inflowing Atlantic water comes from the ALB-2 $\delta^{18}O_{sw}$ reconstruction (Fig. 4.4 f). This record also differentiates three Holocene periods

consistent with those defined by the SST record (Fig. 4.4 c). The ALB-2 $\delta^{18}O_{sw}$ record is compared with another $\delta^{18}O_{sw}$ record (Fig. 4g) that reflects conditions of the subsurface waters from the subtropical gyre (Repschläger *et al.,* 2017). Interestingly, the relationship between these two records changes for the three defined Holocene intervals (Fig. 4.4 f and g). During the Early Holocene, Alboran waters were comparable to those from the STG, consistent with the previously discussed entrance of subtropical waters, while dominant stratified conditions in the Western Mediterranean preserved the tropical signal. During the Middle Holocene phase, while Alboran SST followed a cooling trend, the $\delta^{18}O_{sw}$ record oscillates around its lightest values, even lighter than those from the STG during the same period, and this difference became larger across the interval (Fig. 4.4 f and g). Such a situation suggests that the inflowing Atlantic waters were also fed by some lighter water mass, most likely from a higher-latitude source. This is consistent with the previously discussed enhanced transport of subtropical waters towards higher latitudes during this period that would have led to stronger southward-influenced SPG source waters that would ultimately mix with the Atlantic inflow waters. This situation is consistent with the described intensification of the SPG by Thornalley et al. (2009) and is the dominant influence of subpolar source central waters at intermediate depths in the mid-latitude North Atlantic (Colin *et al.,* 2010). After the 4.2 cal. kyr BP event, the STG and Alboran $\delta^{18}O_{sw}$ records converge, although ALB-2 values remain lighter for most of the interval (Fig. 4.4 f and g). This situation may indicate a reduced southward influence of SPG waters during the Late Holocene, consistent with the interpreted STG source of intermediate waters in the mid-latitude North Atlantic (Colin *et al.,* 2010). The Late Holocene millennial-scale variability is difficult to characterize in this Atlantic Mediterranean $\delta^{18}O_{sw}$ comparison (Fig. 4.4 f and g) due to uncertainties in the relative chronologies and errors in the proxy reconstruction. Thus, further information needs to be explored to ultimately determine the nature of a potential Late Holocene Atlantic– Mediterranean millennial-scale connection.

4.2 A complete procedure to analyse Sr, Nd and Pb isotopes in the detrital sediments fraction.

4.2.1 Digestion Framework

This chapter discusses in detail the main differences found when evaluating different sediment digestion protocols during this thesis. Some of the most important parameters monitored for each digestion protocol comprise the presence/absence of sediment residuals, total elemental recoveries, and consistency of measured radiogenic isotopic ratios. The ultimate goal is to select an optimum protocol for complete lithogenic sediment digestion in the studied samples prior to chromatographic separation steps and isotopic ratio measurements by MC-ICPMS.

Five different digestion protocols have been systematically studied:

(I) Perchloric, nitric and hydrofluoric sand bath digestion protocol.
(II) Nitric and hydrofluoric digestion protocol
(III) Nitric and hydrofluoric microwave-assisted digestion protocol
(IV) Ammonium difluoride digestion protocol.
(V) Nitric, hydrochloric and hydrofluoric digestion protocol.

(I) Perchloric, nitric and hydrofluoric sand bath digestion protocol.

This digestion protocol uses concentrated HNO_3, HF and $HClO_4$ acids in open digestion vessels submerged in a hot sand bath. 50mg of the geological standard BCR-2 were fully digested with this protocol (see section 3.3.1 for details) upon visual inspection. Total elemental recoveries for Sr, Nd and Pb were significantly lower than expected according to the published elemental abundances of the BCR-2 standard (Weis *et al.,* 2006; around 67.5% for Sr (234±10.7 ppm); ~79.0% for Nd (22±1.0 ppm), and ~73.2% for Pb (8± 0.2 ppm) (Fig. 4.5). During this particular digestion protocol, a relatively large amount of HF (10mL) is used to ensure the complete breaking up of the Si-O bonds (mostly silicate structures) and convert them into volatile SiF_4 during evaporation. SiF_4 molecules can assimilate different elements, such as As, B, Ti, Ta or particularly Pb, in their structure, which are totally or partially lost during the evaporation process (Balaram and Subramanyam, 2022). Conversely, no quantitative loss of Sr or Nd has ever been reported in the literature to volatile SiF_4. The relatively low Pb recoveries associated with this digestion protocol could be potentially attributed to the volatile SiF_4. However, this mechanism does not resolve the relatively low Sr and Nd recoveries

The large amount of HF used in this digestion protocol also favours the formation of insoluble Mg-Ca-Al fluoride salts besides the volatile SiF_4. These fluorides differentially incorporate and/or scavenge both trace elements and rare earth elements (REEs) into their structures during sample evaporation due to the formation of insoluble precipitates (Boer *et al.,* 1993; Yokoyama *et al.,* 1999; Makishima *et al.,* 2009). It has been previously demonstrated that the presence of insoluble fluoride salts can yield incomplete elemental recoveries, especially in

terms of Rb-Sr, Sm-Nd and U-Th-Pb (Hu and Qi, 2004). To prevent the formation of insoluble fluoride salts, samples are typically evaporated in the presence of $HClO_4$ acid (Yokoyama *et al.,* 1999). Upon incipient dryness during sample evaporation, a small volume of $HClO_4$ (e.g. 2mL in this digestion protocol) is added to the sample to displace the potential fluoride salts into soluble perchlorate salts. After this addition of perchloric acid, samples are evaporated again, avoiding complete evaporation as $HClO_4$ could react explosively. Therefore, the samples processed with this digestion protocol contained traces of $HClO_4$ that could not be removed prior to elemental analysis in the recoveries ICP-MS and the subsequent chromatographic separation. In order to estimate total elemental recoveries, each sample digestion residue was re-dissolved in 2mL of 1 mol·L^{-1} HNO_3. This specific volume of HNO_3 to re-dissolve the sample ensures to not over-dilute the concentration of the sample. However, this 2mL of 1 mol·L^{-1} HNO_3 were not sufficient to completely re-dissolve the soluble perchlorate salts. It is possible that the undissolved perchlorate salts would have retained a significant fraction of REEs are elements such as Sr, Nd and also Pb and be partially responsible for the relatively low recoveries in the BCR-2 standard.

Regardless of the low recoveries measured, each BCR-2 standard was processed further through chromatographic purification in order to evaluate potential Sr, Nd and Pb isotopic fractionation resulting from the incomplete digestion protocol. However, during this separation, any required elements (Sr, Nd and Pb) were successfully recovered in their elution step. We argue that the residual presence of trace amounts of perchloric acid in the samples can displace the elution profiles of the different elements by changing the specific resin retention capacity. This was the case since the DGA-resin separates and purifies the specific elements from the sample matrix based on different HNO_3 and HCl; indeterminate amounts of $HClO_4$ would have completely displaced the elution profiles. Then, the presence of $HClO_4$ would prevent the successful recovery of each element in their corresponding elution step. This is the reason why no radiogenic isotope ratio analyses were carried out in samples or BCR-2 standards processed with this digestion protocol.

(II) Nitric and hydrofluoric digestion protocol

This digestion protocol uses a mixture of HNO_3 and HF at medium temperatures (120°C) in a closed vessel during the chemical attacks. The combination of both acids can digest the silicates (HF), carbonates and sulphides (HNO_3) minerals and, thus, most of the silicate rocks. Closed vessel reaction during the chemical attacks enables rapid digestion of the refractory minerals, reduces the total reagent volumes, and reduces the contamination in procedural blanks coming from airborne particles. After digestion, container vessels are opened for sample evaporation. Jweda *et al.,* (2015) originally proposed this digestion protocol to digest the BCR-2 samples, and thus, both BCR-2 standards and ALB-2 marine sediment samples were tested with the same digestion protocol.

The BCR-2 standards were completely digested on visual inspection, with satisfactory recoveries for Sr and Pb but poor yields for the Nd (around 90.7% for Sr (314±2.4ppm), ~49.6% for Nd (13.8±0.1 ppm) and ~102.4% for Pb (11.3± 0.1 ppm) (Fig. 4.5). The ALB-2 terrigenous samples were not completely digested upon visual inspection and systematically presented for each sample a blackish residue after digestion. Jweda *et al.,* 2015 proposed placing the samples in an ultrasonic bath for as long as necessary in order to achieve a total digestion completely. In this case, after four additional hours of samples being subject to ultrasounds, the black residue remained in the ALB-2 sediment samples. Due to the inefficiency of this protocol in digesting marine sediment samples, this method was discarded, and the obtained solutions were not further purified through the chromatographic column.

(III) Nitric and hydrofluoric microwave-assisted digestion protocol

This digestion protocol was explored using four different approaches based on variable proportions between HNO_3 and HF volumes. In particular, the four different approaches were: (*A*) 2:1 - HNO_3: HF; (*B*) 2.5:0.5 - HNO_3: HF; (*C*) 1.5:1.5 - HNO_3: HF and (*D*) 1:2 - HNO_3: HF. The samples digested with the two lowest relative proportions of HF (approaches A and B) were apparently digested upon visual inspection (no solid residues visible). In contrast, the samples digested with higher relative proportions of HF (approaches C and D) presented abundant fluoride precipitate residues. Elemental recoveries in the BCR-2 standards for Sr, Nd and Pb were inversely correlated with the relative proportion of HF used for digestion. We argue that an excess of HF with respect to HNO_3 would favour the formation of fluoride precipitates that actively capture in their structures different traces such as Sr and Pb and rare earth elements such as Nd. As a result of fluoride precipitation, elemental yields measured for BCR-2 were relatively lower when compared with the certificated values (Wilson S.A., 1997). This inverse correlation with the relative proportion of HF was not the case for the ALB-2 marine sediment samples. In this case, approach C (1.5:1.5 - HNO_3: HF) showed the highest elemental recoveries, whereas approach D (1:2 - HNO_3: HF) interestingly showed the lowest elemental recoveries. These differences between the BCR-2 and the ALB-2 digestion may result from the different geological nature of these materials, with BCR-2 being a basalt and ALB-2 sediments being predominantly siliciclastic sediments. In this sense, Yokoyama *et al.,* 1999 has observed that the chemical fluorides composition strongly depends on the rock sample's major element composition.

Therefore, due to the mineralogical composition in BCR-2, the formation of fluorides (and subsequent loss of Sr, Nd and Pb) ultimately depends on the total relative amount of HF used for digestion. On the other hand, the fluoride composition in the ALB-2 terrigenous sediments would not depend on the amount of HF used for digestion. The $^{87}Sr/^{86}Sr$ ratios measured for the BCR-2 obtained similar values between the four different digestion approaches and recorded the same values within the error as those previously published by Weis *et al.,* 2006 for BCR-2 (Fig. 4.5). However, Nd and Pb isotope ratios do not yield isotopic ratios in the range of previously published values (Weis *et al.,* 2006). Interestingly, the measured $^{143}Nd/^{144}Nd$ ratio inversely correlates with the relative proportion of HF added in each digestion approach (Fig. 4.5). Thus, when the HF

increases, the $^{143}Nd/^{144}Nd$ ratios decrease. Conversely, $^{208}Pb/^{204}Pb$ and $^{206}Pb/^{204}Pb$ ratios correlate when the relative proportion of HF increases (Fig. 4.5). However, $^{207}Pb/^{204}Pb$ ratios do not show the correlation observed in the other Pb ratios. In the case of the ALB-2 samples, the potential HF effect on the isotopic ratios cannot be clearly established. Such differences in the isotopic ratios behaviours through the different digestion approaches could also be derived from the different mineralogy of both BCR-2 and ALB-2 terrigenous sediment. However, further investigations on fluoride formation during digestion would be needed to understand the observations that resulted from this digestion protocol. Since this method did not yield consistent radiogenic isotope ratios for BCR-2 standards, it was abandoned.

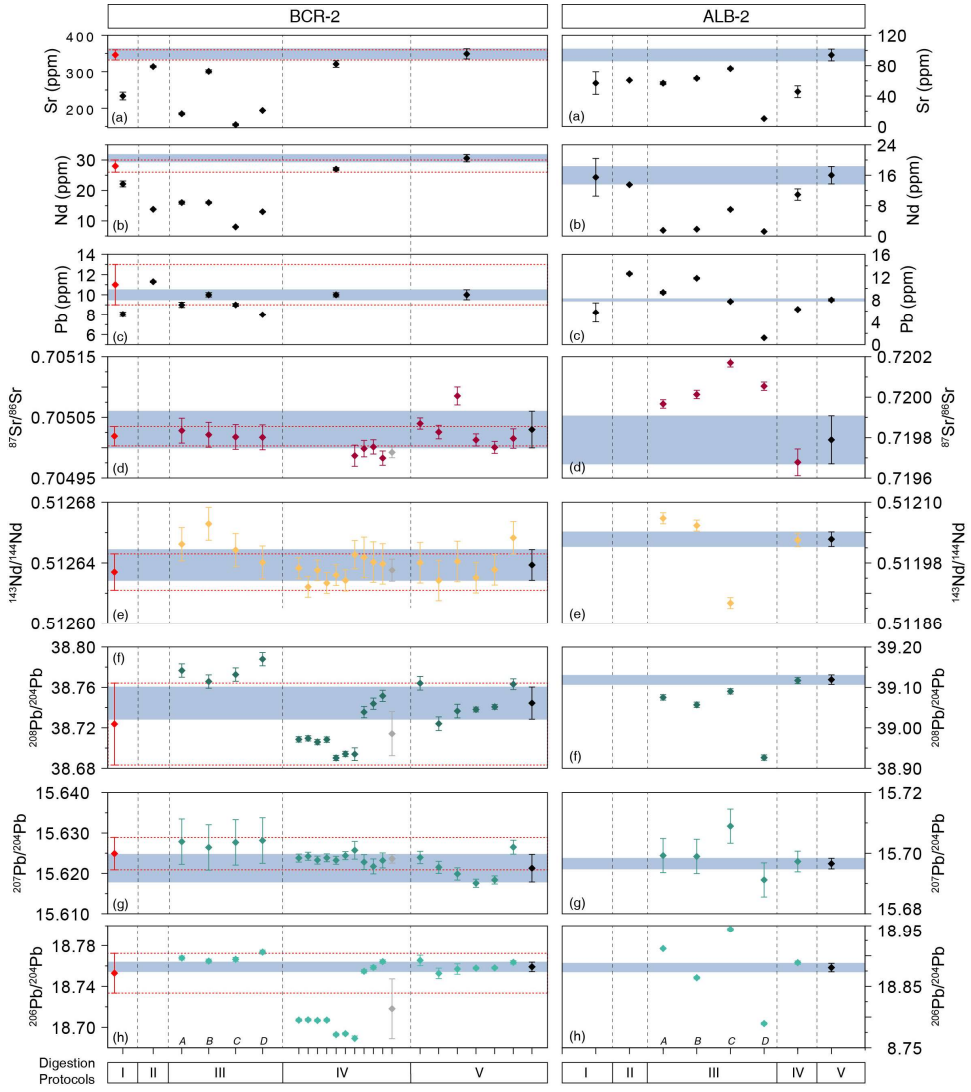

Figure 4.5 - Recuperations and isotopic values for each digestion protocol for both BCR-2 and ALB-2 samples. *From (a) to (c) are shown the recuperation values in ppm with the error bars for each digestion protocol for the BCR-2 and ALB-2 samples. From (d) to (h) are shown the isotopic ratios associated with each digestion protocol. The BCR-2 panel shows in red diamonds the certificated recuperation values (Wilson, S.A., 1997) and the published isotopic values (Weis et al., 2006), both with the associated error. The red dotted band show the limits of the errors. Grey and black diamonds show the average of the measured values for the digestions protocols IV and V, respectively. The blue-filled rectangle shows the limits of the errors associated (2σ standard deviation) to the average value of the digestion V. The ALB-2 panel also shows in digestion V the black diamonds corresponding to the average values. The blue-filled rectangle shows the limits of the errors associated (2σ standard deviation) to the average value of the digestion V for the BCR-2.*

(IV) Ammonium difluoride digestion protocol.

This digestion protocol uses ultra-pure ammonium difluoride (NH_4HF_2) reagent (distilled in-house at LIRA Laboratory), following the method originally proposed by Zhang *et al.,* 2012 and Hu *et al.,* 2013 The BCR-2 standard was completely digested without any visible residue. Conversely, most of the ALB-2 samples were not completely digested, and a black-fine residue was present in most cases. The elemental recovery percentages for the BCR-2 were good for all three elements, Sr, Nd and Pb (> 90% for each element). Conversely, the ALB-2 samples showed recoveries of around 70-80% for Nd and Pb while around 49% for Sr. The low Sr recoveries could be related to the incomplete digestion in the detrital fraction obtained in most of the ALB-2 samples.

The complete BCR-2 sequence of $^{143}Nd/^{144}Nd$, $^{208}Pb/^{204}Pb$ and $^{206}Pb/^{204}Pb$ ratios measured, which is temporally arranged in function of the performed analyses, show a shift in values (Fig. 4.5). Systematically for these radiogenic ratios, the first digestion batch shows lower values than those performed later. However, the isotopic values for those BCR-2 samples digested later agree with the previously published by Weis *et al.,* 2006. This shift is not observed in the $^{207}Pb/^{204}Pb$ ratios, in which all values agree with those reported. Thus, for the second digestions batch, both Nd and the three Pb isotopic systems obtain the referenced values (Fig. 4.5) (Weis *et al.,* 2006). This shit is not observed for the $^{87}Sr/^{86}Sr$ ratios because the first digestion performed is missing, but the ratio values for the second batch are slightly under the BCR-2 reference values (Weis *et al.,* 2006). The observed shift in values could be caused due to the NH_4HF_2 distillation processes. Concretely, for each digestion batch, were used two NH_4HF_2 different distillations. The NH_4HF_2 used for the first temporally digestion batch was more poorly purified than the second one, and that could potentially contaminate the radiogenic ratios by the poor-distilled NH_4HF_2.

Therefore, the ammonium difluoride digestion protocol achieves similar elemental recoveries in both Sr, Nd and Pb than those certificated (Wilson S.A., 1997). However, the bias observed in the values of the $^{143}Nd/^{144}Nd$, $^{208}Pb/^{204}Pb$ and $^{206}Pb/^{204}Pb$ ratios are related to the NH_4HF_2 distillation processes that led to a bias in the isotopic measurements, and thus this digestion protocol was rejected.

(V) Nitric, hydrochloric and hydrofluoric digestion protocol.

This digestion approach uses a relative proportion of 2:2:1 of HNO_3:HCl:HF, which was modified by Yang *et al.,* 2022. Samples using this procedure were, in appearance, completely digested, with satisfactory elemental recoveries for both BCR-2 and ALB-2 samples, without any remaining black residue, not even in the ALB-2 samples. In terms of recoveries, BCR-2 standards showed elemental recoveries close within uncertainty to the certificate values (101% for Sr; ~109% for Nd, and ~91.5% for Pb), and in the case of the ALB-2 samples, the recoveries were higher than the previous digestion procedures (Fig. 4.5)

The isotopic ratios for Sr, Nd and Pb fall well within the certificate values for the BCR-2 samples and presented better external reproducibility than the previous digestion protocols (Fig. 4.5). In particular, the reproducibility obtained for the Pb ratios was even better than those previously published (Weis *et al.,* 2006). This digestion protocol apparently achieves complete digestion of both igneous and marine sediment samples and provides the highest recovery percentages, and radiogenic isotope ratios results match certified reference values for geological standards. Consequently, based on the successful results obtained, this digestion protocol was selected to digest the marine sediment samples.

4.2.2 Chromatographic Separation

Bed-volume column

The elution schemes obtained using the 1mL and 2mL bed-volume column were very similar for the 3 required elements (Fig 3.10 a-b). In both approaches were obtained poor elemental recoveries and also were obtained co-elution with the interfering elements. (Fig. 3.10 a-b). For both approaches, the same elution scheme was performed base on Retzmann *et al.* (2017). However, Retzmann *et al.* (2017) used a fully automated low-pressure chromatographic system (FAST-MC™), while in our case, the chromatographic separations were performed using an electro-valve controlled vacuum system (TrisKem Vaccum Box). Therefore, the elution scheme based on Retzmann *et al.* (2017) cannot achieve the elements' separation in both 1mL and 2mL bed-volume column using the electro-valve controlled vacuum system. Consequently, the bed-volume column has to be assessed in order to improve the elution scheme for this specific chromatographic system. In this sense, by comparing the results of the two bed-volume column approaches were observed a slight displacement of the elements to their elution steps in the 2mL bed-volume column. This slight displacement could be boosted by the bed-volume column enlarged due to the superior efficiency of the separation of analytes significantly increasing with a larger amount of the DGA-Resin, such as suggest Zimmermann *et al.,* 2019. Thus, all further improvements in the chromatographic protocols were based on the 2mL-bed volume columns

Sample loading and matrix rinse

When samples are introduced into the column, three critical variables should be considered: the elemental concentration of the sample, the loading volume, and the acid concentration of the sample. Each of these variables could directly impact the chromatographic separation and purification of the analytes and thus could produce a bias in the resulting isotopic ratios. In this regard, several studies have reported that high matrix loads could directly affect the analytes' elutions and the isotopic results (Guéguen *et al.,* 2015; Smet *et al.,* 2010; de Muynck *et al.,* 2009; Zimmermann *et al.,* 2019). Concretely, it has been reported that sample loadings with Ca concentrations over 500µg could displace the elution picks, overlapping mostly the Sr and Pb, or premature Ca elution could occur during the Sr elution step (Zimmermann *et al.,* 2019). Another problem with loading high-concentration samples is the potential saturation of the used resin in the chromatography. In order to avoid or minimize these effects, all samples of each chromatographic separation batch were diluted with the same dilution factor. This dilution factor is chosen for the sample with less Pb concentration to ensure that all samples would be above 40 ppb of Pb. Finally, the sample was loaded by introducing a final volume of 0.5 mL. In this way, each column was loaded with at least 20ng of Pb. Since Pb is one of the low-concentrated elements in the sediments, this strategy would guarantee enough Pb concentration to be analysed. Thus the dilution used satisfied the compromise of reducing the total matrix effect of the elutions but keeping enough concentration to measure the low-concentration elements.

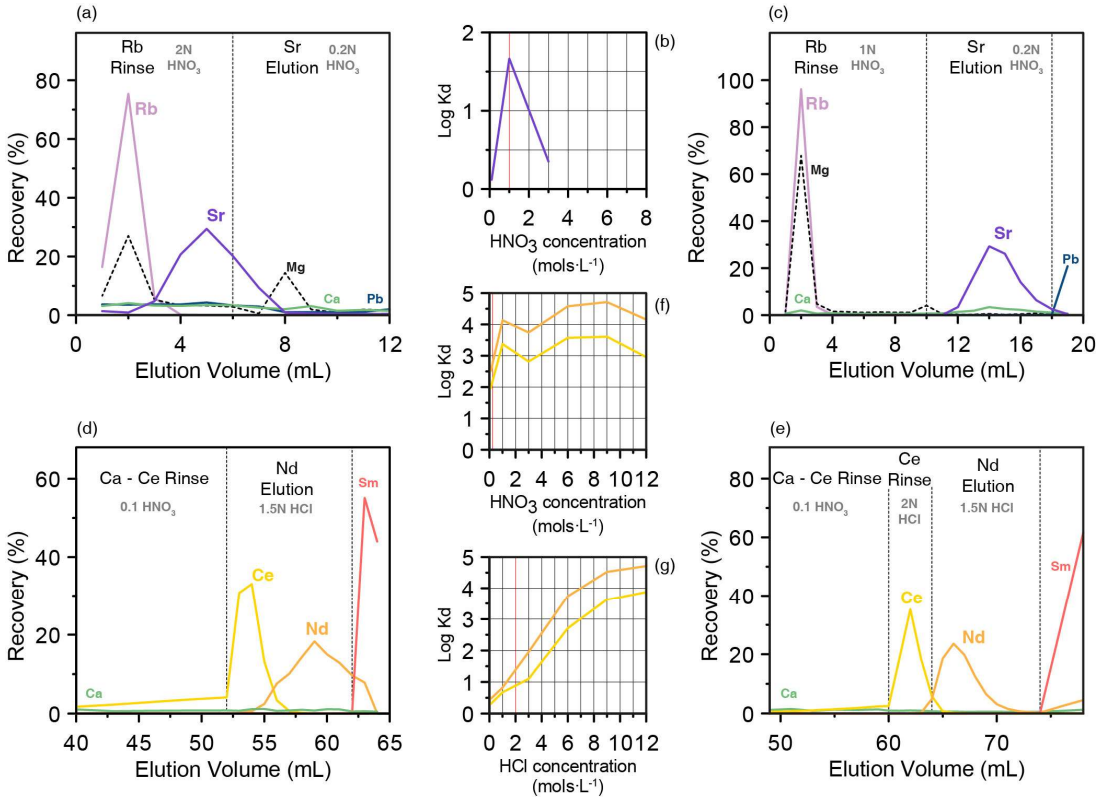

Figure 4.6 - Elution profile improvement within Rb-Sr and Ce-Nd by changing the acid concentrations and volume. *From (a) to (c) Rb and Sr elution separation. (a) Elution profile using 2mL bed-volume column following the Retzmann et al., 2017 scheme. (b) Distribution coefficient (K_d) of Sr on DGA resin in logarithmic scale as a function of HNO_3 molarity. The red line indicates the higher retention HNO_3 molarity of Sr. (c) The proposed improvement of the Rb-Sr separation by changing the HNO_3 molarity of the Rb rinsing and enlarging its elution in 2mL bed-volume column. Also, note that the Sr elution is enlarged. From (d) to (e) Ce and Nd elution separation. (d) Elution profile using 2mL bed-volume column following the Retzmann et al., 2017 scheme. (f) and (g) Distribution coefficient (K_d) of Ce and Nd on DGA resin in logarithmic scale as a function of HNO_3 (f) and HCl (g) molarity. The red line indicates the higher retention of HNO_3 and HCl molarity of Ce and Nd. (e) The proposed improvement of the Ce-Nd separation by adding a specific Ce rinsing step in HCl and enlarging the Nd elution.*

The acid concentration of the sample, which is loaded into the columns in order to separate the analytes, was next explored. Available studies propose different initial acid concentrations depending on the required analytes. Nevertheless, for the isotopic systems of Sr, Nd and Pb on the DGA-Resin, the suggested sample acid concentration is 2 mols·L^{-1} of HNO_3 (Zimmermann *et al.,* 2019, Retzmann *et al.,* 2017; Romaniello *et al.,* 2015). After the sample loading at this 2 mols·L^{-1} of HNO_3 acid concentration, the sample matrix is immediately rinsed at this acid concentration before the Sr elution. When this sample acid concentration was used with the 2mL bed-volume column, Sr was untimely eluted at the Rb rinsing step, thus losing much of the Sr at this Rb rinsing step (Fig 4.6 a). In order to improve the Sr and Rb separation, the retention coefficients (K_d) of the DGA-Resin (Prourmand and Dauphas, 2010) were assessed for those elements that potentially elute during the matrix washing (Fig 4.6 b). In this regard, maxim K_d for the Sr has been reported at HNO_3 concentrations of 1 mol·L^{-1} (Fig 4.6 b; Prourmand and Dauphas, 2010), while the DGA-Resin does not produce any absorption for most of the alkali metals present in the matrix sediment sample such as Na, Mg, K, or even Rb. Consequently, decreasing HNO_3

acid concentration for the sample loading and matrix rinsing from 2 to 1 mol·L^{-1} would better retain the Sr, delaying its elution and, thus, preventing the Rb and Sr co-elution. Moreover, the protocol for the previous matrix washing was also modified using a larger volume of acid, from the 5mL proposed by Retzmann *et al,* (2017) to 8mL and in this way, the complete Rb washing was ensured. The implemented modifications in the acid concentration for the sample loading and matrix rinsing step, as well as in the acid volume for the matrix rinsing, led to a complete delay in the Sr elution and isolating it from the matrix elution, in particular to the Rb (Fig 4.6 c).

The cut-off between Sr and Pb fraction

Sr and Pb are two of the targeted elements, but their separation can become challenging. Retzmann *et al.* (2017) describe an overlapping between these two elements during the last 2mL of the Sr elution (4mL Sr elution in a 1mL bed-volume column). The described co-elution corresponded to a relative amount of 10% of Pb eluting during the Sr step. But in spite of this co-elution, the study did not observe any significant bias in the Sr isotopes. This co-elution problem is resolved in other studies by increasing the total acid volume used for the Sr elution until 8mL using a 3mL bed-volume column (Zimmermann *et al.,* 2019). Alternative modifications to change the bed-volume column could be increasing the total acid volume used for the Sr elution or adjusting its concentration. It is finally chosen to increase the elution acid volume to 8mL for the Sr with the aim to maximize its recovery but avoiding Pb interferences (Fig 4.6 c). This procedure proves to satisfactorily separate Sr from Pb, resolving the overlapping problem, and only 2% of Sr remains present at the first mL of the Pb elution (Fig 4.6 c).

The cut-off between Pb and Ca-Ce fraction

In the case of the Pb, its recovery was made using 8mL of the elution acid (HNO_3)at a concentration of 5 mols·L^{-1}. This elution volume did not affect the following elution profile since most elements do not elute at this acid concentration (Fig 3.6 c).

The cut-off between Ce and Nd fraction

Previously to the elution of Nd, it was necessary to eliminate the Ca and Ce to avoid potential overlaps in the analyses. This was first tried by applying 36mL of HNO_3 at 0.1 mols·L^{-1}, but the Ce slightly elutes during this step (Fig 4.6 d). Upon performing the switch to HCl acid to elute Nd, it is also observed a rapid co-elution of Ce with the Nd cut. In order to resolve this overlapping were assessed the Ce and Nd retention coefficients (K_d) of the DGA-Resin (Prourmand and Dauphas, 2010) for both HNO_3 and HCl (Fig. 4.6 f-g). In this regard, both Ce and Nd show similar K_d in the presence of HNO_3 and HCl (Fig. 4.6 f-g). Thus, the strategy to overcome this overlapping was focused on producing a rapid Ce elution step with 2mL of 2 mols·L^{-1} of HCl (Fig 4.6 e). However, Nd also elutes during this Ce elution step, although it has a delayed response in terms of elution, and thus only 1% of Nd is lost in this step. Immediately, the acid concentration is changed towards 1.5 mols·L^{-1} of HCl to elude and recover Nd (Fig 4.6 e). This procedure proved to resolve the overlapping problem between Ce and Nd.

4.3 Tracing the current sources of the terrigenous particles into the Alboran Sea

4.3.1 Evaluation of potential source areas

Lithogenic particles captured in the ALB-1 sediment trap can arrive transported by rivers or by winds as dust. Since the ALB-1 sediment trap was located nearby the southern continental margin of the Iberian Peninsula, the lithogenic particles could be directly transported by the local river discharges, but they could arrive as dust plumes from Saharan origin.

Southern Iberian Peninsula rivers draining towards the Mediterranean Sea are mainly dominated by torrential seasonal flows, although few rivers, such as the Guadiaro and Guadalhorce, have permanent water sheets. On the southern side of the Alboran Sea, on the north-western coast of Africa, the existing rivers present an enhanced seasonal character. However, the most significant river in terms of flow rate crosses the Middle Atlas towards the Mediterranean Sea, near Saïdia in the eastern Alboran Sea. However, the dominant oceanography in the region difficult the arrival of these river discharges into the North-western Alboran Sea. Both north and south Alboran Sea rivers, independently of their permanent or seasonal flow, incise on the rock substratum and incorporate sediments with the radiogenic signal of the regional geological formations. Some of the metamorphic and igneous complexes (Alpujarride, Fig. 4.7 a) and also the sedimentary complex of Flysch (Fig. 4.7 a) around the Alboran Sea have been widely characterised by radiogenic isotopes (e.g. Varas-Reus, et al. 2017; Rossetti *et al.,* 2013), but others sedimentary or metasedimentary complexes remain with any isotopic information (Maláguide). However, the main permanent rivers (Guadiaro and Guadalhorce) have a portion of their catchment areas inside the Alpujárride Complex. They are more widely extended on the metamorphic units of this complex (Jubrique Unit, Fig. 4.7 a). Therefore, the radiogenic signal of the metamorphic units could be used as an end-member for the potential rivers discharges.

The Mediterranean beaches from the south Iberia Peninsula are mostly formed by lithic sands of metamorphic and metasedimentary composition, whose source areas are the complexes that form the Betic Cordillera (Alpujárride, Maláguide, Nevado-Filábride, and the Neogene deposits; Critelli *et al.,* 2003). In particular, the sand from the beaches and from the river mouths on the coast of Malaga show similar mineralogical composition, and thus both are ultimately related to the fluvial system drainage of the Maláguide and Alpujárride complexes (Critelli *et al.,* 2003). Since the geological source is the same for both kinds of sands, an isotopic differentiation should reflect processes of mineral selection attributed to the erosion, transport and eventual coastal reworking of the beach sands. Since the southern Iberian Peninsula is characterized for having sporadic rain events with torrential character, most of these sand grains would reach the beach after a highly energetic transport process and are further reworked by local coastal drift. The Sr and Nd isotopes of these beach sand formations have been well-

characterized (Fig. 4.7 a; Brems *et al.,* 2013, a,b) and can thus be used as an end-member of Betic Cordillera complex but reworked by high-energy transport processes.

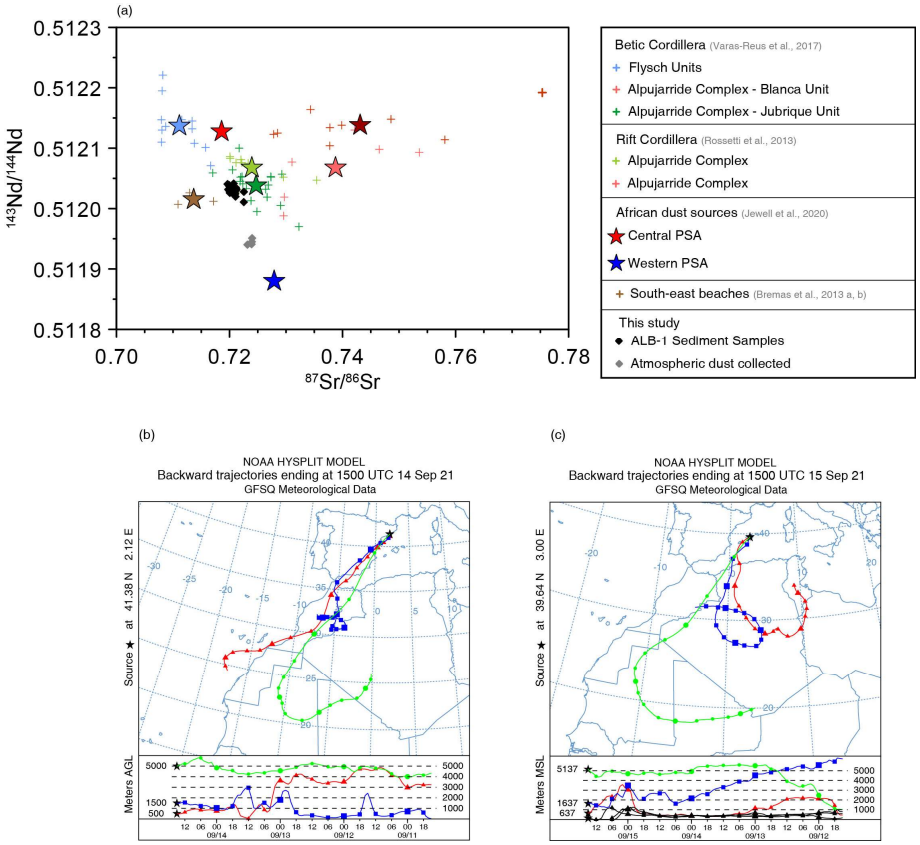

Figure 4.7 – Determination of the potential source areas based on the radiogenic isotopes and the present backward trajectories. *(a) Relation between $^{87}Sr/^{86}Sr$ and $^{143}Nd/^{144}Nd$ signals of the Betic Cordillera complexes in coloured crosses from Varas Reus et al., 2017 and from the Rif Cordillera from Rossetti et al., 2013; Central and Western potential sources areas (PSA) of the Saharan dust from Jewell et al., 2020 in coloured stars; south-east beaches from Bremas et al., 2013 a, b, in brown crosses; ALB-1 signal from the sediment traps in black diamonds and the collected atmospheric dust from the Sineu (SMI) sample and Barcelona (BCN) sample in grew diamonds. (b) and (c) Backward trajectories from the wet deposition event, which collected the BCN and SMI atmospheric dust sample. Backward trajectories are calculated with the NOAA HYSPLIT Model for the 14th of September 2021 for the BCN sample and the 15th of September 2021 for the SMI sample.*

On the other hand, the provenance of the aeolian dust delivered in the Alboran Sea has been well documented to be from the Saharan-Sahel regions. These desert or semi-desert areas are actually the main atmospheric dust-producing regions in the world, and the radiogenic signal of their preferential dust sources areas (PSA; Fig. 2.6) have been well characterized (Guinoiseau *et al.,* 2022, Jewell *et al.,* 2020; Abouchami *et al.,* 2013; Scheuvens *et al.,* 2012). A large radiogenic signal variability exists between each region, making it difficult to trace the provenance and, even more, when the samples to study are not pure atmospheric dust. In order to better characterise the isotopic signal of the aeolian contribution, the radiogenic composition of the three atmospheric dust samples (SMI, BCN, ENA) collected in the Iberian Peninsula have been compared with the radiogenic signal of the described PSAs. The resulting radiogenic signal values show that the three atmospheric dust samples had a Saharan origin and, more concretely, between the Western and Central PSA (Fig. 4.7 a, Jewell *et al.,* 2020). This interpreted source

region based on the resulting radiogenic values has been confirmed by analysing the atmospheric backward trajectories associated with the deposition events of the three studied dust samples (Fig. 4.7 b-c). These results agree with other dust studies that point to the western and west-centre PSAs as the predominant origin of dust plumes towards the Iberian Peninsula (Escudero *et al.,* 2011; Molinero-García *et al.,* 2022; Russo *et al.,* 2020). Therefore, the radiogenic values of the three here collected atmospheric dust samples can be used as an end-member to trace the Saharan dust signal.

In conclusion, the three defined end-members should provide the key to deciphering the provenance or potential transport mechanisms of the lithogenic fraction collected on the ALB-1 sediment trap during the years 1997-1998.

4.3.2 Sources of the terrigenous particles collected in Alboran Sediment Traps

The provenance of the terrigenous particles captured in the ALB-1 sediment trap for the period 1997-1998 is explored by means of a binary system based on the measured radiogenic Sr and Nd isotopes and referenced according to the three previously discussed end-members: Betic Cordillera, Beach and Western Sahara end Members (Fig. 4.8). End-members have been connected by systematic ensembles of mixing lines. The resulting ensembles allow quantifying the mixing rate between the Saharan dust and the Betic Cordillera rock complexes into the collected samples in ALB-1. Moreover, because the mixing-line system incorporates the beach's radiogenic signal, it further allows interpreting the relative energy of the transport processes responsible for delivering these terrigenous particles into the sea (Fig. 4.8).

The result of this exercise indicates that more than 70% of the radiogenic signal corresponds to the Betic Cordillera rock complex while the remaining 30% is attributed to aeolian dust from the Saharan source (Fig. 4.8). Thus, the main source of the lithogenic particles arriving at the ALB-1 sediment trap is from the Betic Cordillera. Therefore, the river contribution from the southern Iberia peninsula is the main source of sediments, while those from the Sahara are secondary sources. Although the Saharan dust is present in almost all the samples, it occurs in low proportions, and it will be diluted within the dominant river runoff contribution of terrigenous supply. In particular, the collected terrigenous particles are located within the mixing-line system in three well-differentiated groups (Fig. 4.8). The samples from Group 1 show a higher contribution of Saharan dust, between 16 and 27% (Fig. 4.8). While Group 2 and particularly Group 3 show a reduced Saharan dust contribution bellow 17% for Group 2 and 10% for Group 3; Fig. 4.8). Therefore, within the whole terrigenous particles captured by the sediment trap, Sharan dust become more diluted from the Group 1 to 3. In terms of transport processes, these three differentiated Groups would indicate changes in the intensity of the different modes of discharge. Group 3 would represent a situation with the highest contribution of river supplies. In contrast, Group 1 would represent the lowest river inputs and enhanced contribution of aeolian transport (Fig. 4.8). These interpretations can be further developed when the beach end member is considered since the mixing line between the rock, and the beach end-members would allow to

interpret changes in the transport energy of the terrigenous particles from the Betic Cordillera rock complexes through the river systems. According to this mixing line, Group 3 represents the conditions with the strongest energy during the river transport, which would indicate an enhanced capacity of the rivers to mobilize sediment from the Betic Cordillera complexes and transport and deliver it toward the sea. Therefore, these observations further reinforce the differentiation of three groups within the terrigenous inputs in the Alboran Sea. Consequently, samples from Group 1 represent a higher proportion of Saharan dust while the transport energy on the rivers was lower. Finally, samples from the Group 2 would represent an intermediate state between the other two groups, when the river supply has still the dominant source of the sediments but physical weathering processes where less intense or energetic; within this Group 2, it would also be expected an intermediate charge of the sedimentary supply.

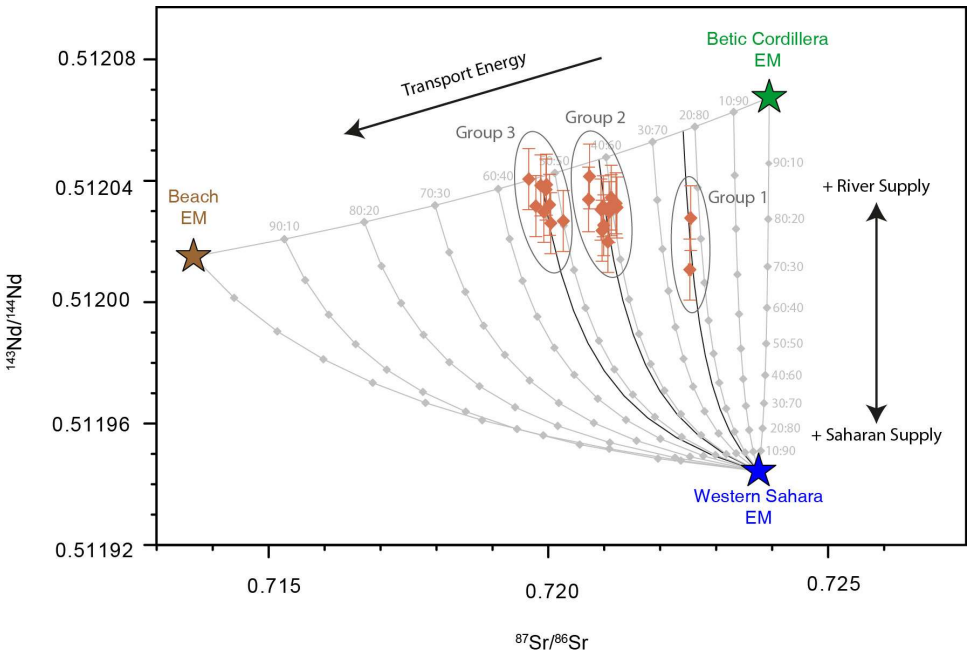

Figure 4.8 - Radiogenic mixing-line system for the lithogenic particles in the Western Mediterranean Sea. Ensemble of mixing lines between the proposed Western Sahara end member with the Betic Cordillera (Varas-Reus et al., 2017) and Beach end members (Brems et al., 2013a, b). The Grey lines show the theoretical radiogenic values of the mixing between each end member. Light grey values (e.g. 90:10) indicate the percentage of contribution of each end member to the resulting mixture. The vertical grey lines indicate the resulting mixing between Western Sahara and the Betic Cordillera end members. The horizontal grey lines indicate the mixing between the Betic Cordillera and the Beach end member. Black arrows show the interpretations of the mixing-line system referred to in the text. Orange diamonds correspond to the distribution of ALB-1-S sediment trap radiogenic values within the mixing line ensemble. Each diamond has associated the associated error bar. Circles around the ALB-1-S sediment trap radiogenic values correspond to the three differentiated groups discussed in the text.

4.3.3 Environmental validation of the radiogenic groups of sediments

The studied samples from the ALB-1 sediment trap represent an annual sequence that brings the valuable opportunity to directly compare the interpretations based on the radiogenic composition of the sediments with measured environmental variables. The temporal distribution of the sedimentary $^{87}Sr/^{86}Sr$ ratios illustrates that the three previously defined groups of sediments, based on the mixing lines systems, have a consistent distribution along the recorded year (Fig. 4.9 c). In this sense, from late fall until mid-winter, the $^{87}Sr/^{86}Sr$ ratios show the lowest values corresponding to the previously described Group 3. Group 2, with medium $^{87}Sr/^{86}Sr$ values, is present from summer until early fall (June to October) and from middle winter until late spring (February to May). Samples from Group 1 correspond to two events of higher $^{87}Sr/^{86}Sr$ ratios that occurred in spring and summer and represent an interruption within the dominance period of Group 2. The comparison of the $^{87}Sr/^{86}Sr$ values with the lithogenic fluxes (Fig. 4.9 c and d) measured in the same ALB-1 sediment trap samples (Fabrés *et al.,* 2002) illustrates consistent patterns with previous interpretations. In this sense, when major lithogenic fluxes occurred (late fall until middle winter), the $^{87}Sr/^{86}Sr$ ratios display the lowest values corresponding to Group 3. According to the mixing lines system from the radiogenic end-members, this group is dominated by terrigenous particles from the Betic Cordillera rock complexes. Fluvial discharges measured on the Guadalhorce river, the one with the closest mouth to the studied area (Fig. 4.9 d), and the precipitation recorded in Malaga meteorological station (Fig. 4.9 d), agree, indicating that fall and early winter represent the period with enhanced precipitation and consistently enhanced river runoff toward the Alboran Sea. Thus, these observations indicate an overall increase of lithogenic fluxes when maxima in precipitation and fluvial discharges occurred. However, the detailed observation of the data does not show an accurate matching between the magnitude of the lithogenic fluxes and the river flow discharges (Fig. 4.9 d; Fabrés *et al.,* 2002). The first river surges from late September to late November 1997 produced a subsequent drastic increase in the lithogenic fluxes. However, these early river surges were relatively modest when there are compared with posterior ones, as those recorded at the beginning of February 1998, which represented the highest one in the record, while the lithogenic fluxes did not show any increase (Fig. 4.9 d). This imbalance between the precipitation or river discharges with the lithogenic fluxes was attributed to Fabrés *et al.* (2002) due to the erosive regime in semi-arid areas, like the south Iberia Peninsula. After the long dry summer period, the first precipitations would increase the capacity to mobilize the sediments in the catchment areas since soils have limited vegetation protection. But the following rainfall events would find less soil availability to erode, reducing the sedimentary charge transported to the sea even though the volume of river flow was comparable or even higher than that associated with the first fall rains. An additional factor to have in consideration is the torrential character of the rainfalls, typical in this region for the fall-early winter rain events, which enhances the erosion capacity of the soils and the river energy with rapid increases of their water sheets that ultimately its transport capacity. Therefore, the sum of these two factors enhanced soil availability after a long dry season, and the torrential character of the rains would amplify the erosion and transport capacity of lithogenic material toward the studied

sediment trap. Conversely, at the end of the wet season, most available sediments are already washed, seasonal vegetation developed, and the torrential character of the rains reduced and consequently, the river discharge of terrigenous sediments would be reduced. These circumstances would explain the previously described contrast between the amount of sediment discharge between the first and last rain events of the fall-winter seasons (Fig 4.9 d). Changes in these patterns of erosion and transport also become reflected in the measured radiogenic $^{87}Sr/^{86}Sr$ signal. After the dry season, when the Guadiaro river reached higher flow volume and, subsequently, the sediment trap received maximum lithogenic fluxes, the $^{87}Sr/^{86}Sr$ values decreased with the appearance of the samples from the described Group 3(Fig 4.9 c). Later, at the end of the wet season, the $^{87}Sr/^{86}Sr$ values increased (Group 2, Fig 4.9 c) even though the river flow rate is comparable to the previous episodes. This would reflect the reduced torrential character of the rains and reduced soil availability. Therefore, the previously interpreted sediment transport patterns associated with the sediment Groups 2 and 3 agree well with the environmental conditions observed during the studied annual cycle. Thus used approach by the radiogenic mixing lines system explains satisfactorily most of the variability detected for the monitored year.

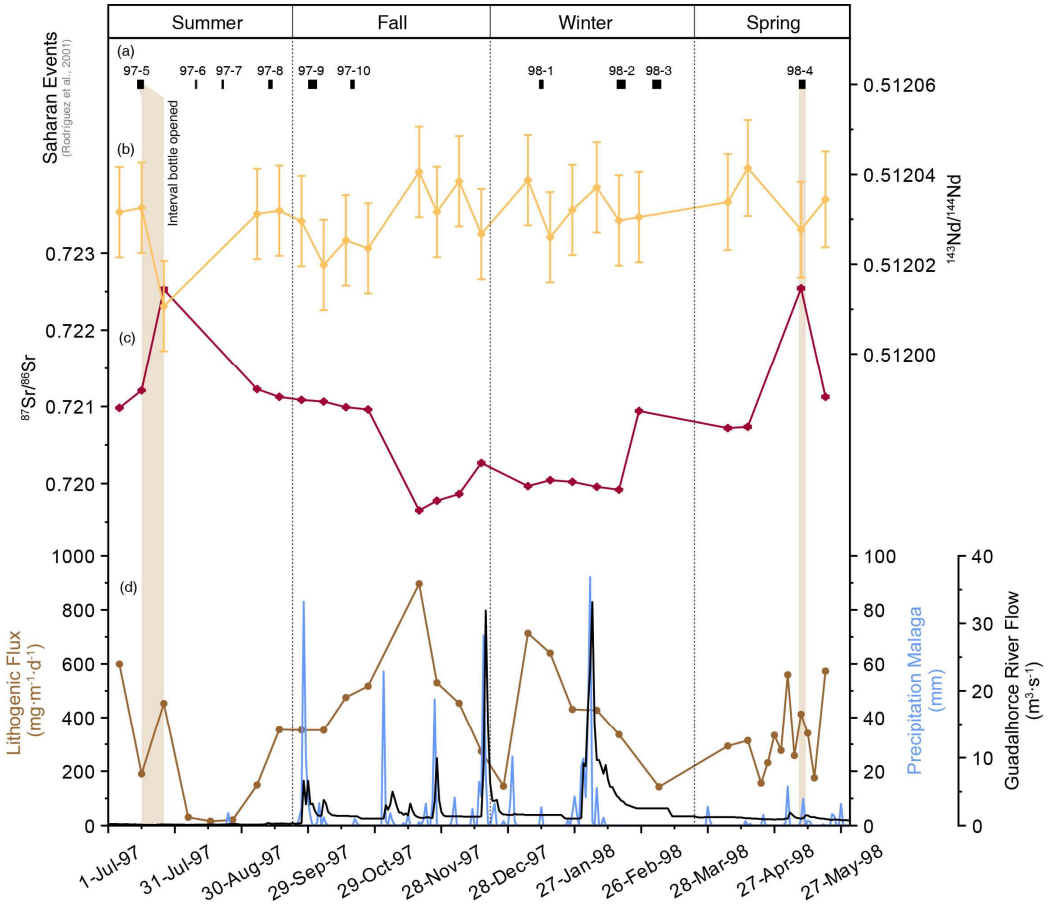

Figure. 4. 9 – Comparison of the radiogenic $^{87}Sr/^{86}Sr$ and $^{143}Nd/^{144}Nd$ records measured on the sediment traps with the instrumental records along the recovered 1997 – 1998 period. *(a) Saharan events captured in an automatic station at Carboneras (Rodriguez et al., 2001). The width corresponds to the total duration of the events, and the numbers above correspond to the names associated with each event referred to the Rodriguez et al., 2001. (b) and (c) $^{143}Nd/^{144}Nd$ and $^{87}Sr/^{86}Sr$ records from the ALB-1-S sediment trap. (d) Ensemble of instrumental data: In brown, the lithogenic fluxes captured in the ALB-1-S sediment trap. In blue, the precipitation in mm in Malaga city. In black, the Guadalhorce river flow. Salmon vertical bars correspond to the temporal period that the sediment traps bottles were opened and thus capturing the Saharan dust events.*

However, sediments from the Group 1 need further analysis to test the previous interpretation as the result of enhanced contribution from the western Saharan end-member (Fig. 4.8; 4.9c; Jewell *et al.,* 2020). The two samples included in the Group 1 correspond to: (i) summer 1997, which integrates particles settled during a 10 days interval (16^{th} to 26^{th} of July 1997) and (ii) spring 1998, integrating 3 days intervals (6^{th} to 9^{th} of May 1998). During the studied annual cycle (from the 1st of July 1997 until the 31st of May 1998), a total of 10 events of Saharan dust discharge over the southern Iberian Peninsula have been described in the literature (Fig 4.9 a; Rodríguez *et al.,* 2001). Two of these events (97-5 and 98-4) perfectly coincide with the presence of sediments from the Group 1 in the ALB-1 sediment trap (Fig 4.9 a and c). Concretely these two dust events burst into the southern Iberian Peninsula during the 14^{th}-17^{th} of July 1997 (event 97-5) and the 8^{th}-11^{th} of May 1998 (event 98-4; Rodríguez *et al.,* 2001) and registered a daily PM10 of 50$\mu g \cdot m^{-3}$ on average. The event in July 1997 was characterized as a dry deposition episode, while the 1998 May event was a wet deposition episode associated with rainfalls produced on the 11th of May. The backward trajectories of both events confirm the sourcing of the air masse over the western Saharan (Fig 4.10). Compared with the other dust events episodes during the studied annual cycle, it is noticeable that some of these other events (97-6, 97-8 and 97-9) collected higher daily amounts of PM10 particles than the other two previously described events. However, the isotopic signal recorded on the terrigenous particles does not show an increase in the Saharan dust signal as the other two samples do. The main explanation would be the enhanced dilution of the Saharan dust signal by river source lithogenic particles. The two samples corresponding to the Group 1 show 16% and 27% of Saharan dust contribution to the terrigenous sedimentary load. It is relevant to remark that both episodes (events 97-5 and 98-4) occurred when the river flow was minimum and likely supplying limited sedimentary charge with limited capacity to dilute the Saharan dust. In this sense, even though other Saharan dust events supply a higher total amount of dust, the river sediment supply was also enhanced with the onset of the wet season and consequently diluting the total Saharan signal.

4.4. Radiogenic isotopes to characterize the hydrological patterns during the Holocene

4.4.1 Sourcing of the Holocene terrigenous particles

Based on the radiogenic isotope results obtained in the sediment trap samples (section 4.3.1 Evaluation of potential sources areas), two main source regions have been defined as the predominant modern sediment sources being transported into the Alboran Sea: The Betic Cordillera rock complexes (southern Iberian Peninsula) supplying sediments through rivers and gullies systems and the Saharan-Sahel desert dust deposition through airborne dust plumes intrusions. Taking into consideration these two sedimentary sources as first-order end members, it is possible to quantify the relative contributions or abundances of different lithogenic sediment "source areas" in the sediment trap time series studied. In addition to these two end members, a third factor was incorporated into the isotopic mixing calculations, which indicates the energy of the river transport that also exerts control on the geochemical isotopic signature of the transported sediments. This evaluation of present-day processes controlling sediment supply sets the bases for understanding and interpreting changes in hydrological patterns occurring during the present interglacial or Holocene period.

During the Holocene, terrigenous particles reaching into Alboran sediments could have varied their main source areas mainly due to climate changes that took place during this period that involved important changes in general atmospheric patterns. In order to understand these changes, the downcore results of Sr and Nd isotopes have been placed in an isotopic mixing lines diagram (Fig. 4.10 a) where in addition to the isotopic end-members considered for the sediment trap samples, a third end-member was included representing central Saharan dust end-members according to Jewell *et al.,* (2020). The Betic Cordillera isotopic end-member has not been modified in this diagram since it is considered that the main southern Iberia fluvial channels did not change at the studied time scale. The resulting mixing source ensemble (Fig. 4.10 a) for the last 15 kyr BP (ALB-2 sediments) indicates that more than 85% of the lithogenic sediments were supplied from the Betic Cordillera rock complexes (Fig. 4.10 a). On the other hand, the residual 15% of the isotopic signal can be attributed preferentially to the Central PSA (Fig. 4.10 a). The downcore Nd and Sr isotope results compare well with present-day values obtained in the ALB-1 sediment trap samples, reinforcing the use of the present-day isotopic mixing-line system as an analogue for past climate changes. This comparison also illustrates that the ALB-2 results are clustered into two main groups well aligned with the two modern analogue groups discussed in section 4.3.1. In particular, the Holocene values fall within groups 2 and 3 (Fig. 4.10 a) and then within the mixing line between the Betic Cordillera rock complex and the beach end-member. Thus, the $^{87}Sr/^{86}Sr$ differences recorded in the ALB2 sediments would also reflect changes in the energy intensity of the terrigenous particles transported through the rivers (Fig. 4.10 a). In particular, the higher $^{87}Sr/^{86}Sr$ values that cluster within Group 2 occurred from the last deglaciation until the Middle Holocene (~7.6 cal. Kyr PB), when a transition occurred towards lower $^{87}Sr/^{86}Sr$ values

that agree with the Group 3 (Fig. 4.10 b). Following our present-day analogy, the middle Holocene transition from higher to lower $^{87}Sr/^{86}Sr$ values (Group 2 to 3) would also reflect changes in the transport energy of the fluvial systems. During the deglacial and Early Holocene periods, terrigenous particles would be washed by more persistent rainfalls, while from the Middle Holocene, the system changed toward an increase in the transport energy that could reflect an enhanced torrential character of the rain patterns. Such torrential rainfall episodes would be preceded by extensive dry periods that would accumulate immobile particles to be later energetically transported at the end of the drought season by torrential flows. Therefore, the obtained $^{87}Sr/^{86}Sr$ record through the Holocene would mainly reflect changes in the rainfall patterns in the south of the Iberian Peninsula.

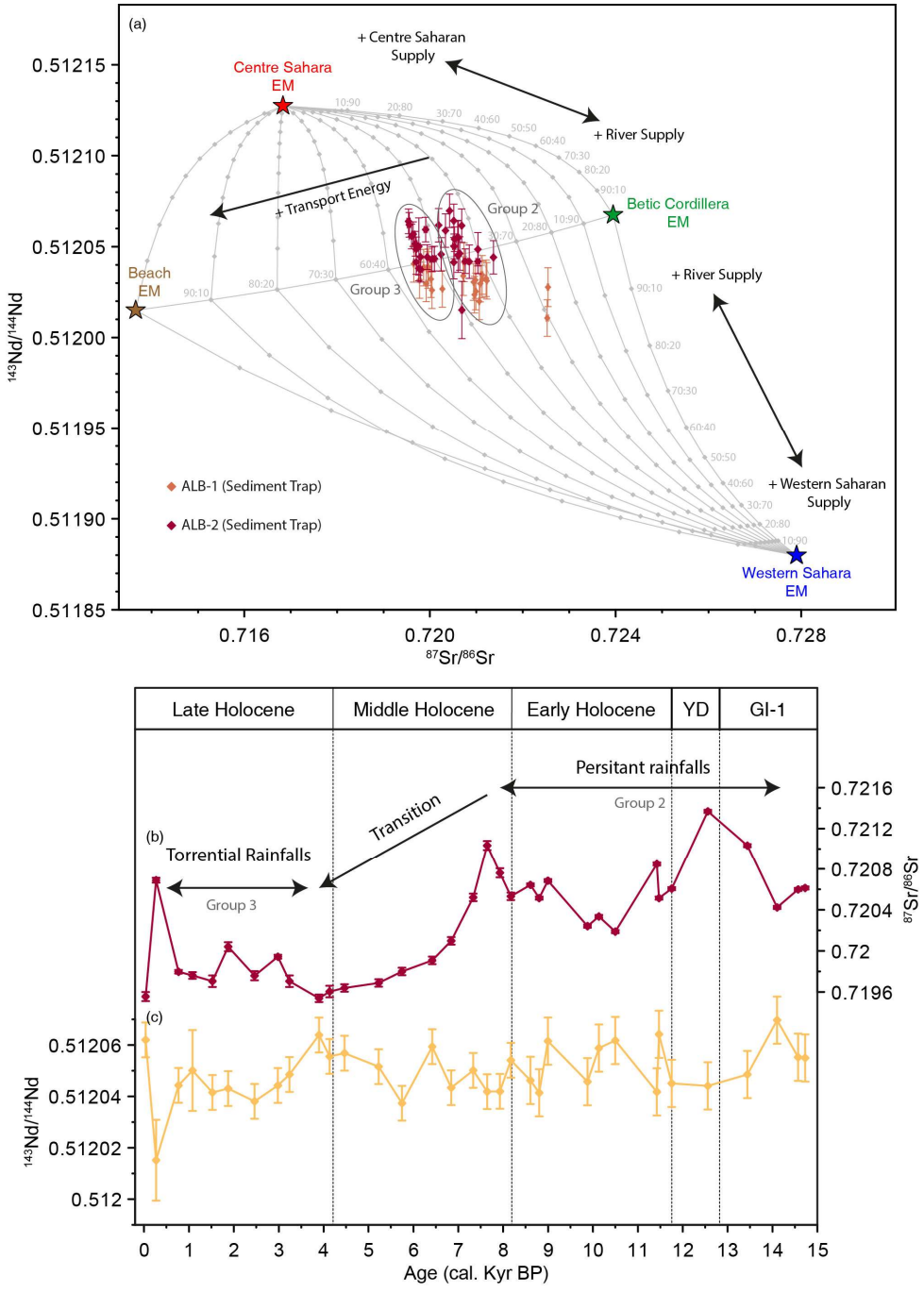

Figure 4.10 – Radiogenic mixing-line system for the lithogenic particles in the Western Mediterranean Sea for the last 16 kyr. *(a) Ensemble of mixing lines between the proposed Western and Central Saharan end member from Jewell et al., 2020 with the Betic Cordillera (Varas-Reus et al., 2017) and Beach end members (Brems et al., 2013a,b). The grey lines show the theoretical radiogenic values of the mixing between each end member. Light grey values (e.g. 90:10) indicate the percentage of contribution of each end member to the resulting mixture. The vertical grey lines indicate the resulting mixing between Western/Central Saharan and the Betic Cordillera end members. The horizontal grey lines indicate the mixing between the Betic Cordillera and the Beach end member. Black arrows show the interpretations of the mixing-line system referred to in the text. Orange diamonds correspond to the distribution of ALB-1-S sediment trap radiogenic values within the mixing line ensemble, and dark red diamonds to the ALB-2 sediment core radiogenic values. Each diamond has associated the associated error bar. Circles around the radiogenic sample values correspond to the two differentiated groups discussed in the text. (b) $^{87}Sr/^{86}Sr$ and (c) $^{143}Nd/^{144}Nd$ records along the last 15 kyr BP. Arrows correspond to the discussed interpretation of the radiogenic values referred to in the text*

One of the main differences between the radiogenic isotope results obtained for the last 15 kyr BP and those from the sediment traps is the absence of results within the defined Group 1 (Fig. 4.10 a), defined as the enriched Saharan-like group. Sediment trap results showed that only during periods of time when river sediment discharges were absent the Saharan dust could be identified by the isotopic Sr and Nd values reflecting dust intrusions carrying the Sahara signal. Therefore, the obtained record for the last 15 kyr BP reveals that if such episodes occurred during the studied period, the signal became diluted by the larger amount of the terrigenous particles transported by the south Iberia river systems that reflect the Sr and Nd values from the Betic Cordillera rock complexes. Also, the nearly invariant Nd isotope signal along the last 15 kyr cal. BP suggest a mostly constant geologic source of the terrigenous particles supplied. In terms of the geological ages in lithogenic materials at the potential source areas, there are remarkable differences in age between the Betic Cordillera rock complexes and the Saharan-Sahel areas. The Sm-Nd model ages in the Betic Cordillera units average 1.7 Ga (10^9years) (Varas-Reus *et al.,* 2017), whereas the Western PSA (Jewell *et al.,* 2020), which is strongly influenced by the West African Craton where the bedrocks age from 3.5 to 2.0 Ga (Begg *et al.,* 2009), and the Central PSA influenced by the Saharan Metacraton ages on 1.0 – 0.54 Ga (van Hinsbergen *et al.,* 2011). Then, the invariant Nd isotopic record would indicate that the age of the continental basement sources did not mostly change during the last 15 kyr BP. This agrees with the mixing-line system based on the three potential end-members suggested. Consequently, the absence of samples matching the defined rich-Saharan-like group (Group 1) within the ALB-2 sediment core reinforces the interpretation that most of the sediments deposited in this part of the Alboran Sea have their source within the Betic Cordillera rock complexes.

4.4.2 Interpretation of the geochemical characterization of the sea sediments

The geochemical composition of sediments can provide further insight into the characteristics of the sedimentary processes. In this regard, the performed PCA groups the elements into two clusters (PC1 with Al, Si and K and PC2 with Zr, Ti, Fe and Rb; Fig 3.6). All these elements are present in a large variety of minerals, which present different responses to weathering processes. In this sense, clays are aluminosilicates (Al and Si oxides hydrated), including accessory elements on their structures (e.g. K, Mg, Fe, Cr, Mn). However, Si is also abundant in the quartz mineral. Both clay and quartz minerals display somewhat opposed

behaviours to weathering processes since quartz is more resistant to chemical weathering and can survive multiple erosion and deposition cycles. Conversely, clay minerals are easily weathered and eroded. Therefore, although they both partially share their chemical composition, they can be discriminated during the erosion and transport phases and thus, any Al or Si variations along the record could reflect changes in the nature of weathering processes. Regarding K, this element is typically associated with potassium-rich minerals such as feldspar, micas and illite (Schneider *et al.,* 1997); in environments with intense chemical weathering processes (warm and humid conditions), feldspar and micas alter or degrade to illite (Al-Ani and Sarapää 2008; Deer *et al.,* 1975). This altered or degraded mineral forms around 50% of the sediments from the western Mediterranean Sea (Bout-Roumazeilles *et al.,* 2007), which predominantly sources from the Betic Cordilleras rock complexes (Martínez-Ruiz *et al.,* 1999). On the other hand, Ti and Zr are dominant in resistant minerals such as zircon, rutile and ilmenite, and thus they should be less mobile during chemical weathering processes (Caracciolo *et al.,* 2011; Perri *et al.,* 2013). Some sedimentary mudrocks, like those being part of the Malaguide Complex (Fig. 1.6), have been shown to form a Zr-increasing effect of sediment recycling (Perri *et al.,* 2013). Therefore, during periods with low erosion, Zr would be immobile; conversely, during periods with higher erosion, this element could be easily transported. Consequently, the relative abundance of these elements in the sedimentary record from the Alboran Sea could reflect climatic-driven changes in the intensity or nature of the weathering/erosion patterns in the surrounding continental areas.

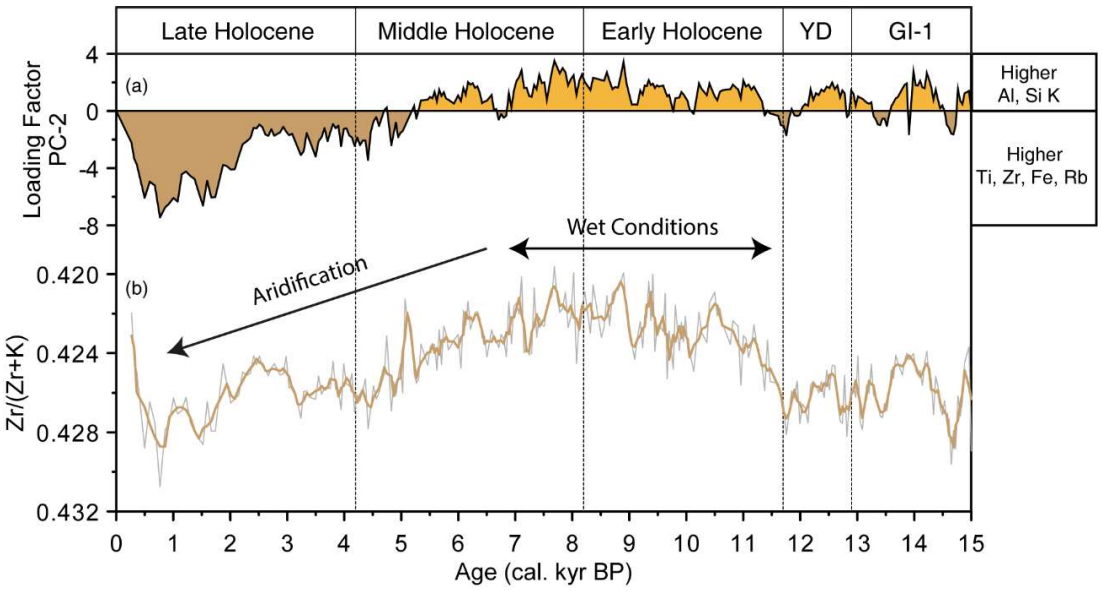

Figure 4.11 - Relation between the statistical PC-2 loading factor with the proposed Zr/(Zr+K) Index. *(a) Loading factor of the PC-2 variable in the PCA-b along the time (Referred to Fig 3.6). Indicate those periods with a higher contribution of Al, Si and K (positive values in light orange) and, conversely, those periods with a higher contribution of Ti, Zr, Fe and Rb (negative values in light brown). (b) Distribution along the time of the Zr/(Zr+K) index, which indicates towards higher values a higher K contribution on the index and, conversely, more Zr contribution towards lower values. Arrows above the Zr/(Zr+K) show the interpretation referred to in the text.*

The relationship between these two groups of elements is explored by applying the relation Zr/(Zr+K), which in turn, agrees well with the resulting statistical weight factor for the PC-2 (Fig 4.11). Lower values of this index reflect an increase of K in the Alboran Sea sediments, likely associated with an enhanced supply of K-rich minerals such as illite. This situation would imply intense chemical weathering processes that could reflect wet and warm conditions that promote silicate illitization. Conversely, higher Zr/(Zr+K) index values indicate an increased supply of Zr-wearing minerals stimulated by weaker chemical weathering processes. This situation could reflect prolonged dry seasons with sporadic intense rainfalls that would enhance physical weathering processes during the rain events, eroding and recycling minerals from the resistant group. Therefore, the Zr/(Zr+K) index would ultimately reflect the hydrological changes controlling the sediment supply from the Betic Cordillera through river systems.

4.4.3 Holocene evolution in the Alboran hydrology

The two independent proxy records of potential hydrological changes over south Iberia $^{87}Sr/^{86}Sr$ and Zr/(Zr+K) index show consistent patterns during the Holocene, providing strong support to the interpretations in terms of hydrological changes. Both records agree in differentiating three distinctive phases during the Holocene (Fig. 4.12 a-b): (a) 11.7 – 7.6 cal. Kyr BP: A period of maximum development of persistent rainfalls (higher $^{87}Sr/^{86}Sr$ values with minimum Zr/(Zr+K) signal) during the early Holocene and part of the Middle Holocene ; (b) 7.6 – 4.2 cal. Kyr PB: A transition period throughout the Middle Holocene with a progressive decrease in $^{87}Sr/^{86}Sr$ ratios while Zr/(Zr+K) values increase, that would indicate a progressive change towards drier conditions with episodic torrential rainfall events; (c) 4.2 – 0 cal. Kyr BP: A dominant arid period for the Late Holocene when the torrential character of the rainfall pattern is more extreme, as reflected by lower $^{87}Sr/^{86}Sr$ ratios and higher Zr/(Zr+K) index.

The described period of maximum precipitation (high $^{87}Sr/^{86}Sr$ ratios and minimum Zr/(Zr+K) values; Fig 4.12-a-b) in the Alboran Sea (11.7 – 7.6 Kyr cal. BP) occurred at the time when the modern hyperarid Saharan desert was vegetated (Jolly *et al.,* 1998; Phelps *et al.,* 2020) and covered in numerous lakes (Hoelzmann *et al.,* 1998; Gasse, 2000). These humid conditions over North Africa correspond to the so-called African Humid Period that extended from 14.8 to 5.5 Kyr cal. PB (deMenocal *et al.,* 2000b; Adkins *et al.,* 2006; Shanahan *et al.,* 2015), and were controlled by the northward expansion of the African rain belts due to a relative maximum in solar radiation during Northern Hemisphere summers (Prentice *et al.,* 2000; Timm *et al.,* 2010; Lézine *et al.,* 2012;). Extensive vegetation cover due to increased precipitation resulted in a period of reduced formation of Saharan dust plumes and thus its contribution to marine sediments (deMenocal *et al.,* 2000b). These climatic conditions significantly limited the transport and arrival of Saharan dust into Alboran Sea sediments, a configuration consistent with the obtained higher $^{87}Sr/^{86}Sr$ ratio values (Fig. 4.12 a). Several paleoclimatic reconstructions further north, in the Iberian Peninsula, also indicate that generalized humid conditions also developed out of Africa and have been typically associated with a notable enhancement of the winter precipitation (Wagner *et al.,* 2019; García-Alix *et al.,* 2021; Columbu *et al.,* 2022). The precipitation

enhancement in the Western Mediterranean region has been associated with changes in the control and positioning of atmospheric cells due to the orbital forcing during precession minima and Northern Hemisphere summer insolation maxima (Bosmans *et al.,* 2015; Wagner *et al.,* 2019). Different authors have attributed the increased humidity to a southward shift of the North Atlantic storm tracks leading moisture towards the southern Iberian Peninsula (Fletcher *et al.,* 2012; Chabaud *et al.,* 2014; García-Alix *et al.,* 2021). The precipitation enhancement described during the early Holocene to the onset of the mid-Holocene (11.7 – 7.6 Kyr cal. BP) also agrees with the recorded low Zr/(Zr+K) values indicating an increase of the chemical weathering due to higher humid conditions (Fig 4.12a-b), supplying more K-rich minerals through the constant fluvial discharges. This is also in consonance with the high $^{87}Sr/^{86}Sr$ values recorded, as enhanced rainfall would be consistent with continuous but less torrential (less energy) character in the sediment transport by river systems. Moreover, the continued wash effect would decrease the sediment availability and the forestall coverage expansion observed during that period (Anderson *et al.,* 2011; Fletcher and Sánchez-Goñiz 2008; Combourrieu-Nebout *et al.,* 2009; Ramos-Román *et al.,* 2018) would enhance this sediment retention (Camuera *et al.,* 2018).

Within the overall humid conditions observed between 11.7 – 7.6 Kyr cal. BP, both $^{87}Sr/^{86}Sr$ ratios and Zr/(Zr+K), record the period of maximum humidity from 9.5 to 7.6 kyr cal. BP (Fig. 4.12a-b). This period has been defined as the Western Mediterranean Humid Period (WMHP; García-Alix *et al.,* 2021; Fig 4.12). This observation agrees well with several marine and terrestrial pollen records that show an expansion of the Mediterranean forest taxa during this specific period (Anderson *et al.,* 2011; Fletcher and Sánchez-Goñiz 2008; Combourrieu-Nebout *et al.,* 2009; Ramos-Román *et al.,* 2018;); and also with geochemical and isotopic records from lake sediments located both north and south of the Alboran Sea (Zielhofer *et al.,* 2017; Mesa-Fernández *et al.,* 2018; García-Alix *et al.,* 2021, 2022). According to stable isotope (deuterium, δD) record from Padul wetland (southern Iberian Peninsula), the rains during the early Holocene and during most of the middle Holocene (11.7 – 5.5 kyr cal. BP) were dominated by an Atlantic source of moisture (Fig.4.12e-f) associated with a southward displacement of the Atlantic storm tracks (García-Alix *et al.,* 2021). Interestingly, the time window identified in this thesis as the most humid period (9.5 – 7.6 kyr cal. BP) coincides with an interval of relative enhancement of rains dominated by local Mediterranean moisture within the overall period of preferential Atlantic sourced rains (García-Alix *et al.,* 2021). Enhanced rain during winter and probably during the fall season would be consistent with minimum energy transport conditions as suggested by $^{87}Sr/^{86}Sr$, with enhanced chemical weathering indicated by Zr/(Zr+K) and higher contribution of Mediterranean source waters indicated by deuterium record from Padul. These maximum humidity conditions also occurred in parallel with the maximum SST recorded in the Alboran Sea (Fig 4.12a-c). The warm sea would contrast with the air temperatures, potentially inducing local convective precipitation, thus increasing the precipitation with the proposed Mediterranean moisture sourcing

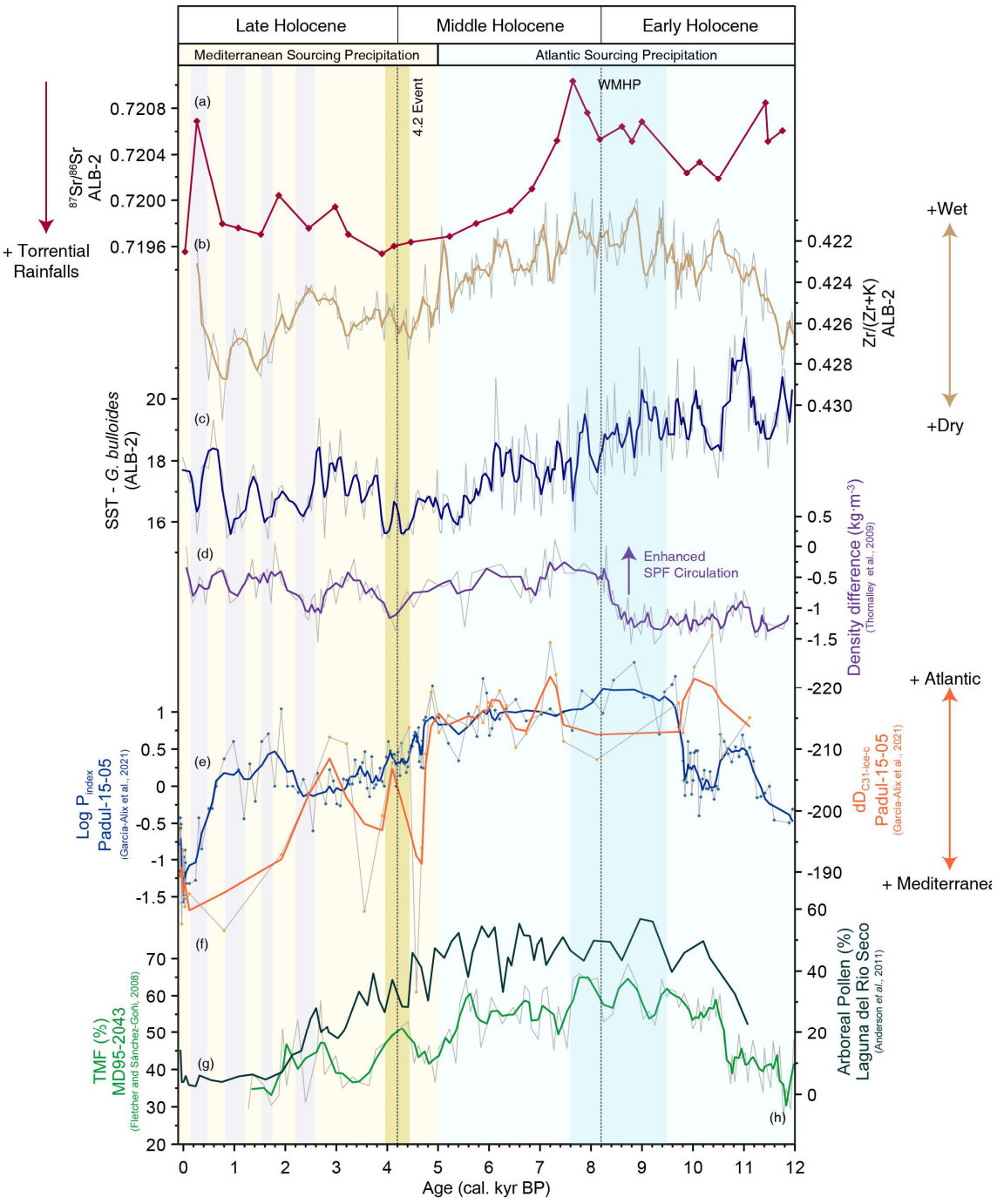

***Figure 4.12 – Holocene hydrography in the Western Mediterranean Sea**. (a) $^{87}Sr/^{86}Sr$ ratio from the ALB-2 core. (b) Zr/(Zr+K) index from the ALB-2 record. (c) SST from the ALB-2 record. (d) Density difference from Thornalley et al., (2009). (e) Precipitation reconstruction from Padul15-05 (Garcia-Alix et al., 2021) (f) Deuterium signal from Padul15-05 (García-Alix et al., 2021), (g) Total Mediterranean Forest from the sediment core MD95-2043 (Fletcher and Sánchez-Goñi, 2008) and Arboreal Pollen (%) from Laguna de los Rios (Anderson et al., 2011). WMHP: Western Mediterranean Humid Period. Vertical coloured bars correspond to those remarked periods in the text.*

At around 7.6 kyr cal. PB, both the $^{87}Sr/^{86}Sr$ and Zr/(Zr+K) records initiate a progressive depletion/increasing trend that culminates at around 4.0 kyr cal. PB when minimum/maximum values are reached (Fig 4.12a-b). The Zr/(Zr+K) index would suggest a continuous decrease in the chemical weathering (lower K-rich minerals supplied) due to a progressive change toward more arid conditions. Consistently, the $^{87}Sr/^{86}Sr$ depletion signal would imply a progressive increase in the energy of rivers transporting sediments, a typical situation in Mediterranean climates with major rain episodes occurring with a strong torrential character. This aridification trend during the middle Holocene agrees with the progressive retirement of the Mediterranean forest taxa while increasing the semi-desert taxa detected in pollen sequences of the region (Fig 4.12g-h; Anderson *et al.,* 2011; Combourrieu-Nebout *et al.,* 2009, Fletcher and Sánchez-Goñiz, 2008). This situation should have also favoured the soil exposure to physical weathering and erosion and, thus, the progressive increase in the contribution of Zr-enriched minerals towards the Alboran sedimentary record. This aridification trend has also been recorded in a precipitation reconstruction based on pollen data (Fig. 4.12g-h) over the southern Iberian Peninsula (García-Alix *et al.,* 2021). This middle Holocene aridification observed in several independent proxies over the western Mediterranean region occurred with the increased transport of relatively warm subtropical Atlantic subsurface waters towards subpolar regions (Repschläger *et al.,* 2017). As a result, a progressive contraction of the SPG was observed between 7 to 5 kyr cal. BP (Colin *et al.,* 2019). This oceanic configuration would lead to a northward position in the North Atlantic westerly wind belt, increasing the storminess in northern latitudes (Goslin *et al.,* 2018) and thus progressively blocking the arrival of North Atlantic winter moisture over the western Mediterranean (Fletcher *et al.,* 2012). In turn, this middle Holocene change would progressively shift winter precipitation towards spring-fall precipitations with more Mediterranean moisture sourcing (Moreno *et al.,* 2014; Zielhofer *et al.,* 2017). This progressive precipitation displacement would have potentially caused an advance of the torrential rainfall events over the westernmost Mediterranean region like nowadays (Gil-Guirado *et al.,* 2022). The torrential effect potentially produced by the seasonal precipitation displacement is observed in the decreasing $^{87}Sr/^{86}Sr$ and increasing Zr/(Zr+K) values. (Fig 4.12a-b). These transitional middle Holocene conditions have also been related to punctual aridification events during North Atlantic cooling spells (Fletcher *et al.,* 2012; Zielhofer *et al.,* 2017), potentially triggered by the northward displacement of the winter storm tracks. In this sense, the early to middle Holocene is characterized by progressive aridification while cooling (Fig. 4.12).

The third interval corresponds to the last 4.2 kyr PB or late Holocene period, when the lowest $^{87}Sr/^{86}Sr$ and the highest Zr/(Zr+K) values were recorded (Fig. 4.12a-b). Both records would indicate arid conditions with sporadic rainfall but with the highest torrential character of the whole Holocene. These arid conditions agree with several marine and lake pollen records around the western Mediterranean, evidencing the overall aridification trend that started at 7.2 kyr cal. BP was fully developed during the late Holocene (Fig. 4.12; Fletcher and Sánchez-Goñiz, 2008; Combourrieu-Nebout *et al.,* 2009; Anderson *et al.,* 2011; Jiménez-Espejo *et al.,* 2014; García-Alix *et al.,* 2017; Mesa-Fernández *et al.,* 2018; Gomes *et al.,* 2020). These arid conditions coexisted

with more intense torrential rainfalls preferentially produced after the dry seasons and then during fall and early winter, such as suggest the $^{87}Sr/^{86}Sr$ and Zr/(Zr+K) values. This situation would be similar to the present-day precipitation patterns in which torrential rainfalls occur during the fall and early winter, mainly produced by Mediterranean cyclogenesis and/or convective events (Jansà et al., 2001; Insua-Costa et al., 2022; Gil-Guirado et al., 2020). In agreement with these observations, the hydrogen isotope record from a south Iberia lake (Fig. 4.12e-f) is also consistent with a shift in the main rainfall source from the Atlantic towards the Mediterranean regions (Toney 2020; García-Alix et al., 2021). The overall predominance of the Mediterranean moisture would lead to forming local cyclogenesis and/or convective precipitations, thus increasing the torrential character observed in the $^{87}Sr/^{86}Sr$ and Zr/(Zr+K) records. During the late Holocene, an increased rate of flooding episodes has also been reported in the Mediterranean Iberian rivers (Benito et al., 2015), which agrees with observed extreme precipitation events.

At the onset of the late Holocene occurred a millennial scale event centred at 4.2 kyr cal. BP, whose Mediterranean impact has recently been reviewed (Bini *et al.,* 2019). In the studied record, this millennial-scale event is well represented with the lowest spring SST (Fig. 4.12a to c) and the lowest recorded $^{87}Sr/^{86}Sr$ values indicating highly energetic conditions in sediment transport (Fig. 4.12a). Zr/(Zr+K) index reflexes this event as an increase in physical weathering (Fig. 4.12b). Thus, based on these records, the 4.2 kyr BP millennial scale event expression in this location would be recorded as a cold and dry event with intense rainfall torrentiality. This cooling is consistent with other *G. bulloides* records in the Alboran Sea (Jiménez-Amat and Zahn, 2015) despite substantially invariant alkenones SST reconstructions being recorded in the Alboran Sea (Cacho *et al.,* 1999; Martrat *et al.,* 2014). The arid expression of this event is more regionally consistent by several proxies around the western Mediterranean (Lamb and van der Kaars, 1995; Arz et al., 2006; Carrión et al., 2007; Fletcher et al., 2012; Jalut et al., 2009; Magny et al., 2009; Jiménez-Moreno and Anderson, 2012; Ramos-Román et al., 2018; Di Rita and Magri, 2019). Interestingly, after the 4.2 kyr BP event, those records with higher resolution (SST and Zr/(Zr+K)) show a succession of intense millennial-scale variability with cold and wet events occurring systematically during periods of weak SPG circulation (Fig 4.12d). A similar pattern of cold-wet events has also been reported by Zielhofer *et al.,* 2017 in the Middle Atlas, attributed to a negative NAO phase leading the Atlantic winter storm tracks towards southern positions during these millennial-scale events. Based on modern modelization (Lohmann *et al.,* 2009), a positive NAO phase cohabits with an enhanced SPG and AMOC strengthening. However, the AMOC strengthening leads the warm and saline water from the STG towards the SPG through the NAC. Consequently, due to the warm and saltier properties of the water masses in the SPG, there is a net buoyancy gain that, ultimately, reduces the AMOC strengthening as well as the SPG. Then, this contributes to a negative NAO phase, which would be associated with an SPG weakening. Thus, the oceanic and atmospheric interactions occurring in the North Atlantic exert changes in the climate patterns with the succession of wet-cold and arid-warm periods in the Alboran Sea (Fig. 4.12)

Chapter 5

Conclusions

“Van plorant els nuvols grisos,
i ens fan anyorar el bon temps”

La gent que estimo, Oques Grasses i Rita Payés

Conclusions

(1) The comparison between four different sea surface temperature (SST) records derived from planktonic foraminifera *G. bulloides* Mg/Ca ratios in the Western Mediterranean Sea show a good agreement in absolute SST values during the Holocene. All SST records also show strong similarities in the millennial-scale variability throughout the studied period. Robust consistency in the compared SST records strongly supports the use of *G. bulloides* Mg/Ca ratios in this region as an SST proxy that reflects changes in the environmental conditions.

(2 The comparison of *G. bulloides* Mg/Ca–SST signal records to previously published alkenone–SST records in the western Mediterranean clearly highlights discrepancies between both proxies. In this thesis, the comparison is further extended into the glacial period, which also shows large discrepancies in the SSTs during the deglaciation, particularly during the second warming phase after the YD period that is clearly described in the alkenone SST but virtually absent in all the Mg/Ca–SST records studied. It is argued that the absence of post-YD warming in the Mg/Ca records reflects the resilient capacity of *G. bulloides* by shifting its preferential growth season in order to compensate for the large SST deglacial warming. It is concluded that during the last glacial period and the onset of deglaciation, *G. bulloides* grew preferentially during the autumn season, characterised by weaker upwelling conditions but with a shift towards spring after the YD with stronger upwelling (colder SST) conditions as it is the case in the present day western Mediterranean. Throughout the Holocene, the SST variability is significantly larger in the Mg/Ca–SST record (~ 4°C) than for the alkenone–SST record (~ 2°C). We interpreted this Mg/Ca–SST variability as a reflect of the climate evolution for a single season (spring), whereas the reduced variability in the alkenone–SST reflects a well-averaged annual signal.

(3) The comparison between four different oxygen isotopes ($\delta^{18}O$) records measured in the planktonic foraminifera *G. bulloides* in the Western Mediterranean Sea shows a strong isotopic gradient between the western and eastern Alboran Sea(about 0.5‰). This observed gradient suggests the fast modification of the Atlantic Inflow Water to a more Mediterranean signal, indicating intense surface mixing with the underlying Mediterranean waters.

(4) The new high-resolution Holocene Mg/Ca–SST record clearly differentiates three intervals: (1) the warmest SST values (19.6±0.8°C) occurred during the Early Holocene (11.7–9 kyr BP); (2) a continuous cooling trend during the Middle Holocene, that culminated with the coldest Holocene SST (15.5±1.5°C) with a double cold peak structure centred at around 4.2 kyr BP; (3) the Late Holocene (4.2 kyr BP–present) without significant cooling/warming trends, but with enhanced millennial-scale oscillations.

The warmest SST of the Early Holocene (11–9 kyr BP) in the Alboran Sea coincided with intense meltwater pulses from the Laurentide ice sheet, which could have led to a reduction in the northward heat transport from the STG towards the North Atlantic that resulted in subtropical heat accumulation that could have contributed to the warmer Atlantic water inflow into the western Mediterranean Sea. The onset of the cooling trend that occurred at 9 kyr BP and the relative

evolution of the $\delta^{18}O_{sw}$ records from the Alboran Sea and the STG indicates the arrival through Gibraltar of more negative $\delta^{18}O_{sw}$ waters from northern latitudes, supporting an enhanced influence of high-latitude North Atlantic conditions in the inflowing waters to the Mediterranean Sea.

The 4.2 kyr BP event is recorded in the Mg/Ca–SST as a double cold peak event, reaching the lowest SST (15.5±1.5°C) of the Holocene. This event marks the onset of enhanced millennial-scale variability that dominated during the Late Holocene. Comparable intensification of millennial-scale variability during this time period has been previously described in the North Atlantic Ocean in relation to the intensity of the SPG. These observations highlight that the Atlantic–Mediterranean water exchange through Gibraltar operated in different modes during the Early and Late Holocene.

(5) Five sediment digestion procedures were tested for geologic standard BCR-2 and marine sediment samples. The best results, both in total element recoveries and isotopic ratios measured, corresponded to the nitric, hydrochloric and hydrofluoric digestion protocol. This protocol achieves to obtain similar recoveries within the errors to the certificate values for Sr, Nd and Pb. Also, the values for Sr, Nd and Pb isotopic ratios were similar within the errors to those previously published. This digestion protocol also achieves complete digestion for the marine sediment samples, thus obtaining higher Sr, Nd and Pb recoveries.

(6) An innovative chromatographic procedure to separate the Sr, Nd and Pb in one single stage has been successfully performed and tested. This new extraction method efficiently separates the Sr, Nd and Pb from the marine sediment matrix simultaneously using 2mL bed-volume columns filled with DGA-Resin (TrisKem International). This procedure also separates each isotopic system from interfering elements (e.g. Rb and Sr, Sm and Nd, Hg and Pb), thus achieving a complete purification of Sr, Nd and Pb. The purification method was further optimised using a controlled-pressured vacuum system (TrisKem Vaccum Box), which allows the processing of 12 samples simultaneously in 5h.

(7) The new radiogenic isotope (Sr, Nd and Pb) characterisation of the lithogenic fraction obtained from the ALB-1 sediment trap provides valuable insights into the main sediment sources in the Alboran Sea at present. The obtained values for the Sr and Nd isotopic ratios compared with the isotopic end member values (Sr and Nd) in two potential sediment sources areas (Saharan dust and the rock complexes from the Betic Cordillera) demonstrate predominant sourcing from the Betic Cordillera as opposed to the Saharan dust. In this comparison is added a third end member (Beach end member) that achieve to classify the sediment particles collected in the ALB-1 sediment trap location as a function of the energy to transport these sediments. Based on isotopic mixing calculations, the ALB-1 lithogenic sediments are differentiated in three isotopic clusters. In combination with present-day instrumental records (rainfalls record, Guadalhorce river discharges and the total lithogenic fluxes captured by the ALB-1 sediment trap), the lower $^{87}Sr/^{86}Sr$ ratios correspond to periods with high precipitations after the dry summer. This

is attributed to the stronger erosion capacity of the first rainfalls after prolonged dry periods, easily mobilising sediments in the catchment area. The typical torrential character of these rains increases the capacity to transport larger amounts of sediments. After most of the readily available sediments are washed at the end of the wet season, the terrigenous load discharged by the rivers is significantly reduced, corresponding with $^{87}Sr/^{86}Sr$ intermediate ratios. The highest $^{87}Sr/^{86}Sr$ ratios correspond to samples recovered during periods when the Saharan dust deposition was not diluted by local river discharge, which also coincides with the dry periods with the minimum fluvial discharges.

(8) The previous evaluation of present-day processes controlling sediment supply set the bases for understanding and interpreting changes in the hydrological patterns occurring during the Holocene period. Consequently, the radiogenic isotope ratios measured in the ALB-2 terrigenous sediment are compared with the isotopic end member values (Sr and Nd) in two potential sediment source areas (Saharan dust and the rock complexes from the Betic Cordillera). The obtained results support that the predominant sediment sourcing areas during the Holocene were driven from the Betic Cordillera rock complexes via river discharges. Based on isotopic mixing calculations after adding the beach end member, the ALB-2 lithogenic sediments during the Holocene are differentiated in two isotopic clusters. These clusters perfectly align with the isotopic values obtained from the sediment trap. The PCA statistical treatment of the geochemical composition of the ALB-2 bulk sediment reveals that the relative changes produced in the Zr and K signal relation respond to changes in the sediment supplied from the Betic Cordillera through rivers systems as a consequence of precipitation variations. The two independent proxy records of $^{87}Sr/^{86}Sr$ and Zr/(Zr+K) differentiate the Holocene in the following three distinctive phases in terms of hydrological changes that occurred in the Alboran Sea: (1) 11.7 – 7.6 cal. Kyr BP: A period of maximum development of persistent rainfalls (higher $^{87}Sr/^{86}Sr$ values with minimum Zr/(Zr+K) signal) during the early Holocene and part of the Middle Holocene; (2) 7.6 – 4.2 cal. Kyr PB: A transition period throughout the Middle Holocene with a progressive decrease in $^{87}Sr/^{86}Sr$ ratios while Zr/(Zr+K) values increase, indicating a progressive change towards drier conditions with episodic torrential rainfall events and (3) 4.2 – 0 cal. Kyr BP: A dominant arid period for the Late Holocene when the torrential character of the rainfall pattern is more extreme, as reflected by lower $^{87}Sr/^{86}Sr$ ratios and higher Zr/(Zr+K) index.

References

Abouchami, W., Näthe, K., Kumar, A., Galer, S.J.G., Jochum, K.P., Williams, E., Horbe, A.M.C., Rosa, J.W.C., Balsam, W., Adams, D., Mezger, K., Andreae, M.O., 2013. Geochemical and isotopic characterization of the Bodélé Depression dust source and implications for transatlantic dust transport to the Amazon Basin. Earth Planet. Sci. Lett. 380, 112–123. doi:10.1016/j.epsl.2013.08.028

Adkins, J., DeMenocal, P., Eshel, G., 2006. The '"African humid period"' and the record of marine upwelling from excess 230Th in Ocean Drilling Program Hole 658C. Paleo 21, 1–14. doi:10.1029/2005PA001200

Ahrens, C.D., 2008. Essentials of meteorology: an invitation to the atmosphere. B. Chpater 473. doi:10.1007/s13398-014-0173-7.2

Ait Brahim, Y., Wassenburg, J.A., Sha, L., Cruz, F.W., Deininger, M., Sifeddine, A., Bouchaou, L., C., S., Edwards, R.L., Cheng, H., 2019. North Atlantic Ice-Rafting, Ocean and Atmospheric Circulation During the Holocene : Insights From Western Mediterranean Speleothems. Geiohysical Res. Lett. 7614–7623. doi:10.1029/2019GL082405

Allan, R. P. & Soden, B. J., (2008). Atmospheric warming and the amplification of precipitation extremes. Science 321, 1481–1484 (2008)

Ali-Ani, T., and Sarapää, O., 2008. Clay and clay mineralogy. Geologian Tutkuskeskus

Amblàs, D., Canals, M., Urgeles, R., Lastras, G., Liquete, C., Hughes-Clarke, J.E., Casamor, J.L., Calafat, A.M. 2006. Morphogenetic mesoscale analysis of the northeastern Iberian margin NW Mediterranean Basin. Marine Geology, 3-20. doi:10.1016/j.margeo.2006.09.009

Anderson, R.S., Jiménez-Moreno, G., Carrión, J.S., Pérez-Martínez, C., 2011. Postglacial history of alpine vegetation, fire, and climate from Laguna de Río Seco, Sierra Nevada, southern Spain. Quat. Sci. Rev. 30, 1615–1629. doi:10.1016/j.quascirev.2011.03.005

Andrews, J.T., Hardadottir, J., Stoner, J.S., Mann, M.E., Kristjansdottir, G.B., Koc, N., 2003. Decadal to millennial-scale periodicities in North Iceland shelf sediments over the last 12000 cal yr: long-term North Atlantic oceanographic variability and solar forcing. Earth Planet. Sci. Lett. 210, 453–465. doi:10.1016/S0012-821X(03)00139-0

Arz, H., Lamy, F., Pätzold, J., 2006. A pronounced dry event recorded around 4.2 ka in brine sediments from the northend Read Sea. Quaternary Research, 66, 3 (432-441). https://doi.org/10.1016/j.yqres.2006.05.006

Ausin, B., Flores, J.A., Sierro, F.J., Cacho, I., Hernández-Almeida, I., Martrat, B., Grimalt, J.O., 2015. Atmospheric patterns driving Holocene productivity in the Alboran Sea (Western Mediterranean): A multiproxy approach. The Holocene 25, 583–595. doi:10.1177/0959683614565952

Ayache, M., Swingedouw, D., Mary, Y., Eynaud, F., Colin, C., 2018. Multi-centennial variability of the AMOC over the Holocene : A new reconstruction based on multiple proxy-derived SST records. Glob. Planet. Change 170, 172–189. doi:10.1016/j.gloplacha.2018.08.016

Azmy, K., Veizer, J., Bassett, M.G., Copper, P., 1999. Silurian strontium isotope stratigraphy. Geol. Soc. Am. Bull. 475–483.

Balaram, V., Subramanyam, K.S. V, 2022. Sample preparation for geochemical analysis: Strategies and significanc. Adv. Sample Prep. 1, 100010. doi:10.1016/j.sampre.2022.100010

Banner, J. L.: Radiogenic isotopes : systematics and applications to earth surface processes and chemical stratigraphy, , 65, 141–194, doi:10.1016/S0012-8252(03)00086-2, 2004.

Bárcena, M.A., Flores, J.A., Sierro, F.J., Pérez-Folgado, M., Fabres, J., Calafat, A., Canals, M., 2004. Planktonic response to main oceanographic changes in the Alboran Sea (Western Mediterranean) as documented in sediment traps and surface sediments. Mar. Micropaleontol. 53, 423–445. d oi:10.1016/j.marmicro.2004.09.009

Barker, S., Greaves, M., Elderfield, H., 2003. A study of cleaning procedures used for foraminiferal Mg/Ca paleothermometry. Geochemistry, Geophys. Geosystems 4, 1–20. doi:10.1029/2003GC000559

Bartlein, P.J., Harrison, S.P., Brewer, S., Connor, S., Davis, B.A.S., Gajewski, K., Guiot, J., Henderson, A., Peyron, O., Prentice, I.C., Scholze, M., Seppä, H., Shuman, B., Sugita, S., Thompson, R.S., Viau, A.E., Williams, J., Wu, H., 2010. Pollen-based continental climate reconstructions at 6 and 21 ka: a global synthesis. Clim. Dyn. 37, 775–802. doi:10.1007/s00382-010-0904-1

Bayon, G., German, C.R., Boella, R.M., Milton, J.A., Taylor, R.N., Nesbitt, R.W., 2002. An improved method for extracting marine sediment fractions and its application to Sr and Nd isotopic analysis. Chem. Geol. 187, 179–199.

Bea, F., Montero, P., Talavera, C., Abu Anbar, M., Scrarrow, J.H., Molina, J., Moreno., J.A., 2010. The palaeogreographic position of Central Iberia in Gondwana during the Ordovician: evidence from zircon chronology and Nd isotopes. Terra, Nova, 22, 341-346 https://doi.org/10.1111/j.1365-3121.2010.00957.x

Begg, G.C., Griffin, W.L., Natapov, L.M., Reilly, S.Y.O., Grand, S.P., O'Neill, C.J., Hronsky, J.M.A., Poudjom Djomani, Y., Swain, C.J., Deen, T., Bowden, P., 2009. The lithospheric architecture of Africa: Seismic tomography, mantle petrology, and tectonic evolution. Geosphere 23–50. doi:10.1130/GES00179.1

Becquerel, H. (1986). Émission de radiation nouvelles par l'uranium métallique. Compt Ren, 122, 1086.

Bellomo, K., Angeloni, M., Corti, S., Hardenberg, J. von, 2021. Future climate change shaped by inter-model differences in Atlantic meridional overturning circulation response Katinka. Nat. Commun. 1–10. doi:10.1038/s41467-021-24015-w

Béthoux, J. P., & Bethoux, J. P. (1980). Mean water fluxes across sections in the Mediterranean Sea, evaluated in the basis of water and salt budgets and of observed salinities. Oceanologica Acta, 3(1), 79–88.

Bemis, B. E., Spero, H. J., Bijma, J., & Lea, D. W. (1998). Reevaluation of the oxygen isotopic composition of planctonic foraminifera: Experimental results and revised paleotemperature equations. Paleoveanography, 13(2), 150–160.

Bini, M., Zanchetta, G., Persoiu, A., Cartier, R., Català, A., Cacho, I., Dean, Jonathan, R., Di Rita, F., Drysdale, R.N., Finnè, M., Isola, I., Jalali, B., Lirer, F., Magri, D., Masi, A., Marks, L., Mercuri, A.M., Peyron, O., Sadori, L., Sicre, M.-A., Welc, F., Zielhofer, C., Brisset, E., 2019. The 4.2 ka BP Event in the Mediterranean region: an overview. Clim. Past 15, 555–577. doi:https://doi.org/10.5194/cp-15-555-2019

Blaauw, M., Christen, J.A., 2011. Bacon manual – v2.2.

Blanchet, C. L., Tjallingii, R., Frank, M., Lorenzen, J., Reitz, A., Brown, K., Brückmann, W. (2013). High- and low-latitude forcing of the Nile River regime during the Holocene inferred from laminated sediments of the Nile deep-sea fan. Earth and Planetary Science Letters, 364, 98–110. https://doi.org/10.1016/j.epsl.2013.01.009

Boer RH, Beukes GJ, Meyer FM, and Smith CB (1993) Fluoride precipitates in silicate wet-chemistry: Implications on REE fractionation. Chemical Geology 104: 93–98.

Bond, G., Kromer, B., Beer, J., Muscheler, R., Evans, M.N., Showers, W., Hoffmann, S., Lotti-Bond, R., Hajdas, I., Bonani, G., 2001. Persistent Solar Influenceon North Atlantic Climate During the Holocene. Science (80-.). 294, 2130–2136. doi:10.1126/science.1065680

Bond, G., Showers, W., Cheseby, M., Lotti, R., Almasi, P., DeMenocal, P., Priore, P., Cullen, H., Hajdas, I., Bonani, G., 1997. A Pervasive Millennial-Scale Cycle in North Atlantic Holocene and Glacial Climates. Science (80-.). 278, 1257–1266. doi:10.1126/science.278.5341.1257

Böning, C.W., Scheinert, M., Dengg, J., Biastoch, A., Funk, A., 2006. Decadal variability of subpolar gyre transport and its reverberation in the North Atlantic overturning. Geophys. Res. Lett. 33, 1–5. doi:10.1029/2006GL026906

Born, A., & Stocker, T. F. (2014). Two stable equilibria of the Atlantic subpolar gyre. Journal of Physical Oceanography, 44(1), 246–264. https://doi.org/10.1175/JPO-D-13-073.1

Bosch, D., Maury, R.C., El Azzouzi, M., Bollinger, C., Bellon, H., Verdoux, P., 2014. Lithos Lithospheric origin for Neogene–Quaternary Middle Atlas lavas (Morocco): Clues from trace elements and Sr-Nd-Pb-Hf isotopes. LITHOS 205, 247–265. doi:10.1016/j.lithos.2014.07.009

Bosmans, J.H.C., Drijfhout, S.S., Tuenter, E., Hilgen, F.J., Lourens, L.J., Rohling, E.J., 2015. Precession and obliquity forcing of the freshwater budget over the Mediterranean. Quat. Sci. Rev. 123, 16–30. doi:10.1016/j.quascirev.2015.06.008

Bout-Roumazeilles, V., Combourieu-Neboutb, N., Peyron, O., Cortijo, E., Landais, A., Masson-Delmotte, V., 2007. Connection between South Mediterranean climate and North African atmospheric circulation during the last 50,000 yr BP North Atlantic cold events. Quat. Sci. Rev. 26, 3197–3215. doi:10.1016/j.quascirev.2007.07.015

Boyer, T. and Mishonov, A.: 14 pp., World Ocean Atlas 2013 Product Documentation, 2013.

Brayshaw, D. J., Rambeau, C. M. C., & Smith, S. J. (2011). Changes in mediterranean climate during the holocene: Insights from global and regional climate modelling. Holocene, 21(1), 15–31. https://doi.org/10.1177/0959683610377528

Bray, N.A., Ochoa, J., Kinder, T.H., 1995. The role of the interface exchange through the Strait of Gibraltar. J. Geophys. Res. 100, 10755–176. doi:10.1029/95JC00381

Brems, D., Ganio, M., Latruwe, K., Balcaen, L., Carremans, M., Gimeno, D., Silvestri, A., Vanhaecke, F., Muchez, P., Degryse, P., 2013a. Isotopes on the beach, Part 1: Strontium Isotope ratios as a provenance indicator for lime raw materials used in Roman glass-making. Archaeometry 2, 214–234. doi:10.1111/j.1475-4754.2012.00702.x

Brems, D., Ganio, M., Latruwe, K., Balcaen, L., Carremans, M., Gimeno, D., Silvestri, A., Vanhaecke, F., Muchez, P., Degryse, P., 2013b. Isotopes on the beach, part 2: Neodymium isotopic analysis for the procenancing of Roman glass-making. Archaeometry 3, 449–464. doi:10.1111/j.1475-4754.2012.00701.x

Buckley, M. W., & Marshall, J. (2016). Observations, inferences, and mechanisms of the Atlantic Meridional Overturning Circulation: A review. Reviews of Geophysics, 54(1), 5–63. https://doi.org/10.1002/2015RG000493

Cacho, I., Grimalt, J.O., Canals, M., 2002. Response of the Western Mediterranean Sea to rapid climatic variability during the last 50,000 years: A molecular biomarker approach. J. Mar. Syst. 33–34, 253–272. doi:10.1016/S0924-7963(02)00061-1

Cacho, I., Grimalt, J.O., Canals, M., Sbaffi, L., Shackleton, N.J., Schönfeld, J., Zahn, R., 2001. Variability of the western Mediterranean Sea surface temperature during the last 25,000 years and its connection with the Northern Hemisphere climatic changes. Paleoceanography 16, 40–52. doi:10.1029/2000PA000502

Cacho, I., Grimalt, J.O., Pelejero, C., Canals, M., Sierro, F.J., Flores, J.A., Shackleton, N., 1999. Dansgaard-Oeschger and Heinrich event imprints in Alboran Sea paleotemperatures. Paleoceanography 14, 698–705. doi:https://doi.org/10.1029/1999PA900044

Camuera, J., Jiménez-Moreno, G., Ramos-Román, M.J., García-Alix, A., Toney, J.L., Anderson, R.S., Jiménez-Espejo, F.J., Kaufman, D., Bright, J., Webster, C., Yanes, Y., Carrión, J.S., Ohkouchi, N., Suga, H., Yamame, M., Yokoyama, Y., Martínez-Ruiz, F., 2018. Orbital-scale environmental and climatic changes recorded in a new ~200,000-year-long multiproxy sedimentary record from Padul, southern Iberian Peninsula. Quat. Sci. Rev. 198. doi:10.1016/j.quascirev.2018.08.014

Canals, M., Amblàs, D., Lastras, G., Sànchez-Vidal, A., Calafat, A., Rayo, X. i Casamor, J.L., 2012. Els canyons submarins; Suplement de la Història Natural dels Països Catalans, La terra a l'univers: astronomia, Addenda geològica, Enciclopèdia Catalana, Barcelona, p. 251-272.

Caracciolo, L., Le Pera, E., Muto, F., Perri, F., 2011. Sandstone petrology and mudstone geochemistry of the Peruc–Korycany Formation (Bohemian Cretaceous Basin, Czech Republic). International Geology Review 53, 1003–1031.

Cardoso Pereira, S., Marta-Almeida, M., Carvalho, A.C., Rocha, A., 2019. Extreme precipitation events under climate change in the Iberian Peninsula. Int. J. Climatol. 1255–1278. doi:10.1002/joc.6269

Carlson, A. E., Legrande, A. N., Oppo, D. W., Came, R. E., Schmidt, G. A., Anslow, F. S., … Obbink, E. A. (2008). Rapid early Holocene deglaciation of the Laurentide ice sheet. Nature Geoscience, 1(9), 620–624. https://doi.org/10.1038/ngeo285

Carrión, J.S., Sánchez-Gómez, P., Mota, J.F., Yll, R., Chaín, C., 2003. Holocene vegetation dynamics, fire and grazing in the Sierra de Gádor, southern Spain. The Holocene 13, 839–849. doi:10.1191/0959683603hl662rp

Català, A., Cacho, I., Frigola, J., Pena, L.D., Lirer, F., 2019. Holocene hydrography evolution in the Alboran Sea : a multi-record and multi-proxy comparison. Clim. th 927–942. doi:https://doi.org/10.5194/cp-15-927-2019

Casanueva, A., Rodríguez-Puebla, C., Frías, M. D., & González-Reviriego, N. (2014). Variability of extreme precipitation over Europe and its relationships with teleconnection patterns. Hydrology and Earth System Sciences, 18(2), 709-725.

Cerdà-Domènech, M., Frigola, J., Sánchez-Vidal, A., Canals, M., 2020. Calibrating high resolution XRF core scanner data to obtain absolute metal concentrations in highly polluted marine deposits after two case studies off Portmán Bay and Barcelona, Spain. Sci. Total Environ. 717, 134778. doi:https://doi.org/10.1016/j.scitotenv.2019.134778

Chabaud, L., Sánchez Goñi, M.F., Desprat, S., Rossignol, L., 2014. Land–sea climatic variability in the eastern North Atlantic subtropical region over the last 14,200 years: Atmospheric and oceanic processes at different timescales. The Holocene 24, 787–797. doi:10.1177/0959683614530439

Chamley, H., 1989. Clay Formation Through Weathering, in: Clay Sedimentology. Springer Berlin Heidelberg.

Chao, T.T., Sanzolone, R.F., 1992. Decomposition techniques. J. Geochemical Explor. 44, 65–106.

Chester, R., Hughes, M.J., 1967. A chemical technique for teh separation of ferro-manganese minerals, carbonate minerals and adsorbed trace elements from pelagic sediments. Chem. Geol. 2, 249–262.

Choppin, G., Liljenzin, J. O., & Rydberg, J. (2002). Radiochemistry and nuclear chemistry. Butterworth-Heinemann

Cisneros, M., Cacho, I., Frigola, J., Canals, M., Masqué, P., Martrat, B., Casado, M., Grimalt, J.O., Pena, L.D., Margaritelli, G., Lirer, F., 2016. Sea surface temperature variability in the central-western Mediterranean Sea during the last 2700 years: A multi-proxy and multi-record approach. Clim. Past 12, 849–869. doi:10.5194/cp-12-849-2016

Cléroux, C., Debret, M., Cortijo, E., Duplessy, J.-C., Dewilde, F., Reijmer, J., Massei, N., 2012. High-resolution sea surface reconstructions off Cape Hatteras over the last 10 ka. Paleoceanography 27, 1–14. doi:10.1029/2011PA002184

Cole, J.M., Goldstein, S.L., deMenocal Peter, B., Hemming, S.R., Grousset, F.E., 2009. Contrasting compositions of Saharan dust in the eastern Atlantic Ocean during the last deglaciation and African Humid Period. Earth Planet. Sci. Lett. 278, 257–266. doi:10.1016/j.epsl.2008.12.011

Colin, C., Frank, N., Copard, K., Douville, E., 2010. Neodymium isotopic composition of deep-sea corals from the NE Atlantic: implications for past hydrological changes during the Holocene. Quat. Sci. Rev. 29, 2509–2517. doi:10.1016/j.quascirev.2010.05.012

Colin, C., Tisnérat-Laborde, N., Mienis, F., Collart, T., Pons-Branchu, E., Dubois-Dauphin, Q., Frank, N., Dapoigny, A., Ayache, M., Swingedouw, D., Dutay, J.-C., Eynaud, F., Debret, M., Blamart, D., Douville, E., 2019. Millennial-scale variations of the Holocene North Atlantic mid-depth gyre inferred from radiocarbon and neodymium isotopes in cold water corals. Quat. Sci. Rev. 211. doi:10.1016/j.quascirev.2019.03.011

Colin, C., Turpin, L., Blamart, D., Frank, N., Kissel, C., S, D., 2006. Evolution of weathering patterns in the Indo-Burman Ranges over the last 280 kyr: Effects of sediment provenance on 87Sr/86Sr ratios tracer. Geochemistry, Geophys. Geosystems. doi:10.1029/2005GC000962

Collins, J.A., Prange, M., Caley, T., Gimeno, L., Beckmann, B., Mulitza, S., Skonieczny, C., Roche, D., Schefuß, E., 2017. Rapid termination of the African Humid Period triggered by northern high-latitude cooling. Nat. Commun. 8. doi:10.1038/s41467-017-01454-y

Columbu, A., Spötl, C., Fohlmeister, J., Hu, H.-M., Chiarini, V., Hellstrom, J., Cheng, H., Shen, C.-C., Waele, J. De, 2022. Central Mediterranean rainfall varied with high northern latitude temperatures during the last deglaciation. Commun. Earth Environ. 1–9. doi:10.1038/s43247-022-00509-3

Combourieu-Nebout, N., Peyron, O., Dormoy, I., Desprat, S., Beaudouin, C., Kotthoff, U., Marret, F., 2009. Rapid climatic variability in the west Mediterranean during the last 25 000 years from high resolution pollen data. Clim. Past 503–521. doi:https://doi.org/10.5194/cp-5-503-2009, 2009.

Combourieu Nebout, N., Peyron, O., Dormoy, I., Desprat, S., Beaudouin, C., Kotthoff, U., Marret, F., 2009. Rapid climatic variability in the west Mediterranean during the last 25 000 years from high resolution pollen data. Clim. Past 5, 503–521. doi:https://doi.org/10.5194/cp-5-503-2009

Combourieu Nebout, N., Turon, J.L., Zahn, R., Capotondi, L., Londeix, L., Pahnke, K., 2002. Enhanced aridity and atmospheric high-pressure stability over the western Mediterranean during the North Atlantic cold events of the past 50 k.y. Geology 30, 863–866. doi:10.1130/0091-7613(2002)030<0863:EAAAHP>2.0.CO;2

Coplen, T.B., 1996. New guidelines for reporting stable hydrogen, carbon, and oxygen isotope-ratio data. Geochim. Cosmochim. Acta 60, 3359–3360. doi:https://doi.org/10.1016/0016-7037(96)00263-3

Critelli, S., Arribas, J., Le Pera, E., Tortosa, A., Marsaglia, K.M., Latter, K.K., 2003. The recycled orogenic sand provenance from an uplifted thrust belt, Betic Cordillera, Southern Spain. J. Sediment. Res. 73, 72–81.

Curry, R.G., McCartney M.S., Joyce, T.M., (1998). Oceanic transport of subpolar climate signals to mid-depth subtropical waters. Nature, 391

de Toma, V., Artale, V., Yang, C., 2022. Exploring AMOC Regime Change over the Past Four Decades through Ocean Reanalyses. Climate 10, 1–21. doi:https://doi.org/ 10.3390/cli10040059

Debret, M., Bout-Roumazeilles, V., Grousset, F., Desmet, M., Mcmanus, J.F., Massei, N., Sebag, D., Petit, J.-R., Copard, Y., Trentesaux, A., 2007. The origin of the 1500-year climate cycles in Holocene North-Atlantic records. Clim. Past 3, 569–575. doi:https://doi.org/10.5194/cp-3-569-2007

Debret, M., Sebag, D., Crosta, X., Massei, N., Petit, J.-R., Chapron, E., Bout-Roumazeilles, V., 2009. Evidence from wavelet analysis for a mid-Holocene transition in global climate forcing. Quat. Sci. Rev. 28, 2675–2688. doi:10.1016/j.quascirev.2009.06.005

Delworth, T.L., Zeng, F., 2016. The Impact of the North Atlantic Oscillation on Climate through Its Influence on the Atlantic Meridional Overturning Circulation. J. Clim. 941–962. doi:10.1175/JCLI-D-15-0396.1

DeMenocal, P., Ortiz, J., Guilderson, T., Adkins, J., Sarnthein, M., Baker, L., Yarusinsky, M., 2000. Abrupt onset and termination of the African Humid Period: Rapid climate responses to gradual insolation forcing. Quat. Sci. Rev. 19, 347–361. doi:10.1016/S0277-3791(99)00081-5

Deniel C., Pin, C., 2001. Single-stage method for the simultaneous isolation of lead and strontium from silicate samples for isotopic measurments. Analytica Chimica Acte, 426, 1, 95-103. https://doi.org/10.1016/S0003-2670(00)01185-5

Desprat, S., Combourieu-Nebout, N., Essallami, L., Sicre, M.A., Dormoy, I., Peyron, O., Siani, G., Bout Roumazeilles, V., Turon, J.L., 2013. Deglacial and holocene vegetation and climatic changes in the southern central Mediterranean from a direct land-sea correlation. Clim. Past 9, 767–787. doi:10.5194/cp-9-767-2013

Dickson RR, Lazier J, Meincke J, Rhines P, Swift J. 1996. Long-term coordinated changes in the convective activity of the North Atlantic. Progress in Oceanography 38: 241–295

Donat, M. G., Lowry, A. L., Alexander, L. V., O'Gorman, P. A., & Maher, N. (2016). More extreme precipitation in the world's dry and wet regions. Nature Climate Change, 6(5), 508-513

Di Rita, F., Fletcher, W.J., Aranbarri, J., Margaritelli, G., Lirer, F., Magri, D., 2018. Holocene forest dynamics in central and western Mediterranean: periodicity, spatio-temporal patterns and climate influence. Sci. Rep. 1–13. doi:10.1038/s41598-018-27056-2

Di Rita, F., and Magri, D., 2019. The 4.2 ka event in the vegetation record of the central Mediterranean. Climate of the Past, 15, 237-251. https://doi.org/10.5194/cp-15-237-2019

Deer, W.A., 1975. The feldspar group, Science, 187, 4175, p 427. DOI: 10.1126/science.187.4175.427

Duffourg, F., & Ducrocq, V. (2011). Origin of the moisture feeding the Heavy Precipitating Systems over Southeastern France. Natural hazards and earth system sciences, 11(4), 1163-1178

Durand-Delga, M., Rossi, P., Olivier, P., Puglisi, D., 2000. Situation structurale et nature ophiolitique de roches basiques jurassiques associées aux flyschs maghrébins du Rif (Maroc) et de Sicile (Italie). Comptes Rendus de l'Académie des Sciences - Series IIA - Earth and Planetary Science 331, 29–38. http://dx.doi.org/10.1016/s1251-8050(00)01378-1.

Elderfield, H., Ganssen, G., 2000. Past temperature and delta18O of surface ocean waters inferred from foraminiferal Mg/Ca ratios. Nature 405, 442–445. doi:10.1038/35013033

Emiliani, C., 1955. Pleistocene Temperatures. The Journal of Geology. Vol. 63, Num. 6 https://doi.org/10.1086/626295

England, J. H., Lakeman, R., Lemmen, S., Bednarski, J.M., Stewart, T.G., Evans, D.J.A., 2008 A millennial-scale record of Arctic Ocean sea ice variability and the demise of the Ellesmere Island ice shelves. Geophys. Res. Lett. 35, L19502

Epstein, S. and Mayeda, T., 1953. Variation of O18 content of waters from natural sources. Geochimica et Cosmochimica Acta, 45, 213-224.

Escudero, M., Stein, A.F., Draxler, R.R., Querol, X., Alastuey, A., Castillo, S., Avila, A., 2011. Source apportionment for African dust outbreaks over the Western Mediterranean using the HYSPLIT model. Atmos. Res. 99, 518–527. doi:10.1016/j.atmosres.2010.12.002

Fabres, J., Calafat, A., Sanchez-Vidal, A., Canals, M., Heussner, S., 2002. Composition and spatio-temporal variability of particle f luxes in the Western Alboran Gyre, Mediterranean Sea. J. Mar. Syst. 34, 431–456.

Fairbridge, Rhodes, W., n.d. History of Paleoclimatology. 2010.

Farah, A., Michard, A., Saddiqi, O., Chalouan, A., Chopin, C., Montero, P., Corsini, M., Bea, F., 2021. The Beni Bousera marbles, record of a Triassic-Early Jurassic hyperextended margin in the Alpujarrides-Sebtides units (Rif belt, Morocco). Earth Sci. Bull. 192, 26. doi:10.1051/bsgf/2021015/5307036/bsgf

Fletcher, W.J., Debret, M., Sanchez-Goñi, M.-F., 2012. Mid-Holocene emergence of a low-frequency millennial oscillation in western Mediterranean climate: Implications for past dynamics of the North Atlantic atmospheric westerlies. The Holocene 0, 1–14. doi:10.1177/0959683612460783

Fletcher, W.J., Sánchez-Goñi, M.F., 2008. Orbital- and sub-orbital-scale climate impacts on vegetation of the western Mediterranean basin over the last 48,000 yr. Quat. Res. 70, 451–464. doi:10.1016/j.yqres.2008.07.002

Frigola, J., Moreno, A., Cacho, I., Canals, M., Sierro, F.J., Flores, J.A., Grimalt, J.O., 2008. Evidence of abrupt changes in Western Mediterranean Deep Water circulation during the last 50 kyr: A high-resolution marine record from the Balearic Sea. Quat. Int. 181, 88–104. doi:10.1016/j.quaint.2007.06.016

Frigola, J., Moreno, A., Cacho, I., Canals, M., Sierro, F.J.J., Flores, J.A.A., Grimalt, J.O.O., Hodell, D.A.A., Curtis, J.H.H., 2007. Holocene climate variability in the western Mediterranean region from a deepwater sediment record. Paleoceanography 22, 2209. doi:10.1029/2006PA001307

Gao, Y.-Q., Yu, L., 2008. Subpolar Gyre Index and the North Atlantic Meridional Overturning Circulation in a Coupled Climate Model. Atmos. Ocean. Sci. Lett. 1, 29–32.

García-Alix, A., Jiménez-Espejo, F. J., Toney, J. L., Jiménez-Moreno, G., Ramos-Román, M. J., Anderson, R. S., ... & Kuroda, J. (2017). Alpine bogs of southern Spain show human-induced environmental change superimposed on long-term natural variations. Scientific reports, 7(1), 1-12

García-Alix, A., Camuera, J., Ramos-Román, M.J., Toney, J.L., Sachse, D., Schefub, E., Jiménez-Moreno, G., Jiménez-Espejo, F.J., López-Avilés, A., Scott Anderson, R., Yanes, Y., 2021. Paleohydrological dynamics in the Western Mediterranean during the last glacial cycle. Glob. Planet. Change 202. doi:https://doi.org/10.1016/j.gloplacha.2021.103527

García-Alix, A., Jimenez-Moreno, G., Gázquez, F., Monedero-Contreras, R., López-Avilés, A., Jiménez-Espejo, F.J., Rodríguez-Rodríguez, M., Camuera, J., Ramos-Román, M.J., Soctt-Anderson, R., 2022. Climatic control on the Holocene hydrology of a playa-lake system in the western Mediterranean. Catena 214. doi:https://doi.org/10.1016/j.catena.2022.106292

Gasse, F., 2000. Hydrological changes in the African tropics since the Last Glacial Maximum. Quat. Sci. Rev. 19, 189–211.

Gerber, E. P., & Vallis, G. K. (2009). On the zonal structure of the North Atlantic Oscillation and annular modes. Journal of the Atmospheric Sciences, 66(2), 332-352

Gil-Guirado, S., Pérez-Morales, A., Pino, D., Peña, J.C., López Martínez, F., 2022. Flood impact on the Spanish Mediterranean coast since 1960 based on the prevailing synoptic patterns. Sci. Total Environ. 807. doi:10.1016/j.scitotenv.2021.150777

Gomes, S.D., Fletcher, W.J., Rodrigues, T., Stone, A., Abrantes, F., Naughton, F., 2020. Time-transgressive Holocene maximum of temperate and Mediterranean forest development across the Iberian Peninsula reflects orbital forcing. Palaeogeogr. Palaeoclimatol. Palaeoecol. 550, 109739. doi:https://doi.org/10.1016/j.palaeo.2020.109739

Goslin, J., Fruergaard, M., Sander, L., Gałka, M., Menviel, L., Monkenbusch, J., Thibault, N., Clemmensen, L.B., 2018. Holocene centennial to millennial shifts in North-Atlantic storminess and ocean dynamics. Sci. Rep. 1–12. doi:10.1038/s41598-018-29949-8

Grossmann, I., Klotzbach, P.J., 2009. A review of North Atlantic modes of natural variability and their driving mechanisms. J. Geophys. Res. 114, 1–14. doi:10.1029/2009JD012728

Grimalt-Gelabert, M., Alomar-Garau, G., & Martin-Vide, J. (2021). Synoptic causes of torrential rainfall in the Balearic Islands (1941–2010). Atmosphere, 12(8), 1035

Grousset, F.E., Biscaye, P.E., Zindlerm A., Prospero, J., Chester, A., 1988. Neodymium isotopes as a tracers in marine sediments and aerosols: North Atlantic. Earth and Planetary Science leters. 87, 4, 367-378.

Grousset, F.E., Rognon, P., Coudé-Gaussen, G., Pédemay, Ph., 1992. Palaeogeography, Palaeoclimatology, Palaeoceanography, 93, 3-4, 203-212.

Grousset, F.E., Parra, M., Bory, A., Martinez, Ph., Bertrand, Ph., Shimmield, G., Ellam, R.M., 1998. Quaternary Science Reviews, 17, 4-5, 395-409.

Grousset, F. E. and Biscaye, P. E.: Tracing dust sources and transport patterns using Sr , Nd and Pb isotopes, , 222, 149–167, doi:10.1016/j.chemgeo.2005.05.006, 2005.

Guéguen, F., Isnard, H., Nonell, A., Vio, L., Vercourter, T., Chartier, F., 2015. Neodymium isotope ratio measurements by LC-MC-ICPMS for nuclear applications: investigation of isotopic fractionation and mass bias correction. J. Anal. At. Spectrom. 443–452. doi:10.1039/c4ja00361f

Guerrera, F., Martín-Martín, M., Perrone, V., Tramontana, M., 2005. Tectono-sedimentary evolution of the southern branch of the Western Tethys (Maghrebian Flysch Basin and Lucanian Ocean): consequences for Western Mediterranean geodynamics. Terra Nova 17, 358–367. http://dx.doi.org/10.1111/j.1365 3121.2005.00621.x.

Guinoiseau, D., Singh, S.P., Galer, S.J.G., Abouchami, W., Bhattacharyya, R., Kandler, K., Bristow, C., Andreae, M.O., 2022. Characterization of Saharan and Sahelian dust sources based on geochemical and radiogenic isotope signatures. Quat. Sci. Rev. 293, 107729. doi:10.1016/j.quascirev.2022.107729

Gutjahr, M., Frank, M., Stirling, C.H., Klemm, V., Flierdt, T. Van De, Halliday, A.N., 2007. Reliable extraction of a deepwater trace metal isotope signal from Fe–Mn oxyhydroxide coatings of marine sediments. Chem. Geol. 242, 351–370. doi:10.1016/j.chemgeo.2007.03.021

Guy Rothwell, R., Rack, F.R., 2006. New techniques in sediment core analysis : an introduction. Geol. Soc. 267, 1–29.

Häkkinen, S., Rhines, P.B., Worthen, D.L., 2011. Warm and saline events embedded in the meridional circulation of the northern North Atlantic. J. G 116, 1–13. doi:10.1029/2010JC006275

Hastings, W., Emerson, S.R., Nelson, B.K., 1996. Vanadium in foraminiferal calcite: Evaluation of a method to determine paleo-seawater vanadium concentrations. Geochim. Cosmochim. Acta 60, 3701–3715.

Hemleben, C., Spindler, M., & Anderson, O. R. (1989). Modern planktonic foraminifera. Springer Science & Business Media.

Hembleden, C., 1989. Modern Planktonic Foraminifera, Springer, 363.

Hernández-Almeida, I., Bárcena, M.A., Flores, J.A., Sierro, F.J., Sanchez-Vidal, A., Calafat, A., 2011. Microplankton response to environmental conditions in the Alboran Sea (Western Mediterranean): One year sediment trap record. Mar. Micropaleontol. 78, 14–24. doi:10.1016/j.marmicro.2010.09.005

Heussner, S., Ratti, C., Carbonne, J., 1989. The PPS 3 time-series sediment trap and the trap sample processing techniques used during the ECOMARGE experiment. Cont. Shelf Res. 10, 943–958.

Hodkinson, J.R., 1966. Particle Sizing by Means of the Forward Scattering Lobe. Appl. Opt. 5, 839–844.

Hoefs, J., 1987. Stable isotope geochemistry. Springer, Berlin HeidelbergNew York, 241 pp.

Hoelzmann, P., Jolly, D., Harrison, S.P., Laarif, F., Bonnefille, R., Pachur, H.-J., 1998. Mid-Holocene land-surface conditions in northern Africa and the Arabian peninsula: A data set for the analysis of biogeophysical feedbacks in the climate system. Global Biogeochem. Cycles 12, 35–51.

Hoogakker, B. A., Chapman, M. R., McCave, I. N., Hillaire-Marcel, C., Ellison, C. R., Hall, I. R., & Telford, R. J. (2011). Dynamics of North Atlantic deep water masses during the Holocene. Paleoceanography, 26(4).

Hoogakker, B. A. A., Klinkhammer, G. P., Elderfield, H., Rohling, E. J., and Hayward, C., 2009. Mg/Ca paleothermometry in high salinity environments, Earth Planet. Sc. Lett., 284, 583–589, doi:10.1016/j.epsl.2009.05.027.

Horwitz, E. P., Mcalister, D. R., Bond, A. H., Jr, R. E. B., Mcalister, D. R., Bond, A. H. and Novel, R. E. B.J.: Novel Extraction of Chromatographic Resins Based on Tetraalkyldiglycolamides : Characterization and Potential Applications Novel Extraction of Chromatographic Resins Based on Tetraalkyldiglycolamides : Characterization and Potential Applications, , 6299, doi:10.1081/SEI-200049898, 2007.

Huang, B., Hu, Z.Z., Schneider, E.K., Wu, Z., Xue, Y., Klinger, B., 2012. Influences of tropical-extratropical interaction on the multidecadal AMOC variability in the NCEP climate forescast system. Climate dynamics. 39, 3, 531-555.

Hu, Y., Li, D., Liu, J., 2007. Abrupt seasonal variation of the ITCZ and the Hadley circulation. Geophys. Res. Lett. 34, 1–5. doi:10.1029/2007GL030950

Hu ZC, Gao S, Liu YS, et al. (2010) NH4F assisted high pressure digestion of geological samples for multi-element analysis by ICP-MS. Journal of Analytical Atomic Spectrometry 25: 408–413.

Hu, Z., Zhang, W., Liu, Y., Chen, H., Gaschnig, R.M., Zong, K., Li, M., Gao, S., Hu, S., 2013. Rapid bulk rock decomposition by ammonium fluoride (NH4 F) in open vessels at an elevated digestion temperature. Chem. Geol. 355, 144–152. doi:10.1016/j.chemgeo.2013.06.024

Hu, Z. and Qui, L. (2014). Sample digestion methods Sample Digestion Methods,, doi:10.1016/B978-0-08-095975-7.01406-6, 2019.

Imbrie,J. and Imbrie, K., 1979. Ice Ages: Solving the Mystery, short Hills, NJ, Enslow

Insua-costa, D., Senande-Rivera, M., Llasat, M.C., Miguez-Macho, G., 2022. A global perspective on western Mediterranean precipitation extremes. Clim. Atmos. Sci. 1–8. doi:10.1038/s41612-022-00234-w

IPCC. Pörtner, H. O., Roberts, D. C., Adams, H., Adler, C., Aldunce, P., Ali, E., ... & Birkmann, J. (2022). Climate change 2022: Impacts, adaptation and vulnerability. IPCC Sixth Assessment Report, 37-118.

Irrgeher, J., Galler, P., Prohaska, T., 2016. 87Sr/86Sr isotope ratio measurements by laser ablation multicollector inductively coupled plasma mass spectrometry: Reconsidering matrix interferences in bioapatites and biogenic carbonates. Spectrochim. Acta Part B 125, 31–42. doi:10.1016/j.sab.2016.09.008

Izuka, S. K. (1988). Relationship of magnesium and other minor elements in tests of Cassidulina subglobosa and C. oriangulata to physical oceanic properties. The Journal of Foraminiferal Research, 18(2), 151-157.

Jacobsen, S.B., Wasserburg, G.J., 1980. Sm-Nd ISOTOPIC EVOLUTION OF CHONDRITES STEIN. Earth Planet. Sci. Lett. 50, 139–155.

Jalali, B., Sicre, M.-A., Bassetti, M.-A., Kallel, N., 2016. Holocene climate variability in the North-Western Mediterranean Sea (Gulf of Lions). Clim. Past 12, 91–101. doi:10.5194/cp-12-91-2016

Jalali, B., Sicre, M., Azuara, J., Pellichero, V., Combourieu-Nebout, N., 2019. Influence of the North Atlantic subpolar gyre circulation on the 4.2 ka BP event. Clim. Past 701–711. doi:https://doi.org/10.5194/cp-15-701-2019

Jalut, G., Dedoubat, J. J., Fontugne, M., & Otto, T. (2009). Holocene circum-Mediterranean vegetation changes: climate forcing and human impact. Quaternary international, 200(1-2), 4-18.

Jansà, A., Genoves, A., Picornell, M.A., Campins, J., Riosalido, R., Carretero. O., 2001. Western Mediterranean cyclones and heavy rain. Part 2: Statistical approach. Meteorological Applications, 8, 1, 43-56. https://doi.org/10.1017/S1350482701001049

Jansen, J.H.F., Van der Gaast, S.J., Koster, B., Vaars, A.J., 1998. CORTEX, a shipboard XRF-scanner for element analyses in split sediment cores. Mar. Geol. 151, 143–153.

Jarvis, I., & Jarvis, K. E. (1992). Plasma spectrometry in the earth sciences: techniques, applications and future trends. Chemical Geology, 95(1-2), 1-33.

Jewell, A.M., Cooper, M.J., Milton, J.A., James, R.H., Crocker, A.J., Wilson, P.A., 2022. Chemical isolation and isotopic analysis of terrigenous sediments with emphasis on effective removal of contaminating marine phases including barite. Chem. Geol. 589, 120673. doi:10.1016/j.chemgeo.2021.120673

Jewell, A.M., Drake, N., Crocker, A.J., Bakker, N.L., Kunkelova, T., Bristow, C.S., Cooper, M.J., Milton, J.A., Breeze, P.S., Wilson, P.A., 2020. Three North African dust source areas and their geochemical fingerprint. Earth Planet. Sci. Lett. 1, 116645. doi:10.1016/j.epsl.2020.116645

Jiménez-Amat, P., Zahn, R., 2015. Offset timing of climate oscillations during the last two glacial-interglacial transitions connected with large-scale freshwater perturbation. Paleoceanography 30, 768–788. doi:10.1002/2014PA002710

Jiménez-Espejo, F. J., García-Alix, A., Jiménez-Moreno, G., Rodrigo-Gámiz, M., Anderson, R. S., Rodríguez-Tovar, F. J., ... & Pardo-Igúzquiza, E. (2014). Saharan aeolian input and effective humidity variations over western Europe during the Holocene from a high altitude record. Chemical Geology, 374, 1-12.

Jiménez-Moreno, G., & Anderson, R. S. (2012). Holocene vegetation and climate change recorded in alpine bog sediments from the Borreguiles de la Virgen, Sierra Nevada, southern Spain. Quaternary Research, 77(1), 44-53.

Jolly, D., Prentice, I.C., Bonnefille, R., Aziz, B., Bengo, M., Brenac, P., Bruchet, G., David, B., Cazet, J.-P., Cheddadi, R., Edorh, T., Elenga, H., El Moutaki, S., Guiot, J., Laarif, F., Lamb, H., Lezine, A.-M., Maley, J., Mbenza, M., Peyron, O., Reille, M., Reynaud-Farrera, I., Riollet, G., Ritchie, J.C., Roche, E., Scott, L., Ssemmanda, I., Straka, H., Umer, M., Campo, E. van, Vilimumbalo, S., Vincens, A., Waller, M., 1998. Biome reconstruction from pollen and plant macrofossil data for Africa and the Arabian peninsula at 0 and 6000 years. J. Biogeogr. 25, 1007–1027.

Jung, S.J.A., Davies, G.R., Ganssen, G.M., Kroon, D., 2004. Stepwise Holocene aridi¢cation in NE Africa deduced from dust-borne radiogenic isotope records. Earth Planet. Sci. Lett. 221. doi:10.1016/S0012-821X(04)00095-0

Jullien, E., Grousset, F.E., Malaize, B., Duprat, J., Sánchez-Goñi, M.F., Eynaud, F., Charlier, K., 2007. Low-latitude “dusty events” vs. high-latitude “icy Heinrich events”. Quaternary Research 68 (3), 379–386

Jweda, J., Bolge, L., Class, C., Goldstein, S.L., 2015. High Precision Sr-Nd-Hf-Pb Isotopic Compositions of USGS Reference Material BCR-2. Geostand. Geoanalytical Res. 40, 101–115. doi:10.1111/j.1751-908X.2015.00342.x

Kemle-von Mücke, S., & Hemleben, C. (1999). Foraminifera. South Atlantic Zooplankton, 1, 43-73.

Khodayar, S., Davolio, S., Girolamo, P. Di, Brossier, C.L., Flaounas, E., Fourrie, N., Lee, K., Ricard, D., Vie, B., Bouttier, F., Caldas-alvarez, A., Ducrocq, V., 2021. Overview towards improved understanding of the mechanisms leading to heavy precipitation in the western Mediterranean : lessons learned from HyMeX. Atmos. Chem. Phys. 21, 17051–17078. doi:https://doi.org/10.5194/acp-21-17051-2021

Khodayar, S., Kalthoff, N., Kottmeier, C., 2018. Atmospheric conditions associated with heavy precipitation events in comparison to seasonal means in the western mediterranean region. Clim. Dyn. 51, 951–967. doi:10.1007/s00382-016-3058-y

Khodayar, S., Pastor, F., Valiente, J.A., Benetó, P., Ehmele, F., 2022. What causes a heavy precipitation period to become extrem? The exceptional October of 2018 in the Western Mediterranean. Weather Clim. Extrem.

Kim, J.-H., Rimbu, N., Lorenz, S.J., Lohmann, G., Nam, S., Schouten, S., Ru, C., Schneider, R.R., 2004. North Pacific and North Atlantic sea-surface temperature variability during the Holocene. Quat. Sci. Rev. 23, 2141–2154. doi:10.1016/j.quascirev.2004.08.010

Kim, J.-H. et al (2007). Impacts of the North Atlantic gyre circulation on Holocene climate off northwest Africa. Geology 35, 387–390 (2007).

Kissel, C., Van Toer, A., Laj, C., Cortijo, E., and Michel, E.: (2013) Variations in the strength of the North Atlantic bottom water during Holocene, Earth Planet. Sc. Lett., 369–370, 248–259, 2013.

Knippertz P., Wernlo, H., 2010. A Lagrangian climatology of tropical moisture exports to the Northenr Hemispheric Extratropics. Journal of Climate, 22, 4, 987-1003.

Köppen, W., 1936. Das georaphische System der Klimate. Borntraeaer Sci. Publ.

Krichak, S. O., Breitgand, J. S., Gualdi, S., & Feldstein, S. B. (2014). Teleconnection–extreme precipitation relationships over the Mediterranean region. Theoretical and applied climatology, 117(3), 679-692.

Krichak, S. O., Barkan, J., Breitgand, J. S., Gualdi, S., & Feldstein, S. B. (2015). The role of the export of tropical moisture into midlatitudes for extreme precipitation events in the Mediterranean region. Theoretical and Applied Climatology, 121(3), 499-515.

Koul, V., Tesdal, J.-E., Bersch, M., Hjálmar, H., Brune, S., Borchert, L., Haal, H., Schrum, C., Baehr, J., 2020. Unraveling the choice of the north Atlantic subpolar gyre index. Sci. Rep. 1–12. doi:10.1038/s41598-020-57790-5

Kucera, M., Darling, K.F., 2002. Cryptic species of planktonic foraminifera: their effect on palaeoceanographic reconstructions. R. Soc. 360, 695–718. doi:10.1098/rsta.2001.0962

Kucera, M., Weinelt, Mara, Kiefer, T., Pflaumann, U., Hayes, A., Weinelt, Martin, Chen, M. Te, Mix, A.C., Barrows, T.T., Cortijo, E., Duprat, J., Juggins, S., Waelbroeck, C., 2005. Reconstruction of sea-surface temperatures from assemblages of planktonic foraminifera: multi-technique approach based on geographically constrained calibration data sets and its application to glacial Atlantic and Pacific Oceans. Quat. Sci. Rev. 24, 951–998. doi:10.1016/j.quascirev.2004.07.014

Laepple, T., & Huybers, P. (2013). Reconciling discrepancies between Uk37 and Mg/Ca reconstructions of Holocene marine temperature variability. Earth and Planetary Science Letters, 375, 418-429.

Lacombe, H., Gascard, J. C, Cornella, J., and Béthoux, J. P.: Response of the Mediterranean to the water and energy fluxes across its surface, on seasonal and interannual scales, Oceanol. Acta, 4, 247–255, 1981.

Lamb, H.F., van der Kaars, S., 1955. Vegetational response to Holocene climatic change: pollen and palaeolimnological data from the Middle Atlas, Morocco. The Holocene, 5, 4. https://doi.org/10.1177/095968369500500402

Langehaugh, H.R., Medhaug, I., Eldevik, T., Ottera, O.H., 2012. Arctic/Atlantic Exchanges via the Subpolar Gyre. J. Clim. 2421–2439. doi:10.1175/JCLI-D-11-00085.1

Le, J., Shackelton, N.J., 1992. Carbonate dissolution fluctiations in the Western Equatorial Pacific during the Late Quaternary. Paleoceanography and Paleoclimatology. https://doi.org/10.1029/91PA02854

Lea, D., 1999. Trace elements in foraminiferal calcite in Modern foraminifera. Luer Academic Press, UK. pp.259-277.

Lézine, A.-M., Hély, C., Grenier, C., Braconnot, P., Krinner, G., 2011. Sahara and Sahel vulnerability to climate changes , lessons from Holocene hydrological data. Quat. Sci. Rev. 30, 3001–3012. doi:10.1016/j.quascirev.2011.07.006

Le, J., & Shackleton, N. J. (1992). Carbonate dissolution fluctuations in the western equatorial Pacific during the late Quaternary. Paleoceanography, 7(1), 21-42

Lionello, P., Malanotte-Rizzoli, P., Boscolo, R., Alpert, P., Artale, V., Li, L., Luterbacher, J., May, W., Trigo, R., Tsimplis, M., Ulbrich, U., Xoplaki, E., 2006. The Mediterranean climate: An overview of the main characteristics and issues. Dev. Earth Environ. Sci. 4, 1–26. doi:10.1016/S1571-9197(06)80003-0

Lionello, P., 2012. The Climate of the Mediterranean Region: From the Past to the Future, 1st ed. Elsevier Inc. doi:10.1016/B978-0-12-416042-2.00009-4.

Lisiecki, L. E., and Raymo, M. E., 2005.. A Pliocene-Pleistocene stack of 57 globally distributed benthic δ18O records. Paleoceanography, 201, 1–17. https://doi.org/10.1029/2004PA001071.

Lohmann, K., Drange, Æ. H. and Bentsen, Æ. M.: Response of the North Atlantic subpolar gyre to persistent North Atlantic oscillation like forcing, , 273–285, doi:10.1007/s00382-008-0467-6, 2009.

Lorente-Plazas, R., Montavez, J.P., Ramos, A.M., Jerez, S., Trigo, R.M., Jimenez-Guerrero, P., 2020. Unusual Atmospheric-River-Like structures coming from Africa induce extrem precipitation over the western Mediterranean sea. JGR Atmosphere. https://doi.org/10.1029/2019JD031280

Lorenz, S.J., Lohmann, G., 2004. Acceleration technique for Milankovitch type forcing in a coupled atmosphere-ocean circulation model: method and application for the Holocene. Clim. Dyn. 23, 727–743. doi:10.1007/s00382-004-0469-y

Magny, M., Peyron, O., Sadori, L., Ortu, E., Zanchetta, G., Vannière, B., Tinner, W., 2012. Contrasting patterns of precipitation seasonality during the Holocene in the south- and north-central Mediterranean. J. Quat. Sci. 27, 290–296. doi:10.1002/jqs.1543

Magny, M., Vannière, B., Znachetta, G., Fouache, E., Touchais, G., Petrika, L., Coussot, C., Walter-Simonnet, A-V., Arnaud, F. 2009. Possible complexity of the climatic event around 4300-3800 cal. BP in the central and western Mediterranean. The Holocene, 19, 6. https://doi.org/10.1177/0959683609337360

Makishima A, Tanaka R, and Nakamura E (2009) Precise elemental and isotopic analyses in silicate samples employing ICP MS: Application of hydrofluoric acid solution and analytical techniques. Analytical Sciences 25: 1181–1187.

Marchal, O., Cacho, I., Stockera, T.F., Grimalt, J.O., Calvo, E., Martrat, B., Shackleton, N., Vautravers, M., Cortijo, E., Kreveld, S. van, Andersson, C., Koç, N., Chapman, M., Sbaffi, L., Duplessy, J.-C., Sarnthein, M., Turon, J.-L., Duprat, J., Jansen, E., 2002. Apparent long-termcooling of the sea surface in the northeast Atlantic and Mediterranean during the Holocene. Quat. Sci. Rev. 21, 455–483. doi:10.1016/S0277-3791(01)00105-6

Marchitto, T.M., DeMenocal, P.B., 2003. Late Holocene variability of upper North Atlantic Deep Water temperature and salinity. Geochemistry, Geophys. Geosystems 4, 1100. doi:10.1029/2003GC000598

Mariet C, Belhadj O, Leroy S, Carrot F, and Me´tricha N (2008) Relevance of NH4F in acid digestion before ICP-MS analysis. Talanta 77: 445–450.

Mariotti, A., Zeng, N., Lau, K.M., 2002a. Euro-Mediterranean rainfall and ENSO—a season- ally varying relationship. Geophys. Res. Lett. 29, 1621.

Mariotti, A., Struglia, M.V., Zeng, N., Lau, K.-M., 2002b. The hydrological cycle in the Mediterranean region and implications for the water budget of the Mediterranean Sea. J. Clim. 15, 1674–1690. doi: 10.1175/1520-0442(2002)015.

Martínez-Ruíz, F., Comas, M.C., Alonso, B., 1999. Mineral associations and geochemical indicators in upper miocene to pleistocene sediments in the alboran basin. Proc. Ocean Drill. Program, Sci. Results 161, 21–36.

Martínez, C., Campins, J., Jansà, A., Genovés, A., 2008. Heavy rain events in the Western Mediterranean: an atmospheric pattern classification. Adv. Sci. Reserch 61–64. doi:https://doi.org/10.5194/asr-2-61-2008

Martrat, B., Grimalt, J.O., Lopez-Martínez, C., Cacho, I., Sierro, F.J., Flores, J.A., Zhang, R., Canals, M., Curtis, J.H., Hodell, D.A., 2004. Abrupt Temperature changes in the Western Mediterranean oer the past 250,000 years. Science (80-.). 306, 1762–1765. doi:10.1126/science.1101706

Martrat, B., Jimenez-amat, P., Zahn, R., Grimalt, J.O., 2014. Similarities and dissimilarities between the last two deglaciations and interglaciations in the North Atlantic region. Quat. Sci. Rev. 99, 122–134. doi:10.1016/j.quascirev.2014.06.016

McCartney, M.S., Talley, L.D., 1982. The subpolar mode water of North Atlantic Ocean. Am. Meteorol. Soc. 12, 1169–1188. doi:https://doi.org/10.1175/1520-0485(1982)012<1169:TSMWOT>2.0.CO;2

Menviel, L., Govin, A., Avenas, A., Miessner, Katrin, J., Grant, K.M., Tzedakis, P.C., 2021. Drivers of the evolution and amplitude of African Humid Periods. Commun. Earth Environ. doi:10.1038/s43247-021-00309-1

Mesa-Fernández, J.M., Jiménez-Moreno, G., Rodrigo-Gámiz, M., García-Alix, A., Jiménez-Espejo, F.J., Martínez-Ruiz, F., Scott Anderson, R., Camuera, J., Ramos-Román, M.J., 2018. Vegetation and geochemical responses to Holocene rapid climate change in the Sierra Nevada (southeastern Iberia): the Laguna Hondera record. Clim. Past 1687–1706. doi:https://doi.org/10.5194/cp-14-1687-2018

Míková, J. and Denková, P.: Modified chromatographic separation scheme for Sr and Nd isotope analysis in geological silicate samples, , 52, 221–226, doi:10.3190/jgeosci.015, 2007.

Millot, C., 2009. Another description of the Mediterranean Sea outflow. Prog. Oceanogr. 82, 101–124. doi:10.1016/j.pocean.2009.04.016

Millot, C., 1999. Circulation in the Western Mediterranean Sea. J. Mar. Syst. 20, 423–442. doi:10.1016/S0924-7963(98)00078-5

Molinero-García, A., Martín-García, J.M., Fernández-González, M.V., Delgado, R., 2022. Provenance fingerprints of atmospheric dust collected at Granada city (Southern Iberian Peninsula). Evidence from quartz grains. Catena 208. doi:10.1016/j.catena.2021.105738

Moreno, A., Cacho, I., Canals, M., Prins, M.A., Sánchez-Goñi, M.-F., Grimalt, J.O., Weltje, G.J., 2002. Saharan Dust Transport and High-Latitude Glacial Climatic Variability: The Alboran Sea Record. Quat. Res. 58, 318–328. doi:10.1006/qres.2002.2383

Moreno, A., Sancho, C., Bartolomé, M., Oliva-Urcia, B., Delgado-Huertas, A., Estrela, M.J., Corell, D., López-Moreno, J.I., Cacho, I., 2014. Climate controls on rainfall isotopes and their effects on cave drip water and speleothem growth: the case of Molinos cave (Teruel, NE Spain. Clim. Dyn. 221–241. doi:10.1007/s00382-014-2140-6

Moros, M., Emeis, K., Risebrobakken, B., Snowball, I., Kuijpers, A., McManus, J., Jansen, E., 2004. Sea surface temperatures and ice rafting in the Holocene North Atlantic: climate influences on northern Europe and Greenland. Quat. Sci. Rev. 23, 2113–2126. doi:10.1016/j.quascirev.2004.08.003

Muynck, D. De, Huelga-Suarez, G., Heghe, L. Van, Degryse, P., Vanhaecke, F., 2009. Systematic evaluation of a strontium-specific extraction chromatographic resin for obtaining a purified Sr fraction with quantitative recovery from complex and Ca-rich matrices. J. Anal. At. Spectrom. 1498–1510. doi:10.1039/b908645e

Nadkarni, R. A. (1984). Applications of microwave oven sample dissolution in analysis. Analytical Chemistry, 56(12), 2233-2237.

Nier, A.O., 1938. The isotopic constitution of Srtrontium, Barium, Bismuth, Thallium and Mercury. Phys. Rev. 5.

Nieto Ferreira, 2021. Cut-off lows and extreme precipitation in Eastern Spain: Current and future climate. Atmosphere, 12, 7. https://doi.org/10.3390/atmos12070835

Nieto-Moreno, V., Martinez-Ruiz, F., Giralt, S., Gallego-Torres, D., García-Orellana, J., Masqué, P., Ortega-Huertas, M., 2013. Climate imprints during the “Medieval Climate Anomaly” and the “Little Ice Age” in marine records from the Alboran Sea basin. The Holocene 0, 1–11. doi:10.1177/0959683613484613

Nóbrega, J. A., Santos, M. C., de Sousa, R. A., Cadore, S., Barnes, R. M., & Tatro, M. (2006). Sample preparation in alkaline media. Spectrochimica Acta Part B: Atomic Spectroscopy, 61(5), 465-495

Nürnberg, D., 1995. Magnesium in tests of Neogloboquadrina pachyderma sinistral from high northern and southern latitudes. Journal of Foraminiferal Research. 25, 350-368.

Nürnberg, D., Bijma, J., Hembleben, c., 1996. Assessing the realiability of magnesium in foraminiferal calcite as a proxy for wáter mass temperaturas. Geochimica et Cosmochimica Acta, 60, 803-814.

Olsen, J., Anderson, N. J., and Knudsen, M. F.: Variability of the North Atlantic Oscillation over the past 5200 years, Nat. Geosci., 5, 808–812, doi:10.1038/ngeo1589, 2012.

Oppo, D. W., McManus, J. F., & Cullen, J. L. (2003). Deepwater variability in the Holocene epoch. Nature, 422(6929), 277-277.

Palanques, A., de Madron, X. D., Puig, P., Fabres, J., Guillén, J., Calafat, A., ... & Bonnin, J. (2006). Suspended sediment fluxes and transport processes in the Gulf of Lions submarine canyons. The role of storms and dense water cascading. Marine Geology, 234(1-4), 43-61.

Pena, L.D., Calvo, E., Cacho, I., Eggins, S., Pelejero, C., 2005. Identification and removal of Mn-Mg-rich contaminant phases on foraminiferal tests: Implications for Mg/Ca past temperature reconstructions. Geochemistry, Geophys. Geosystems 6. doi:10.1029/2005GC000930

Perner, K., Moros, M., Jennings, A., Lloyd, J., and Knudsen, K.: Holocene palaeoceanographic evolution off West Greenland, Holocene, 23, 374–387, 2013.

Perri, F., Critelli, S., Martín-Algarra, A., Martín-Martín, M., Perrone, V., Mongelli, G., Zattin, M., 2013. Triassic redbeds in the Malaguide Complex (Betic Cordillera-Spain): Petrography, geochemistry and geodynamic implications. Earth Sci. Rev. 117, 1–28. doi:10.1016/j.earscirev.2012.11.002

Phelps, L.N., Chevalier, M., Shanahan, T.M., Aleman, J.C., Courtney-Mustaphi, C., Kiahtipes, C.A., Broennimann, O., Marchant, R., Shekeine, J., Quick, L.J., Davis, B.A.S., Guisan, A., Manning, K., 2020. Asymmetric response of forest and grassy biomes to climate variability across the African Humid Period: influenced by anthropogenic disturbance? Ecography (Cop.). 1118–1142. doi:10.1111/ecog.04990

Pierre, C., 1999. The oxygen and carbon isotope distribution in the Mediterranean water masses. Mar. Geol. 153, 41–55. doi:10.1016/S0025-322798.00090-5.

Pin, D., Boriot, D., Bassin, C., Poitrasson, F., 1994. Concomitant separation of strontium and smarium-neodymium for isotopic analysis in silicate samples, based on specific extraction chromatography. Analytica Chimica Acta, 294, 2, 30, 209-217. https://doi.org/10.1016/0003-2670(94)00274-6

Pin, C., Santos Zalduegui, J.F., Sequential separation of light rare-earth elements, thorium and uranium by miniaturized extraction crhomatography: Apllication to isotopic analyses for silicate rocks. Analytica Chimica Acta, 339, 1-2, 79-89. https://doi.org/10.1016/S0003-2670(96)00499-0

Pin C., Bassin, C., 1992. Evaluation of a strontium-specific extraction chromatography method for isotopic analysis in geological materials. Analytica Chimica Acta. 269, 2, 20, 249-255. https://doi.org/10.1016/0003-2670(92)85409-Y

Potts, P.J., 1987. A Handbook of silicate rock analysis. Anal. Chim. Acta 201, 91794.

Potts PJ and Robinson P (2003) Sample preparation of geological samples, soils and sediments. In: Mester Z and Sturgeon R (eds.) Sample Preparation for Trace Element Analysis, pp. 723–763. The Netherlands: Elsevier.

Pourmand, A., Dauphas, N., 2010. Distribution coefficients of 60 elements on TODGA resin : Application to Ca, Lu, Hf, U and Th isotope geochemistry. Talanta 81, 741–753. doi:10.1016/j.talanta.2010.01.008

Povea, P., Cacho, I., Moreno, A., Mennéndez, M., Méndez, F.J., 2015. A new procedure for the lithic fraction characterization in marine sediments from high productivity areas : Optimization of analytical and statistical procedures. Limnol. Oceanogr. Methods 127–137. doi:10.1002/lom3.10013

Prahl, F., Herbert, T., Brassell, S.C., Ohkouchi, N., Pagani, M., Repeta, D., Rosell-Melé, A., Sikes, E., 2000. Status of alkenone paleothermometer calibration: Report from Working Group 3. Geochemistry, Geophys. Geosystems 1. doi:10.1029/2000GC000058

Prentice, I.C., Jolly, D., 2000. Mid-Holocene and Glacial-Maximum Vegetation Geography of the Northern Continents and Africa. J. Biogeogr. 27, 507–519.

Raczek, I., Jochum, K.P., Hofmann, A.W., (2003). Neodymium and Strontium Isotope Data for USGS Reference Materials BCR-1, BCR-2, BHVO-1, BHVO-2, AGV-1, AGV-2, GSP-1, GSP-2 and Eigh MPI-DINF Reference Glasses. Geostandards and Geoanalytical Research. https://doi.org/10.1111/j.1751-908X.2003.tb00644.x

Ramos-Román, M.J., Jiménez-Moreno, G., Camuera, J., García-Alix, A., Anderson, R.S., Jiménez-Espejo, F.J., Sachse, D., Toney, J.L., Carrión, J.S., Webster, C., Yanes, Y., 2018. Millennial-scale cyclical environment and climate variability during the Holocene in the western Mediterranean region deduced from a new multi- proxy analysis from the Padul record (Sierra Nevada , Spain). Glob. Planet. Change 168, 35–53. doi:10.1016/j.gloplacha.2018.06.003

Ramos, A.M., Cortesi, N., Trigo, R.M., 2014. Circulation weather types and spatial variability of daily precipitation in the Iberian Peninsula. Front. Earth Sci. 2, 1–17. doi:10.3389/feart.2014.00025

Rao, K.K., Paulinose, V.T., Jayalakshmy, K.V., Panikkar, B.M., Krishnan Kutty, M., 1987. Distribution of Living Planktonic Foraminifera in the Coastal Upwelling Region of Kenya, Africa. Indian J. Mar. Sediments 17, 121–127.

Rathbum, A.E., Deckker, P. De, 1997. Magnesium and strontium compositions of Recent benthic foraminifera from the Coral Sea, Australia and Prydz Bay, Antarctica. Mar. Micropaleontol. 32, 231–248.

Reimer, P.J., Bard, E., Bayliss, A., Beck, J.W., Blackwell, P.G., Bronk, C., Caitlin, R., Hai, E.B., Edwards, R Lawrence Friedrich, M., Grootes, P.M., Guilderson, T.P., Haflidason, H., Hajdas, I., Hatté, C., Heaton, T.J., Hoffmann, D.L., Hogg, A.G., Hughen, K.A., Kaiser, K.F., Kromer, B., Manning, S.W., Niu, M., Reimer, R.W., Richards, D.A., Scott, E.M., Southon, J.R., Staff, R.A., Turney, C.S.M., van der Plicht, J., 2013. INTCAL13 AND MARINE13 RADIOCARBON AGE CALIBRATION CURVES 0–50,000 YEARS CAL BP. Radiocarbon 55, 1869–1887. doi:https://doi.org/10.2458/azu_js_rc.55.16947

Renssen, H., Seppä, H., Heiri, O., Roche, D. M., Goosse, H., & Fichefet, T. (2009). The spatial and temporal complexity of the holocene thermal maximum. Nature Geoscience, 2(6), 411–414. https://doi.org/10.1038/ngeo513

Repschläger, J., Garbe-Schönberg, D., Weinelt, M., Schneider, R., 2017. Holocene evolution of the North Atlantic subsurface transport. Clim. Past Discuss. 13, 333–344. doi:doi:10.5194/cp-2016-115

Repschläger, J., Weinelt, M., Kinkel, H., Andersen, N., Garbe-Schönberg, D., & Schwab, C. (2015). Response of the subtropical North Atlantic surface hydrography on deglacial and Holocene AMOC changes. Paleoceanography, 30(5), 456–476. https://doi.org/10.1002/2014PA002637

Retzmann, A., Zimmermann, T., Pröfrock, D., Prohaska, T., Irrgeher, J., 2017. A fully automated simultaneous single-stage separation of Sr, Pb, and Nd using DGA Resin for the isotopic analysis of marine sediments. Anal. Bioanal. Chemestry 5463–5480. doi:10.1007/s00216-017-0468-6

Revel, M., Ducassou, E., Grousset, F. E., Bernasconi, S. M., Migeon, S., Revillon, S., … Bosch, D. (2010). 100,000 Years of African monsoon variability recorded in sediments of the Nile margin. Quaternary Science Reviews, 29(11–12), 1342–1362. https://doi.org/10.1016/j.quascirev.2010.02.006

Richter, T.O., Gaast, S.J. van der, Koster, B., Vaars, A., Gieles, R., Stigter, Henko, C., Haas, H. de, Van Weering, T.C.E., 2006. The Avaatech XRF Core Scanner : technical description and applications to NE Atlantic sediments. Geol. Soc. 39–50.

Rigual-Hernández, A.S., Sierro, F.J., Bárcena, M.A., Flores, J.A., Heussner, S., 2012. Seasonal and interannual changes of planktic foraminiferal fluxes in the Gulf of Lions NW Mediterranean. and their implications for paleoceanographic studies: Two 12-year sediment trap records. Deep. Res. Part I Oceanogr. Res. Pap. 66, 26–40. doi:10.1016/j.dsr.2012.03.011.

Rimbu, N., Lohmann, G., Lorenz, S.J., Kim, J.H., Schneider, R.R., 2004. Holocene climate variability as derived from alkenone sea surface temperature and coupled ocean-atmosphere model experiments. Clim. Dyn. 23, 215–227. doi:10.1007/s00382-004-0435-8

Roberts, N., Moreno, A., Valero-Garcés, B.L., Corella, J.P., Jones, M., Allcock, S., Woodbridge, J., Morellón, M., Luterbacher, J., Xoplaki, E., Türkeş, M., 2012. Palaeolimnological evidence for an east–west climate see-saw in the Mediterranean since AD 900. Glob. Planet. Change 84–85, 23–34. doi:10.1016/j.gloplacha.2011.11.002

Rodríguez, S., Quero, X., Alastuey, A., Kallos, G., Kakaliagou, O., 2001. Saharan dust contributions to PM10 and TSP levels in Southern and Eastern Spain. Atmospheric Environment, 35, 2433-2447.

Rodrigo-Gámiz, M., Martínez-Ruiz, F., Chiaradia, M., Jiménez-Espejo, F.J., Ariztegui, D., 2015. Radiogenic isotopes for deciphering terrigenous input provenance in the western Mediterranean. Chem. Geol. 410, 237–250. doi:10.1016/j.chemgeo.2015.06.004

Rodrigo-gámiz, M., Martínez-Ruiz, F., Jiménez-Espejo, F.J., Gallego-Torres, D., Nieto-Moreno, V., Romero, O., Ariztegui, D., 2011. Impact of climate variability in the western Mediterranean during the last 20,000 years: oceanic and atmospheric responses. Quat. Sci. Rev. 30, 2018–2034. doi:10.1016/j.quascirev.2011.05.011

Rodrigo-Gámiz, M., Martínez-Ruíz, F., Rampen, S.W., Schouten, S., Sinninghe Damsté, J.S., 2014. Sea surface temperature variations in the western Mediterranean Sea over the last 20 kyr: A dual-organic proxy (UK′37 and LDI) approach. Paleoceanography 29, 87–98. doi:10.1002/2013PA002466.Received

Rogerson, M., Cacho, I., Jimenez-Espejo, J., Reguera, M.I., Sierro, F.J., Martinez-Ruiz, F., Frigola, J., Canals, M., 2008. A dynamic explanation for the origin of the western Mediterranean organic-rich layers. Geochemistry, Geophys. Geosystems 9. doi:10.1029/2007GC001936

Rohling, E.J., Abu-Zied, R.H., Casford, J.S.L., Hayes, A., Hoogakker, B., 2009. The marine environment: present and past, The physical geography of the Mediterranean. Oxford University Press, Oxford, 33–67.

Romaniello, S.J., Field, M.P., Smith, H.B., Gordon, G.W., Kim, M.H., Anbar, A.D., 2015. Fully automated chromatographic puri fi cation of Sr and Ca for isotopic analysis. J. Anal. At. Spectrom. 1906–1912. doi:10.1039/c5ja00205b

Rosenthal, Y., Boyle, E.A., Slowey, N., 1997. Temperature control on the incorporation of magnesium, strontium, fluorite and cadmium into benthic foraminiferal shells from Little Bahama Bank : Prospects for thermocline paleoceanography. Geochemica et Cosmochimica Acta, 61, 3633-3643.

Rossetti, F., Dini, A., Lucci, F., Bouybaouenne, M., Faccenna, C., 2013. Early Miocene strike-slip tectonics and granite emplacement in the Alboran Domain (Rif Chain, Morocco): significance for the geodynamic evolution of Western Mediterranean. Tectonophysics 608, 774–791. doi:10.1016/j.tecto.2013.08.002

ROTHWELL, G., & FRANK R. RACK. (2006). New techniques in sediment core analysis : an introduction. Geological Society, London, Special Publication, 267, 1–29.

Ruddiman, William, F., 2001. Earth's Climate: Past and Future. Freeman and Company, NY.

Russo, A., Sousa, P.M., Durão, R.M., Ramos, A.M., Salvador, P., Linares, C., Díaz, J., Trigo, R.M., 2020. Saharan dust intrusions in the Iberian Peninsula: Predominant synoptic conditions. Sci. Total Environ. 717, 137041. doi:10.1016/j.scitotenv.2020.137041

S., R., Querol, X., Alastuey, A., Kallos, G., Kakaliagou, O., 2010. Saharan dust contributions to PM10 and TSP levels in Southern and Eastern Spain. Atmos. Environ. 35.

Sabatier, P., Dezileau, L., Colin, C., Briqueu, L., Bouchette, F., Martinez, P., Siani, G., Raynal, O., Von Grafenstein, U., 2012. 7000 years of paleostorm activity in the NW Mediterranean Sea in response to Holocene climate events. Quat. Res. 77, 1–11. doi:10.1016/j.yqres.2011.09.002

Sánchez-Navas, A., García-Casco, A., & Martín-Algarra, A. (2014). Pre-Alpine discordant granitic dikes in the metamorphic core of the Betic Cordillera: Tectonic implications. Terra Nova, 26(6), 477-486.

Schepanski, K., Tegen, I., Macke, A., 2012. Comparison of satellite based observations of Saharan dust source areas. Remote Sens. Environ.123, 90–97. https://doi .org /10 .1016 /j .rse .2012 .03 .019.

Scheuvens, D., Schütz, L., Kandler, K., Ebert, M., Weinbruch, S., 2013. Bulk composition of northern African dust and its source sediments — A compilation. Earth-Science Rev. 116, 170–194. doi:10.1016/j.earscirev.2012.08.005

Schneider, R.R., Price, B., Miiller, P.. J., Kroon, D., Alexander, I., 1997. Monsoon related variations in Zaire (Congo) sediment load and influence of fluvial silicate supply on marine productivity in the east equatorial Atlantic during the last 200,000. Paleoceanography 12, 463–481.

Schiebel, R., & Hemleben, C. (2017). Planktic foraminifers in the modern ocean. Planktic Foraminifers in the Modern Ocean. https://doi.org/10.1007/978-3-662-50297-6

Shackleton, N.J., 1967. Oxygen isotope analyses and Pleistocene temperatures re-assessd. Nature, 215, 15-17.

Shackleton, N.J., 1974. Attainment of isotopic equilibrium between ocean water and the benthonic foraminifera genus Uvigerina: Isotopic changes in the ocean during the last glacial. Colloq. Int. du C.N.R.S 203–209.

Shaltout, M., Omstedt, A., 2014. Recent sea surface temperature trends and future scenarios for the Mediterranean Sea. Oceanologia 56, 411–443. doi:10.5697/oc.56-3.411

Shaman, J. and Tziperman, E., (2011). An atmospheric teleconnection linked ENSO and Southwestern European Precipitation. Journal of Climate, 24, 1, 124-239. https://doi.org/10.1175/2010JCLI3590.1

Shanahan, T.M., Mckay, N.P., Hughen, K.A., Overpeck, J.T., Otto-Bliesner, B., Heil, C. fford W., King, J., Scholz, C.A., Peck, J., 2015. The time-transgressive termination of the African Humid. Nat. Geosci. 8, 140–144. doi:10.1038/NGEO2329

Sicre, M.-A., Ternois, Y., Miquel, J.-C., Marty, J.-C., 1999. Alkenones in the Northwestern Mediterranean sea: interannual variability and vertical transfer. Geiohysical Res. Lett. 26, 1735–1738. doi:https://doi.org/10.1029/1999GL900353

Sierro, F.J., Hodell, D.A., Curtis, J.H., Flores, J.A., Reguera, I., Ba, M.A., Grimalt, J.O., Cacho, I., Colmenero-Hidalgo, E., Bárcena, M.A., Grimalt, J.O., Cacho, I., Frigola, J., Canals, M., 2005. Impact of iceberg melting on Mediterranean thermohaline circulation during Heinrich events. Paleoceanography 20, 1–13. doi:10.1029/2004PA001051

Smet, I., Muynck, D. De, Vanhaecke, F., Elburg, M., 2010. From volcanic rock powder to Sr and Pb isotope ratios: a fit-for-purpose procedure for multi-collector ICP-mass spectrometric analysis. J. Anal. At. Spectrom. 1025–1032. doi:10.1039/b926335g

Smith, A.C., Wynn, P.M., Barker, P.A., Leng, M.J., Noble, S.R., Tych, W., 2016. North Atlantic forcing of moisture delivery to Europe throughout the Holocene. Sci. Total Environ. 1–7. doi:10.1038/srep24745

Sutton, R.T., Hodson, D.L.R., 2005. Atlantic Ocean Forcing of North American and European Summer Climate. Science (80-.). 309, 115–119. doi:10.1126/science.1109496

Tanaka, T., Togashi, S., Kamioka, H., Amakawa, H., Kagami, H., Hamamoto, T., Yahara, M., Orihashi, Y., Yoneda, S., Shimizu, H., Kunimaru, T., Takahashi, K., Yanagi, T., Nokano, T., Fujimaki, H., Shinjo, R., Asahara, Y., Tanimizu, M., Dragusanu, C., 2000. JNdi-1: a neodymium isotopic reference in consistency with LaJolla neodymium. Chem. Geol. 279–281.

Taylor, A.K., Benedetti, M.M., Haws, J.A., Lane, C.S., 2018. Mid-Holocene Iberian hydroclimate variability and paleoenvironmental change : molecular and isotopic insights from Praia Rei Cortiço, Portugal. J. Quat. Sci. 33, 79–92. doi:10.1002/jqs.3000

Ternois, Y., Sicre, M.-A., Boireau, A., Contes, M.H., Eglinton, G., 1997. Evaluation of long-chain alkenones as paleo-temperature indicators in the Mediterranean Sea. Deep. Res. I 44, 271–286. doi:https://doi.org/10.1016/S0967-0637(97)89915-3

Taszarek, M., Allen, J. T., Marchio, M. & Brooks, H. E. (2021) Global climatology and trends in convective environments from ERA5 and rawinsonde data. NPJ Clim. Atmos. Sci. 4, 1–11 (2021).

Thornalley, D.J.R., Elderfield, H., McCave, I.N., 2009. Holocene oscillations in temperature and salinity of the surface subpolar North Atlantic. Nature 457, 711–714. doi:10.1038/nature07717

Timm, O., Köhler, P., Timmermann, A., Menviel, L., 2010. Mechanisms for the Onset of the African Humid Period and Sahara Greening 14.5–11 ka BP. J. Clim. 23, 2612–2633. doi:10.1175/2010JCLI3217.1

Tinner, W., van Leeuwen, J.F.N., Colombaroli, D., Vescovi, E., van der Knaap, W.O., Henne, P.D., Pasta, S., D'Angelo, S., La Mantia, T., 2009. Holocene environmental and climatic changes at Gorgo Basso, a coastal lake in southern Sicily, Italy. Quat. Sci. Rev. 28, 1498–1510. doi:10.1016/j.quascirev.2009.02.001

Tintore, J., La Violette, P.E., Blade, I., Cruzado, A., 1988. A study of an intense density front in eastern Alboran Sea: the Almeria-Oran Front. J. Phys. Oceanogr. 18, 1384–1397. doi:https://doi.org/10.1175/1520-0485(1988)018<1384:ASOAID>2.0.CO;2

Tjallingii, R., Röhl, U., Kölling, M., 2007. Influence of the water content on X-ray fluorescence core-scanning measurements in soft marine sediments. Geochemistry, Geophys. Geosystems 1–12. doi:10.1029/2006GC001393

Toney, J.L., García-Alix, A., Jiménez-Moreno, G., Anderson, R.S., Moossen, H., Seki, O., 2020. New insights into Holocene hydrology and temperature from lipid biomarkers in western Mediterranean alpine wetlands. Quat. Sci. Rev. 240. doi:10.1016/j.quascirev.2020.106395

Toucanne, S., Jouet, G., Ducassou, E., Bassetti, M., Dennielou, B., Morelle, C., Minto, A., Lahmi, M., Touyet, N., Charlier, K., Lericolais, G., Mulder, T., 2012. A 130,000-year record of Levantine Intermediate Water flow variability in the Corsica Trough, western Mediterranean Sea. Quat. Sci. Rev. 33, 55–73. doi:10.1016/j.quascirev.2011.11.020

Toyofuku, T., Kitazato, H., Kawahata, H., Tsuchiya, M., Nohara, M., 2000. Evaluation of Mg/Ca thermometry in foraminifera: Comparison of experimental results and measurements in nature. Paleoceaography, 15, 456-464.

Trigo, R.M., Osborn, T.J., Corte-Real, J.M., 2002. The North Atlantic Oscillation influence on Europe: climate impacts and associated physical mechanisms. Clim. Res. 20, 9–17. doi:10.3354/cr020009

Turato, B., Reale, O., Siccardi, F., (2004). Water vapor source of the October 2000 Piedmont Flood. Journal of Hydrometeorology, 5, 4, 693-712. https://doi.org/10.1175/1525-7541(2004)005<0693:WVSOTO>2.0.CO;2

Tzedakis, P.C., 2007. Seven ambiguities in the Mediterranean palaeoenvironmental narrative. Quat. Sci. Rev. 26, 2042–2066. doi:10.1016/j.quascirev.2007.03.014

Tzedakis, P.C., Raynaud, D., Mcmanus, J.F., Berger, A., Brovkin, V., Kiefer, T., 2009. Interglacial diversity. Nat. Geosci. 2, 751–755. doi:10.1038/ngeo660

Urey, H.C., 1947. The thermodynamics of isotopic substances, Journal of the Chemical Society of London, 562-581.

van Aken, H. M., Femke de Jong, M., Yashayaev, I., (2011). Decadal and multi-decadal variability of Labradors Sea Water in the north-western North Atlantic Ocean derived from tracer distributions: Heat budget, ventilation, and advection. Deep Sea Research Part I: Oceanographic Research Papers. 58, 5, 505-523

Van Hinsbergen, D.J.J. Van, Buiter, S.J.H., Torsvik, Trond, H., Gaina, C., Webb, S.J., 2011. The formation and evolution of Africa from the Archaean to Present : introduction The formation and evolution of Africa from the Archaean to Present : introduction. Geolo 357, 1–8. doi:10.1144/SP357.1

Varas-Reus, M.I., Garrido, C.J., Marchesi, C., Bosch, D., Acosta-Vigil, A., Hidas, K., Barich, A., Booth-Rea, G., 2017. Sr-Nd-Pb isotopic systematics of crustal rocks from the western Betics (S . Spain): Implications for crustal recycling in the lithospheric mantle beneath the westernmost Mediterranean. Lithos 276, 45–61. doi:10.1016/j.lithos.2016.10.003

Velasco, J.P.B., Baraza, J., Canals, M., Balón, J., 1996. La depresión periférica y el lomo contourítico de Menorca: evidencias de la actividad de corrientes de fondo al N del Talud Balear. Geogaceta 20.

Versteegh, G.J.M., de Leeuw, J.W., Taricco, C., Romero, A., 2007. Temperature and productivity influences on Uk'37 and their possible relation to solar forcing of the Mediterranean winter. Geochemistry, Geophys. Geosystems 8, 1–14. doi:10.1029/2006GC001543

Volkman, J.K., Eglinton, G., Corner, E.D.S., Sargent, J.R., 1980. Novel unsaturated straight-chain C37-C39 methyl and ethyl ketones in marine sediments and coccolithophore Emiliania huxleyi. Phys. Chem. Earth 12, 219–227. doi:https://doi.org/10.1016/0079-1946(79)90106-X

Volkov, D.L., Baringer, M., Smeed, D., Johns, W., Landerer, F.W., 2019. Teleconnection between the Atlantic Meridional Overturning Circulation and Sea Level in the Mediterranean Sea. J. Clim. 935–955. doi:10.1175/JCLI-D-18-0474.1

Wagner, B., Vogel, H., Francke, A., Friedrich, T., Donders, T., Lacey, J.H., Leng, M.J., Regattieri, E., Sadori, L., Wilke, T., Zanchetta, G., Albrecht, C., Bertini, A., Combourieu-Nebout, N., Cvetkoska, A., Giaccio, B., Grazhdani, A., Huaeffe, T., Holtvoeth, J., Joannin, S., Jovanovska, E., Just, J., Kouli, K., Kousis, I., Koutsodendris, A., Krastel, S., Logos, M., Leicher, N., Levkov, Z., Lindhorst, K., Masi, A., Melles, M., Mercuri, A.M., Nomade, S., Nowaczyk, N., Panagiotopoulos, K., Peyron, O., Reed, J.M., Sagnotti, L., Sinopoli, G., Stelbrink, B., Sulpizio, R., Timmermann, A., Tofilovska, S., Torri, P., Wagner-Cremer, F., Wonik, T., Zhang, X., 2019. Mediterranean winter rainfall in phase with African monsoons during the past 1.36 million years. Nature 573. doi:10.1038/s41586-019-1529-0

Wanner, H., Beer, J., Bütikofer, J., Crowley, T.J., Cubasch, U., Flückiger, J., Goosse, H., Grosjean, M., Joos, F., Kaplan, J.O., Küttel, M., Müller, S.A., Prentice, I.C., Solomina, O., Stocker, T.F., Tarasov, P., Wagner, M., Widmann, M., 2008. Mid- to Late Holocene climate change : an overview. Quat. Sci. Rev. 27, 1791–1828. doi:10.1016/j.quascirev.2008.06.013

Weijer, W., Haine, T., Siddiqui, A., Cheng, W., Veneziani, C., Kurtakoti, P.K., 2022. Interactions between the Artic Mediterranean and the Atlantic Meridional Overturning Circulation: A Review. Oceanography Special Is. doi:https://doi.org/10.5670/oceanog.2022.130

Weis, D., Kieffer, B., Maerschalk, C., Barling, J., Williams, G.A., Hanano, D., Pretorius, W., Mattielli, N., Mahoney, J.B., 2006. High-precision isotopic characterization of USGS reference materials by TIMS and MC-ICP-MS. Geochemistry, Geophys. Geosystems 7. doi:10.1029/2006GC001283

Weldeab, S., Emeis, K-C., Hemleben, C., Siebel., W. (2002). Provenance of lithogenic surface sediments and pathways of riverines suspended matter in the Eastern Mediterranean Sea: evidence from $^{143}Nd/^{144}Nd$ and $^{87}Sr/^{86}Sr$ ratios. Chemical Geology, 186, 1-2, 139-149. https://doi.org/10.1016/S0009-2541(01)00415-6

Weldeab, S., Emeis, K-C., Hemleben, C., Vennemann, T.W., Schulz, H., (2002). Sr and Nd isotopes composition of Late Pleistocene sapropels and nansapropelic sediments from the Eastern Mediterraenan Sea: implications for detrital influx and cimatic conditions in source areas. Geochemica et Cosmochimica Acta, 66, 20, 3585-3598. https://doi.org/10.1016/S0016-7037(02)00954-7

Weldeab S., Siebel, W., Wehausen, R., Emeis, K-C., Schmiedl, G., Hemleben, C. (2003). Late Pleistocene sedimentation in the Western Mediterranean Sea: implications for productivity changes and climatic conditions in the catchment areas. Pelaeogeography, paleoclimatology, palaeoecology, 190, 121-137.

Wilson, S.A. (1997). Basalt, Columbia River, BCR-2. Preliminary - U.S. Geological Survey Certificate of Analisis.

Winschall, A., Sodemann, H., Pfahl, S., & Wernli, H. (2014). How important is intensified evaporation for Mediterranean precipitation extremes? Journal of Geophysical Research: Atmospheres, 119(9), 5240-5256

Wombacher, F., Rehka, M., No, C., Zu, C.-, 2003. Investigation of the mass discrimination of multiple collector ICP- MS using neodymium isotopes and the generalised power law. J. Anal. At. Spectrom. 18, 1371–1375. doi:10.1039/b308403e

Wu, J., Böning, P., Pahnke, K., Tachikawa, K., & de Lange, G. J. (2016). Unraveling North-African riverine and eolian contributions to central Mediterranean sediments during Holocene sapropel S1 formation. Quaternary Science Reviews, 152, 31–48. https://doi.org/10.1016/j.quascirev.2016.09.029

Yang, R., Li, T., Stubbs, D., Chen, T., Liu, S., Kemp, D.B., Li, W., Yang, S., Chen, Jianfang, Elliott, T., Dellwig, O., Chen, Jun, Li, G., 2022. Stable tungsten isotope systematics on the Earth's surface. Geochim. Cosmochim. Acta. doi:10.1016/j.gca.2022.01.006

Yashayaev, I. (2007). Hydrographic changes in the Labrador Sea, 1960-2005. Progress in Oceanography, 73(3–4), 242–276. https://doi.org/10.1016/j.pocean.2007.04.015

Yokoyama, T., Makishima, A., Nakamura, E., 1999. Evaluation of the coprecipitation of incompatible trace elements with fluoride during silicate rock dissolution by acid digestion. Chem. Geol. 175–187.

Zhai, X., Johnson, H. L., Marshall, D., (2014). A simpli model of the response of the Atlantic to the North Atlantic Oscillation. Journal of Climate, 27, 11. https://doi.org/10.1175/JCLI-D-13-00330.1

Zhang, W., Hu, Z., Liu, Y., Chen, H., Gao, S., Gaschnig, R.M., 2012. Total Rock Dissolution Using Ammonium Bi fl uoride NH4HF2) in Screw-Top Te fl on Vials: A New Development in Open-Vessel Digestion. Anal. Chemestry 84, 10686–10693. doi:10.1021/ac302327g

Zielhofer, C., Fletcher, W.J., Mischke, S., De Batist, M., Campbell, J.F.E., Joannin, S., Tjallingii, R., El Hamouti, N., Junginger, A., Stele, A., Bussmann, J., Schneider, B., Lauer, T., Spitzer, K., Strupler, M., Brachert, T., Mikdad, A., 2017. Atlantic forcing ofWestern Mediterranean winter rain minima during the last 12,000 years Christoph. Quat. Sci. Rev. 157, 29–51. doi:10.1016/j.quascirev.2016.11.037

Zimmermann, T., Retzmann, A., Schober, M., Pröfrock, D., Prohaska, T., Irrgeher, J., 2019. Matrix separation of Sr and Pb for isotopic ratio analysis of Ca-rich samples via an automated simultaneous separation procedure. Spectrochim. Acta Part B 151, 54–64. doi:10.1016/j.sab.2018.11.009

Annexes

ANNEXE 1: Foraminifera Mg/Ca cleaning procedure

Necessary material:

- Micropipette (100-1000 µl)
- Micropipette (10-100 µl)
- Pipette tips (100 – 1000 µl)
- Pipette tips (50- 1000 µl)

Chemical reagents

- Citric acid + NH_3
- 0.1 M NaOH
- 0.001 M HNO_3

Procedure

Remember to prepare routinely a procedure blank

Clay Removal

1. Clean the work space before start.
2. Clean the micropipette (10-100 µl).
3. Add 20-30µl of MilliQ water with the micropipette to the eppendorf vials containing sample already crashed.
4. Sonicate briefly (20-30s) in the ultrasounds bath.
5. Add 300-400µl of MilliQ water with the water dispenser. Each vial must be treated individually at this stage (slightly bang the vial with the spatula).
6. Allow sample to settle (30s) and remove the overlying solution with the 1000µl-pipette at 650 µl. Leave about 20-30µl of MilliQ water in the vials.
7. Clean the pipette between samples (2x HNO3 + 3x MilliQ water).
8. Repeat steps 4-7 two more times. Clay rich samples should be repeated as many times as necessary
9. Add few drops of Methanol (200 µl) into each vial.
10. Sonicate briefly (20-30s) in the ultrasounds bath.
11. Allow sample to settle for a few seconds, slightly tap the vial with the spatula in order to remove bubbles)
12. Remove the supernatant solution with the 1000µl-pipette at 650 µl.
13. Repeat steps 9-12 one more time.
14. Fill the Eppendorf with MilliQ water.
15. Allow sample to settle for a few seconds and remove the supernatant solution with a 1000µl- pipette at 650 µl.

Reductive cleaning

This is the more time-consuming step of the whole procedure. Safety glasses, lab coats must be worn all the time at this step. Work ALWAYS ***UNDER THE GAS HOODS.***

The ultrasonic bath must be heated (over 90ºC) before starting with this step (about 2 hours).

Turn on the heater for the MilliQ water used in step 6 (about 15 min).

1. Prepare a mixture of 500µl of hydrazine hydroxide and 2000µl of the Citric acid + NH_3 (stored in the special hydroxide container)
2. Add 100µl of the final mixture to each vial and secure caps in order to prevent sample to pop up while reacting.
3. Place the sample rack into the thermal ultrasonic bath for 30 minutes (bath has to be at 90ºC), sonicating briefly (5-10s) every 2 minutes (Use the timer and prepare a table to mark each sonication step).
4. Immediately after the bath, place again the sample rack into the gas hood and CAREFULLY open vials (at this stage, some vials could tend to pop up) and squirt MilliQ water into the vials (including lids) as soon as possible in order to slow down the reaction.
5. Tap the vials with the spatula in order to remove bubbles and remove the overlying solution with the 1000µl-pipette at 650 µl.
6. Repeat steps 4-5 two more times.
7. Add 400µl of MilliQ water (aprox 80ºC) into the vials and wait for 5 minutes.
8. Remove the overlying solution with the 1000µl-pipette at 650 µl (after light tapping to remove bubbles)
9. Repeat steps 7-8 one more time.
10. Squirt cold MilliQ water into the vials.
11. Remove the overlying solution with a 1000µl-pipette at 650 µl (after light tapping to remove bubbles).

It is VERY IMPORTANT to remove any reagent that could remain into the samples to prevent further dissolution.

Switch off the temperature control in the ultrasonic bath

Oxidative cleaning

Heat the water bath before starting this step (about 1 hour).

1. Prepare the Alkali buffered 1% H_2O_2 solution: Add 100 µl of Hydrogen peroxide (stored in the fridge) to 10 ml 0.1M NaOH.
2. Add 250µl of alkali buffered 1% H_2O_2 to each vial and secure the caps of the vials to prevent popping open.
3. Place the rack of samples into the hot bath for 5 minutes. At 2.5 minutes remove the rack momentarily and rap on the bench top in order to remove the bubbles.
4. After the 5 minutes, remove the rack and rap again on the bench top, and then place it into the ultrasonic bath, sonicating briefly (10-15s).
5. Repeat steps 3-4 one more time.
6. Immediately after fill vials with MilliQ water in order to slow down the reaction. Add water also to the vials caps.
7. Remove the overlying water with a 1000µl-pipette at 650 µl. At this step foraminifera fragments tend to be attached to the vial walls, shake vials to let fragments to settle down (sample lost can be critical at this step).
8. Repeat steps 6-7 two more times.

Weak acid leaching

1. Add 250µl of 0.001M HNO_3 to each sample.
2. Ultrasonicate samples for 30s.
3. Add MilliQ water into each sample in order to slow down reaction.
4. Tap the vials with the spatula in order to remove bubbles and remove the overlying water with a 1000µl-pipette at 650 µl .
8. Repeat steps 3-4 one more times.
9. Pipette out water as much as possible with a 10-100µl micropipette

Reagents preparation

Reductive reagent (Citric acid+NH_4)

Work under the gas hood

1. Weight 5,25g of Citric Acid in a precipitates glass
2. Add 100 ml of NH_4 (30%)
3. Place precipitates glass in a hot plate (40-50ºC) with a magnetic spinner to promote mixing.
4. Transfer to a pre-cleaned plastic bottle and store in the fridge

Oxidizing reagent (to remove organic matter)

1. Hydrogen peroxide 30% w/v. (stored in fridge).
2. 0.1M sodium hydroxide (Aristar grade) in MilliQ water

0.1M NaOH = 4g / litre. (NaOH = 40.00g g mol^{-1})

Weak acid leach

0.001 M HNO_3

- 0.5 litre bottle: 34.7µl HNO_3 (65%) + MilliQ water
- 1 litre bottle: 69.4 µl HNO_3 (65%) + MilliQ water

ANNEXE 2: Foraminifera Mg/Ca dissolution procedure

Necessary material:

- Micropipette (100-1000 µl)
- Micropipette (10-100 µl)
- Pipette tips (100 – 1000 µl)
- Pipette tips (50- 1000 µl)

Chemical reagents

- 1% ultrapure HNO3

Procedure

Dissolution

Dissolution should be done the day before of measurements with the ICP-MS

Make sure that you already have a list with the sample code and dissolution order.

1. Add 400µl of 1% HNO_3 (ultrapure) to each sample (make it in groups of 6).
2. Individually place samples into the ultrasonic bath (about 15 seg) to promote dissolution.
3. Be sure that all the samples are correctly dissolved. Repeat the step 2 as times as necessary
4. Shake the vials to homogenize solution.
5. Place samples (groups of 6) into the micro centrifuge device, place them in the rotor symmetrically. Centrifuge samples for 5 minutes at 6000 rpm.
6. Transfer **370**µl of sample into clean eppendorf using a clean tip.
7. Transfer an aliquot into other vial.

Reagents preparation

1% ultrapure HNO_3 Aristar grade

- 1/5 dilution from 5% ultrapure HNO_3 Aristar grade with MilliQ water

ANNEXE 3: Foraminifera isotopes cleaning procedure

Necessary material:

- Micropipette (100-1000 µl)
- Pipette tips (100 – 1000 µl)
- Vial rack
- Ultrasonic bath

Chemical reagents

- Methanol

Procedure

1. Introduce samples for isotopic measurements into clean vials.
2. Add few drops of methanol to the vials containing the samples.
3. Place the vial rack in the ultrasonic bath during 30seconds.
4. Remove the excess of methanol with the pipette leaving a small drop at the bottom.
5. Dry the samples under the laminar flux fume hood at the cleaning laboratory.
6. Once samples are dry putt caps and store it until the analysis in the mass spectrometer.

ANNEXE 4: Marine sediment leaching Procedure

The following procedure is necessary to remove the organic matter, biogenic carbonate and authigenic precipitates in marine clays, as well as the Fe-Mn oxides. Three steps are outlined: organic matter elimination with oxygen peroxide, carbonate leaching with buffered acetic acid, and reductive leaching of Fe-Mn oxides with hydroxylamine hydrochloride (HH).
This procedure is adapted from Chester and Hughes, Chemical Geology, 2, 249-262, 1967.

Preparing leaching solutions

For organic matter elimination

Depending on the samples nature can be used oxygen peroxide (H_2O_2) at 10% or/and at 30%

For 1L of H_2O_2 at 10%

a) Begin with 834mL of UP-Water
b) Add 166mL of H_2O_2 at 30%

For biogenic carbonate elimination

During this step is needed glacial acetic acid (CH_3COOH), sodium acetate (CH_3COONa) and sodium hydroxide (NaOH).

For 1L of buffered Acetic Acid

a) Begin with 500mL of UP-Water
b) Dissolve 28g of NaAC in to the 500mL UP-Water.
c) Add 27mL of glacial AC
d) Fill the solution up to 1L.

pH should be around 4. If the pH is under 4 add a few pellets of NaOH until pH 4.

For Fe-Mn oxides elimination

During this step is needed: hydroxylamine hydrochloride (HH), glacial acetic acid (CH_3COOH), Na-EDTA (Ethylenediaminetetraacetic acid trisodium salt hydrate), sodium hydroxide (NaOH).

For 2L of 0.05M HH – 15% Acetc Acid – 0.03M Na—EDTA buffered at pH=4 with NaOH.

a) Begin with 250mL of UP-Water.
b) Dissolve 6.95g of HH in to the 250mL of UP-Water.
c) In a graduated test tub add 300mL of glacial AC and fill up to 1L
d) Mix in to the final bottle the 250mL of HH with 1L AC (V_f=1250ml)
e) In the empty HH beaker ad 500ml of UP-Water
f) Dissolve 22.33g of Na-EDTA in to the 500mL of UP-Water
g) Mix the 500mL of Na-EDTA to the final bottle (V_f=1750ml)
h) Fill up the final bottle up to 2000mL.

Leave the final solution around 8 hours. After this time fill up until 2000mL if it is necessary and control the pH which should be around 4. If pH is under this value, add a few pellets of NaOH until pH 4.

Leaching Procedure

Sample Preparing

a) Around 100mg of dry sediment samples is taken and grinded to obtain a very fine dust.
b) Sample is placed in a 50mL conic centrifuge tube.

1st Step - Organic Matter Elimination

Different percentages of H_2O_2 can be used depending on the total organic matter in the samples.

a) Add 35mL of H_2O_2 at 30% in the conic centrifuge tube
b) Disaggregate the sample by using the vortex mixer until all the sediment is resuspended.
c) Gentle unscrew the cap in order to liberate the gas from reaction.
d) Shake the samples for ~8 hours
e) Heat the samples at 60°C overnight.
f) Shake the samples for ~8 hours
g) Heat the samples at 60°C overnight.

Rinse to eliminate the H_2O_2 residue

h) Fill the conic centrifuge tube with the sample inside up to 50mL with UP-Water.
i) Disaggregate and mix the sample by using the vortex mixer until all the sediment is resuspended.
j) Centrifuge the samples during 15 min at 5000 rpm.
k) Remove the supernatant.

Repeat from a) to k) two times more.

After the third repetition repeat the rinse step from h) to k) two times more in order to assure that all possible H_2O_2 residue is removed.

2nd Step – Biogenic Carbonate Elimination

For this step is used the buffered acid acetic

Short buffered acid acetic attack

a) Add 35mL of buffered acid acetic in the conic centrifuge tube
b) Disaggregate the sample by using the vortex mixer until all the sediment is resuspended.
c) Gentle unscrew the cap in order to liberate the gas from reaction.
d) Shake the samples for ~6 hours

Rinse to eliminate the buffered acid acetic residue

e) Fill the conic centrifuge tube with the sample inside up to 50mL with UP-Water.
f) Disaggregate and mix the sample by using the vortex mixer until all the sediment is resuspended.
g) Centrifuge the samples during 30 min at 2500 rpm.
h) Remove the supernatant.

Long buffered acid acetic attack

i) Add 35mL of buffered acid acetic in the conic centrifuge tube
j) Disaggregate the sample by using the vortex mixer until all the sediment is resuspended.
k) Gentle unscrew the cap in order to liberate the gas from reaction.

l) Shake the samples overnight

Rinse to eliminate the buffered acid acetic residue

m) Fill the conic centrifuge tube with the sample inside up to 50mL with UP-Water.
n) Disaggregate and mix the sample by using the vortex mixer until all the sediment is resuspended.
o) Centrifuge the samples during 30 min at 2500 rpm.
p) Remove the supernatant.

Repeat the long buffered acid acetic attack one more time, from i) to p).

After the second long buffered acid acetic attack repeat the rinse step, from m) to p) two times more in order to assure that all possible buffered acid acetic residue is removed.

Leaches can be repeated until all carbonate is removed, signs of which include:

- *Colour of samples are uniform and dark-medium brown.*
- *There is no CO_2 gas pressure build-up during leaching.*
- *No bubbles appears when the centrifuge tube is opened*

During the washing steps, centrifuging is done low speeds for 30 minutes due to high or medium centrifuge speeds create sediment clumping which are nearly impossible to disaggregate.

The leach takes on a yellowish or light brown coloration when all acetic acid with dissolved carbonate is removed. This is because all charged species from the acetic acid and dissolved carbonate have been removed and the solution is pure water. The lack of ionic charge allows colloids to become suspended in the solution. When this coloration appears, attempt to remove coloration by centrifuging for long durations (>1 hour), or by adding a few drops of clean buffered acetic acid solution and centrifuging.

3rd Step – Fe-Mn oxides elimination

For this step is used the HH solution

Short HH solution attack

a) Add 15mL of the HH solution in the conic centrifuge tube
b) Disaggregate the sample by using the vortex mixer until all the sediment is resuspended.
c) Shake the samples for ~4 hours

Rinse to eliminate the HH solution

d) Fill the conic centrifuge tube with the sample inside up to 30mL with UP-Water.
e) Disaggregate and mix the sample by using the vortex mixer until all the sediment is resuspended.
f) Centrifuge the samples during 30 min at 2500 rpm.
g) Remove the supernatant.

Long HH solution attack

a) Add 15mL of the HH solution in the conic centrifuge tube
b) Disaggregate the sample by using the vortex mixer until all the sediment is resuspended.
c) Shake the samples overnight

Rinse to eliminate the HH solution

d) Fill the conic centrifuge tube with the sample inside up to 50mL with UP-Water.

e) Disaggregate and mix the sample by using the vortex mixer until all the sediment is resuspended.
f) Centrifuge the samples during 30 min at 2500 rpm.
g) Remove the supernatant.

After the long HH solution attack repeat the rinse step, from d) to g) two times more in order to assure that all possible HH solution residue is removed.

Prior-preparation for digestion

a) Add 5mL of UP-Water in each sample.
b) Disaggregate and mix the sample by using the vortex mixer until all the sediment is resuspended.
c) Next step is going to be performed in to the Clean Lab.

ANNEXE 5: Digestion for the detrital fraction and sample preparation

This digestion procedure has been adapted from adapted from Yang *et al.*, 2022. Last modification was on May 2022.

IMPORTANT NOTES: It is recommended to do not digest more than 12 samples at the same time, including blanks and BCR-2. All material must to be cleaned, even pipette tips.

Sample Preparation before digestion

a) Label both caps and walls each Teflon vial with the name of the sample.
b) Once labeled, weight each Teflon vial and note down the weights.
c) Take each sample from the centrifuge tub and agitate on the vortex until al sediment is resuspended
d) Transfer the 5mL sample from the conic centrifuge tub to each Teflon vial.
e) Add 5mL of UP-Water to the conic centrifuge tub and agitated in order to remove any possible sample residue.
f) Transfer this 5mL UP-water from each sample to each Teflon vial.
g) Evaporated the samples at 60°C until complete dryness (but not burn)
h) Once each Teflon Vial is cold, weight the samples.

BCR-2 Preparation before the digestion

a) Add and label a Teflon vial for the certificate standard reference material (BCR-2).
b) Weigh the empty Teflon vial.
c) Transfer around 50mg of BCR-2 powder to the Teflon Vial.

   Note: 50mg of BCR-2 can be used for 3-4 batch of chromatography separations.

d) Weight the BCR-2 sample.

Digestion Procedure (2:2:1)

For the steps a) to i) you must always need be accompanied with another person due to control possible splits of the HF acid. Be really carefully to manipulate the HF acid. Before to manipulate the HF prepare the acid neutralizer kit in an accessible location in the lab. If you need to transfer the HF acid from the bottle to the HF dispenser use the specific HF Personal Protective Equipment (PPE).

For this digestion procedure, HNO_3 and HCl acids are double-distilled.

1st step – 2:2:1 Acid Mixture

a) Prepare the material. Dispenser Teflon vials for HCl, HNO_3 and HF.
b) Make batches of three samples and open each samples from one batch. When open the samples leave the cap on the sample.
c) Add 2mL of HNO_3 in each batch.

Lift the cap for the first Teflon vial with the sample from the batch, add the 2mL of HNO_3 and then put the cap on the sample. Repeat the same scheme for the three samples of the batch. Once the three samples are with the acid, close each sample and start with the next batch.

d) Prepare two pipettes (1mL volume). One for the HCl and the other for the HF.
e) Open the samples from one batch and leave the cap on the sample.
f) Open the HCl Teflon dispenser.
g) Add 2mL of HCl in the three samples of one batch. Leave each cap on the sample without closing.
h) Immediately, in the same batch add 1mL of HF. Once the acid HF is added in one batch, throw the HF pipette tip into the tip container.
i) Close strongly the three samples of the batch.
j) Repeat form e) to i) for each batch of three samples.

k) Once all samples are with the 2:2:1 acid proportion, gently move in circles the sample in order to mix the acids and the sample.
l) Heat the samples at 120°C during 48h.

2nd Step – Aqua Regia and evaporation

a) After 48h, cold down the samples.
b) Move the sample in order to remove the small drops emplaced on the caps.

Be careful during the following steps. Inside each sample three is HF.

c) Open the samples in batches of three.
d) Add 3mL of HCl and 1mL of HNO_3
e) Close the samples from each batch
f) Repeat from c) to e) for each batch of three samples.
g) Gently move in circles the sample in order to mix the acids.

h) Open the samples and put them on the evaporator.
i) Evaporate the samples at 100°C during 2h and then rise the temperature at 120°C until samples forms a dens-pearl texture.

Do not burn the samples. Approximately at 120°C samples are dried after 3-4h. Each sample will get the texture at different times. Then, you should control each samples to do not burn them.

3rd Step – Aqua Regia and evaporation

a) Cold down the samples.
b) Add 3mL of HCl and 1mL of HNO_3 acid in each samples in batches of three.
c) Close the sample strongly.
d) Gently move in circles the sample in order to mix the acids and secure to dissolve the dens-pearl.
e) Heat the samples at 120°C during 1h.

f) After 1h, cold down the samples.
g) Move the sample in order to remove the small drops emplaced on the caps.

Observe the sample. If residues are observed in the samples, repeat the 3rd Step as much times needed (From a to f). If any residue is observed continue with the procedure.

h) Open the samples and put them on the evaporator.
i) Evaporate the samples at 100°C during 1h and then rise the temperature at 120°C until samples forms a dens-pearl texture.

Do not burn the samples. Approximately at 120°C samples are dried after 2-3h. Each sample will get the texture at different times. Then, you should control each samples to do not burn them.

4th Step – Chloride displacement

a) Cold down the samples.
b) Add 1mL of HNO_3 in each sample in batches of three.
c) Close the samples from each batch.
d) Gently move in circles the sample in order to dissolve the dens-pearl.
e) Heat the samples at 120°C during 1h.

f) After 1h, cold down the samples.
g) Move the sample in order to remove the small drops emplaced on the caps.
h) Open the samples and put them on the evaporator.
i) Evaporate the samples at 90°C during 1-2h until forms a dens-pearl texture.

Do not burn the samples. Each sample will get the texture at different times. Then, you should control each samples to do not burn them.

5th Step – Sample re-dissolution in 1M

a) Cold down the samples.
b) Add 2mL of 1M of HNO_3 in each sample in batches of three.
c) Close the samples from each batch.
d) Gently move in circles the sample in order to dissolve the dens-pearl.
e) Heat the samples at 120°C during 1h.
f) Storage the samples in the Teflon vials until the ICP-MS analysis.

Sample preparation before chromatography extraction with DGA

Before starting, prepare two pair of cleaned Eppendorf, one to transfer the sample and another for the aliquots.

Aliquots preparation

a) Transfer the samples from the Teflon vials to the labeled 2mL Eppendorf.
b) Centrifuge the samples during 5 minutes.

   Observe the samples if residues appears on the bottom of the Eppendorf.

c) Transfer 20µL of each sample to the aliquot Eppendorf.
d) Add 990µL of 2% HNO_3 to the aliquots.
e) Agitate the aliquots in order to mix the samples.
f) Annalise the aliquots in the ICP-MS.

Sample dilutions

a) Calculate the concentrations of Rb, Sr, Nd, Pb, Tl, Sm and Ca from your samples
b) Find the sample with low Pb concentration. This sample is your limiting sample.
c) For the limiting sample, calculate the dilution to obtain a final solution of 1mL at 40ppb of Pb.
d) Apply this dilution for all the sample of the digestion batch, including blanks and BCR-2.

ANNEXE 6: DGA Elution Profile for sediment samples

This elution profile is performed to be used in 2ml-bed volume column in the controlled-pressured vacuum system. This elution has been adapted from Retmann *et al.,* 2017. Last modification was on March 2022.

Cartridge cleaning and conditioning
1 - Add 10mL MQ water
2 - Add 5mL 5N HNO_3 (Pb cleaning)
3 - Add 10mL 1N HNO_3 (cartridge conditioning)

Sample loading and rubidium rinsing
4 – Load sample in 0.5mL 1N HNO_3
5 – Add 8mL 1N HNO_3

Strontium pick up
6 – Add 8mL 0.2N HNO_3

Lead pick up
7 – Add 8mL 5N HNO_3

Ca and Ce rinsing
8 – Add 35mL 0.1N HNO_3
9 – Add 2mL 2N HCl

Neodymium pick up
10 – Add 12mL 1.5N HCl

Samarium and cleaning cartridge
11 – Add 20mL 0.1N HCl
12 – Add 10mL 5N HNO_3
13 – Add 10mL MQ water

ANNEXE 7: Sr-Spec Elution Profile for sediment samples after DGA

This elution profile is performed to be used in 1ml-bed volume column in the controlled-pressured vacuum system. Last modification was on march 2022.

Sample acidification from Sr-DGA elution to Sr-Spec
0 – Add 2.76mL $HNO_{3\ (DD)}$ concentrate to the Sr-Sample eluted in DGA

Cartridge cleaning and conditioning
1 - Add 20mL MQ water (Sr cleaning)
2 - Add 10mL 4N HNO_3 (cartridge conditioning)

Sample loading and rubidium rinsing
3 – Load sample in 10.76mL 4N HNO_3
4 – Add 5mL 4N HNO_3

Strontium pick up
5 – Add 10mL MQ water

Cleaning cartridge
6 – Add 10mL MQ Water
7 – Add 10mL 6N HCl
8 – Add 10mL MQ Water
9 – Add 5mL 6N HCl
10 – Add 5mL MQ Water

Clim. Past, 15, 927–942, 2019
https://doi.org/10.5194/cp-15-927-2019

Climate of the Past
Open Access
EGU

Holocene hydrography evolution in the Alboran Sea: a multi-record and multi-proxy comparison

Albert Català[1], Isabel Cacho[1], Jaime Frigola[1], Leopoldo D. Pena[1], and Fabrizio Lirer[2]

[1]Grup de Recerca Consolidat en Geociències Marines, Departament de Dinàmica de la Terra i de l'Oceà, Universitat de Barcelona (UB), Barcelona, Spain
[2]Istituto di Scienze Marine (ISMAR)-CNR, Sede di Napoli, Naples, Italy

Correspondence: Albert Català (al_catala@ub.edu)

Received: 26 November 2018 – Discussion started: 29 November 2018
Accepted: 26 April 2019 – Published: 23 May 2019

Abstract. A new high-resolution deglacial and Holocene sea surface temperature (SST) reconstruction is presented for the Alboran Sea (western Mediterranean), based on Mg/Ca ratios measured in the planktonic foraminifera *Globigerina bulloides*. This new record is evaluated by comparison with other Mg/Ca SST records and previously published alkenone SST reconstructions from the same region for both the Holocene and glacial periods. In all cases there is a high degree of coherence between the different Mg/Ca SST records but strong discrepancies when compared to the alkenone SST records. We argue that these discrepancies are due to differences in the proxy response during deglaciation which we hypothesize to reflect a resilience strategy of *G. bulloides,* changing its main growth season, and consequently Mg/Ca records a shorter deglacial warming than alkenones. In contrast, short-term Holocene SST variability is larger in the Mg/Ca SST than in the alkenone SST records. We propose that the larger Mg/Ca SST variability is a result of spring temperatures variability, while the smoothed alkenone SST variability represents averaged annual temperatures. The Mg/Ca SST record differentiates the Holocene into three periods: (1) the warmest SST values occurred during the Early Holocene (11.7–9 cal. kyr BP), (2) a continuous cooling trend occurred during the Middle Holocene that culminated in the coldest Holocene SST having a double cold peak structure centred at around 4.2 cal. kyr BP, and (3) the Late Holocene (4.2 cal. kyr BP to present) did not follow any clear cooling/warming trend although millennial-scale oscillations were enhanced. This SST evolution is discussed in the context of the changing properties in the Atlantic inflow water associated with North Atlantic circulation conditions and also with local hydrographical and atmospheric changes. We propose that a tight link between North Atlantic circulation patterns and the inflow of surface waters into the Mediterranean played a major role in controlling Holocene climatic variability of this region.

1 Introduction

Overall, Holocene climate evolution (11.7 cal. kyr BP to present) is considered more stable than during the previous glacial period (115–17.7 cal. kyr BP; Bond et al., 1997; Cacho et al., 1999; Martrat et al., 2014). However, there is an increasing number of worldwide distributed Holocene climate records that reveal significant changes in both the long-term patterns pathed by orbital forcing (e.g. Marchal et al., 2002; Lorenz and Lohmann, 2004; Tzedakis, 2007; Wanner et al., 2008; Tinner et al., 2009; Bartlein et al., 2011) and millennial- and centennial-scale variability (e.g. Bond et al., 1997, 2001; Andrews et al., 2003; Marchitto and deMenocal, 2003; Moros et al., 2004; Debret et al., 2007, 2009; Thornalley et al., 2009; Giraudeau et al., 2010; Nieto-Moreno et al., 2011). In an oceanic context, and particularly for the North Atlantic, there is solid evidence for Holocene changes in several oceanographic parameters linked to Atlantic Meridional Overturning Circulation (AMOC), such as heat exchange within the subpolar gyre (SPG) and the subtropical gyre (STG) (Bond et al., 1997, 2001; Thornalley et al., 2009; Colin et al., 2010; Repschläger et al., 2017; Jalali et al., 2019). Studies on Holocene atmospheric conditions over the North Atlantic region suggest the occurrence of north-

ward and southward displacements of the winter storm tracks (Fletcher et al., 2012; Desprat et al., 2013; Chabaud et al., 2014; Zielhofer et al., 2017). The western Mediterranean Sea is very sensitive to changes in Atlantic Ocean conditions. These oceanic and atmospheric connections have been well-documented and described for the last glacial period (Cacho et al., 1999; Moreno et al., 2002; Sierro et al., 2005; Frigola et al., 2008; Toucane et al., 2012) when intense millennial-scale variability occurred that was associated with major changes in the AMOC (the so-called Dansgaard–Oeschger cycles and Heinrich events). However, even though the Holocene climate variability over the western Mediterranean has also been extensively studied (i.e. Cacho et al., 2001; Frigola et al., 2007; Rodrigo-Gámiz et al., 2011; Ausin et al., 2015; Jalali et al., 2016), unlike the glacial periods, potential connections to the changes that occurred in the North Atlantic Ocean still remain unclear.

One of the limitations in the study of Holocene climate variability is the sensitivity of the climate proxies. During this period, the natural range of variability for sea surface temperature (SST) or $\delta^{18}O_{sw}$ is relatively small, and these natural changes are often below the magnitude of the proxy sensitivity. For this reason, to validate the climate value of the proxy signals for the Holocene, it is critical to reproduce them in comparable records and ideally with independent proxies. With this goal, here we present a new high-resolution Holocene SST record based on the Mg/Ca ratio in the planktonic foraminifera *G. bulloides* from core ALB-2 of the Alboran Sea. This record is also compared with three other Mg/Ca ratios for *G. bulloides* derived SST records from the western Mediterranean, two new ones (MD95-2043 and MD99-2343), and another that was previously published (ODP 976; Jiménez-Amat and Zahn, 2015). The western Mediterranean Sea has been intensively studied and several SST records exist, mostly based on the application of the UK'37 index measured on alkenones (Cacho et al., 2001; Martrat et al., 2004; Rodrigo-Gámiz et al., 2014; Ausin et al., 2015). This multicore and multi-proxy approach comparison enables a discussion of the proxy limitations in order to identify some SST changes which have discrepancies between the two considered proxies. The new high-resolution Mg/Ca SST record allows us to discuss the Holocene SST evolution in this region and to hypothesize potential links with changes in the North Atlantic circulation.

2 Regional settings

Climate in the western Mediterranean is characterized by warm and dry summers, while autumn and winter are mild and humid. During winters, westerly winds are displaced southward, thus causing storms to create more humid conditions over the western Mediterranean (Trigo et al., 2002; Combourieu Nebout et al., 2009; Fletcher et al., 2012; Roberts et al., 2012; Nieto-Moreno et al., 2011). At the end of summer and in early autumn the temperature differences between the air masses and the surface Mediterranean can produce violent precipitation events (Lionello et al., 2006; Sabatier et al., 2012).

Alboran Sea oceanography (Fig. 1a and b) is controlled by the exchange of water masses between the Mediterranean and the Atlantic Ocean. The low-salinity Atlantic waters enter the Mediterranean Sea as a surface layer while high-salinity waters from the Mediterranean outflow into the Atlantic Ocean as an intermediate water mass (Mediterranean Outflow Water, MOW). Surface waters at the Alboran Sea are typically defined as Modified Atlantic Water (MAW), composed mainly of a mixing of Surface Atlantic Water (SAW) and the Eastern North Atlantic Central Water (ENACW) (Bray et al., 1995; Millot, 2009) (Fig. 1a and b). This ENACW has been characterized as waters from two different source areas converging in the northwest of the Iberian Peninsula. One source has a subpolar origin (ENACWsp), which is formed near 46° N around the Celtic Sea (McCarteney and Talley, 1982). The other source has a subtropical origin (ENACWst) formed near 35° N around the Azores islands (Fiúza, 1984) (Fig. 1a). Hydrographic properties of these water masses are related to changes in heat and salt transport through the STG–SPG that ultimately modulate the AMOC (i.e. Cléroux et al., 2012; Thornalley et al., 2009; Gao and Yu, 2008; Böning et al., 2006). The MAW inflow describes two anticyclonic gyres in the Alboran Sea (western and eastern Alboran gyres, WAG and EAG), which change its properties as the inflow water progresses eastward (Fig. 1b). Deeper in the water column of the Alboran Sea, the Levantine Intermediate Water (LIW) occurs at 220–600 mwd (metres water depth) and the Western Mediterranean Deep Water (WMDW), under 600 mwd. The ALB-2 core is located in the centre of the WAG. Sediment fluxes based on sediment traps from the same location show relatively high values attributed to a funnelling effect by the gyre, thus capturing particles from the edges and moving them towards the centre (Fabres et al., 2002).

3 Materials and methods

Core HER-GC-ALB-2 (here abbreviated as ALB-2) was retrieved from the Alboran Sea (36°0′44.80″ N, 4°16′24.38″ W; 1313 m) during the HERMESIONE cruise in 2009 (Fig. 1b), on board B/O *Hespérides*. Core ALB-2 was recovered with a gravity core system and covers a continuous sequence of 337 m length. Information on the other sediment cores included in the discussion appears in Table S1 of Supplement.

Geochemical analyses were performed on planktonic foraminifera *G. bulloides* sampled every 1 cm. The individual specimens were hand-picked between 250 and 355 µm size fractions in order to obtain a homogenous population.

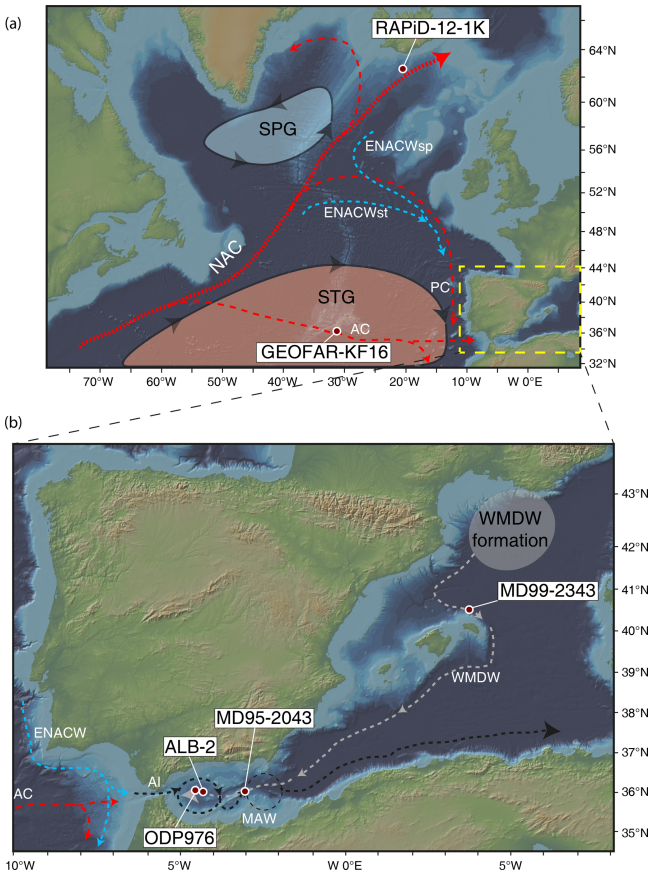

Figure 1. Schematic modern surface and central hydrography of the North Atlantic currents. Basic map obtained from Marine Geoscience Data System ©2008–2018 – all rights reserved. Warm surface currents are shown by dashed red arrows. **(a)** Central currents are shown by dashed light-blue arrows. **(b)** Oceanographic gyres are represented by red circles. Abbreviations are listed as follows: NAC, North Atlantic Current; AC, Azores Current; PC, Portugal Current; ENACWsp, East North Atlantic Central Water Subpolar; ENACWst, East North Atlantic Central Water Subtropical; SPG, Subpolar Gyre; STG, Subtropical Gyre; WMDW, Western Mediterranean Deep Water; AI, Atlantic inflow; MAW, Modified Atlantic Water. Red dots circled white indicate the core locations.

The selected specimens showed apparently well-preserved and clean shells.

3.1 Stable isotopes

Around 10 specimens of *G. bulloides* per sample were crushed between two glass slides under a binocular microscope in order to open the chambers and allow for cleaning of the shells' interiors. Samples were cleaned with 500 µL of methanol in an ultrasonic bath for 30 s in order to mobilize the clay residues. The residual methanol was removed and samples were dried prior to analysis. The analyses were performed with an isotope-ratio mass spectrometer (IRMS), Finnigan-MAT 252, which was linked online to a single acid bath CarbonKiel-II carbonate preparation device at the Scientific and Technological Centre of the University of Barcelona (CCiT-UB). The analytical precision of laboratory standards for δ^{18}O was better than 0.08 ‰. Calibration to Vienna Pee Dee Belemnite (VPDB) was carried out following NBS-19 standards (Coplen, 1996).

Seawater δ^{18}O ($\delta^{18}O_{sw}$) was obtained after removing the temperature effect, using the Shackleton paleotemperature equation (Shackleton, 1974) on the *G. bulloides* δ^{18}O signal using the *G. bulloides* Mg/Ca SST values. The results are expressed in the SMOW (Standard Mean Ocean Water) water standard ($\delta^{18}O_{sw}$) after the correction of Craig (1965).

3.2 Chronologies

The chronology of core ALB-2 is based on 14 ^{14}C AMS dates measured on planktonic foraminifera samples that were hand-picked from the 215–355 µm fraction (8–33 mg). The top 10 radiocarbon dates are based on monospecific samples of *Globorotalia inflata*, and the four older dates are based on multi-specific samples of planktonic foraminifera (Table S2). Radiocarbon ages were calibrated using MARINE13 calibration curves (Reimer et al., 2013). The age model was built using the Bayesian statistics software Bacon with the statistical package R (Blaaw and Christien, 2011) for marine sediments (Supplement Fig. S3). From the core top to the first ^{14}C AMS date (10 cm), the age model was calculated using a linear regression, assuming the age of the core top to be that of the sediment core recovery (2009 CE). The chronology at the base of the core was established using isotopic stratigraphy by correlating a well-expressed positive excursion in the δ^{18}O-ALB-2 to a well-dated comparable structure in the δ^{18}O-MD95-2043 measured in both cases on *G. bulloides* (Table S2 and Fig. S3). According to the generated age model, the ALB-2 core covers the last 15 cal. kyr BP with an average sedimentation rate of 22 cm kyr^{-1}, providing a time resolution of about 45 years for the applied sampling interval (1 cm).

The age model for MD99-2343 was improved from that originally published by Frigola et al. (2007), with nine new ^{14}C AMS dates incorporated into the previous age model (Table S4). The updated age model has 19 ^{14}C AMS dates covering the last 17 cal. kyr BP. This updated age model was also built using the Bayesian statistics software Bacon with the statistical package R (Blaaw and Christien, 2011) for marine sediments (Fig. S5). The upper 20 cm of this core was lost during its retrieval, but for chronological purposes the age of the missed core top was assumed to be the recovered year (1999 CE). The chronology during deglaciation was improved by adding two tie points, by correlating a marked δ^{18}O structure in both the Minorca core MD99-2343 and the Alboran core MD95-2043 (Tables S4 and S5).

3.3 *G. bulloides* Mg/Ca ratios and sea surface temperature estimates

Mg/Ca measurements in core ALB-2 were made on samples containing 50–60 specimens of *G. bulloides,* gently crushed between two glass slides under a binocular microscope, in order to open the chambers and allow the removal of contaminant phases from the shells' interiors. The cleaning protocol for the foraminifera shells was based on the full procedure described by Pena et al. (2005) which includes the reductive step. Once cleaned, each sample was dissolved in ultra-pure 1 % nitric acid with Rh as an internal standard. After dissolution, samples were centrifuged to remove any potential undissolved mineral particles. Procedural blanks were routinely produced to detect any potential contamination problem during the sample cleaning and dissolution process.

Instrumental analyses were performed in an inductively coupled plasma mass spectrometer (ICP-MS), PerkinElmer Elan 6000, at CCiT-UB. Every four samples, a standard solution was analysed. The standard solution was prepared gravimetrically with known concentrations of Mg, Ca, Mn, and Al, and it was produced with a ratio (element/Ca) comparable to that expected for the samples. Analytical reproducibility obtained relative to the gravimetric standard samples was 1.62 % (1σ) for the Mg/Ca ratio. Moreover, all Mg/Ca ratios in this core were corrected using the same gravimetric standard for each ICP-MS round using a standard-sample bracketing (SSB) method, in order to correct the instrumental drift.

The *G. bulloides* Mg/Ca ratios were then compared with other analysed ratios, i.e. Al/Ca and Mn/Ca, in order to identify potential contamination by any remaining manganese oxides and/or aluminosilicates in the samples (Barker et al., 2003; Pena et al., 2005). Such potential contamination could provide anomalous high *G. bulloides* Mg/Ca ratios and therefore overestimate the inferred SST values. In the ALB-2 record, Mn/Ca ratios above 2σ (0.29 mmol mol^{-1}; over standard deviations of the average Mn/Ca values) were removed (Fig. S6a). The Al/Ca ratio was considered to potentially indicate the presence of unremoved silicates (likely clays), and those samples with values above 2σ (1.74 mmol mol^{-1}) were also removed (Fig. S6b).

The *G. bulloides* Mg/Ca records from cores MD95-2043 and MD99-2343 were produced following a comparable procedure to that described for the ALB-2 core, but, for these cores, the data to estimate analytical reproducibility and the Mn/Ca and Al/Ca ratios to evaluate the potential interference of contamination phases were not available. Consequently, the uncertainties associated with these complementary SST records are larger than those associated with the ALB-2 sediment core, which is the main focus of this study. *G. bulloides* Mg/Ca ratios from core ODP 976, also included in the discussion, have already been published by Jiménez-Amat and Zahn (2015).

The *G. bulloides* Mg/Ca ratios of the four discussed sediment cores have been converted to SST by applying the calibration from Cisneros et al. (2016). This calibration is based on *G. bulloides* Mg/Ca ratios available from core top samples from the North Atlantic Ocean (Elderfield and Gansen, 2000) and the addition of core top samples from the western Mediterranean Sea. These Mediterranean samples extend the temperature range of the original calibration toward the warmer edge, and thus the obtained calibration better covers the oceanographic conditions of the western Mediterranean. This calibration provides realistic SST for the *G. bulloides* bloom season around April–May across the western Mediterranean (Cisneros et al., 2016). Since this calibration was performed on non-reductive cleaned samples, the Mg/Ca ratios of those cores cleaned with the full reductive cleaning procedure were increased by 12 % prior to the calibration application. This percentage accounts for the selective dissolution of high-Mg calcite that introduces this cleaning step (Barker et al., 2003; Rosenthal et al., 2004). However, it has been proposed that foraminifera Mg/Ca ratios could be also affected by salinity, particularly in high-salinity environments such as the Mediterranean Sea, challenging its applicability as an SST proxy (Ferguson et al., 2008). But the sensitivity of Mg/Ca ratios to high-salinity environments, according to culture experiments, appears to be far lower than that previously proposed in base-to-core top sediments (Hönisch et al., 2013). In addition, the anomalous high Mg/Ca ratios detected in high-salinity environments such as the Mediterranean Sea and Red Sea have been attributed to high-Mg diagenetic overprints (Hoogakker et al., 2009; van Raden et al., 2011). In the case of the studied Mediterranean cores, the obtained ratios are coherent within the expected ranges of the calibration and appear not to be affected by secondary diagenetic calcite.

4 Results and discussion

4.1 Holocene evolution in western Mediterranean *G. bulloides* – δ^{18}O records

We now compare the new δ^{18}O record from ALB-2 to other previously published high-resolution δ^{18}O records from the western Mediterranean (Cacho et al., 1999; Frigola et al., 2007; Jiménez-Amat and Zahn, 2015) in order to evaluate the regional significance of the recorded signal (Fig. 2). The main patterns in the δ^{18}O records show an extraordinary resemblance to each other, and even several centennial-scale structures can be correlated through the cores, taking into account the individual core chronological uncertainties (Fig. 2c). The isotopic depletion associated with the last termination ends in all four records at around 9 cal. kyr BP. Throughout the Holocene, all the *G. bulloides* δ^{18}O records are rather stable, with several short oscillations (0.2 ‰–0.3 ‰) and a slight enrichment trend toward the Late Holocene (Fig. 2b). This comparison supports the regional value of the captured paleoceanographic signal and the robustness of the individual age models.

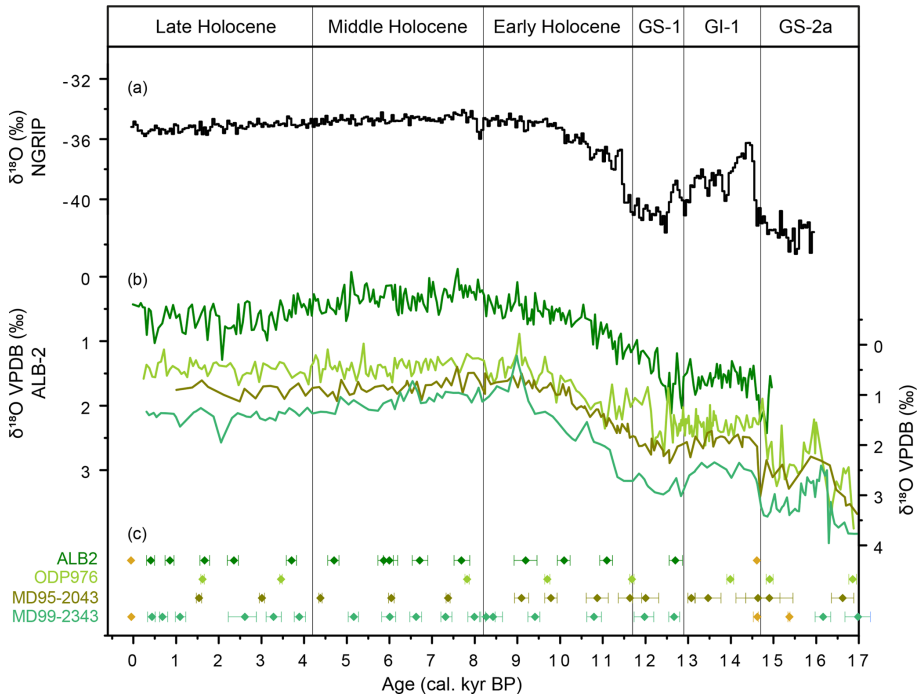

Figure 2. Comparison of δ^{18}O (VPDB) records and their ^{14}C calibrated dates from the western Mediterranean Sea over the last 17 cal. kyr BP. **(a)** δ^{18}O ‰ NGRIP record. (b) From the top to the base in green colour: ranges of δ^{18}O ‰ (VPDB) records from the cores ALB-2, ODP976 (Combourieu-Nebot et al., 2002), MD95-2043 (Cacho et al., 1999), and MD99-2343 (Minorca drift). Note ALB-2 δ^{18}O ‰ (VPDB) record is plotted with an independent y axis from the others in order to help with figure compression. **(c)** ^{14}C calibrated dates with the available errors from each record shown above. Each date is coloured the same as the record, excluding the yellow dots, which represent tie points.

In terms of absolute values of the *G. bulloides* δ^{18}O records, clear differences can be detected between the cores. Both the ALB-2 and ODP976 cores, located in the westernmost part of the Alboran Sea, display the lightest values (note that the curves in Fig. 2b are plotted on independent y axes). Core MD95-2043, located in the eastern part of the Alboran Sea, shows heavier δ^{18}O values than the other two Alboran records (Fig. 2b). Finally, core MD99-2343, located north of the island of Minorca, shows the heaviest δ^{18}O values. Such an isotopic pattern is consistent with the regional oceanography, showing the lightest δ^{18}O values at those sites with a stronger influence of North Atlantic surface inflow, while the δ^{18}O values become heavier along its path into the Mediterranean Sea. This situation reflects the excess of evaporation within the Mediterranean Sea that results in an enhancement of the salinity (Béthoux, 1980; Lacombe et al., 1981) but also of the marine water δ^{18}O values. It is interesting to note that the presented isotopic records show a strong gradient between the western and eastern Alboran Sea (about 0.5 ‰), probably due to strong surface mixing with the underlying Mediterranean waters driven by the two anticyclonic gyres (Tintore et al., 1988; Millot, 1999), supporting the argument that the Atlantic inflow became rapidly modified within the Alboran Sea. The isotopic change from the eastern Alboran Sea core (MD95-2043) and the Minorca core (MD99-2343) is even larger ($\sim$ 0.7 ‰), reflecting the long path of these inflowing Atlantic waters through the western Mediterranean before reaching Minorca.

4.2 Sea surface temperatures: multi-record and multi-proxy comparison

According to the ALB-2 Mg/Ca SST record, the Holocene maximum temperatures (20.0 ± 1.0 °C; uncertainties of the average values represent 1σ; uncertainty values are those derived from the Mg/Ca SST calibration) were reached at the onset of the Holocene $\sim$ 11.0 kyr (Fig. 3b); a general cooling trend until the present characterizes this record, punctuated by several short-term oscillations (maximum of 2 °C). However, the ALB-2 SST record can be divided into three main intervals. The first interval corresponds to most of the Early Holocene (11.7–9 cal. kyr BP) when SSTs were warmest and relatively stable (no significant trend), oscillating at around an average value of $\sim 17.2 \pm 1.3$ °C (Fig. 3b). The second interval displays a general cooling trend of $\sim$ 4 °C ending at around 4.2 cal. kyr BP when minimum Holocene SSTs were reached ($\sim 13.6 \pm 1.2$ °C) (Fig. 3b). The last and most recent interval does not show any clear warming/cooling trend (average SST of $\sim 14.9 \pm 1.2$ °C) and intense SST oscillations ($\sim$ 2.0 °C) of longer durations than those recorded during previous intervals (Fig. 3b).

The ALB-2 *G. bulloides* Mg/Ca SST record has been compared to three other SST records from the western Mediterranean Sea that were calculated following the same Mg/Ca SST procedure (Fig. 3b–e). The comparison between the four chronology records is very robust (Fig. 2c) and totally independent for the Holocene period (ALB-2 and MD99-2343: this study; ODP976: Combourieu Nebout et al., 2002; MD95-2043: Cacho et al., 1999). The sampling resolution of the ALB-2 record is higher than for the other sites, but the main patterns agree well between all the compared records. Maximum SSTs occurred around 11 cal. kyr BP in all records, and also a general cooling trend can be observed during the Early–Middle Holocene, ending in all cases before the Late Holocene (Fig. 3b–e). Absolute values also show a good agreement; when the resolution is high enough, some millennial-scale structures can even be correlated between the four records. This multicore comparison strongly supports the value of *G. bulloides* Mg/Ca in this region as an SST proxy and gives confidence that the obtained SST records reflect true regional environmental conditions. Nevertheless, these Mg/Ca SST reconstructions show differences from the previous published SST reconstructions based on alkenone measurements that need further discussion (Fig. 3f; Cacho et al., 2001; Martrat et al., 2004, 2014; Jiménez-Amat and Zahn, 2015).

Alkenone SST reconstructions are based on the relative abundance of di- and tri-unsaturated C_{37} alkenones – mostly produced in the Alboran Sea by the marine coccolithophore *Emiliania huxleyi* (Volkman et al., 1980; Prahl et al., 2000; Ausin et al., 2015). The comparison between *G. bulloides* Mg/Ca SST and the alkenone SST (also studied by Jiménez-Amat and Zahn, 2015) shows remarkable differences in both their absolute values and main patterns, even when both proxies are measured for the same core, as observed in core MD95-2043 and also ODP 976 (Fig. 4c and d). For the Holocene, maximum SSTs in the alkenone record were reached later than for the Mg/Ca SST records ($\sim$ 10 cal. kyr BP), and thenceforth the alkenone SST record shows a rather flat pattern for the whole Holocene, with a slight cooling trend of about 1 °C. In contrast, ALB-2 *G. bulloides* Mg/Ca SST (Fig. 4c–e) shows larger variability over both the short and long term. Holocene absolute SST values in the alkenone record are warmer (20–18 °C) than those recorded by the Mg/Ca record (20–13 °C).

Alkenone SST records have been interpreted and calibrated with annual average temperatures (Ternois et al., 1997; Sicre et al., 1999; Prahl, et al., 2000; Cacho et al., 2001; Versteegh et al., 2007; Martrat et al., 2004, 2014). This is consistent with the results from sediment trap series from the western Mediterranean Sea that detect coccolith productivity throughout the year, although enhanced during the spring and autumn seasons and more scarce during the very stratified and oligotrophic summer months (Bárcena et al., 2004; Hernández-Almeida et al., 2011). In contrast, sediment trap studies from the same region indicate that *G. bulloides* has a narrower seasonal window, growing during the spring months (April–May); however, a secondary smaller bloom occurs during autumn (November–December) (Bárcena et al., 2004; Rigual-Hernández et al., 2012). This information fits well with the results of the reviewed *G. bulloides* Mg/Ca calibration for the western Mediterranean (Cisneros et al., 2016). The preferential depth habitat of *G. bulloides* is above the thermocline within the upper 60 m of the water column (Schiebel and Hembleben, 2017) as well, because it needs nutrients supplied by vertical mixing (Rao et al., 1988; Hemleben et al., 1989; Kemle-von Mücke and Hemleben, 1999; Bárcena et al., 2004). Present seasonal and depth temperature distribution at the ALB-2 location can be evaluated with the World Ocean Atlas 2013 (Boyer and Mishonov, 2013) data set that averages measurements from 1955 to 2012 (Fig. 4a). Annual average temperatures of 17.8 °C occur for the upper 10 m of the water column, in good agreement with core top alkenone SST reconstructions (Fig. 4a). On the other hand, the estimated core top *G. bulloides* Mg/Ca SST of the ALB-2 core is 15.5 °C, showing a closer match to the measured temperatures at 25–45 m depth during spring (April–May), in agreement with the main season and depth habitat of *G. bulloides* (Bárcena et al., 2004; Rigual-Hernández et al., 2012; Schiebel and Hembleben, 2017). The *G. bulloides* habitat preference has been further tested through the estimation of the theoretical carbonate $\delta^{18}O$ signal expected for present sea water conditions of the upper 100 mwd (Fig. 4b). This estimation is based on the available data from Pierre (1999), and detailed information on the procedure is provided in the Supplement (Sect. S7). This exercise illustrates that the measured *G. bulloides* $\delta^{18}O$ values in the top samples from ALB-2 (0.42 ± 0.1 ‰) are indeed comparable to those estimated for April–May from 5 to 40 mwd (Fig. 4b). Therefore, isotopic composition confirms the interpreted *G. bulloides* habitat of 25–45 m depth during the April–May months based on the Mg/Ca data. Consequently, alkenone–Mg/Ca SST offset is consistent with the habitat preferences for both season and depth of the two proxy carriers involved, *E. huxleyi* and *G. bulloides* (Fig. 4a–b).

Another differential feature between the two proxies is the rather smooth behaviour of the alkenone signal, in contrast to the Mg/Ca signal (Figs. 3 and 4). This has previously been reported and attributed to the intrinsic characteristics of the proxy measurements (Laepple and Huybers, 2013). The number of individuals that integrate the SST signal in a single measurement is several orders of magnitude larger in the alkenones, averaging the signal of all alkenones contained in the sample, while the Mg/Ca analyses average about 40–50 specimens (Laepple and Huybers, 2013). This situation favours the integration of several averaged years in the alkenone SST signal while the Mg/Ca SST signal will be more sensitive to a unique season (spring) and with a higher weighting toward the most favourable growth years (Jiménez-Amat and Zahn, 2015). As a consequence, Mg/Ca records should result in a higher noise signal but may re-

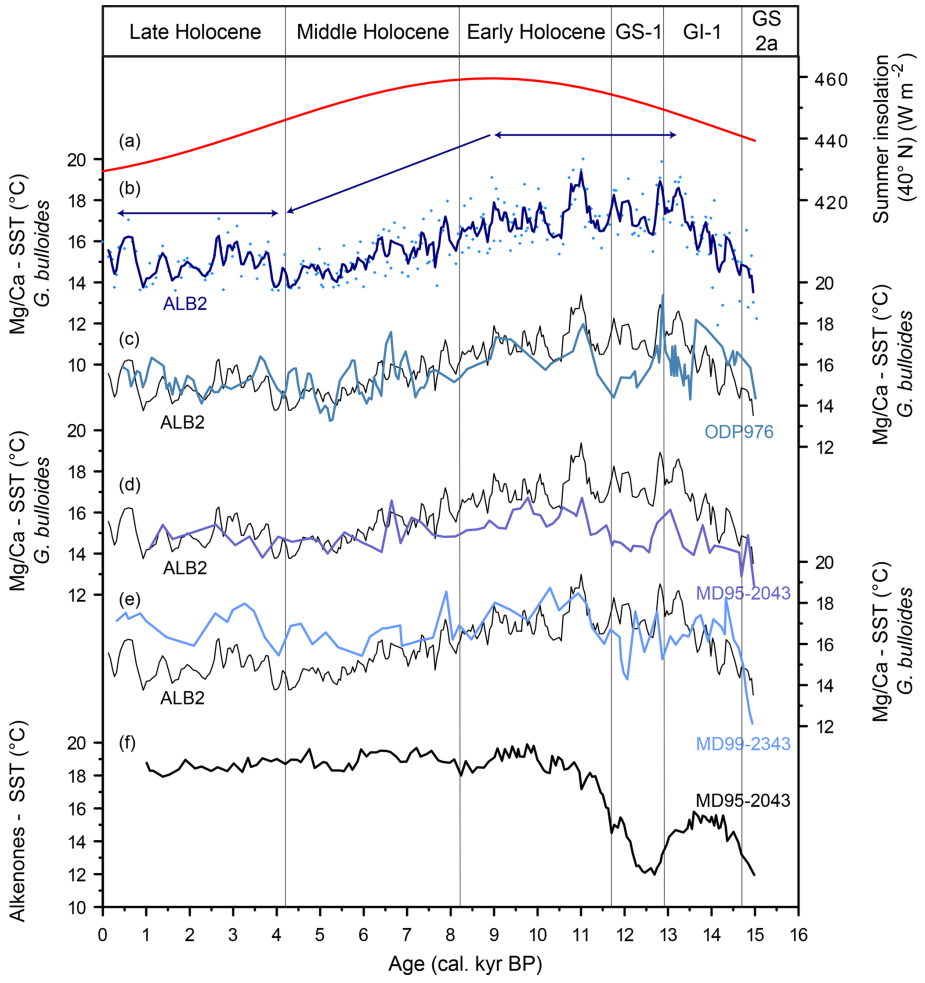

Figure 3. Western Mediterranean SST multi-record comparison for the last 16 cal. kyr BP. **(a)** In red, summer insolation at 40° N; **(b)** Mg/Ca SST (°C) from the ALB-2. Light-blue dots correspond to each SST result; the three-point average is shown by the bold dark-blue line. Dark-blue arrows above the record correspond to the three Holocene intervals described in the text **(c, d, e)**: Mg/Ca SST (°C) from ODP976 (Jiménez-Amat and Zahn, 2015), MD95-2043, and MD99-2343, respectively (bold blue lines), compared with the ALB-2 three-point average Mg/Ca SST (°C) (black line underneath). Note that both records from each plot are plotted on the same *y* axis. **(f)** Alkenone SST (°C) from MD95-2043 (Cacho et al., 1999).

flect better extreme changes within single seasons than the alkenone record, whereas seasonal changes may become diluted in the large averaged signal.

In addition, we need to point out that the larger difference between the studied Mg/Ca and alkenone SST reconstructions correspond to the deglacial period (at the end of GS-1 or the Younger Dryas – YD). Both alkenone and Mg/Ca SST records show a cooling of ∼ 3–4 °C at the onset of the GS-1 (YD), but the big difference occurs at the end of this interval. Both the alkenones and Mg/Ca records show an early intra-YD warming (Cacho et al., 2001), and then the alkenone SSTs continue the deglacial warming while the Mg/Ca record shows a cooling trend. In order to better explore this discrepancy we have also compared these two records for the glacial period in Fig. 4c–e. *G. bulloides* Mg/Ca SSTs during the last glacial period record the same oscillations and absolute values as do alkenone SSTs, and they both agree on the first warming of the deglaciation, but clearly the second warming phase of deglaciation does not appear in any of the three considered Mg/Ca records (Fig. 4c–e). Thus, this is a proxy characteristic that may reflect the limited capacity of *G. bulloides* to adapt to the large temperature change that occurred during deglaciation. *G. bulloides* has different genotypes adapted to different ranges of water temperatures, from transitional to subpolar waters (Kucera and Darling 2002; Kucera et al., 2005), but *G. bulloides* starts to be scarce in water with temperatures over 20 °C. This agrees with the maximum temperatures recorded during both the glacial and interglacial periods in the Mg/Ca records (Fig. 4c–e). Consequently we can interpret that *G. bulloides* has a resilient capacity to change its growth season in order to survive the large deglacial SST changes in

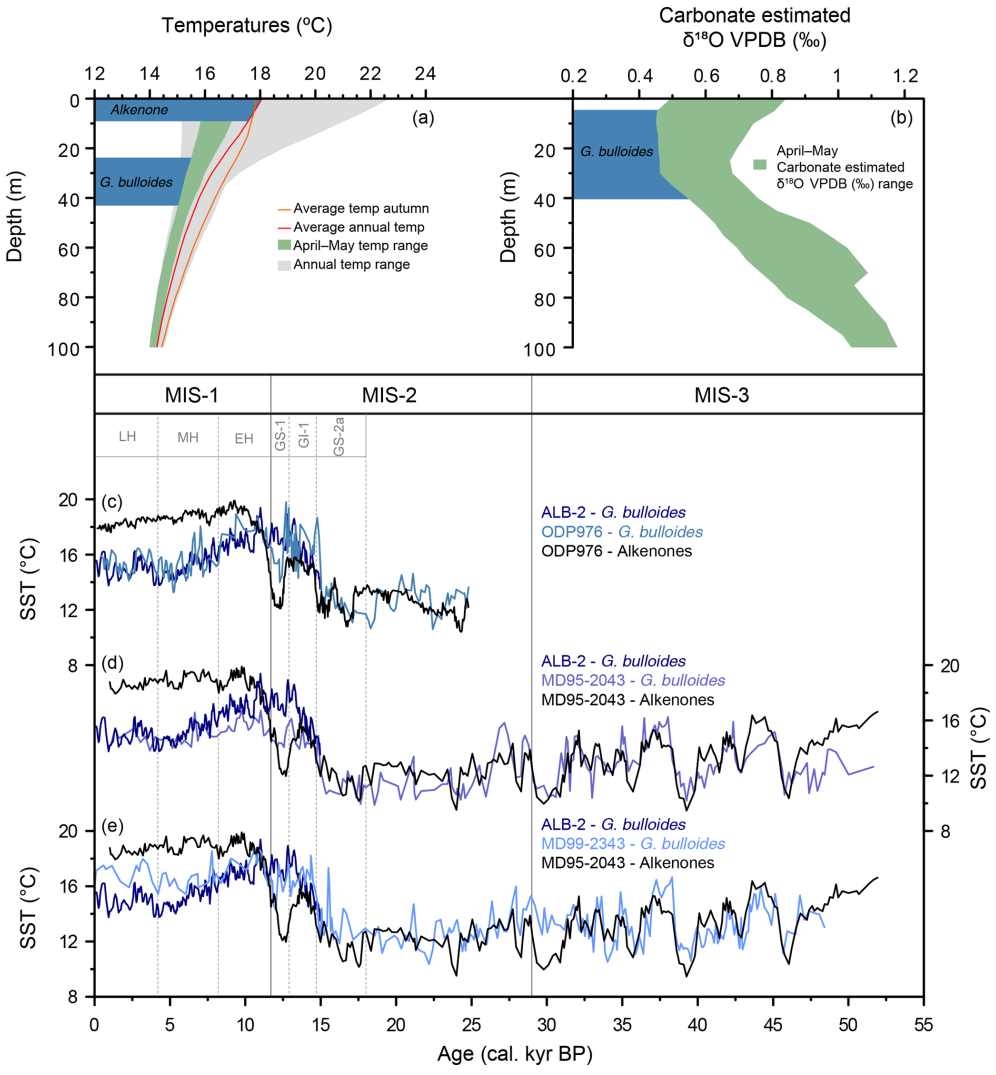

Figure 4. Western Mediterranean SST from alkenone and *G. bulloides* Mg/Ca multi-comparison for the last interglacial and the following (present) interglacial period. **(a)** Temperatures. **(b)** Carbonate estimated δ^{18}O VPDB (‰) profile for the first 100 m from site 503737B, obtained from WOA13 0.25deg measured during the years 1955–2012 (Boyer and Mishonov, 2013). The horizontal blue band indicates the preferential depth in relation to the profile temperatures **(a)** and carbonate estimated δ^{18}O VPDB (‰) **(b)** of *G. bulloides* (average April–May temperatures and carbonate estimated δ^{18}O VPDB (‰) in green) and alkenones (annual average temperatures in red). Note that each of the following comparisons have the same *y* axis. **(c)** The blue lines (ALB-2; this study and ODP976; Jiménez-Amat and Zahn, 2015) show *G. bulloides* Mg/Ca SST compared with the alkenone SST (Martrat et al., 2014) from the same ODP976 record. **(d)** The blue lines (ALB-2 and MD95-2043; both in this study) show *G. bulloides* Mg/Ca SST compared with the alkenone SSTs from the same MD95-2043 record (Cacho et al., 1999). **(e)** The blue lines (ALB-2 and MD99-2343; both in this study) show *G. bulloides* Mg/Ca SST compared with alkenone SST from the MD95-2043 record (Cacho et al., 1999).

the region. We propose that, during the glacial period as well as the first part of deglaciation, *G. bulloides* could have had its maximum representation during the autumn bloom when upwelling conditions reappeared after the warm sea summer stratification. That could have allowed *G. bulloides* to grow in a relatively mild upwelling season during the glacial period. Nowadays autumn SST values are comparable to the annual average SST values, and that could explain the comparable SST values of both alkenone and Mg/Ca proxies. However the second deglacial warming might have been too extreme for *G. bulloides* and they would have therefore moved to the spring upwelling bloom with colder SSTs than those during autumn. Consequently we hypothesize that the absence of the second deglacial warming in the *G. bulloides* Mg/Ca record may reflect a resilience strategy to change its habitat toward the spring bloom. At the beginning of the Holocene, when SST variability was lower and within its habitat tolerance, *G. bulloides* became a good sensor of

interglacial SST variability (Figs. 3 and 4). Alternatively, it can be argued that *G. bulloides* changed its preferential depth growth habitat in order to survive that large deglacial SST warming. However, in any case, we consider that the shorter deglacial warming of the Mg/Ca SST, in contrast to the alkenone SST record, reflects a resilience strategy of *G. bulloides* rather than reflecting the actual intensity of the deglacial SST warming in the region. In contrast, during the Holocene, the SST changes were within the *G. bulloides'* range of tolerance, and thus this part of the record should truly record SST changes. It is important to remark that any change in the habitat preference of G. *bulloides* would have also affected the $\delta^{18}O$ signal – this is particularly relevant when a temperature correction is applied to this record in order to obtain $\delta^{18}O_{sw}$. In that case, the application of the alkenone SST record would introduce a large heavy anomaly in the $\delta^{18}O_{sw}$ during deglaciation, and that would reflect the habitat change of one of the proxy carriers rather than actual changes in the regional oceanography. This observation reveals the relevance of using signals ($\delta^{18}O$ and SST) of the same species of foraminifera for such estimations.

4.3 Holocene evolution in Alboran surface hydrography

The overall Holocene SST evolution in the Alboran Sea is described in three different phases (Fig. 5c): (a) a maximum SST during the Early Holocene (11–9 cal. kyr BP), (b) a cooling trend throughout the Middle Holocene (9–4.2 cal. kyr BP), and (c) relatively colder temperatures with intense millennial-scale oscillations for the Late Holocene (4.2–0 cal. kyr BP). This general SST pattern also agrees well with that described for the North Atlantic and western Mediterranean Sea in relation to regional data compilations (Marchal et al., 2002; Kim et al., 2004; Rimbu et al., 2004; Wanner et al., 2008) and with the expected Holocene redistribution of solar energy by the changing orbital configuration according to the atmosphere–ocean general circulation model of Lorenz and Lohmann (2004) (Fig. 5a and c). Nevertheless, the magnitude of the Holocene SST changes in the Alboran Sea (above 5 °C) exceeds that expected by simply orbital changes in insolation (~ 1.6 °C in atmosphere) (Lorenz and Lohmann, 2004). Therefore, other factors need to be considered to explain the magnitude of the recorded SST changes.

The period of maximum SST in the Alboran Sea (11–9 cal. kyr BP) occurred while the North Atlantic Ocean was still under the influence of meltwater pulses from the Laurentide ice sheet (Fig. 5b) that injected freshwater over the surface of the North Atlantic Ocean. This situation induced a stratification in the North Atlantic and consequently a weakening of the SPG circulation (Thornalley et al., 2009). At lower latitudes, it has been proposed that the heat transport from the STG toward the North Atlantic was reduced (Repschläger et al., 2017). The consequent heat accumulation in the STG could have hence contributed to a warmer inflow into the Mediterranean Sea and thus may have led to the observed maximum SST in the Alboran Sea (Fig. 5c). But it is also relevant to note that this Early Holocene warm period (11–9 cal. kyr BP) in the Alboran Sea corresponds to the last stage of an organic-rich layer (ORL) formation (Fig. 5e). This ORL has been associated with a strong western Mediterranean stratification phase, resulting from the deglacial sea level rise, which reduced vertical mixing (Cacho et al., 2002; Rogerson et al., 2008). As a consequence of this situation, the modification of Atlantic inflow water along its path into the Mediterranean could have been reduced, thus favouring the persistence of warm conditions in the inflowing subtropical waters.

At around 9 cal. kyr BP, the Alboran SST record (Fig. 5c) starts a progressive cooling trend that culminates in reaching minimum values of around 4.2 cal. kyr BP. The onset of this cooling trend is coincident with the development of a well-mixed surface layer (Fig. 5b) in the North Atlantic due to the reduction of deglacial melting (Thornalley et al., 2009). This situation would have allowed enhanced transport of subtropical waters towards higher latitudes, releasing the previous heat accumulation in the STG and potentially leading to cooler water flowing into the Mediterranean Sea. In addition, 9 cal. kyr BP also marked the end of the western Mediterranean stratification phase that led to the formation of the last ORL in the Alboran Sea (Fig. 5e). This end occurred at the time of a strong increase in the speed of deep water currents (Fig. 5d) associated with the formation of the WMDW (Frigola et al., 2007). The reduction in surface stratification in the Alboran Sea would have led to increased water mixing of the inflowing Atlantic waters that could have contributed to the observed cooling trend. This situation was apparently also linked to an increase in the local upwelling conditions developed by the establishment of the western anticyclonic gyre of the Alboran Sea that, according to coccolith assemblages, occurred after 7.7 cal. kyr BP (Ausin et al., 2015). In addition, the described SST cooling trend for this period could also have been promoted by some additional atmospheric forcing. Several authors have suggested a southward displacement of North Atlantic westerlies during this period, inducing a southern penetration of winter storm tracks (Desprat et al., 2013; Fletcher et al., 2012; Chabaud et al., 2014; Zielhofer et al., 2017). Therefore, a combination of factors, internal and external to the Alboran Sea, could have accounted for the observed SST cooling trend from 9 kyr until 4.2 cal. kyr BP, when a change occurred in both the short- and long-term variability.

At about 4.2 cal. kyr BP a double cold peak structure of a minimum SST occurred (Fig. 5c), reaching ~ 13.6 °C, representing the minimum values of the record. After this event, the long-term cooling trend ceased while an intense millennial-scale variability developed, involving SST oscillations over 2 °C. This event is apparently synchronous with a peak in the record of deep water current intensity (Fig. 5d), suggesting that deep convection was strengthened

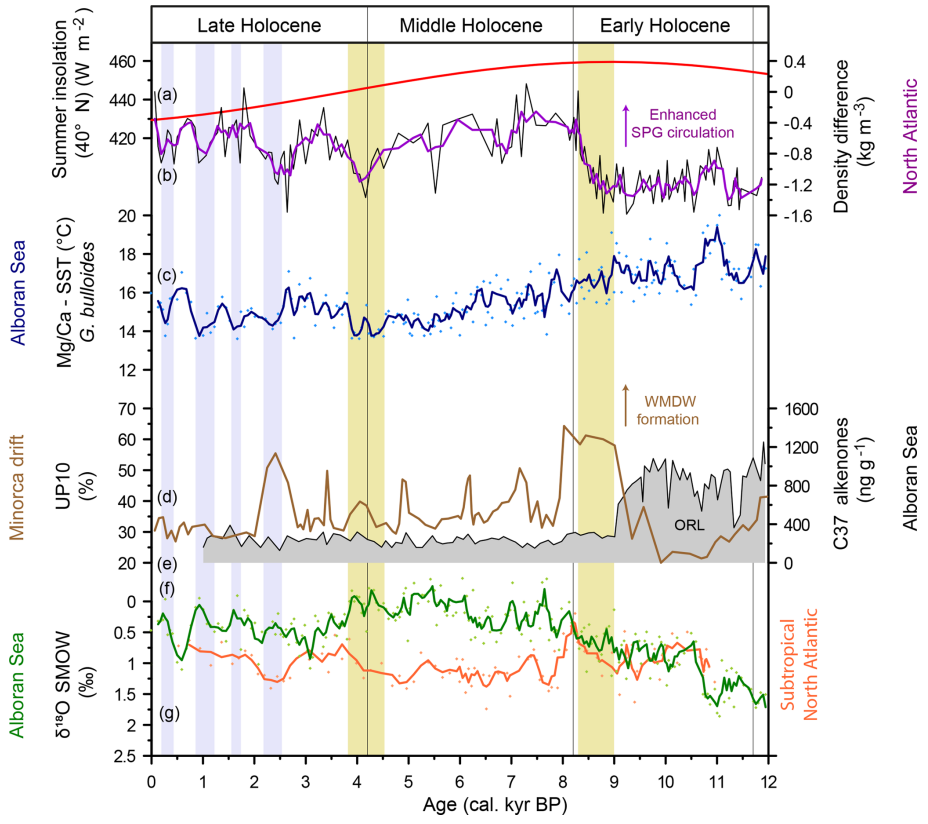

Figure 5. Holocene evolution for the Alboran Sea surface hydrography related to oceanographic processes in the North Atlantic. **(a)** In red, the summer insolation at 40° N. **(b)** In purple, the three-point average of density differences (kg m^{-3}) between *G. bulloides* and *G. inflate* from the North Atlantic record RAPiD-12-1K (Thornalley et al., 2009). **(c)** The new Mg/Ca SST (°C) presented in this work from the ALB-2 (Alboran Sea) – light-blue dots correspond to each SST result and the bold dark-blue line corresponds to the three-point average. **(d)** In brown, the UP10 fraction (%) from the Minorca drift core MD99-2343 (Frigola et al., 2007). **(e)** The grey filled line represents the concentration of C_{37} alkenones in the Alboran Sea record MD95-2043 (Cacho et al., 2002). **(f)** In green, the new $\delta^{18}O_{sw}$ ‰ (SMOW) presented in this work from the ALB-2 (Alboran Sea). **(g)** In orange, the calculated $\delta^{18}O_{sw}$ ‰ (SMOW) from the south Azores record GEOFAR-KF16 (Repschläger et al., 2017). Centred vertical bars: 8.4–9 cal. kyr BP corresponds to the Alboran Sea and North Atlantic synchrony in oceanographic changes; 4.2 cal. kyr BP corresponds to the double peach structure observed for ALB-2 Mg/Ca SST. The four vertical grey bars during the Late Holocene correspond to cold events of the ALB-2 Mg/Ca SST.

in the western Mediterranean Sea during this 4.2 cal. kyr BP event but not more than during previous and later Holocene events of this record (Frigola et al., 2007). On the other hand, the North Atlantic record (Fig. 5b) indicates that the 4.2 cal. kyr BP event corresponded to one of the Holocene's millennial-scale stratification events, interpreted as a weak mode of SPG circulation (Thornalley et al., 2009). This situation contrasts with that observed during the Early Holocene period, when weak SPG circulation coexisted with maximum SSTs in the Alboran Sea. Interestingly, after the 4.2 cal. kyr BP event, both the Alboran and the North Atlantic records show an intense millennial-scale variability, with minima in Alboran SSTs occurring systematically during periods of weak SPG circulation (Fig. 5b and c). However, further information would be required to establish a mechanism that could potentially link these apparent changes in the Late Holocene AMOC to properties in the Atlantic inflow in the Alboran Sea.

Further insight into the Holocene evolution of the inflowing Atlantic water comes from the ALB-2 $\delta^{18}O_{sw}$ reconstruction (Fig. 5f). This record also differentiates three Holocene periods consistent with those defined by the SST record (Fig. 5c). The ALB-2 $\delta^{18}O_{sw}$ record is compared with another $\delta^{18}O_{sw}$ record (Fig. 5g) that reflects conditions of the subsurface waters from the subtropical gyre (Repschläger et al., 2017). Interestingly, the relationship between these two records changes for the three defined Holocene intervals (Fig. 5f and g). During the Early Holocene, Alboran waters were comparable to those from the STG, consistent with the previous discussed entrance of subtropical waters, while dominant stratified conditions in the Western Mediterranean preserved the tropical signal. During the Middle Holocene phase, while Alboran SST followed a cooling

trend, the $\delta^{18}O_{sw}$ record oscillates around its lightest values, even lighter than those from the STG during the same period, and this difference became larger across the interval (Fig. 5f and g). Such a situation suggests that the inflowing Atlantic waters were also fed by some lighter water mass, most likely from a higher-latitude source. This is consistent with the previously discussed enhanced transport of subtropical waters towards higher latitudes during this period that would have led to stronger southward-influenced SPG source waters that would ultimately mix with the Atlantic inflow waters. This situation is consistent with the described intensification of the SPG by Thornalley et al. (2009) and is the dominant influence of subpolar source central waters at intermediate depths in the mid-latitude North Atlantic (Colin et al., 2010). After the 4.2 cal. kyr BP event, the STG and Alboran $\delta^{18}O_{sw}$ records converge although ALB-2 values remain lighter for most of the interval (Fig. 5f and g). This situation may indicate a reduced southward influence of SPG waters during the Late Holocene, consistent with the interpreted STG source of intermediate waters in the mid-latitude North Atlantic (Colin et al., 2010). The Late Holocene millennial-scale variability is difficult to characterize in this Atlantic–Mediterranean $\delta^{18}O_{sw}$ comparison (Fig. 5f and g) due to uncertainties in the relative chronologies and errors in the proxy reconstruction. Thus, further information needs to be explored to ultimately determine the nature of a potential Late Holocene Atlantic–Mediterranean millennial-scale connection.

5 Conclusions

The analysis of Mg/Ca SSTs and the $\delta^{18}O$ from the ALB-2 record have allowed the reconstruction of the paleoceanography of the Alboran Sea during the Holocene and its possible interactions with the Atlantic Ocean. The comparison of new generated oxygen isotopes ($\delta^{18}O$) and Mg/Ca SST records from ALB-2 with other western Mediterranean records confirms a common oceanographic signal and suggests the fast modification of the Atlantic inflow water to a more Mediterranean signal, indicating intense surface mixing with the underlying Mediterranean waters.

The western Mediterranean Mg/Ca SST signal strongly supports the value of this proxy to reconstruct true regional environmental conditions, despite significant differences that emerge when it is compared to previously published alkenone SST records. This proxy comparison is extended to the glacial period, which reveals a major proxy difference during deglaciation, particularly during the second warming phase after the YD period, which is nearly absent in all the Mg/Ca SST records. This damped warming in the Mg/Ca record reflects the resilient capacity of *G. bulloides* to change the growth season in order to compensate for the large SST deglacial warming. Therefore, during the last glacial period as well as for the first part of deglaciation, *G. bulloides* mostly grew during the milder upwelling season (autumn), while, after the YD, *G. bulloides* minimized the impact of the warming by mostly developing during the colder upwelling season (spring), which is also the present situation. In contrast, during the Holocene, SST variability is far larger in the Mg/Ca SST record ($\sim 5\,^{\circ}C$) than for the alkenone SST record ($\sim 2\,^{\circ}C$). We interpreted this Mg/Ca SST variability as a true climate evolution for a single season (spring), whereas the reduced variability in the alkenone SST reflects a well-averaged annual signal.

The new high-resolution Holocene Mg/Ca SST record differentiates three intervals according to its main patterns: (1) the warmest SST values occurred during the Early Holocene (11.7–9 cal. kyr BP); (2) during the Middle Holocene, there was a continuous cooling trend that culminated with the coldest Holocene SST with a double cold peak structure centred at around 4.2 cal. kyr BP; (3) the Late Holocene (4.2 cal. kyr BP–present) did not follow any clear cooling/warming trend, but millennial-scale oscillations were enhanced. This general Holocene SST evolution matches to some extent of solar energy redistribution by the changing orbital configuration; nevertheless, the intensity of the changes and the short-term variability requires the action of some other factors.

The warmest SST of the Early Holocene (11–9 cal. kyr BP) occurred while intense meltwater pulses from the Laurentide ice sheet could have led to a reduction in the northward heat transport from the STG towards the North Atlantic, and the consequent heat accumulation could have contributed to the warm inflow to the Mediterranean Sea. The onset of the cooling trend occurred at 9 cal. kyr BP, and the relative evolution of the $\delta^{18}O_{sw}$ records from the Alboran Sea and the STG suggest the arrival through Gibraltar of light waters from northern latitudes, supporting an enhanced influence of high-latitude North Atlantic conditions in the inflowing waters to the Mediterranean Sea.

The 4.2 cal. kyr BP event is recorded in the Mg/Ca SST as a double cold peak event, reaching the lowest SST of the Holocene; it ended the cooling trend of the previous interval. This 4.2 cal. kyr BP event marks the onset of an intense millennial-scale variability that dominated during the Late Holocene and that coincides with an event of intense WMDW formation. Comparable millennial-scale variability has been previously described further north in the North Atlantic Ocean, in relation to the intensity of the SPG. The latest connections between these North Atlantic changes and the Alboran Sea need further information to be fully understood, but our observations highlight that the Atlantic–Mediterranean connections through the inflow waters operated in a different way during the Early and Late Holocene.

Data availability. Data produced in this paper can be found via the following links. HER-GC-ALB-2 age model: https://doi.org/10.1594/PANGAEA.901744 (Català et al., 2019a). HER-GC-ALB-2 $\delta^{18}O$:

https://doi.org/10.1594/PANGAEA.901663 (Català et al., 2019b). HER-GC-ALB-2 sea surface temperatures and Mg/Ca data: https://doi.org/10.1594/PANGAEA.901666c (Català et al., 2019). MD99-2343 age model update: https://doi.org/10.1594/PANGAEA.901685d (Català et al., 2019). MD99-2343 sea surface temperatures and Mg/Ca data: https://doi.org/10.1594/PANGAEA.901678e (Català et al., 2019). MD95-2043 sea surface temperatures and Mg/Ca data: https://doi.org/10.1594/PANGAEA.901746f (Català et al., 2019).

Supplement. The supplement related to this article is available online at: https://doi.org/10.5194/cp-15-927-2019-supplement.

Competing interests. The authors declare that they have no conflict of interest.

Acknowledgements. This research has been financially supported by the ERC Consolidator Grant TIMED (683237) and CHIMERA project (CTM2016-75411-R). Core ALB-2 was recovered by the HERMESIONE expedition on board R/V *Hespérides* in 2009. The GRC Geociències Marines thank the Generalitat de Catalunya for the Grups de Recerca Consolidats grant 2017 SGR 315. Leopoldo D. Pena acknowledges support from the Ramón y Cajal program (MINECO, Spain). Isabel Cacho thanks the ICREA Academia programme from the Generalitat de Catalunya. We are grateful to Montse Guart (Dept. Dinàmica de la Terra i de l'Oceà, Universitat de Barcelona), Maite Romero, Antoni Padró, and Joaquím Perona (Centres Científics i Tecnològics, CCiT-UB) for technical support and Grant George Buffett for language improvements. We also acknowledge the guest editor and the anonymous reviewers for their comments, which improved this paper.

Review statement. This paper was edited by Raymond Bradley and reviewed by three anonymous referees.

References

Andrews, J. T., Hardadottir, J., Stoner, J. S., Mann, M. E., Kristjansdottir, G. B., and Koc, N.: Decadal to millennial-scale periodicities in North Iceland shelf sediments over the last 12 000 cal yr: long-term North Atlantic oceanographic variability and solar forcing, Earth Planet. Sc. Lett., 210, 453–465, https://doi.org/10.1016/S0012-821X(03)00139-0, 2003.

Ausin, B., Flores, J. A., Sierro, F. J., Cacho, I., Hernández-Almeida, I., Martrat, B., and Grimalt, J. O.: Atmospheric patterns driving Holocene productivity in the Alboran Sea (Western Mediterranean): A multiproxy approach, Holocene, 25, 583–595, https://doi.org/10.1177/0959683614565952, 2015.

Bárcena, M. A., Flores, J. A., Sierro, F. J., Pérez-Folgado, M., Fabres, J., Calafat, A., and Canals, M.: Planktonic response to main oceanographic changes in the Alboran Sea (Western Mediterranean) as documented in sediment traps and surface sediments, Mar. Micropaleontol., 53, 423–445, https://doi.org/10.1016/j.marmicro.2004.09.009, 2004.

Barker, S., Greaves, M., and Elderfield, H.: A study of cleaning procedures used for foraminiferal Mg/Ca paleothermometry, Geochem. Geophy. Geosy., 4, 1–20, https://doi.org/10.1029/2003GC000559, 2003.

Bartlein, P. J., Harrison, S. P., Brewer, S., Connor, S., Davis, B. A. S., Gajewski, K., Guiot, J., Henderson, A., Peyron, O., Prentice, I. C., Scholze, M., Seppä, H., Shuman, B., Sugita, S., Thompson, R. S., Viau, A. E., Williams, J., and Wu, H.: Pollen-based continental climate reconstructions at 6 and 21 ka: a global synthesis, Clim. Dynam., 37, 775–802, https://doi.org/10.1007/s00382-010-0904-1, 2011.

Béthoux, J. P.: Mean water fluxes across sections in the Mediterranean Sea, evaluated in the basis of water and salt budgets and of observed salinities, Oceanol. Acta, 3, 79–88, 1980.

Blaauw, M. and Christen, J. A.: Flexible paleoclimate age-depth models using an autoregressive gamma process, Bayesian Anal., 6, 457–474, https://doi.org/10.1214/11-BA618, 2011.

Bond, G., Showers, W., Cheseby, M., Lotti, R., Almasi, P., DeMenocal, P., Priore, P., Cullen, H., Hajdas, I., and Bonani, G.: A Pervasive Millennial-Scale Cycle in North Atlantic Holocene and Glacial Climates, Science, 278, 1257–1266, https://doi.org/10.1126/science.278.5341.1257, 1997.

Bond, G., Kromer, B., Beer, J., Muscheler, R., Evans, M. N., Showers, W., Hoffmann, S., Lotti-Bond, R., Hajdas, I., and Bonani, G.: Persistent Solar Influenceon North Atlantic Climate During the Holocene, Science, 294, 2130–2136, https://doi.org/10.1126/science.1065680, 2001.

Böning, C. W., Scheinert, M., Dengg, J., Biastoch, A., and Funk, A.: Decadal variability of subpolar gyre transport and its reverberation in the North Atlantic overturning, Geophys. Res. Lett., 33, 1–5, https://doi.org/10.1029/2006GL026906, 2006.

Boyer, T. and Mishonov, A.: 14 pp., World Ocean Atlas 2013 Product Documentation, 2013.

Bray, N. A., Ochoa, J., and Kinder, T. H.: The role of the interface exchange through the Strait of Gibraltar, J. Geophys. Res., 100, 10755–10176, https://doi.org/10.1029/95JC00381, 1995.

Cacho, I., Grimalt, J. O., Pelejero, C., Canals, M., Sierro, F. J., Flores, J. A., and Shackleton, N.: Dansgaard-Oeschger and Heinrich event imprints in Alboran Sea paleotemperatures, Paleoceanography, 14, 698–705, https://doi.org/10.1029/1999PA900044, 1999.

Cacho, I., Grimalt, J. O., Canals, M., Sbaffi, L., Shackleton, N. J., Schönfeld, J., and Zahn, R.: Variability of the western Mediterranean Sea surface temperature during the last 25,000 years and its connection with the Northern Hemisphere climatic changes, Paleoceanography, 16, 40–52, https://doi.org/10.1029/2000PA000502, 2001.

Cacho, I., Grimalt, J. O., and Canals, M.: Response of the Western Mediterranean Sea to rapid climatic variability during the last 50,000 years: A molecular biomarker approach, J. Mar. Syst., 33–34, 253–272, https://doi.org/10.1016/S0924-7963(02)00061-1, 2002.

Català, A., Cacho, I., Frigola, J., Peña, L. D., Lirer, F.: Deglacial and Holocene sea surface temperature (SST) and δ^{18}O reconstruction from the western Mediterranean Sea, PANGAEA, https://doi.org/10.1594/PANGAEA.901667, 2019a.

Català, A., Cacho, I., Frigola, J., Peña, L. D., Lirer, F.: Stable Isotopes (δ^{18}O) analysis of G. bulloides from

sediment core HER-GC-ALB2 (ALB-2), PANGAEA, https://doi.org/10.1594/PANGAEA.901663, 2019b.

Català, A., Cacho, I., Frigola, J., Peña, L. D., Lirer, F.: Sea surface temperature (SST) and Mg/Ca analysis of G. bulloides from sediment core HER-GC-ALB2 (ALB-2), PANGAEA, https://doi.org/10.1594/PANGAEA.901666, 2019c.

Català, A., Cacho, I., Frigola, J., Peña, L. D., Lirer, F.: Age-model update from sediment core MD99-2343, PANGAEA, https://doi.org/10.1594/PANGAEA.901685, 2019d.

Català, A., Cacho, I., Frigola, J., Peña, L. D., Lirer, F.: Sea surface temperature (SST) and Mg/Ca analysis of G. bulloides from sediment core MD99-2343, PANGAEA, https://doi.org/10.1594/PANGAEA.901678, 2019d.

Català, A., Cacho, I., Frigola, J., Peña, L. D., Lirer, F.: Sea surface temperature (SST) and Mg/Ca analysis of G. bulloides from sediment core MD95-2043, PANGAEA, https://doi.org/10.1594/PANGAEA.901746, 2019e.

Chabaud, L., Sánchez Goñi, M. F., Desprat, S., and Rossignol, L.: Land–sea climatic variability in the eastern North Atlantic subtropical region over the last 14,200 years: Atmospheric and oceanic processes at different timescales, Holocene, 24, 787–797, https://doi.org/10.1177/0959683614530439, 2014.

Cisneros, M., Cacho, I., Frigola, J., Canals, M., Masqué, P., Martrat, B., Casado, M., Grimalt, J. O., Pena, L. D., Margaritelli, G., and Lirer, F.: Sea surface temperature variability in the central-western Mediterranean Sea during the last 2700 years: a multi-proxy and multi-record approach, Clim. Past, 12, 849–869, https://doi.org/10.5194/cp-12-849-2016, 2016.

Cléroux, C., Debret, M., Cortijo, E., Duplessy, J.-C., Dewilde, F., Reijmer, J., and Massei, N.: High-resolution sea surface reconstructions off Cape Hatteras over the last 10 ka, Paleoceanography, 27, 1–14, https://doi.org/10.1029/2011PA002184, 2012.

Colin, C., Frank, N., Copard, K., and Douville, E.: Neodymium isotopic composition of deep-sea corals from the NE Atlantic: implications for past hydrological changes during the Holocene, Quaternary Sci. Rev., 29, 2509–2517, https://doi.org/10.1016/j.quascirev.2010.05.012, 2010.

Combourieu Nebout, N., Turon, J., Zahn, R., Capotondi, L., Londeix, L., and Pahnke, K.: Enhanced aridity and atmospheric high-pressure stability over the western Mediterranean during the North Atlantic cold events of the past 50 k.y., Geology, 30, 863–866, 2002.

Combourieu Nebout, N., Peyron, O., Dormoy, I., Desprat, S., Beaudouin, C., Kotthoff, U., and Marret, F.: Rapid climatic variability in the west Mediterranean during the last 25 000 years from high resolution pollen data, Clim. Past, 5, 503–521, https://doi.org/10.5194/cp-5-503-2009, 2009.

Coplen, T. B.: New guidelines for reporting stable hydrogen, carbon, and oxygen isotope-ratio data, Geochim. Cosmochim. Ac., 60, 3359–3360, https://doi.org/10.1016/0016-7037(96)00263-3, 1996.

Craig, H.: The measurement of oxygen isotope paleotemperatures, in: Stable Isotopes in Oceanographic Studies and Paleotemperatures, edited by: Tongiorgi, E., Consiglio Nazionale delle Ricerche, Laboratorio di Geologia Nucleare, Pisa, 1–24, 1965.

Debret, M., Bout-Roumazeilles, V., Grousset, F., Desmet, M., McManus, J. F., Massei, N., Sebag, D., Petit, J.-R., Copard, Y., and Trentesaux, A.: The origin of the 1500-year climate cycles in Holocene North-Atlantic records, Clim. Past, 3, 569–575, https://doi.org/10.5194/cp-3-569-2007, 2007.

Debret, M., Sebag, D., Crosta, X., Massei, N., Petit, J.-R., Chapron, E., and Bout-Roumazeilles, V.: Evidence from wavelet analysis for a mid-Holocene transition in global climate forcing, Quaternary Sci. Rev., 28, 2675–2688, https://doi.org/10.1016/j.quascirev.2009.06.005, 2009.

Desprat, S., Combourieu-Nebout, N., Essallami, L., Sicre, M. A., Dormoy, I., Peyron, O., Siani, G., Bout Roumazeilles, V., and Turon, J. L.: Deglacial and Holocene vegetation and climatic changes in the southern Central Mediterranean from a direct land-sea correlation, Clim. Past, 9, 767–787, https://doi.org/10.5194/cp-9-767-2013, 2013.

Elderfield, H. and Ganssen, G.: Past temperature and delta18O of surface ocean waters inferred from foraminiferal Mg/Ca ratios, Nature, 405, 442–445, https://doi.org/10.1038/35013033, 2000.

Fabres, J., Calafat, A., Sanchez-Vidal, A., Canals, M., and Heussner, S.: Composition and spatio-temporal variability of particle fluxes in the Western Alboran Gyre, Mediterranean Sea, J. Marine Syst., 33–34, 431–456, doi.org/10.1016/S0924-7963(02)00070-2, 2002.

Ferguson, J. E., Henderson, G. M., Kucera, M., and Rickaby, R. E. M.: Systematic change of foraminiferal Mg/ Ca ratios across a strong salinity gradient, Earth Planet. Sc. Lett., 265, 153–166, https://doi.org/10.1016/j.epsl.2007.10.011, 2008.

Fiúza, A. F. G.: Hidrologia e dinamica das aguas costeiras de Portugal, PhD Thesis, Universidade de Lisboa, 1984.

Fletcher, W. J., Debret, M., and Sanchez-Goñi, M.-F.: Mid-Holocene emergence of a low-frequency millennial oscillation in western Mediterranean climate: Implications for past dynamics of the North Atlantic atmospheric westerlies, Holocene, 0, 1–14, https://doi.org/10.1177/0959683612460783, 2012.

Frigola, J., Moreno, A., Cacho, I., Canals, M., Sierro, F. J., Flores, J. A., Grimalt, J. O., Hodell, D. A., and Curtis, J. H.: Holocene climate variability in the western Mediterranean region from a deepwater sediment record, Paleoceanography, 22, 2209, https://doi.org/10.1029/2006PA001307, 2007.

Frigola, J., Moreno, A., Cacho, I., Canals, M., Sierro, F. J., Flores, J. A., and Grimalt, J. O.: Evidence of abrupt changes in Western Mediterranean Deep Water circulation during the last 50 kyr: A high-resolution marine record from the Balearic Sea, Quatern. Int., 181, 88–104, https://doi.org/10.1016/j.quaint.2007.06.016, 2008.

Gao, Y.-Q. and Yu, L.: Subpolar Gyre Index and the North Atlantic Meridional Overturning Circulation in a Coupled Climate Model, Atmos. Ocean. Sci. Lett., 1, 29–32, 2008.

Giraudeau, J., Grelaud, M., Solignac, S., Andrews, J. T., Moros, M., and Jansen, E.: Millennial-scale variability in Atlantic water advection to the Nordic Seas derived from Holocene coccolith concentration records, Quaternary Sci. Rev., 29, 1276–1287, https://doi.org/10.1016/j.quascirev.2010.02.014, 2010.

Hemleben, C., Spindler, M., and Roger Anderson, O.: Modern Planktonic Foraminifera, Spinger, https://doi.org/10.1007/978-1-4612-3544-6, 1989.

Hernández-Almeida, I., Bárcena, M. A., Flores, J. A., Sierro, F. J., Sanchez-Vidal, A., and Calafat, A.: Microplankton response to environmental conditions in the Alboran Sea (Western Mediterranean): One year sediment trap record, Mar. Micropaleon-

tol., 78, 14–24, https://doi.org/10.1016/j.marmicro.2010.09.005, 2011.

Hönisch, B., Allen, K. A., Lea, D. W., Spero, H. J., Eggins, S. M., Arbuszewski, J., DeMenocal, P., Rosenthal, Y., Russell, A. D., and Elderfield, H.: The influence of salinity on Mg/ Ca in plank- tic foraminifers – evidence from cultures, core-top sediments and complementary δ18O, Geochim. Cosmochim. Ac., 121, 196–213, 2013.

Hoogakker, B. A. A., Klinkhammer, G. P., Elderfield, H., Rohling, E. J., and Hayward, C.: Mg/Ca paleothermometry in high salinity environments, Earth Planet. Sc. Lett., 284, 583–589, https://doi.org/10.1016/j.epsl.2009.05.027, 2009.

Jalali, B., Sicre, M.-A., Bassetti, M.-A., and Kallel, N.: Holocene climate variability in the North-Western Mediterranean Sea (Gulf of Lions), Clim. Past, 12, 91–101, https://doi.org/10.5194/cp-12-91-2016, 2016.

Jalali, B., Sicre, M.-A., Azuara, J., Pellichero, V., and Combourieu-Nebout, N.: Influence of the North Atlantic subpolar gyre circulation on the 4.2 ka BP event, Clim. Past, 15, 701–711, https://doi.org/10.5194/cp-15-701-2019, 2019.

Jiménez-Amat, P. and Zahn, R.: Offset timing of climate oscillations during the last two glacial-interglacial transitions connected with large-scale freshwater perturbation, Paleoceanography, 30, 768–788, https://doi.org/10.1002/2014PA002710, 2015.

Kemle-von Mücke, S. and Hemleben, C.: Foraminifera, in: South Atlantic Zooplankton, edited by: Boltovskoy, D., Backhuys Publishers, Leiden, the Netherlands, 1999.

Kim, J.-H., Rimbu, N., Lorenz, S. J., Lohmann, G., Nam, S., Schouten, S., Ru, C., and Schneider, R. R.: North Pacific and North Atlantic sea-surface temperature variability during the Holocene, Quaternary Sci. Rev., 23, 2141–2154, https://doi.org/10.1016/j.quascirev.2004.08.010, 2004.

Kucera, M. and Darling, K. F.: Cryptic species of planktonic foraminifera: their effect on palaeoceanographic reconstructions, Philos. T. Roy. Soc. A, 360, 695–718, https://doi.org/10.1098/rsta.2001.0962, 2002.

Kucera, M., Weinelt, M., Kiefer, T., Pflaumann, U., Hayes, A., Weinelt, M., Chen, M. Te, Mix, A. C., Barrows, T. T., Cortijo, E., Duprat, J., Juggins, S., and Waelbroeck, C.: Reconstruction of sea-surface temperatures from assemblages of planktonic foraminifera: multi-technique approach based on geographically constrained calibration data sets and its application to glacial Atlantic and Pacific Oceans, Quaternary Sci. Rev., 24, 951–998, https://doi.org/10.1016/j.quascirev.2004.07.014, 2005.

Lacombe, H., Gascard, J. C, Cornella, J., and Béthoux, J. P.: Response ofthe Mediterranean to the water and energy fluxes across its surface, on seasonal and interannual scales, Oceanol. Acta, 4, 247–255, 1981.

Laepple, T. and Huybers, P.: Reconciling discrepancies between Uk37 and Mg/Ca reconstructions of Holocene marine temperature variability, Earth Planet. Sc. Lett., 375, 418–429, 2013.

Lionello, P., Malanotte-Rizzoli, P., Boscolo, R., Alpert, P., Artale, V., Li, L., Luterbacher, J., May, W., Trigo, R., Tsimplis, M., Ulbrich, U., and Xoplaki, E.: The Mediterranean climate: An overview of the main characteristics and issues, Dev. Earth Environ. Sci., 4, 1–26, https://doi.org/10.1016/S1571-9197(06)80003-0, 2006.

Lorenz, S. J. and Lohmann, G.: Acceleration technique for Milankovitch type forcing in a coupled atmosphere-ocean circulation model: method and application for the Holocene, Clim. Dynam., 23, 727–743, https://doi.org/10.1007/s00382-004-0469-y, 2004.

Marchal, O., Cacho, I., Stockera, T. F., Grimalt, J. O., Calvo, E., Martrat, B., Shackleton, N., Vautravers, M., Cortijo, E., Kreveld, S. van, Andersson, C., Koç, N., Chapman, M., Sbaffi, L., Duplessy, J.-C., Sarnthein, M., Turon, J.-L., Duprat, J., and Jansen, E.: Apparent long-termcooling of the sea surface in the northeast Atlantic and Mediterranean during the Holocene, Quaternary Sci. Rev., 21, 455–483, https://doi.org/10.1016/S0277-3791(01)00105-6, 2002.

Marchitto, T. M. and DeMenocal, P. B.: Late Holocene variability of upper North Atlantic Deep Water temperature and salinity, Geochem. Geophy. Geosy., 4, 1100, https://doi.org/10.1029/2003GC000598, 2003.

Martrat, B., Grimalt, J. O., Lopez-Martínez, C., Cacho, I., Sierro, F. J., Flores, J. A., Zhang, R., Canals, M., Curtis, J. H., and Hodell, D. A.: Abrupt Temperature changes in the Western Mediterranean oer the past 250,000 years, Science, 306, 1762–1765, https://doi.org/10.1126/science.1101706, 2004.

Martrat, B., Jimenezamat, P., Zahn, R., and Grimalt, J. O.: Similarities and dissimilarities between the last two deglaciations and interglaciations in the North Atlantic region, Quaternary Sci. Rev., 99, 122–134, https://doi.org/10.1016/j.quascirev.2014.06.016, 2014.

Millot, C.: Circulation in the Western Mediterranean Sea, J. Mar. Syst., 20, 423–442, https://doi.org/10.1016/S0924-7963(98)00078-5, 1999.

Millot, C.: Progress in Oceanography Another description of the Mediterranean Sea outflow, Prog. Oceanogr., 82, 101–124, https://doi.org/10.1016/j.pocean.2009.04.016, 2009.

Moreno, A., Cacho, I., Canals, M., Prins, M. A., Sánchez-Goñi, M.-F., Grimalt, J. O., and Weltje, G. J.: Saharan Dust Transport and High-Latitude Glacial Climatic Variability: The Alboran Sea Record, Quaternary Res., 58, 318–328, https://doi.org/10.1006/qres.2002.2383, 2002.

Moros, M., Emeis, K., Risebrobakken, B., Snowball, I., Kuijpers, A., McManus, J., and Jansen, E.: Sea surface temperatures and ice rafting in the Holocene North Atlantic: climate influences on northern Europe and Greenland, Quaternary Sci. Rev., 23, 2113–2126, https://doi.org/10.1016/j.quascirev.2004.08.003, 2004.

Nieto-Moreno, V., Martínez-Ruiz, F., Giralt, S., Jiménez-Espejo, F., Gallego-Torres, D., Rodrigo-Gámiz, M., García-Orellana, J., Ortega-Huertas, M., and de Lange, G. J.: Tracking climate variability in the western Mediterranean during the Late Holocene: a multiproxy approach, Clim. Past, 7, 1395–1414, https://doi.org/10.5194/cp-7-1395-2011, 2011.

Pena, L. D., Calvo, E., Cacho, I., Eggins, S., and Pelejero, C.: Identification and removal of Mn-Mg-rich contaminant phases on foraminiferal tests: Implications for Mg/Ca past temperature reconstructions, Geochem. Geophy. Geosy., 6, Q09P02, https://doi.org/10.1029/2005GC000930, 2005.

Pierre, C.: The oxygen and carbon isotope distribution in the Mediterranean water masses, Mar. Geol., 153, 41–55, 1999.

Prahl, F., Herbert, T., Brassell, S. C., Ohkouchi, N., Pagani, M., Repeta, D., Rosell-Melé, A., and Sikes, E.: Status of alkenone paleothermometer calibration: Report from Working Group 3, Geochem. Geophy. Geosy., 1, 2000GC000058, https://doi.org/10.1029/2000GC000058, 2000.

Rao, K. K., Paulinose, V. T., Jayalakshmy, K. V., Panikkar, B. M., and Krishnan Kutty, M.: Distribution of Living Planktonic Foraminifera in the Coastal Upwelling Region of Kenya, Africa, Indian J. Mar. Sediments, 17, 121–127, 1988.

Reimer, P. J., Bard, E., Bayliss, A., Beck, J. W., Blackwell, P. G., Bronk, C., Caitlin, R., Hai, E. B., Edwards, R Lawrence Friedrich, M., Grootes, P. M., Guilderson, T. P., Haflidason, H., Hajdas, I., Hatté, C., Heaton, T. J., Hoffmann, D. L., Hogg, A. G., Hughen, K. A., Kaiser, K. F., Kromer, B., Manning, S. W., Niu, M., Reimer, R. W., Richards, D. A., Scott, E. M., Southon, J. R., Staff, R. A., Turney, C. S. M., and van der Plicht, J.: Intcal13 and marine13 radiocarbon age calibration curves 0–50 000 Years cal BP, Radiocarbon, 55, 1869–1887, https://doi.org/10.2458/azu_js_rc.55.16947, 2013.

Repschläger, J., Garbe-Schönberg, D., Weinelt, M., and Schneider, R.: Holocene evolution of the North Atlantic subsurface transport, Clim. Past, 13, 333–344, https://doi.org/10.5194/cp-13-333-2017, 2017.

Rigual-Hernández, A. S., Sierro, F. J., Bárcena, M. A., Flores, J. A., and Heussner, S.: Seasonal and interannual changes of planktic foraminiferal fluxes in the Gulf of Lions (NW Mediterranean) and their implications for paleoceanographic studies: two 12-year sediment trap records, Deep-Sea Res. Pt. I, 66, 26–40, https://doi.org/10.1016/j.dsr.2012.03.011, 2012.

Rimbu, N., Lohmann, G., Lorenz, S. J., Kim, J. H., and Schneider, R. R.: Holocene climate variability as derived from alkenone sea surface temperature and coupled ocean-atmosphere model experiments, Clim. Dynam., 23, 215–227, https://doi.org/10.1007/s00382-004-0435-8, 2004.

Roberts, N., Moreno, A., Valero-Garcés, B. L., Corella, J. P., Jones, M., Allcock, S., Woodbridge, J., Morellón, M., Luterbacher, J., Xoplaki, E., and Türkeş, M.: Palaeolimnological evidence for an east–west climate see-saw in the Mediterranean since AD 900, Global Planet. Change, 84–85, 23–34, https://doi.org/10.1016/j.gloplacha.2011.11.002, 2012.

Rodrigo-Gámiz, M., Martínez-Ruiz, F., Jiménez-Espejo, F. J., Gallego-Torres, D., Nieto-Moreno, V., Romero, O., and Ariztegui, D.: Impact of climate variability in the western Mediterranean during the last 20,000 years: oceanic and atmospheric responses, Quaternary Sci. Rev., 30, 2018–2034, https://doi.org/10.1016/j.quascirev.2011.05.011, 2011.

Rodrigo-Gámiz, M., Martínez-Ruíz, F., Rampen, S. W., Schouten, S., and Sinninghe Damsté, J. S.: Sea surface temperature variations in the western Mediterranean Sea over the last 20 kyr: A dual-organic proxy (UK′37 and LDI) approach, Paleoceanography, 29, 87–98, https://doi.org/10.1002/2013PA002466, 2014.

Rogerson, M., Cacho, I., Jimenez-Espejo, J., Reguera, M. I., Sierro, F. J., Martinez-Ruiz, F., Frigola, J., and Canals, M.: A dynamic explanation for the origin of the western Mediterranean organic-rich layers, Geochem. Geophy. Geosy., 9, Q07U01, https://doi.org/10.1029/2007GC001936, 2008.

Rosenthal, Y., Perron-Cashman, S., Lear, C. H., Bard, E., Barker, S., Billups, K., Bryan, M., Delaney, M., deMenocal, P. B., Dwyer, G. S., Elderfield, H., German, C. R., Greaves, M., Lea, D. W., Marchitto Jr, T. M., Pak, D. K., Paradis, G. L., Russell, A. D., Schneider, R. R., Scheiderich, K., Stott, L., Tachikawa, K., Tappa, E., Thunell, R., Wara, M., Weldeab, S., and Wilson, P. A.: Interlaboratory comparison study of Mg/Ca and Sr/Ca measurements in planktonic foraminifera for paleoceanographic research, Geochem. Geophy. Geosy., 5, Q04D09, https://doi.org/10.1029/2003GC000650, 2004

Sabatier, P., Dezileau, L., Colin, C., Briqueu, L., Bouchette, F., Martinez, P., Siani, G., Raynal, O., and Von Grafenstein, U.: 7000 years of paleostorm activity in the NW Mediterranean Sea in response to Holocene climate events, Quaternary Res., 77, 1–11, https://doi.org/10.1016/j.yqres.2011.09.002, 2012.

Schiebel, C. and Hemleben, C.: Planktic Foraminifers in the Modern Ocean, Springer, https://doi.org/10.1007/978-3-662-50297-6, 2017.

Shackleton, N.: Attainment of isotopic equilibrium between ocean water and the benthonic foraminifera genus Uvigerina: isotopic changes in the ocean during the last glacial, CNRS, Colloq. Int., 219, 203–209, 1974

Sicre, M.-A., Ternois, Y., Miquel, J.-C., and Marty, J.-C.: Alkenones in the Northwestern Mediterranean sea: interannual variability and vertical transfer, Geiohysical Res. Lett., 26, 1735–1738, https://doi.org/10.1029/1999GL900353, 1999.

Sierro, F. J., Hodell, D. A., Curtis, J. H., Flores, J. A., Reguera, I., Colmenero-Hidalgo, E., Bárcena, M. A., Grimalt, J. O., Cacho, I., Frigola, J., and Canals, M.: Impact of iceberg melting on Mediterranean thermohaline circulation during Heinrich events, Paleoceanography, 20, 1–13, https://doi.org/10.1029/2004PA001051, 2005.

Ternois, Y., Sicre, M.-A., Boireau, A., Contes, M. H., and Eglinton, G.: Evaluation of long-chain alkenones as paleo-temperature indicators in the Mediterranean Sea, Deep. Res. Pt. I, 44, 271–286, https://doi.org/10.1016/S0967-0637(97)89915-3, 1997.

Thornalley, D. J. R., Elderfield, H., and McCave, I. N.: Holocene oscillations in temperature and salinity of the surface subpolar North Atlantic, Nature, 457, 711–714, https://doi.org/10.1038/nature07717, 2009.

Tinner, W., van Leeuwen, J. F. N., Colombaroli, D., Vescovi, E., van der Knaap, W. O., Henne, P. D., Pasta, S., D'Angelo, S., and La Mantia, T.: Holocene environmental and climatic changes at Gorgo Basso, a coastal lake in southern Sicily, Italy, Quaternary Sci. Rev., 28, 1498–1510, https://doi.org/10.1016/j.quascirev.2009.02.001, 2009.

Tintore, J., La Violette, P. E., Blade, I., and Cruzado, A.: A study of an intense density front in eastern Alboran Sea: the Almeria-Oran Front, J. Phys. Oceanogr., 18, 1384–1397, https://doi.org/10.1175/1520-0485(1988)018<1384:ASOAID>2.0.CO;2, 1988.

Toucanne, S., Jouet, G., Ducassou, E., Bassetti, M., Dennielou, B., Morelle, C., Minto, A., Lahmi, M., Touyet, N., Charlier, K., Lericolais, G., and Mulder, T.: A 130,000-year record of Levantine Intermediate Water flow variability in the Corsica Trough, western Mediterranean Sea, Quaternary Sci. Rev., 33, 55–73, https://doi.org/10.1016/j.quascirev.2011.11.020, 2012.

Trigo, R. M., Osborn, T. J., and Corte-Real, J. M.: The North Atlantic Oscillation influence on Europe: climate impacts and associated physical mechanisms, Clim. Res., 20, 9–17, https://doi.org/10.3354/cr020009, 2002.

Tzedakis, P. C.: Seven ambiguities in the Mediterranean palaeoenvironmental narrative, Quaternary Sci. Rev., 26, 2042–2066, https://doi.org/10.1016/j.quascirev.2007.03.014, 2007.

van Raden, U. J., Groeneveld, J., Raitzsch, M., and Kucera, M.: Mg/Ca in the planktonic foraminifera Globorotalia inflata and Globigerinoides bulloides from Western Mediterranean plankton

tow and core top samples, Mar. Micropaleontol., 78, 101–112, https://doi.org/10.1016/j.marmicro.2010.11.002, 2011.

Versteegh, G. J. M., de Leeuw, J. W., Taricco, C., and Romero, A.: Temperature and productivity influences on U37 K0 and their possible relation to solar forcing of the Mediterranean winter, Geochem. Geophy. Geosy., 8, 1–14, https://doi.org/10.1029/2006GC001543, 2007.

Volkman, J. K., Eglinton, G., Corner, E. D. S., and Sargent, J. R.: Novel unsaturated straight-chain C_{37}-C_{39} methyl and ethyl ketones in marine sediment and a coccolithophore Emiliania huxleyi, Phys. Chem. Earth, 12, 219–227, doi.org/10.1016/0079-1946(79)90106-X, 1980.

Wanner, H., Beer, J., Bütikofer, J., Crowley, T. J., Cubasch, U., Flückiger, J., Goosse, H., Grosjean, M., Joos, F., Kaplan, J. O., Küttel, M., Müller, S. A., Prentice, I. C., Solomina, O., Stocker, T. F., Tarasov, P., Wagner, M., and Widmann, M.: Mid- to Late Holocene climate change: an overview, Quaternary Sci. Rev., 27, 1791–1828, https://doi.org/10.1016/j.quascirev.2008.06.013, 2008.

Zielhofer, C., Fletcher, W. J., Mischke, S., De Batist, M., Campbell, J. F. E., Joannin, S., Tjallingii, R., El Hamouti, N., Junginger, A., Stele, A., Bussmann, J., Schneider, B., Lauer, T., Spitzer, K., Strupler, M., Brachert, T., and Mikdad, A.: Atlantic forcing of Western Mediterranean winter rain minima during the last 12,000 years Christoph, Quaternary Sci. Rev., 157, 29–51, https://doi.org/10.1016/j.quascirev.2016.11.037, 2017.

Supplement of Clim. Past, 15, 927–942, 2019
https://doi.org/10.5194/cp-15-927-2019-supplement

Climate of the Past
Open Access
EGU

Supplement of

Holocene hydrography evolution in the Alboran Sea: a multi-record and multi-proxy comparison

Albert Català et al.

Correspondence to: Albert Català (al_catala@ub.edu)

Table S1: Core location and information included in the discussion.

Table S2: Radiocarbon ^{14}C AMS dates from the ALB-2 core. Dates are calibrated with the MARINE13 calibration curves (Reimer, et al., 2013)

Figure S3: ALB-2 age-depth model based on Bayesian accumulations simulations (Blaauw and Christen, 2011). (a) The three upper plots show the stable MCMC run achieved (left), the prior (green line) and posterior (grey) distributions of the accumulation rates (middle), and the prior (green line) and posterior (grey) distributions of the memory (right). The main graph shows (c) the age-depth model with its errors. Yellow dots, correspond to those tie-points (most recent, the recovering year of the core, and the last pone is product of the correlation with the well-expressed event in (b) MD99-2343 record. (d) Show the location of these dates on the ALB-2 $\delta^{18}O$ ‰ (VPDB). (e) Show the accumulation rates in (cm/kyr).

Table S4: Radiocarbon ^{14}C AMS dates from the MD99-2343 core. Dates are calibrated with the MARINE13 calibration curves (Reimer, et al., 2013)

Figure S5: MD99-2343 age-depth improved from the original published by Frigola et al. (2007). The age model is based on Bayesian accumulations simulations (Blaauw and Christen, 2011). (a) The three upper plots show the stable MCMC run achieved (left), the prior (green line) and posterior (grey) distributions of the accumulation rates (middle), and the prior (green line) and posterior (grey) distributions of the memory (right). The main graph shows (c) the age-depth model with its errors. Yellow dots, correspond to those tie-points (most recent, the recovering year of the core, and the other two points are product of the correlation with the well-expressed event in (b) MD95-2043 record. (d) Show the location of these dates on the MD99-2343 $\delta^{18}O$ ‰ (VPDB). (e) Show the accumulation rates in (cm/kyr).

Figure S6: Comparison for all ALB-2 data obtained between the G. bulloides Mg/Ca ratios with (a) Al/Ca and (b) Mn/Ca ratios (Pena et al., 2005). In both plots red dots are those samples that were removed to avoid possibles interferences in Mg/Ca – SST.

Section 7: The theoretical carbonate $\delta^{18}O$ signal in VPDB (‰) has been estimated for the upper 100 meters in the studied area and during different seasons after: (1) Estimating the present local $\delta^{18}O$ and salinity relationship in base to the Alboran Sea data from Pierre (1999): $S(psu)=0.995* \delta^{18}O_{sw}-35.668$. (2) This equation has been applied to obtain the theoretical $\delta^{18}O_{sw}$ for the upper 100 mwd in the studied area at different seasons in base to the salinity data from site 503737B, obtained from WOA13 0.25deg, and integrates water measurements from 1955 to 2012. (3) This estimated $\delta^{18}O_{sw}$ has been transferred to carbonate $\delta^{18}O$ through the temperature equation form Shackleton, 1974: $T(°C)=16.9-4(\delta_c-\delta_{sw})$ and after the standard conversion $\delta_{sw}(VPDB)=0.99973* \delta_{sw}(SMOW)-0.27$. Temperature data was obtained from site 503737B, (WOA13 0.25deg measured during the years 1955–2012).

REFERENCES

Blaauw, M. and Christen, J. A.: Bacon manual – v2.2, , 1–11, 2011.

Frigola, J., Moreno, A., Cacho, I., Canals, M., Sierro, F. J., Flores, J. A., Grimalt, J. O., Hodell, D. A. and Curtis, J. H.: Holocene climate variability in the western Mediterranean region from a deepwater sediment record, Paleoceanography, 22, 2209, doi:10.1029/2006PA001307, 2007.

Frigola, J., Moreno, A., Cacho, I., Canals, M., Sierro, F. J., Flores, J. A. and Grimalt, J. O.: Evidence of abrupt changes in Western Mediterranean Deep Water circulation during the last 50 kyr: A high-resolution marine record from the Balearic Sea, Quat. Int., 181(1), 88–104, doi:10.1016/j.quaint.2007.06.016, 2008.

Pena, L. D., Calvo, E., Cacho, I., Eggins, S. and Pelejero, C.: Identification and removal of Mn-Mg-rich contaminant phases on foraminiferal tests: Implications for Mg/Ca past temperature reconstructions, Geochemistry, Geophys. Geosystems, 6(9), doi:10.1029/2005GC000930, 2005.

Pierre, C.: The oxygen and carbon isotope distribution in the Mediterranean water masses, Mar. Geol., 153, 41–55, 1999.

Reimer, P. J., Bard, E., Bayliss, A., Beck, J. W., Blackwell, P. G., Bronk, C., Caitlin, R., Hai, E. B., Edwards, R Lawrence Friedrich, M., Grootes, P. M., Guilderson, T. P., Haflidason, H., Hajdas, I., Hatté, C., Heaton, T. J., Hoffmann, D. L., Hogg, A. G., Hughen, K. A., Kaiser, K. F., Kromer, B., Manning, S. W., Niu, M., Reimer, R. W., Richards, D. A., Scott, E. M., Southon, J. R., Staff, R. A., Turney, C. S. M. and van der Plicht, J.: INTCAL13 AND MARINE13 RADIOCARBON AGE CALIBRATION CURVES 0–50,000 YEARS CAL BP, Radiocarbon, 55(4), 1869–1887, doi:https://doi.org/10.2458/azu_js_rc.55.16947, 2013.

Shackleton, N.: Attainment of isotopic equilibrium between ocean water and the benthonic foraminifera genus Uvigerina: isotopic changes in the ocean during the last glacial, CNRS, Colloq. Int., 219, 203–209, 1974

World Ocean Atlas 2013 Product Documentation. T Boyer, Ed.; A. Mishonov, Technical Ed.; 14 pp.

Supplementari Figure
Table S1

Core	Location		Depth (mwd)	References
	Latitude	Longitude		
HER-GC-ALB-2	36°0'44.80" N	4°16'24.38" W	1313	Català *et al*., 2019
ODP976	36°12' N	4°18' W	1108	Jiménez-Amat and Zahn, 2015
MD95-2043	36°8'598" N	2°37'269" W	1841	Cacho *et al*., 1999
MD99-2343	40°29.84' N	4°01.69' E	2391	Frigola *et al*., 2007

Supplementari Figure
Table S2

Depth, cm	Specie	Age ^{14}C years BP	2σ error	Calendar Years
0	Tie Point (Recovered core year)	-	-	-56
10	*G. inflata*	725	25	407
15	*G. inflata*	1334	29	856.5
26	*G. inflata*	2097	26	1668
36	*G. inflata*	2688	26	2355.3
62	*G. inflata*	3778	28	3706.8
83	*G. inflata*	4538	27	4703.1
112	*G. inflata*	5370	30	5866
114	*G. inflata*	5773	31	5996.9
131	*G.inflata*	6200	90	6709.5
153	*G.inflata*	7170	85	7686.8
184	*G. inflata, N. pachyderma, G. bulloides*	8814	41	9192.1
209	*G. inflata, N. pachyderma*	9190	35	10094.2
231	*G. inflata, N. pachyderma*	10084	45	11094
265	*G. inflata, N. pachyderma, G. bulloides*	11194	42	12699.8
314	Tie Point (MD95-2043)	-	-	14610

Supplementari Figure
Figure S3

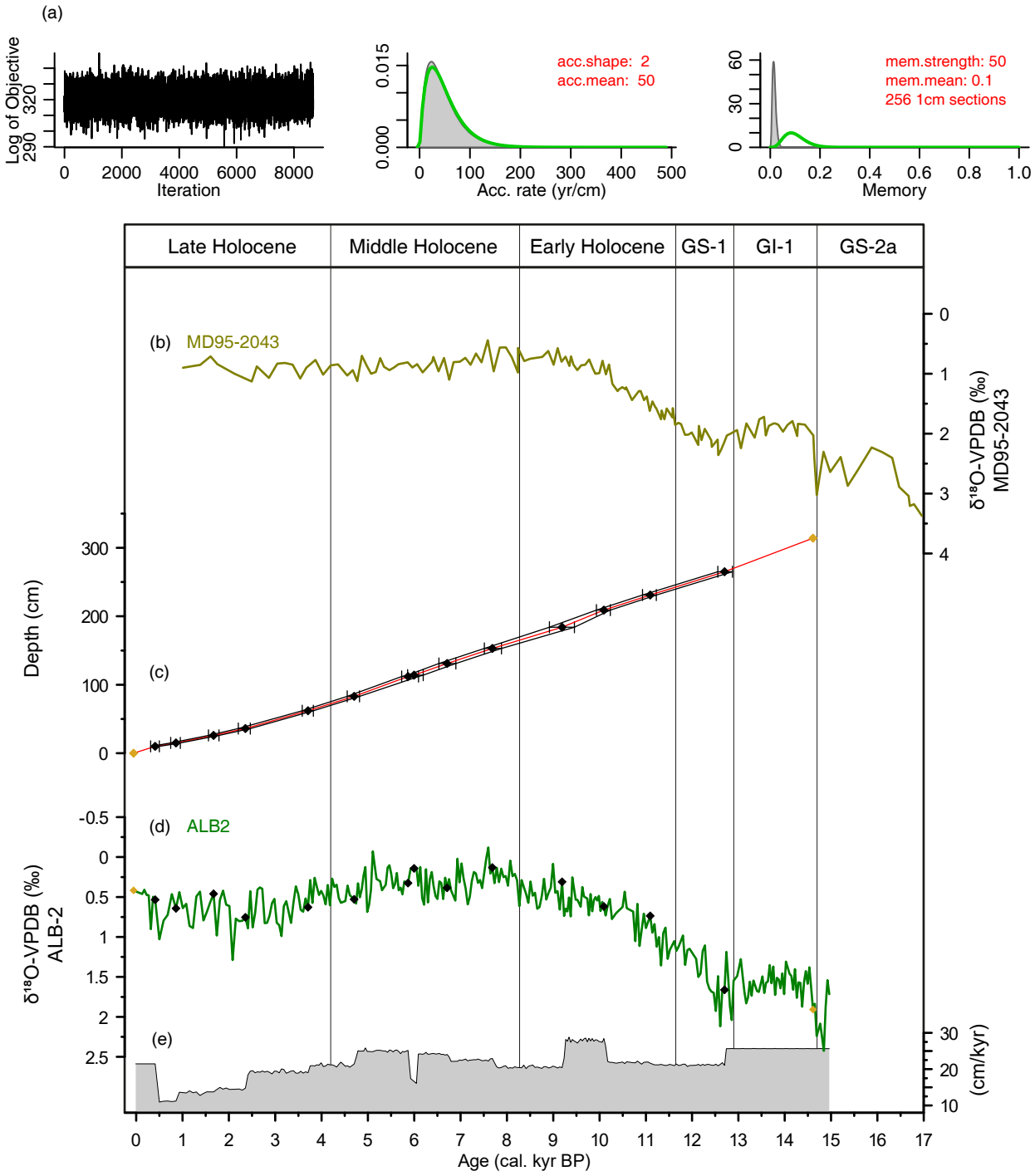

Supplementari Figure
Table S4

Depth, cm	Isotop Event/Radiocarbon Samples	Age ^{14}C years BP	2σ error	Calendar Years
0	Tie Point (Recovered core year)			-49
28	^{14}C AMS	790	89	436
42	^{14}C AMS	1090	61	680.3
54	^{14}C AMS	1520	90	1093.6
88	^{14}C AMS	3110	94.5	2612.4
118	^{14}C AMS	3390	142.5	3283.2
144	^{14}C AMS	3880	111	3887.9
184	^{14}C AMS	4850	128.5	5164.5
208	^{14}C AMS	5720	388.5	6009
238	^{14}C AMS	6210	135.5	6624.8
274	^{14}C AMS	6720	74	7314.6
296	^{14}C AMS	7580	107	7990.4
308	^{14}C AMS	7700	121	8266.4
312	^{14}C AMS	7660	85.5	8427.7
334	^{14}C AMS	8750	106	9411.1
364	^{14}C AMS	9890	180	10793
398	^{14}C AMS	10650	207	11978.1
418	^{14}C AMS	11200	116	12670.4
485	Tie Point - Base of GI-1			14622.4
534	Tie Point - Top Anomaly GS-2a			15373.2
568	^{14}C AMS	14550	344	16163.3
604	^{14}C AMS	13850	345	16980.9

Supplementari Figure
Figure S5

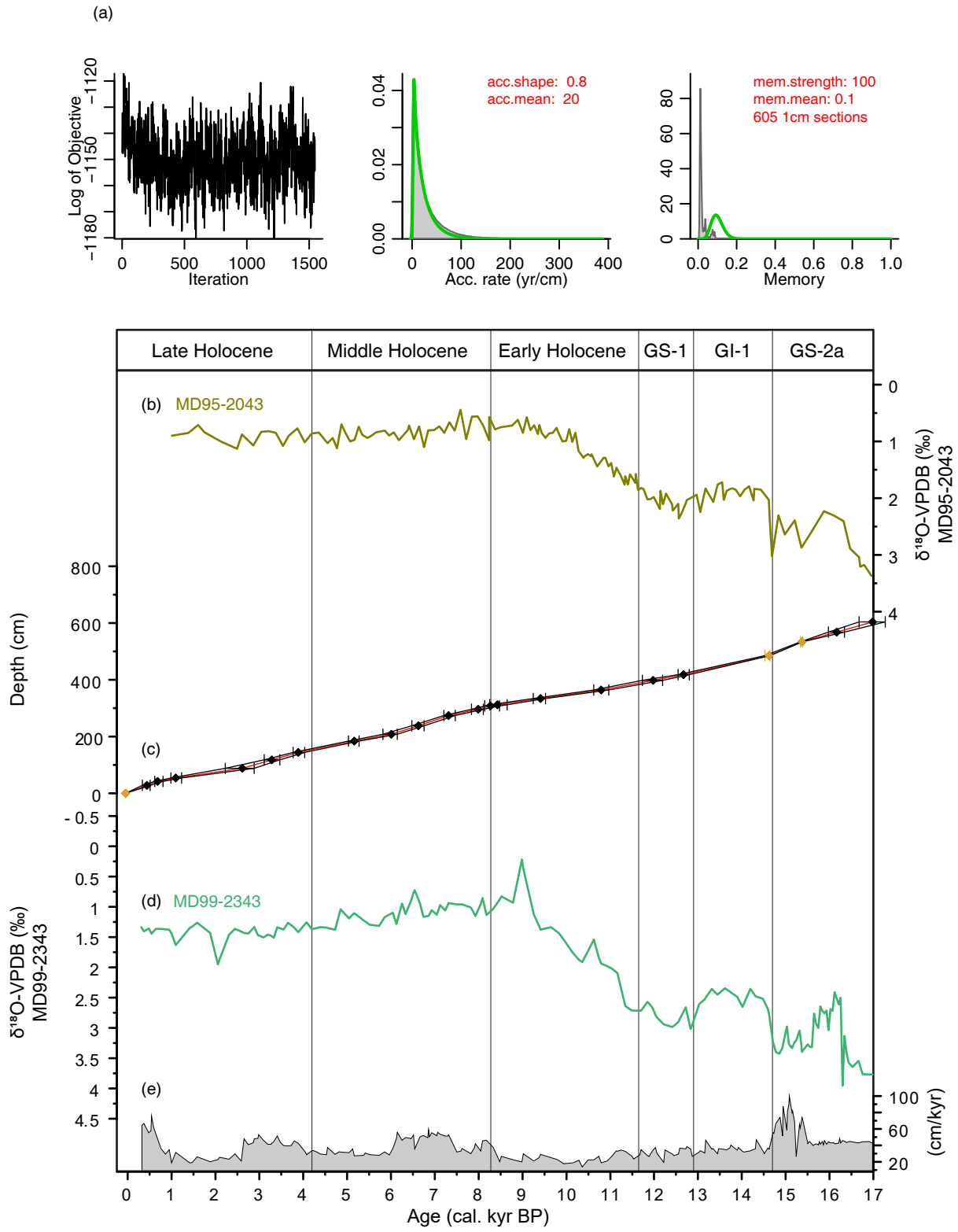

Supplementari Figure
Figure S6